

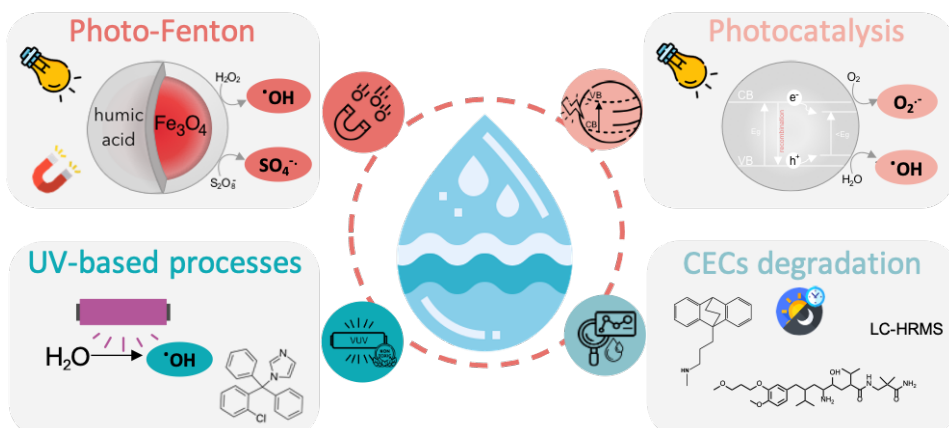


Università degli Studi di Torino

Doctoral School of the University of Torino

PhD Programme in Chemical and Materials Sciences XXXIII Cycle

Removal of CECs using photoactive materials; assessment of degradation paths and mechanism by means of high-resolution analytical techniques



Nuno Paulo Ferreira Gonçalves

Supervisor:

Prof. Alessandra Bianco Prevot



Università degli Studi di Torino

Doctoral School of the University of Torino

PhD Programme in Chemical and Materials Sciences XXXIII cycle

Removal of CECs using photoactive materials; assessment of degradation paths and mechanism by means of high-resolution analytical techniques

Candidate: **Nuno Paulo Ferreira Gonçalves**

Supervisor: Prof. **Alessandra Bianco Prevot**

Jury Members: Prof. **Debora Fabbri**
Università di degli Studi di Torino
Dipartimento di Chimica

Prof. **Antonio Arques**
University of Valencia
Department of Textile and Paper Engineering

Prof. **Vasilios A Sakkas**
University of Ioannina
Department of Chemistry

Head of the Doctoral School: Prof. Alberto Rizzuti

PhD Programme Coordinator: Prof. Bartolome Civalieri

Torino, 2021

Acknowledgements

First of all, a special acknowledgement to my family: my parents and brothers for all the support that made this international adventure much easier but most of all to Mirtha, my wife, for all the encouragement with enthusiasm, for embrace a new life in Italy and for making everything much easier and fun.

I want to thank Alessandra Bianco Prevot, my supervisor, for the humanity, guidance, advice, dedication and keen interest above all the overwhelming attitude to help, meticulous scrutiny and scientific approach that allowed me to grow as a researcher and helped me to accomplish this work. I also want to show highly appreciation to Paola Calza who also followed me during these three years, for all the guidance, prompt inspirations, suggestions with enthusiasm and dynamism that have been always helpful for all my problems, doubts and questions. A special thank also to Marco Minella and Debora Fabbri who gave me many guides on the laboratory experiments. Thanks also to all the people that I had the opportunity to work with: Maria Cristina Paganini, Erik Cerrato, Mattia Costamagna, Lucia Iezzi, Simone Baleuri, Federica Dal Bello and Claudio Medana.

During these years I could travel a lot and work in different places around Europe that were very important for my research work but also my personal development. I wish to thank Peter Roslev for having hosted me in Aalborg in the kindest possible way, for all the scientific discussions and the inspiring scientific approach, it was a great experience. Thank to Victor Candelario for hosted me in Copenhagen, for the support, flexibility and all the understanding in particular during the pandemic times. Thank to Stéphane Bouchonnet for the kindness reception during the journey in Paris and for sharing all the scientific knowledge. My gratitude also to Marcello Brigante, that hosted me in Clermont Ferrand, for all the guidance and for sharing his expertise.

Last but not least, a special thanks to all member of the AQUAlity project, especially to the ESRs colleagues for all the joy and fun during our meetings. In particular to those that I had the opportunity to collaborate with: Masho Belay, Zsuzsanna Varga, Ilaria Berruti, Oihane del Puerto and Dimitra Papagiannaki.

Finally, I want to thank all my colleagues of my research group and all my friends that were always with me during these three years. Thank you all.

Preface

Contaminants of emerging concern (CECs) are pointed as one of the main threats to the water quality for the next decades. One of the main goals of this PhD thesis was focused on the development and testing new catalysts to be used as advanced oxidation processes for the removal of those recalcitrant pollutants. New magnetic particles coated with humic acid were prepared as heterogeneous photo-Fenton catalyst. These materials were tested for the removal of CECs and the degradation conditions explored. Additionally, new semiconductor-based photocatalysts were prepared by the addition of transition metals as doping agents. The effect of the synthesis method, doping element and doping concentration on the photocatalytic properties was investigated for the pollutants removal.

Moreover, the non-invasive Vacuum-UV irradiation was explored for the removal of a persistent antifungal drug (clotrimazole). The inhibition on the drug ecotoxicity to test organisms was investigated as well as their ability to remove the pollutant at environmental concentrations.

Another main goal of this PhD thesis was also focused on the elucidation of the degradation pathways of water pollutants. For this, the degradation of two selected CECs (maprotiline and aliskiren) was investigated for the first time by means of high-resolution mass spectrometry. The photodegradation mechanisms were explored by spiking river water at realistic concentrations and the effect of natural water constituents explored. The formation of the identified photoproducts in the environment was then confirmed by retrospective suspected screening of digitally achieved chromatograms.

Abbreviations and Acronyms

AOPs	Advanced oxidation processes
BPA	Bisphenol A
CB	Conduction band
CBZ	Carbamazepine
CDI	Collision-induced dissociation
CECs	Contaminants of emerging concern
DOM	Dissolved organic matter
FTIR	Fourier transform infrared spectroscopy
FoA	Frequency of appearance
H	Hydrothermal method
HA	Humic acid
HPLC	High-performance liquid chromatography
IBU	Ibuprofen
IC	Inorganic carbon
LC-HRMS	Liquid chromatography-high resolution mass spectrometry
LCA	Life cycle assessment
MQ	Milli-Q
MPs	Magnetic particles
P	Precipitation method
SEM	Scanning electron microscopy
SG	Sol-gel method
STPW	Sewage treatment plant water
TGA	Thermogravimetric analysis
TOC	Total organic carbon
TC	Total carbon
TPs	Transformation products
UV	Ultraviolet
VB	Valence band
VUV	Vacuum ultraviolet
WW	Wastewater
WWTPs	Waste water treatment plants
XPS	X-ray photoelectron spectroscopy
XRD	X-ray diffraction analysis
5-TBA	5-tolylbenzotriazole
4-CP	4-chlorophenol

Symbols

k	Kinetic constant value
e^-	Electron
h^+	Hole
E_g	Band gap

Table of Contents

Chapter 1 - State of the Art	10
1.1 <i>Motivation and Objectives</i>	10
1.2 <i>Pollution and Water Treatment</i>	11
1.2.1 Contaminants of Emerging Concern.....	12
1.2.2 EU Directives.....	16
1.3 <i>Water Treatment Processes</i>	18
1.3.1 Heterogeneous (photo)-Fenton-like.....	18
1.3.2 Photocatalysis.....	21
1.3.3 UV based AOPs.....	25
Chapter 2 - Heterogeneous Photo-Fenton Processes	27
2.1 <i>Humic Acid Coated Magnetic Particles for Wastewater Treatments</i>	28
2.1.1 Motivation.....	29
2.1.2 Materials and Methods.....	30
2.1.3 Results and Discussion.....	34
2.1.4 Conclusions.....	48
2.2 <i>Photo-Activation of Persulfate and Hydrogen Peroxide by Humic Acid Coated Magnetic Particles</i>	49
2.2.1 Motivation.....	50
2.2.2 Materials and Methods.....	51
2.2.3 Results and Discussion.....	52
2.2.4 Conclusions.....	62
Chapter 3 - Development of Oxides Doped with Transition Metals and their Exploitation to Pollutants Abatement	64
3.1 <i>Materials and Methods</i>	65
3.2 <i>Iron Doped ZnO Materials for Pollutants Removal</i>	70
3.2.1 Motivation.....	71
3.2.2 Results and Discussion.....	71
3.2.3 Conclusions.....	79
3.3 <i>Cobalt Doped ZnO Materials For Pollutants Abatement</i>	81
3.3.1 Motivation.....	82
3.3.2 Results and Discussion.....	82
3.3.3 Conclusions.....	95
Chapter 4 - Vacuum-UV for Pollutants Removal and Ecotoxicity Mitigation	96
4.1 <i>Antifungal Clotrimazole Removal by Vacuum UV Irradiation – Toxicity Attenuation</i>	97
4.1.1 Motivation.....	98
4.1.2 Materials and Methods.....	99
4.1.3 Results.....	107
4.1.4 Discussion.....	113
4.1.5 Conclusions.....	117
Chapter 5 - Elucidation of Degradation Pathways of CECs	118
5.1 <i>Chemical Selection Approach</i>	119
5.1.1 Materials and Methods.....	120
5.2 <i>Elucidation of Maprotiline Degradation Pathways</i>	128
5.2.1 Motivation.....	129
5.2.2 Results and Discussion.....	129

5.2.3	Conclusions.....	152
5.3	<i>Elucidation of Aliskiren Degradation Pathways</i>	154
5.3.1	Motivation.....	155
5.3.2	Results and Discussion.....	156
5.3.3	Conclusions.....	166
Chapter 6 -	General Conclusions	168
References		171
Appendix A		191
Appendix B		194
Appendix C		196
Appendix D		199
Appendix E		202
Appendix F		209
Summary of PhD activities		212

Chapter 1 - State of the Art

1.1 Motivation and Objectives

The data presented in this PhD thesis is part of a multidisciplinary project that received funding from the European Union's Horizon 2020 research and innovation program under the Marie Skłodowska-Curie - Grant Agreement No 765860 (AQUALity). The goals of this individual PhD project, were focused developing and testing new photoactive materials for the removal of contaminants of emerging concern (CECs) from water and the investigation of the degradation mechanism of these substances. The scientific activities were divided in four different tasks accordingly to the flowing specific aims:

1. Preparation and testing new magnetic nanoparticles to be used as heterogeneous (photo)-Fenton catalyst for pollutants removal;
2. Preparation and testing doped semiconductors based photocatalysts for pollutants removal;
3. Investigation of UV based oxidation processes for pollutants removal and toxicity mitigation;
4. Elucidation of degradation pathways of previously selected CECs by means of high-resolution analytical techniques.

1.2 Pollution and Water Treatment

The scientific progress observed in the last few decades had a remarkable impact on the modern human lifestyle. The development of countless chemical substances, part of our daily routine activities, is now severely affecting the quality of water resources. Due to population growth, accelerated urbanization and economic development, the quantity of wastewater generated and its overall pollution load are increasing globally. However, 80% of the global wastewater flows back into the ecosystem without being treated or reused [1]. Consequently, ensuring sufficient and safe water supplies for everyone is becoming increasingly challenging. Averting a global water crisis, the United Nations launched the international Water Decade Action (2018-2028) to mobilize action to transform how we manage water [2]. A more circular and therefore more sustainable economy requires the reduction of water pollution, minimizing the release of hazardous chemicals and materials and improve the way we manage wastewater.

Accordingly to the European Chemical Agency, in 2018 there were more than 21 000 chemicals manufactured in or imported to the EU above one ton a year [3]. In parallel, more than 4000 new substances are being registered daily to the Chemical Abstracts Service (CAS). However, adequate toxicological and ecotoxicological data have been produced for only a very small fraction of these chemicals, and data on environmental pathways and ecotoxicological effects are even sparser. Many chemicals are applied directly to the environment or are discharged after use through industrial discharge pipes and/or municipal sewage. The large volumes and the complexity of the wastewater matrix make the removal of those pollutants a complex challenge. Designed to remove known pollutants at significant concentrations, the classic wastewater treatment plants (WWTPs) are even less effective removing pollutants from a growing class, the so-called contaminants of emerging concern.

1.2.1 Contaminants of Emerging Concern

The widespread presence of contaminants of emerging concern (CECs) is a major threat to aquatic ecosystems worldwide [4]. According to NORMAN network (“NORMAN Databases”), a CEC is defined as “a substance currently not included in routine environmental monitoring programs that may be a candidate for future legislation due to its adverse effects and/or persistency”. These substances are not necessarily new, most of them are “emerging” as result of the improvement in analytical techniques that recently allowed to detect and track trace concentrations in aquatic media [6,7]. Their “concern” rises from the scarce information about their environmental fate, their hazards to human health and ecosystems, the degradation pathway and toxicity of their degradation products. The presence of a large number of contaminants coupled with the continuous improvement capability to detect new pollutants make CECs a complex challenge for regulatory agencies [8,9].

CECs comprise a wide range of compounds such as pharmaceuticals, personal care products, hormones, food additives, artificial sweeteners, PFAs (per- and polyfluoroalkyl), pesticides and dyes among others [6,9,10]. Due to their distinct usually low concentration (ng L^{-1} to few $\mu\text{g L}^{-1}$), chemical properties (polarity, functional groups, solubility, ...) and potential persistence, CECs are poorly removed by conventional wastewater treatment methodologies and are thus frequently detected in the WWTP effluents [11,12]. These effluents act as a constant low-level source of such substances to the environment. Their environmental hazardousness is not related to their (usually low) concentrations, but to their continuous discharge, persistence, and often high biological activity [13,14]. The classic classification to evaluate the potential environmental impact based on lipophilicity, toxicity (acute and chronic) revealed to be insufficient in the case of CECs. Consequence of the constant presence in the environment due to the continuous release of these substances can have “pseudo-persistence” properties.

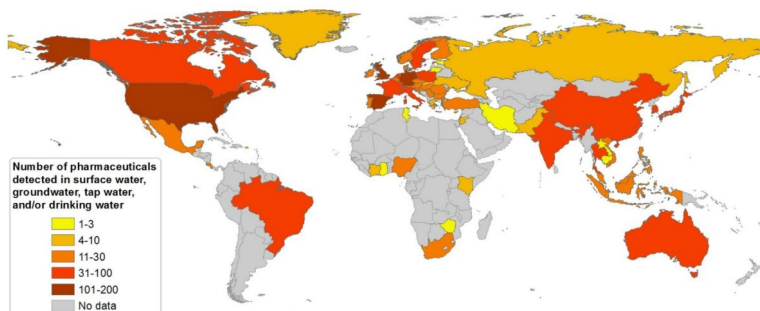


Figure 1.1. Global Detection of pharmaceutical substances in drinking/tap waters, ground- and surface waters. Reproduced from ref [15].

Pharmaceuticals have emerged in the past few decades as the CECs epicenter [10,15–17]. The increasing number of new medicines together with their extensive use, persistence and high biological activity enlarged drastically their environmental impact [18]. Pharmaceuticals reach the environment mainly by excretions and erroneous disposal in the domestic sewer, hospital effluents and animal/fish farming, being frequently detected in surface water, groundwater and also drinking water (Figure 1.1) [15,19]. They include fungicides and antibiotics, painkillers, opioids, hormones, birth control pills, antidiabetics, beta-blockers, lipid regulators, impotence drugs, tranquilizers, antidepressants and other medicines (Figure 1.2). Designed to be biologically active, pharmaceuticals represent a high environmental risk even at very low concentrations.

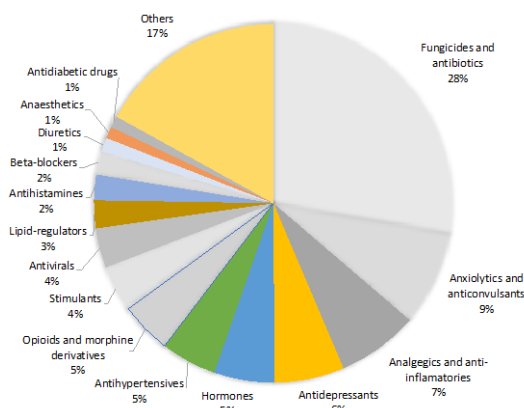


Figure 1.2. Therapeutic groups detected in European surface waters expressed as a percentage relative to the total number of pharmaceuticals. Adapted from [20].

1.2.1.1 Environmental Fate of CECs

Once entered the aquatic environment, CECs may undergo several transformations such as hydrolysis, microbial degradation, interactions with dissolved organic matter, and sunlight photodegradation. Photodegradation reactions in surface waters comprise direct and indirect photolysis. Direct photolysis involves sunlight absorption by the pollutant with its transformation, while during indirect photolysis photoactive compounds absorbed sunlight. In the second case, dissolved organic matter (DOM), nitrite and nitrate can generate reactive species, such as the hydroxyl radical ($\cdot\text{OH}$), singlet oxygen ($^1\text{O}_2$) and DOM triplet states (^3DOM), which can react with pollutants [21,22].

Despite river dilution and environmental degradation, high amounts of pharmaceuticals have been reported in water as well as in the biota [23,24]. For instance, three azole fungicides including climbazole, carbendazim and clotrimazole were detected in fish muscle tissues at significant concentrations [25,26]. Moreover, azole exposure has been related to the reduction of fish growth [27], and to the masculinization of wild fish populations [28]. Fungicides, that together with antibiotics represent 28% of drugs detected in water (see Figure 1.2) may also pose a potential risk to other non-target organisms including aquatic macrophytes, algae and fishes [29,30]. Besides the impacts on biota, there is also evidence of azoles involvement in antifungal resistance with potential impact on human health [31,32].

Due to high consumption, antidepressants represent more than 6% of the drugs found in the environment, as shown in Figure 1.2. Like many other therapeutic groups, antidepressants are of particular concern resulted not only of the well-known several side-effects on the human central nervous system, but also to the mortality increase, developmental retardation, morphological anomalies and effects on reproduction, growth, and immune functions of fish [33,34]. Alarmingly, a study monitoring pharmaceuticals in the Baltic Sea region [35] detected maprotiline (antidepressant drug) in around 50% of influents and

effluents wastewater treatment plants with only 44% of removal from the wastewater treatment plants. Moreover, the study also reports significant bioaccumulation with a concentration of more than 170 µg/kg of maprotiline in blue mussels in the same region.

Besides the obvious harmful threat resulting from the presence of these substances in the drinking water, a huge risk for humans surge from the food chain by processes of bioaccumulation and biomagnification [25,36]. Several CECs have been detected in seafood including endocrine disruptors, brominated flame retardants, polycyclic aromatic hydrocarbons and derivatives, pharmaceuticals and personal care products [17].

Furthermore, besides the potential hazards of these species, questions remain about the persistence and ecotoxicity of their photoproducts resulted from their biological and environmental degradation. As example, the moderately non-toxic ibuprofen drug is described to result in intermediates more toxic than the parent compound [37]. Sinclair et al. [38] analysing the toxicity of hundreds of photoproducts of several chemicals, observed that even if the majority of the products showed comparable or lower toxicity compared with the parent molecule, 20% were >3 times more toxic while 9% were >10 times more toxic than the parent molecule. Thus, it is of high importance to investigate the pollutants environmental fate and the formation of their transformation products (TPs) and ecotoxicological properties.

Even with the strong evidence of the presence of CECs in drinking water, most of the countries do not have monitoring programmes to routinely test for the presence of CECs in drinking water due to practical difficulties, such as high costs and lack of availability of routine analytical technologies and laboratory infrastructures. To protect and improve the aquatic environment the policy makers have been establishing legal frameworks for water protection and management. Currently, only Switzerland has legislation to improve surface water quality by reducing the load of CECs from WWTPs though the

implementation of advanced treatment on urban wastewater up to 2040 [39]. Which requires the removal of 80% relative to the raw water of twelve defined representative CECs [40].

1.2.2 EU Directives

The EU Water Framework Directive aims to prevent and reduce pollution, promote sustainable water use, protect and improve the aquatic environment [41]. Guided by these frameworks' member states are therefore requested to draw up specific programs of measures to achieve the objectives. With the scientific progress and the advances in the analytical methods, constant developments have been made since the introduction of the first Directive focused on identifying substances with high risk to the aquatic systems, back in 2000 (2000/60/EC) [42]. The first list of 33 priority substances, introduced with the Directive 2008/105/EC, [43] was based on potential adverse effects in the aquatic environment and risk for human health. With the Directive 2013/39/EU the list was extended to 45 priority substances, supplemented by additional 15 compounds in the Watch List, that are required to be monitored by the member states so that sufficient information is collected about their occurrence and risk. Additionally, this Directive was focused on the prevention and elimination of pollution sources, simultaneously with the implementation of actions to improve water and wastewater treatment solutions.

Very recently, the more targeted new Drinking Water Directive (EU) 2020/2184, [44] was adopted to define the essential quality standards for the water intended for human consumption. In response to the European Citizens' Initiative 'Right2Water' the EU updated the existing safety standards to improve the access to safe drinking water, aligned with the recommendations of the World Health Organization. The new Directive aims not only to ensure the quality standards but also increase the transparency for the consumer along the supply

drinking water systems. This new Directive challenges the actual drinking water supply stakeholders with significant requirements to be implemented in the member states within a period of few years. As an example, the previously recommended preventive risk-based approach (Directive (EU) 2015/1787), will become mandatory by monitoring in-depth the whole water system supply along the catchment area, treatment storage and distribution. Additionally, the Directive aims to harmonize the quality standards of all the materials and products in contact with water. Finally, the Directive establishes updated standard values for substances/pollutants from different categories such as, radioactivity, microbiological, chemical and disinfection by-products.

In order to address the growing alarm of CECs the Directive introduces for the first-time limits for PFAs, microcistine-LR and Bisphenol A, selected as a benchmark endocrine-disrupting compound. In addition, nonylphenol and Beta-estradiol were added to the Watch List due to their endocrine-disrupting properties and the risk for human health. The incorporation of CECs in the Watch List aims to allow a flexible and dynamic response to those substances by the acquisition of knowledge about the most appropriate monitoring approaches and the relevance for human concern. The fast-growing threat microplastics were also added to this Watch List.

Appropriate monitoring parameters of those substances or pollutants that can constitute a risk to human health are now required in the catchment areas as well as the definition and implementation of preventive measurements. For example, the installation of technologies (e.g., membrane filtration, UV disinfection) to prevent and remove those substances or pollutants. Only with a combined effort, with the policy makers to significantly improve the wastewater treatment processes will be possible to progressively reduce the release of pollutants into the environment and in this way their impact on drinking water sources.

1.3 Water Treatment Processes

Advanced Oxidation Processes

Advanced oxidation processes (AOPs) have been attracting wide attention, since they can be extremely efficient in the degradation and mineralization of organic contaminants, including CECs. AOPs work through the action of highly oxidizing species, mainly hydroxyl radicals ($\cdot\text{OH}$, $E^\circ = 2.8 \text{ V}$) but also sulfate radical ($\text{SO}_4^{\cdot-}$, $E^\circ = 2.6 \text{ V}$) or valence band holes in the case of heterogeneous photocatalysis, [45–49], able to react with pollutants promoting their transformation into more biodegradable compounds or even their mineralization. The diversity of advanced oxidation approaches together with the recent increasing number of publications reflect efforts of the scientific community on the application of AOP for water remediation. AOPs can be classified depending on the process for the generation of reactive species and the most common AOPs are based on photocatalytic, chemical (e.g., ozonation), UV based and Fenton processes, as shown in Figure 1.3.

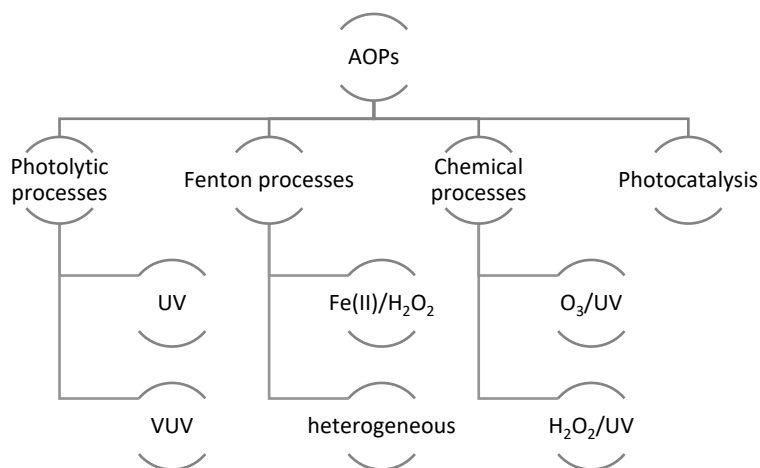
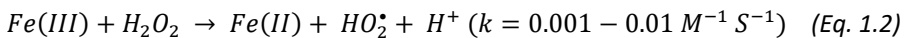
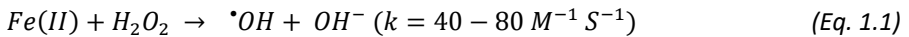


Figure 1.3. Diversity of advanced oxidation processes.

1.3.1 Heterogeneous (photo)-Fenton-like

Among AOPs there is increasing interest in Fenton, photo-Fenton and Fenton-like processes that generate highly reactive species [50–55] through the

reactions between iron and H_2O_2 or other alternative oxidants (e.g. $S_2O_8^{2-}$) at acidic or even circumneutral pH, often in the presence of complexing agents able to form iron complexes [56–60]. The homogeneous Fenton reaction is interesting because both, Fe and H_2O_2 are environmentally friendly species, the reaction kinetic is usually fast and does not require complex reactors to be carried out. However, the reaction needs the pH adjustment to acidic medium (optimum conditions at pH 3) and subsequent neutralization impacting the process cost [61]. Additionally, the formation of sludge to be removed and then dismissed increases the overall treatment cost and does not allow the recycling of the iron-based catalyst. H_2O_2 is activated by Fe^{2+} by electron transfer generating $\bullet OH$ and Fe^{3+} (Eq. 1.1). Even if the Fe^{2+} ions can be re-generated by H_2O_2 according to the reductive steps of the Haber and Weiss catalytic cycle [62], the reduction of Fe^{3+} to Fe^{2+} is usually the rate determining step of the process (Eq. 1.2) [58]. Consequently, the continuous addition of Fe^{2+} is necessary.



Different strategies have been proposed to increase the rate of Fe^{3+} reduction. Among these, the ferric species can be photoreduced upon photolysis of dissolved $Fe(III)$ [63] according to Equations 1.3-1.4.



Light induced Fe^{3+} reduction occurs with fast kinetics, thus overcoming the Fenton's limitation. Fe^{3+} can be indeed photo reduced to Fe^{2+} keeping the system catalytic.

Heterogeneous photo-Fenton reaction with iron-based magnetic materials and H_2O_2 has been proposed as a promising alternative to the classic homogeneous process [64]. The mechanism behind heterogeneous (photo-)Fenton reactions has not been fully assessed, and it is worth to be studied in deeper details. In particular, the role of the iron species in the

operative catalytic cycle has been only partially clarified. The heterogeneous catalyst (Figure 1.4) is often not only an iron reservoir able to maintain an effective concentration of iron in solution, but often its surface plays an active and catalytic role as previously reported [50,65].

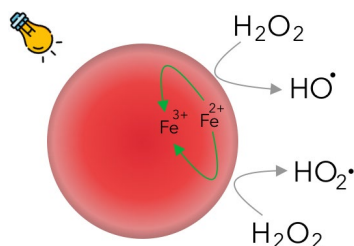


Figure 1.4. Schematic representation of heterogeneous photo-Fenton the activation of H₂O₂

Furthermore, the chemical nature and the texture of the iron-based catalyst influence abruptly its activity affecting the working conditions (pH range, under irradiation vs dark activity, recyclability...) [65,66]. Fe₃O₄ magnetic particles (MPs) used as iron source in Fenton and photo-Fenton processes have attracted significant interest due to their negligible toxicity, low cost, facile recovery (by means of a magnetic field) and reuse [52]. Recently, the potential application of MPs in heterogeneous Fenton and photo-Fenton processes for the removal of CECs has been investigated [65,67,68].

Magnetite is a mixed Fe(II)/Fe(III) oxide and it is well recognized crucial importance of the Fe(II) ions in the structure to activate heterogeneous Fenton-like processes [51,69]. The main problem using magnetite relies on the air oxidation of Fe(II) producing a passive Fe(III) oxide layer that inhibits the catalytic activation of H₂O₂. The stabilization of the Fe(II) surface species with organic coating can reduce the oxidation of the magnetic phase (magnetite/maghemite) to hematite [70]. Humic(-like) substances have been previously investigated to enhance the Fe₃O₄ stability, increase the dispersion and prevent the aggregation [71–73], even though the effective role played by humic(-like) substances in the oxidation mechanism is still not fully solved [47,74–78]. Recently, Aparicio et al.

investigated the photo-Fenton oxidation of the psychiatric drug carbamazepine in the presence of core-shell magnetite-humic acids nanoparticles observing that the MPs were excellent iron sources to sustain the photo-Fenton process [79].

1.3.2 Photocatalysis

Heterogeneous photocatalysis is another AOP that can play a fundamental role due to its ability to generate highly reactive oxidizing species able to remove a wide range of contaminants [80]. The development of eco-friendly oxide-based semiconductors proved to allow the conversion of solar energy for the oxidation or reductive processes for the H₂ generation from water splitting [81], CO₂ reduction into fuels [82] and water remediation.

Among semiconductors, titanium dioxide (TiO₂) has been the most studied catalyst in past decades. Due to its low production cost and good chemical stability, it has been broadly investigated in the photo-degradation of organic compounds [83–85]. During the activation process the catalyst is photo-induced by light with energy ($h\nu$) equal or higher than the excitation energy (E_g), electrons from the filled valence band (VB) are promoted to an empty conduction band (CB), generating electron-hole (e^-/h^+) pairs (Figure 1.5). These charges can then migrate to the catalyst surface and promote redox reactions, wherein the h^+ reacts with water and hydroxide ions to produce hydroxyl radicals while e^- reacts with oxygen to produce superoxide (Eq. 1.5 – 1.7).



These reactive species can then react with organic pollutants during the photocatalytic oxidation, following the steps [86]: *i*) organic pollutants diffuse from the liquid phase to the surface of catalyst; *ii*) adsorption of the pollutants on the materials surface; *iii*) oxidation and reduction reactions in the adsorbed

phase; *iv*) desorption of the products; and *v*) removal of the products from the interface region, as represented in Figure 1.5.

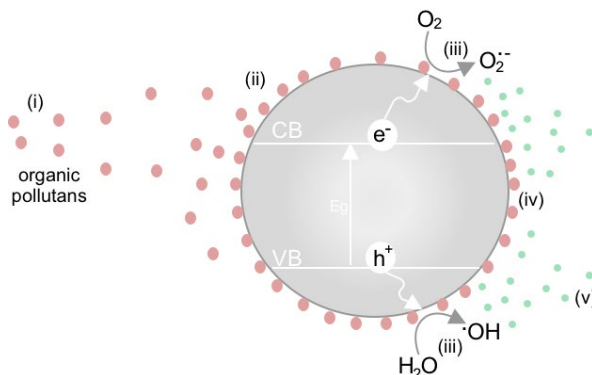


Figure 1.5. Schematic representation of heterogeneous oxidation steps.

As previously reported [87,88], the application of TiO_2 using solar energy is highly restricted by its large band gap (3.2 eV) which falls in the UV range and the low quantum efficiency. As a matter of fact, the UV component of the solar radiation impinging the earth surface is just the 5%, not enough to efficiently activate TiO_2 as photocatalyst. Considerable efforts have been devoted to improve their properties or on developing new semiconductor photocatalysts to be applied for water remediation. In search of the photocatalytic holy grail many semiconductors have been investigated such as WO_3 , Al_2O_3 , Sb_2O_3 and ZnO among many others [89–92].

Comparable to TiO_2 , ZnO is an n-type semiconductor with favorable electrical, excellent optical and mechanical properties. As reported by Liang et al. [93], the production cost of ZnO represents roughly 25% of the benchmark TiO_2 . ZnO has a broad direct band gap (3.37 eV), large excitation binding energy (60 meV), deep ultraviolet light adsorption and good resistance to electromagnetic radiation photocorrosion [94,95]. Moreover, Fenoll et al. [96] comparing the activity of ZnO and TiO_2 for the degradation of two fungicides (cyprodinil and fludioxonil) in water under solar irradiation observed better photocatalytic activity for ZnO catalyst. Due to these advantages, ZnO has been

increasingly pointed as the most promising semiconductor oxide photocatalyst. In addition, besides the good photocatalytic properties, ZnO has also good antibacterial properties [97].

1.3.2.1 Doped semiconductor photocatalysts

The semiconductor photocatalytic activity is mainly driven by the light adsorption (bandgap energy) and the ability to then generate reactive species (mainly $\cdot\text{OH}$). However, this process can be compromised by the fast recombination rate between the photogenerated electron/holes pairs. This is indeed the main drawback of ZnO semiconductors.

The introduction of doping agents has been explored to reduce the charge recombination and, thus, lead to a higher degradation efficiency of organic pollutants. By incorporating impurities such as metals or non-metals is possible to modify the physical and chemical properties and shift the valence band energy to the visible region [98]. Recent studies have demonstrated that non-metal dopants such as carbon, nitrogen, sulfur and fluorine can shift the bandgap of ZnO by introducing more oxygen vacancy defects on the surface of nanoparticles. More specifically, these small sizes elements can diffuse through the lattice interstices and bind to the atoms via oxidation process [99]. The introduction of these elements proved also to enhance the hydroxyl radicals generation what can be explained by the electron scavenging effect, reducing the charges recombination and allowing the h^+ to generate $\cdot\text{OH}$ radicals (Figure 1.6).

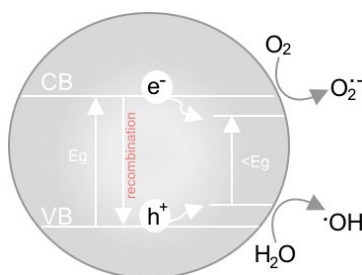


Figure 1.6. Schematic representation of doped semiconductor oxide.

In the same way, other elements like transition metals, rare earth metals, noble metals and other metals have shown advantages in tuning ZnO properties and the photocatalytic activity. Similarly to non-metal dopants, metal doping can act as a charge trap reducing the extent of the electron-hole pairs recombination [100,101]. Moreover, the doping with metals of d block solves the problem related to photo-corrosion of zinc oxide which becomes more stable and thus more appealing to be used in wastewater treatment [102]. The positive role of transition metal doping is expressed through the introduction of additional energy levels inside the oxide band gap. Furthermore, the addition of transition metals changes the chemical surrounding of Zn^{2+} ions, induces reticular distortions and increases the fraction of defects. In particular, the oxygen vacancies, if present in optimal concentrations, can act as traps for the electrons and guarantee a better efficiency in the electrons /holes charge separation. The incorporation of transition metal ions in oxides semiconductors appears to be a complex function of dopant concentration and its distribution, strongly dependent on each metal ion electron donor density and its d electron configuration.

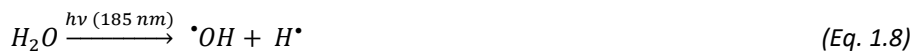
Numerous studies have report using transition metal such as Al, Mn, Fe, Co, Ni, and Cu to affect positively the properties of different semiconductors oxide based materials. As example, Yun et al. [103] reported that higher loads of organic compounds can be adsorbed on Al-doped ZnO compared to pure ZnO based on the high light harvesting efficiency. On the other hand, the incorporation of Fe, can contribute to more oxygen defects on ZnO along with an increase in the charge density of ZnO, which subsequently can induce higher catalytic performance [104,105]. Cobalt is considered one of the most effective doping species due to its abundant electronic states and also it appears to suit well for tailoring the electronic structure, by substitution of Co^{2+} on the host lattice without inducing significant distortions in the oxide reticulum [106–108]. In addition, the incorporation of cobalt ions has shown an increase in the number

of oxygen vacancies in the ZnO structure that are usually leading to efficient separation of photogenerated charges carriers [109,110]. However, the introduction of cobalt with different concentrations on ZnO lattice is reported to induce a change in the morphology on the microstructures suggesting that structure and activity strongly depend on the synthesis method [111].

1.3.3 UV based AOPs

Ultraviolet (UV) based AOPs has been used for water disinfection and has appeared as a promising technology to remove unwanted chemicals from the water cycle and can potentially mitigate environmental impacts [112]. In the UV based processes, the oxidizing species are usually formed from the exposition of hydrogen peroxide (UV/H₂O₂) or ozone (UV/O₃) to UV irradiation [113–115].

Vacuum-UV (VUV) technology is based on UV radiation at wavelength lower than 190 nm (VUV range) that allow the in-situ formation of reactive species (manly [•]OH) by direct water dissociation without chemical addition, Equations 1.8-1.9 [116]. Common VUV lamps are characterized by the emission of radiation at 185 nm (VUV) and at 254 nm (UVC), and represent a promising technology for organic micropollutants removal in treatment of, e.g., wastewater and drinking water [117–120].



VUV photolysis of water is a highly efficient method for the generation of advanced oxidation conditions and the formation rate of hydroxyl radicals is comparable to other advanced oxidation processes. For this reason and due to the advantage that does not require the addition of chemical, VUV has been pointed as a promising technique for water remediation. The VUV process has been used to remove many different organic pollutants, such as chlorinated compounds, pesticides and pharmaceuticals [116,119]. Xie et al. [116] reported

high effectiveness of VUV irradiation to remove three different persistent pollutants (bisphenol A, nitrobenzene and dimethyl phthalate) even in the presence of a complex water matrix. Recently VUV irradiation was reported to efficiently degrade and mineralize dimethoate (organophosphorus pesticide) with roughly 98% removal within 10 min of exposure whereas only 5% was removed under UV in the same experimental time [118]. The authors also evidenced their economic feasibility by determining the electrical energy-per-order in small-scale water treatment. With the recent progress in clean energy and with the technological development VUV can represent an attractive solution for both, pollutants removal and water disinfection without the addition of any chemicals [117,121].

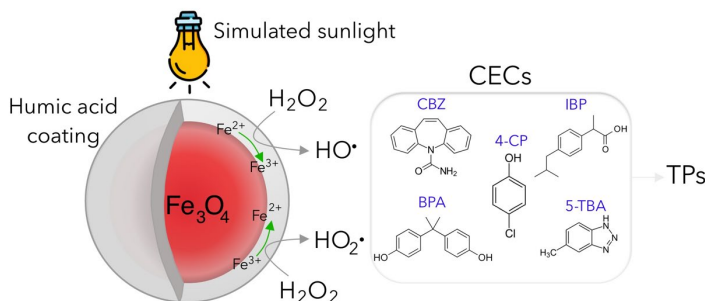
Chapter 2 - Heterogeneous Photo-Fenton Processes

In this chapter is reported the preparation of magnetic particles coated with humic acid by co-precipitation method using different amounts of HA, both in anoxic and oxygenated conditions. The materials were tested in aqueous solutions for pollutants removal in the presence of H_2O_2 at different pH in the dark and under simulated sunlight irradiation.

In the second part it is reported a comparative study of the best performing material for the activation of H_2O_2 and $\text{S}_2\text{O}_8^{2-}$ under UVA/UVB irradiation in aqueous media using bisphenol A (BPA) as a model pollutant

2.1 Humic Acid Coated Magnetic Particles for Wastewater Treatments

Adapted from:



Humic acid coated magnetic particles as highly efficient heterogeneous photo-Fenton materials for wastewater treatments

Nuno P.F. Gonçalves, Marco Minella, Debora Fabbri, Paola Calza, Cosimino Malitesta, Elisabetta Mazzotta, Alessandra Bianco Prevot

Chemical Engineering Journal 390 (2020) 124619

My direct contribution:

I declare that I have prepared, and characterized the MPs described in this sub-chapter. I have also performed all the degradation experiments. The XPS analysis were performed by Cosimino Malitesta, Elisabetta Mazzotta at the University of Salento. The TGA data analysis were performed in collaboration with Scalarone Dominique at the University of Turin.

2.1.1 Motivation

As it was seen in Section 1.3.1, heterogeneous photo-Fenton using iron-based magnetic materials has been proposed as an alternative to the homogeneous Fenton process to remove contaminants of emerging concern (CECs) because of the low cost, facile recovery and reuse. The iron-based material is not only a reservoir to maintain an effective concentration of iron in solution, but it also activates H_2O_2 at the surface. Magnetite (mixture of Fe(II)/Fe(III)) can act as iron source and allow its easy recovery by means of a magnetic field. As previous evidenced, Fe(II) is essential to keep the system active for the generation of reactive species. Coating with humic acid can prevent the oxidation of Fe(II) and improve the water dispersion. In this way, we prepared magnetic particles (MPs) coated with different amount of humic acid (HA), prepared by co-precipitation method, testing both anoxic (to avoid the Fe(II) oxidation during the synthesis) and oxygenated conditions.

The materials were characterized by different techniques (XPS, XRD, TGA, SEM and FTIR). The ability of those materials to promote Fenton and photo-Fenton-like processes under sunlight simulator at different pH was investigated using 4-chlorophenol as standard substrate. The stability was evaluated by determining the iron leaching in solution under irradiation and in the dark, in the presence and absence of H_2O_2 . A correlation between the reactivity to activate H_2O_2 and the iron species at the surface of the magnetic particles (MPs) was carried out by XPS analysis.

The best performing material was then tested for the abatement of CECs, namely Carbamazepine, Ibuprofen, Bisphenol A and 5-Tolybenzotriazole also in real wastewater. The obtained results demonstrated the potential application of the heterogeneous (photo)-Fenton process activated by these inexpensive and environmental friendly materials in advanced wastewater treatments.

2.1.2 Materials and Methods

Materials

$\text{FeCl}_3 \cdot 6\text{H}_2\text{O}$ and $\text{FeSO}_4 \cdot 7\text{H}_2\text{O}$ were purchased from Carlo Erba Reagents; HA sodium salts (technical, 50–60%) from Aldrich-Chemie; 4-chlorophenol, Bisphenol A, Carbamazepine, Ibuprofen, 5-Tolylbenzotriazole, acetonitrile (gradient grade) and H_3PO_4 from Sigma-Aldrich. All the chemical reagents were used as received. Suspensions and standard solutions were prepared in Milli-Q water.

The real wastewater samples were collected in a WWTP at the northern area of Italy (October 27th, 2017). The samples used were obtained from the outflow of the primary clarifier tank. This real sample was used after a rough pre-filtration step, carried out through a grade qualitative filter paper (Whatman) to remove large suspended solids and filtered using a hydrophilic 0.45 μm Sartolon Polyamide filter (Sartorius Biolab).

Materials synthesis and characterization

HA coated magnetite particles were prepared following the co-precipitation procedure reported in the literature with some minor modifications aiming to avoid the Fe^{2+} oxidation [71]. In detail, the MPs were prepared by co-precipitation method under nitrogen; 35 mL of a $\text{FeCl}_3 \cdot 6\text{H}_2\text{O}$ (6.42 g) and 4.17 g of $\text{FeSO}_4 \cdot 7\text{H}_2\text{O}$ water solution (molar ratio $\text{Fe(III)}/\text{Fe(II)} = 1.5$) were added to 65 mL of deoxygenated water at 90 °C, under vigorous mechanic stirring and N_2 continuous flow. Then, 10 mL of NH_4OH (25%) and 50 mL of HA solution at different concentrations were added rapidly and sequentially and a mixture of Fe(II) and Fe(III) hydroxides with adsorbed HA were co-precipitated. The mixture was kept for 30 min at 90 °C, and then cooled down to room temperature under continuous stirring and nitrogen flow. The obtained MPs were separated by centrifugation and washed with 40 mL of water five times. The MPs were dried in a Tube Furnace under nitrogen flow at 80 °C for 15h to dry the materials and

promote the formation of the oxidic lattice. The resulting MPs were manually crumbled. Depending on the different wt.% of HA in the initial solution (namely 0.25 wt.%, 0.5 wt.%, 1 wt.%, 2 wt.% and 4 wt.%), the obtained MPs were coded Fe₃O₄/0.25HA, Fe₃O₄/0.5HA, Fe₃O₄/1HA, Fe₃O₄/2HA, and Fe₃O₄/4HA, respectively. The bare Fe₃O₄ MPs were prepared with a similar procedure without the addition of HA solution. Materials coded ox-Fe₃O₄/0.5HA (addition of a 0.5 wt.% HA solution) and ox-Fe₃O₄ (no addition of HA) were prepared with a similar procedure, but in air (both during the synthesis and drying process).

The morphology of the synthesized MPs was determined by scanning electron microscopy (SEM), with a Phenom Pro instrument operating at 5, 10 and 15 kV, 50.0 mA beam current and 50 pA probe intensity. Thermo-gravimetric analyses (TGA) were performed on a TA Q500 (TA Instruments), working under air atmosphere. The weight losses and the degradation profiles were evaluated by heating ca. 10–15 mg of each sample applying a heating ramp from 30 to 800 °C (rate 10 °C/min). X-ray diffraction (XRD) pattern of the powders were recorded with an Analytical X'PertPro equipped with an X'Celerator detector powder diffractometer using Cu K_α radiation generated at 45 kV and 40 mA. The 2θ range was from 20° to 100° (spinner mode) with a step size (2θ) of 0.03 and a counting time of 0.6 s. Fourier transform infrared (FTIR) were taken on a Bruker spectrometer recorded with 128 scans at 4 cm⁻¹ for a wavenumber range of 4000 to 400 cm⁻¹. XPS measurements were recorded with an AXIS ULTRA DLD (Kratos Analytical) photoelectron spectrometer using a monochromatic AlK_α source (1486.6 eV) operated at 150W (10 kV, 15 mA). Base pressure in the analysis chamber was 5.3×10⁻⁹ torr. Survey scan spectra were recorded using a pass energy of 160 eV and a 1 eV step. High resolution spectra were acquired using a pass energy of 20 eV and a 0.1 eV step. The hybrid lens mode was used for all measurements. In each case the area of analysis was about (700×300) μm². During the data acquisition a system of neutralization of the charge has been used. Processing of the spectra was accomplished by CasaXPS Release 2.3.16

software. For the analysis of high-resolution spectra all peaks were fitted using Shirley background and GL (30) lineshape (a combination of Gaussian 70% and Lorentzian 30%). For quantitative analysis, the relative sensitivity factors present in the library of CasaXPS for the areas of the signals were used. Surface charging was corrected considering adventitious C 1s (binding energies (BE) = 285 eV).

Degradation procedure

The degradation experiments in Fenton-like condition were carried out in a beaker with a total volume of 50 mL protected from light under magnetic stirring, while experiments in photo-Fenton-like condition were performed in closed Pyrex glass cells filled with 5 mL under magnetic stirring and irradiated for different times (1 to 60 min) in a sunlight simulator (Solarbox, CO.FO.Me.Gra, Milan) equipped with a xenon lamp (1500 W) with a cut-off filter at below 340 nm. On top of the suspensions the irradiance was 18 W m^{-2} in the 295–400 nm range (similar to the natural sunlight UV irradiance at middle European latitude in sunny days) [22]. The suspension temperature was $\sim 45^\circ\text{C}$. Hydrogen peroxide (1.0 mmol L^{-1}) was added to the suspension of MPs (100 mg L^{-1}). The initial concentration of 4-chlorophenol (4-CP, $\text{pK}_a = 9.4$ [122]) was 0.2 mmol L^{-1} . The pH was adjusted with H_2SO_4 . After the reaction time, 0.33 mL of methanol were added to the 5 mL of the suspension to quench the thermal Fenton reaction, then the samples were filtered using a $0.45 \mu\text{m}$ filter (Sartorius, hydrophilic PTFE). An equilibration time of 30 minutes was always adopted to highlight possible adsorption and in dark degradation.

Degradation experiments with CECs were performed with initial concentration of 0.2 mmol L^{-1} for Ibuprofen (IBP, $\text{pK}_a = 5.3$ [123]), Bisphenol A (BPA, $\text{pK}_a = 9.6$ [124]), 5-tolylbenzotriazole (5-TBA, $\text{pK}_a = 8.6$ for the conjugated acid [125]) and 0.1 mmol L^{-1} for Carbamazepine (CBZ, $\text{pK}_a = 13.9$ [126]). Moreover, a degradation experiment in the same real matrix but on a mixture of these compounds was carried out with each CEC at an initial concentration 20

$\mu\text{mol L}^{-1}$. The real wastewater sample had total organic carbon (TOC) = $9.7 \text{ mg}^{\text{C}} \text{ L}^{-1}$, Inorganic Carbon (IC) = $68.4 \text{ mg}^{\text{C}} \text{ L}^{-1}$, Total Nitrogen (TN) $31.3 \text{ mg}^{\text{N}} \text{ L}^{-1}$ and pH = 8.3.

The degradation experiments were carried out in triplicate, the results averaged and the error bars reported in the relevant plots. The repetitions showed high robustness and reproducibility of the adopted experimental procedures.

Analysis

The concentration of 4-chlorophenol was measured through a YL9300 HPLC system equipped with a YL9330 Column Compartment and a YL9150 autosampler. The column was a RP C18 column (LiChroCART®, Merck, 12.5 cm × 0.4 cm; 5 μm packing). 4-chlorophenol was analyzed in isocratic mode using a 10:90% v/v acetonitrile:phosphoric acid solution ($1 \times 10^{-2} \text{ M}$) as mobile phase (flow rate of 1 mL min^{-1} , UV detection 220 nm). The retention time of 4-CP was 12 min. The CECs mixture was analyzed through the same instrument using as mobile phase acetonitrile and phosphoric acid solution ($1 \times 10^{-2} \text{ M}$) with the following gradient: 0 min, 80:20 v/v; 10 min, 65:35 v/v; 20 min, 35:65 v/v; 25 min, 80:20 v/v (flow rate of 1 mL/min , UV detection 200 nm). The retention times of the analyzed CECs were 5-Tolylbenzotriazole: 6.0 min; Carbamazepine: 12.1 min; Bisphenol A: 15.5 min; Ibuprofen: 22.1 min. The mineralization of 4-CP and the other investigated CECs could not be followed by monitoring the TOC concentration during the degradations due to the slight leaching of the HA coating. This was previously observed with similar materials [75].

TC, IC and TN were measured using a Shimadzu TOC-5000 analyzer (catalytic oxidation on Pt at $680 \text{ }^{\circ}\text{C}$). The calibration was performed using standards of potassium phthalate, $\text{NaHCO}_3/\text{Na}_2\text{CO}_3$ and KNO_3 .

The determination of Fe released in solution was evaluated by a spectrophotometric procedure. The total iron was determined by reducing the

Fe(III) to Fe(II) with ascorbic acid (4×10^{-4} M) and complexing the Fe(II) with phenanthroline (4×10^{-3} M) in acidic conditions (buffer pH=3: H_3PO_4 1 mmol L^{-1} , NaH_2PO_4 3 mmol L^{-1}). The Fe(II) was determined in the same way, without the reduction step, and Fe(III) was obtained as the difference between total iron and Fe(II) [127]. The calibration was performed using a commercial standard solution of Fe(III) (1000 $\text{mg}^{\text{Fe}} \text{L}^{-1}$, Sigma-Aldrich). The spectrophotometric analyses were performed using a Varian CARY 100 Scan double-beam UV-vis spectrophotometer, using quartz cuvettes with 10 mm path length and working at 510 nm.

2.1.3 Results and Discussion

Materials Characterization

The morphology of the synthesized MPs was investigated by SEM. Figure A1 (see Appendix A) shows the recorded micrographies. The adopted method of synthesis gave very heterogeneous samples composed of aggregates of primary particles with dimensions that ranged from tens of μm to sub-micrometer dimensions. Furthermore, no correlation between the particles texture and the amount of HA used during the synthesis was observed, as well as there was no clear difference in the morphology of the MPs synthesized in anoxic condition and in air. The HR-TEM analyses of analogous MPs were carried out by Magnacca et al. [128] and Carlos et al. [129]. They observed nanometric particles roughly spherical in shape (average particle size in the 10 nm range), with a crystalline core and an external layer of organic matter with less than 1 nm thickness. The TGA curves recorded under air on MPs/HA and bare magnetite are shown in Figure A2. The first slight weight loss (30–150 °C) was related to the loss of physisorbed water, whereas - from the comparison between the pure magnetite and the hybrids TGA profiles - that in the 200-800 °C range was assigned to the loss of the chemically adsorbed HA coating due to the combustion of the organic

fraction. Weight losses calculated in the 200-800 °C range revealed a higher HA loading on the MPs when prepared in the presence of higher HA concentration (Table A1 and Figure A2).

X-ray diffraction (XRD) patterns for MP/HA (Figure A3) showed reflections at $2\theta = 30.1^\circ, 35.4^\circ, 43.0^\circ, 53.9^\circ, 57.2^\circ,$ and 62.6° , in agreement with the reflections produced by the (220), (311), (400), (422), (511), and (440) planes of reference magnetite [130,131]. The Scherrer analysis of the peak related to the (311) plane gave a rough estimation of the crystalline domains in the 12-16 nm range in agreement with the HR-TEM micrographs of the primary particles previously reported [128,129].

The FTIR spectra of HA, Fe_3O_4 and $\text{Fe}_3\text{O}_4/\text{HA}$ MPs are shown in Figure A4. In the HA spectra the peak at $\sim 3400\text{ cm}^{-1}$ was attributed to the stretching vibrations of -OH groups; 2920 cm^{-1} and 2850 cm^{-1} were assigned to CH_2 , - CH_3 species; the $\sim 1600\text{ cm}^{-1}$ and $\sim 1400\text{ cm}^{-1}$, were attributed to the stretching of -COOH groups. The peak with strong absorption at $\sim 550\text{ cm}^{-1}$ shown on Fe_3O_4 MPs spectra was attributed to Fe-O bond. The intensity increase of the organic matter-related peaks were observed on $\text{Fe}_3\text{O}_4/\text{HA}$ MPs spectrum confirming the HA coating on magnetite structure. These results were in agreement with the literature [129,132].

Additionally, Magnacca et al. reported on analogous materials that: *i*) the point of zero charge - evaluated through the measuring of the zeta potentials (ζ) at different pH - changed from 7.2 on the bare Fe_3O_4 to 3.0 for the HA coated materials as a consequence of the presence at the surface of carboxylic and phenolic moieties; *ii*) the samples exhibited superparamagnetic characteristics, including zero coercivity and remanence [128].

X-ray photoelectron spectroscopy (XPS) analyses were performed on MPs prepared using different amounts of HA, both in anoxic and oxygenated conditions aiming at evaluating the effect of synthesis experimental conditions on the surface chemical composition and possibly correlating it to the observed

reactivity in pollutants degradation. XPS has been largely used since long time to distinguish and to quantify Fe^{2+} and Fe^{3+} species [133,134]. These oxidation states can be indeed easily evaluated by Fe 2p region, considering chemical shift and multiplet splitting occurring for these species. Several examples of XPS application to iron oxide species have been reported, including nanoparticle and magnetic systems [134,135]. Fitting of the Fe 2p region requires the knowledge of the standard spectra of potential present iron oxide species, such as FeO, Fe_3O_4 , Fe_2O_3 (namely $\alpha\text{-Fe}_2\text{O}_3$ and $\gamma\text{-Fe}_2\text{O}_3$) and FeOOH (namely $\alpha\text{-FeOOH}$ and $\gamma\text{-FeOOH}$). In this regard, a very accurate work, which was used for interpreting our results, is reported in the literature [136]. In the survey spectra (data not shown), the major peaks were represented, as expected, by C 1s, O 1s and Fe 2p, with the presence of traces of S 2p, Cl 2p and N 1s originating from FeCl_3 , FeSO_4 and NH_4OH used in the synthesis. For a more detailed analysis, high-resolution XPS Fe 2p spectra were recorded. These spectra were fitted using multiplet peaks: an example is reported in Figure 2.1, referred to $\text{Fe}_3\text{O}_4/0.5\text{HA}$ prepared under anoxic environment. All investigated samples resulted to be very similar in terms of Fe 2p speciation being in all cases characterized by multiplet peaks which can be ascribed to Fe^{3+} of an oxidized form of iron, possibly $\gamma\text{-FeOOH}$ on the basis of literature data [136], suggesting a higher degree of oxidation of surface MPs in comparison to bulk. As shown in Figure 2.1, two peaks can be identified, denoted as pre-peak and surface peak, located at 708.7 eV and 713.6 eV, respectively. The low-intensity pre-peak on the low-binding-energy (BE) side of the envelope accounts for the formation of Fe ions with a lower than normal oxidation state by the production of defects (in which iron is in different coordination conditions - usually lower - than on the ordered crystallographic planes) in neighboring sites [136]. The high-BE surface peak referred to surface defective structures exhibiting different binding energies compared with that of the bulk structure because of surface termination, which frequently could result in a decreased symmetry [136]. Interestingly, while the abundance of pre-peak was almost

similar in all investigated samples, a remarkable variation of surface peak intensity was observed with varying particle synthesis experimental conditions, as reported in Figure 2.1. It can be observed that, for samples prepared under nitrogen environment, the percentage area of surface peak increased when passing from bare MPs to ones prepared with HA 0.5 wt.%, then decreasing to values slightly lower than that recorded on Fe_3O_4 . These results well correlated with the observed particles activity of the studied heterogeneous catalysts (highest reactivity for $\text{Fe}_3\text{O}_4/0.5\text{HA}$, *vide infra*) suggesting an active role of these surface sites during the photo-activated degradation process on the investigated MPs (see section below). In the case of materials prepared in air (data not shown), no significant difference was observed between Fe_3O_4 and $\text{Fe}_3\text{O}_4/0.5\text{HA}$, being in both cases the estimated abundance of surface peak similar to that of bare samples prepared in anoxic conditions. Finally, the presence of surface HA can be estimated from O 1s high-resolution signal, as shown in Figure 2.2, reporting the comparison among O 1s spectra of Fe_3O_4 and some of the analyzed samples prepared in anoxic conditions. With the increase of humic acid percentage, an increase of two component peaks at about 532 eV and 534 eV can be observed, attributed to HA on the basis of the comparison with O 1s spectrum of HA alone, thus suggesting that the actual surface amount of HA reflects the one used in the preparation of the particles.

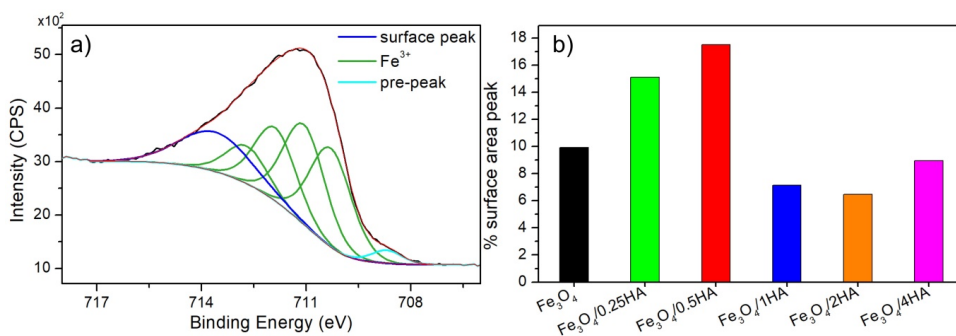


Figure 2.1. High-resolution spectrum of Fe 2p region of $\text{Fe}_3\text{O}_4/0.5\text{HA}$ prepared under anoxic conditions (a). Spectrum is charging corrected. Percentage of the surface peak in all samples prepared in anoxic conditions (b)

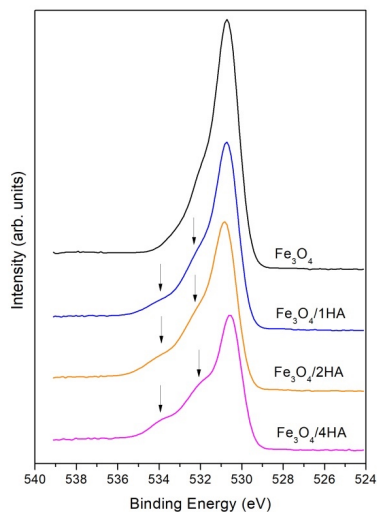


Figure 2.2. High-resolution spectra of $o\ 1s$ region of selected MPs samples prepared under anoxic conditions. Arrows indicate component peaks increasing with the ha increase. Spectra are charging corrected.

Fenton- and photo-Fenton-like degradation of 4-chlorophenol

Preliminary experiments were performed in order to evaluate the efficiency of all MPs towards the degradation of 4-CP at pH 3 (the optimum pH in the homogeneous Fenton reaction). The possible 4-CP adsorption by the MPs was investigated by comparing the nominal concentration of pollutant and that recorded in solution at the end of the equilibration time. Neither significant adsorption nor degradation were observed in the presence of MPs alone (<5%). During degradation experiments, in the presence of MPs/HA under irradiation, the pH value was measured over time and comparing the initial pH with that measured at the end of the degradation no significant change over time was observed ($\Delta\text{pH} \leq 0.1$).

Figure 2.3 shows the results obtained for both, Fenton and photo-Fenton, revealing an increase on the 4-CP degradation for HA coated MPs comparing with bare Fe_3O_4 , in agreement with the literature [137]. The photolysis of H_2O_2 in the adopted irradiation conditions and in the absence of MPs led to negligible 4-CP abatement (see Figure 2.3b). The MPs prepared by adding 0.5 wt.% of HA

solution promoted 4-CP complete degradation after less than 5 minutes of irradiation or 30 minutes in the dark (note the different time axis between Figure 2.3a and 2.3b), while the 4-CP degradation decreased in the presence of MP/HA prepared with higher or lower HA amounts.

In the dark, in all cases except for the bare Fe_3O_4 , it was observed an exponential decay for 4-CP with the irradiation time ($C/C_0 = \exp(-k \times t)$, where C_0 and c are the substrate initial concentration and after the reaction time t , respectively and k is the pseudo first-order kinetic constant of the process. This gave an indication of a constant production of reactive species during the time interval. The 4-CP observed disappearance on Fe_3O_4 followed a different behavior with a sigmoidal profile easily fitted by the equation $C/C_0 = \exp(a+b \times t+c \times t^2)$, where a , b , and c are the fitting constants. In this case, it was observed that the process did not follow a first order kinetic, but the observed rate in the beginning of the reaction was lower. During the first minutes of reaction the system generated/cumulated active forms of iron (e.g., Fe(II) in solution and/or Fe^{2+} species at the surface) able to activate the degradation. This would explain the sigmoidal profile and the activation time observed and previously reported on bare magnetite [65]. Note that the sigmoidal fitting curves reported in Figure 2.3 (and later) has no kinetic meaning and it were reported to help following the degradation profiles and to underline that in these cases the mechanism of transformation is more complex than a process simply described with a pseudo-first order kinetic process in which the concentration of reactive species reaches the steady state condition.

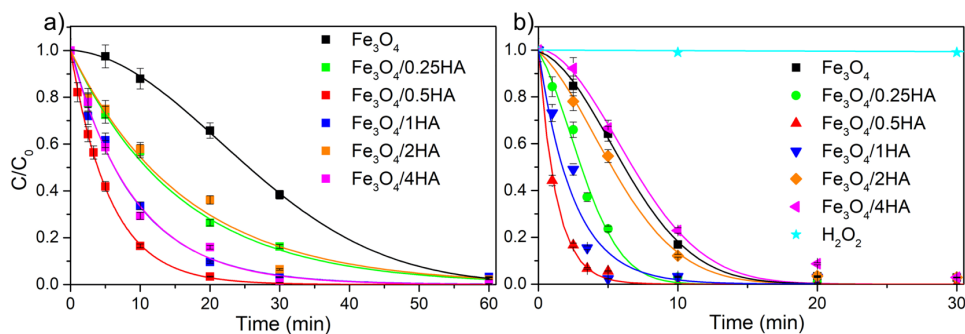


Figure 2.3. Fenton-like (a) and photo-Fenton-like (b) degradation of 4-CP. Conditions: $C_0 = 0.2 \text{ mmol L}^{-1}$, $[H_2O_2] = 1.0 \text{ mmol L}^{-1}$, $[MPs] = 100 \text{ mg L}^{-1}$, pH 3

Under irradiation it was observed an increase of the 4-CP degradation rate in all cases with a total disappearance of 4-CP before 20 minutes of irradiation. A pseudo first-order transformation was observed only with $Fe_3O_4/0.5HA$ and $Fe_3O_4/1HA$, which showed the fastest transformation rate. In all other cases, a sigmoidal behavior was observed. Also, it was possible to suppose the presence of a process able to produce catalytic species that, once sufficiently accumulated in the system, were able to efficiently react with H_2O_2 promoting a fast substrate transformation.

The pH influence was investigated by adjusting the pH to 3, 4, 4.5 and 5. At the explored experimental pH range 4-CP exists as neutral specie being its $pK_a = 9.4$ [122]. Moreover, based on the data present in the literature for similar materials [75], reporting zero point charge of 2.3, we can assume that also in the present case the surface charge of MPs is negative in the explored pH range. Therefore, the working pH explored (from 3 to 5) had no impact on the 4-CP adsorption on MPs surface because the coulombic interaction between the neutral substrate and the negatively charged surface [75] did not change in this quite narrow pH range, as confirmed by the negligible difference between the nominal 4-CP concentration and the one measured in solution after the equilibration time. As a consequence, any eventual change in the reactivity at the different explored pH could not be related to changes in the adsorption of the substrate at the MPs surface.

Figure 2.4 shows the disappearance of 4-CP under irradiation in the presence of the two best performing materials, namely $\text{Fe}_3\text{O}_4/0.5\text{HA}$ and $\text{Fe}_3\text{O}_4/1\text{HA}$, comparing with Fe_3O_4 . For all pH the $\text{Fe}_3\text{O}_4/0.5\text{HA}$ showed the fastest degradation comparing with $\text{Fe}_3\text{O}_4/1\text{HA}$ and more clearly with Fe_3O_4 . For all materials it was observed a decrease of the transformation rate increasing the pH. Analogous results were observed for the experiments performed in the dark, pointing out a slower abatement comparing with the irradiated system (Figure A5).

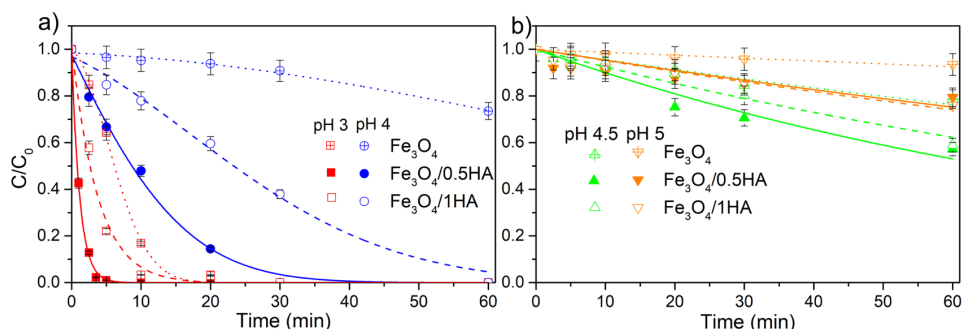


Figure 2.4. Photo-Fenton-like degradation of 4-CP (0.2 mmol L^{-1}) with H_2O_2 (1.0 mmol L^{-1}) and 100 mg L^{-1} MPs at adjusted pH (3, 4, 4.5 and 5). Crossed open symbols: bare materials; solid symbols: $\text{Fe}_3\text{O}_4/0.5\text{HA}$; open symbols: $\text{Fe}_3\text{O}_4/1\text{HA}$.

An effective degradation of 4-CP was observed up to pH 4, at pH 4.5 the process was yet operative, although with slower kinetics, only under irradiation. At pH 4.5 in the dark the 4-CP degradation was blocked. As recently reported for the degradation of Ibuprofen [138], the impact of changing the operative pH from 3 to 4 is not negligible on the overall economic balance of a Fenton process. In particular, the shift of the pH from 3 to 4 can save costs related to the pH adjusting reagents of roughly 30 %; note that the cost of the pH adjusting reagents accounts for an important fraction (roughly 40%) of the overall cost of the reagents used to carry out a thermal Fenton process [61].

The 4-CP main transformation products were identified as hydroxyquinone and benzoquinone by comparing the retention times of original standards. These hydroxylated products resulted from the electrophilic attack on the aromatic ring

of 4-CP presumably by the generated hydroxyl radicals, as previously observed in thermal Fenton and Fenton-like processes [139,140]. The observed transformation products suggested a dominant role of the hydroxyl radicals as reactive species in the adopted experimental conditions. This was recently demonstrated with the same materials and in similar conditions through competitive experiments by using isopropanol as selective $\bullet\text{OH}$ scavengers [141].

Iron release in solution

Several previous studies, dealing with the use of magnetite-based materials in Fenton-like and photo-Fenton-like processes, reported a strongly dependency of the efficiency on the dissolution of iron, revealing that the oxidation proceeds mostly *via* homogeneous Fenton [65]. The total amount of Fe released in solution at pH=3 and its Fe(II)/Fe(III) speciation were determined spectrophotometrically. The effect of HA on the MPs iron leaching was evaluated by comparing the $\text{Fe}_3\text{O}_4/0.5\text{HA}$ and $\text{Fe}_3\text{O}_4/1\text{HA}$ behavior with the Fe_3O_4 in the presence and absence of H_2O_2 and upon irradiation or in the dark (Figure 2.5). Since the free-Fe(II) released in solution, for both, $\text{Fe}_3\text{O}_4/0.5\text{HA}$ (Figure 2.5a) and $\text{Fe}_3\text{O}_4/1\text{HA}$ MPs (Figure 2.5b) was $\sim 0.8 \times 10^{-2} \text{ mmol L}^{-1}$ at time zero compared to $\sim 0.3 \times 10^{-2} \text{ mmol L}^{-1}$ observed for Fe_3O_4 MPs (Figure 2.5c), an intrinsic effect can be attributed to the HA. As expected, for all MPs the free-Fe(II) in solution decreased in the presence of H_2O_2 due to its oxidation to Fe(III) and consequent production of $\bullet\text{OH}$. The amount of iron released in solution was higher with $\text{Fe}_3\text{O}_4/0.5\text{HA}$ than in the presence of the bare Fe_3O_4 and $\text{Fe}_3\text{O}_4/1\text{HA}$ both in the dark and under irradiation. Moreover, an increase on iron leaching was observed for all MPs upon irradiation clearly indicating the photodissolution of the catalyst as previously reported [65]. The iron released in solution, at higher rate under irradiation, was mainly Fe(II) probably due to the lower product of solubility values (K_{ps}) of the Fe(III) hydroxides with respect to Fe(II) hydroxides. The highest dissolution observed with $\text{Fe}_3\text{O}_4/0.5\text{HA}$ is in agreement with the XPS analysis that

showed a surface richer of surface defective structures, presumably more prone to be (photo)dissolved. The iron released in the best condition for the substrate degradation (i.e. under irradiation, pH 3, H_2O_2) was always below the limit for the discharge of water in surface bodies imposed by the common environmental legislations (e.g. for the Italian legislation the limit is 3.6×10^{-2} mM [142]). This means that in a real scenario at the end of the treatment the water might be discharged without any additional treatment for the abatement of the iron.

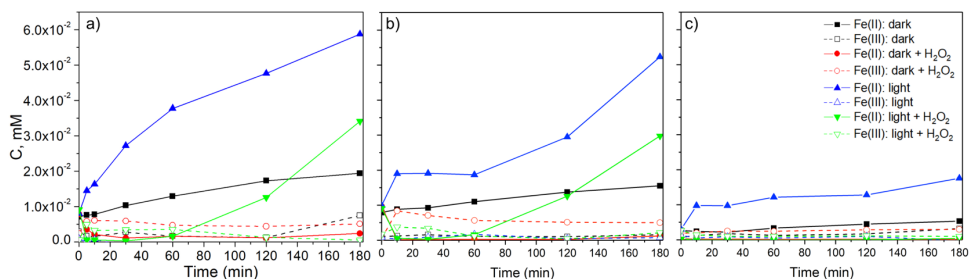


Figure 2.5. *Fe(II) and Fe(III) released in solution, in the dark and under irradiation, at pH 3 in the presence or absence of H_2O_2 (1 mmol L^{-1}) after removing the 100 mg L^{-1} of $\text{Fe}_3\text{O}_4/0.5\text{HA}$ (a); $\text{Fe}_3\text{O}_4/1\text{HA}$ (b) and Fe_3O_4 (c)*

To evaluate the contribution of Fe(II)/Fe(III) ions released in solution on H_2O_2 activation, degradation experiments were performed by adding 4-CP and H_2O_2 to the supernatant.

Figure 2.6 shows the 4-CP degradation upon irradiation for $\text{Fe}_3\text{O}_4/0.5\text{HA}$ and $\text{Fe}_3\text{O}_4/1\text{HA}$ supernatants solutions. 4-CP abatement was observed for both systems. This effect was attributed to homogeneous reactivity promoted by the dissolved iron. However, the 4-CP abatement was considerably lower if compared to the same experiments performed in the related heterogeneous conditions.

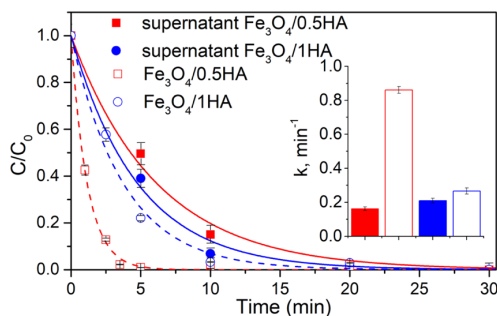


Figure 2.6. Effect of iron ions released in solution on the 4-chlorophenol (0.2 mmol L^{-1}) abated in the presence of H_2O_2 (1.0 mmol L^{-1}) at pH 3 with $Fe_3O_4/0.5HA$ and $Fe_3O_4/1HA$ (100 mg L^{-1}) under irradiation. Inset: first-order kinetic constants of the process.

The results shown in Figure 2.6 highlighted the active role of the Fe_3O_4/HA MPs either as iron reservoir that produced continuously active Fe(II) species at the surface or in solution (especially under irradiation) or as support of catalytic sites where efficient electron transfer between Fe(II) species and H_2O_2 occurred. The second hypothesis seems to be more robust. The comparison between the kinetics of dissolution (relatively slow, see the time axis of Figure 2.5) and that of 4-CP degradation in the best experimental conditions (i.e. 4-CP half-time in the 0.5-1 min range, at pH 3 and under irradiation) suggested an operative role of the surface sites, and consequently a process that occurred mainly at the solid/liquid interface. Indeed, the significant difference between the degradation rates observed in the supernatant and in the related heterogeneous conditions cannot be rationalized simply on the basis of the role of iron reservoir for the MPs.

To better understand the impact of inert atmosphere during the materials synthesis, the MPs prepared with 0.5 wt.% of HA in air atmosphere (ox- $Fe_3O_4/0.5HA$) were tested toward 4-CP. Figure 2.7 a lower degradation rate for the ox- $Fe_3O_4/0.5HA$, both in dark and upon irradiation, comparing with the material prepared under inert atmosphere. Moreover, the kinetic profile observed when using ox- $Fe_3O_4/0.5HA$ under irradiation, features a sigmoidal shape, analogously to the 4-CP disappearance observed on Fe_3O_4 (Figure 2.3).

According to these results, the enhancement of the H_2O_2 activation from the materials prepared under nitrogen might be attributed to the higher bulk $\text{Fe(II)}/\text{Fe(III)}$ ratio, as manifest by its non-reddish color.

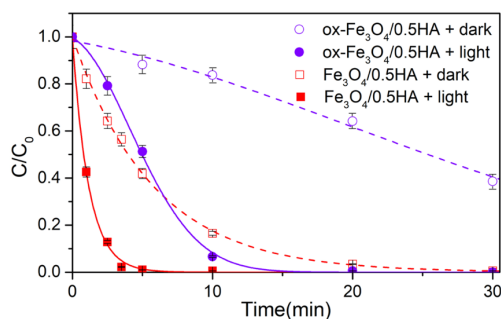


Figure 2.7. Degradation of 4-CP (0.2 mmol L^{-1}) in the presence of $\text{ox-Fe}_3\text{O}_4/0.5\text{HA}$ and $\text{Fe}_3\text{O}_4/0.5\text{HA}$ (100 mg L^{-1}) at pH 3 and H_2O_2 (1.0 mmol L^{-1}), in the dark and under irradiation

Photodegradation of CECs

The best performing material, namely $\text{Fe}_3\text{O}_4/0.5\text{HA}$, was tested toward 4 CECs commonly found in the environment, belonging to different categories and with distinctive chemical structure, representing a wide range of water pollutants, precisely: bisphenol A (BPA, a phenolic compound used in plastic industry), ibuprofen (IBU, an aromatic carboxylic acid used as anti-inflammatory drug), carbamazepine (CBZ, a tricyclic compound with a carboxamides functional group used as psychiatric drug) and 5-tolylbenzotriazole (5-TBA, a corrosion inhibitor with a benzotriazole ring). The molecular structure of the investigated CECs is reported in Figure A6. The CECs abatement was tested separately in a single-compound experiment with the initial concentration of 0.2 mmol L^{-1} , excepting the CBZ (0.1 mmol L^{-1}) for solubility reasons. The Fenton-like and the photo-Fenton-like activity were evaluated in the dark and under irradiation, at pH 3 and 4, in the presence of 100 mg L^{-1} of $\text{Fe}_3\text{O}_4/0.5\text{HA}$ and adding 1.0 mmol L^{-1} of H_2O_2 (Figure 2.8). Based on the pK_a values of the investigated compounds, only 5-TBA was present as cation in all the investigated pH range, while the other compounds were in their neutral form. The effect of the pH on the CECs

degradation was the same for all pollutants being the most efficient condition at pH 3. It was observed a degradation higher than 80% of BPA, CBZ and 5-TBA after 1h under irradiation, while only 35% of IBP was removed. From these, it is not possible to evidence any significant effect of neutrality/charge at pH 3; indeed BPA (neutral) and 5-TBA (cation) featured similar degradation profile.

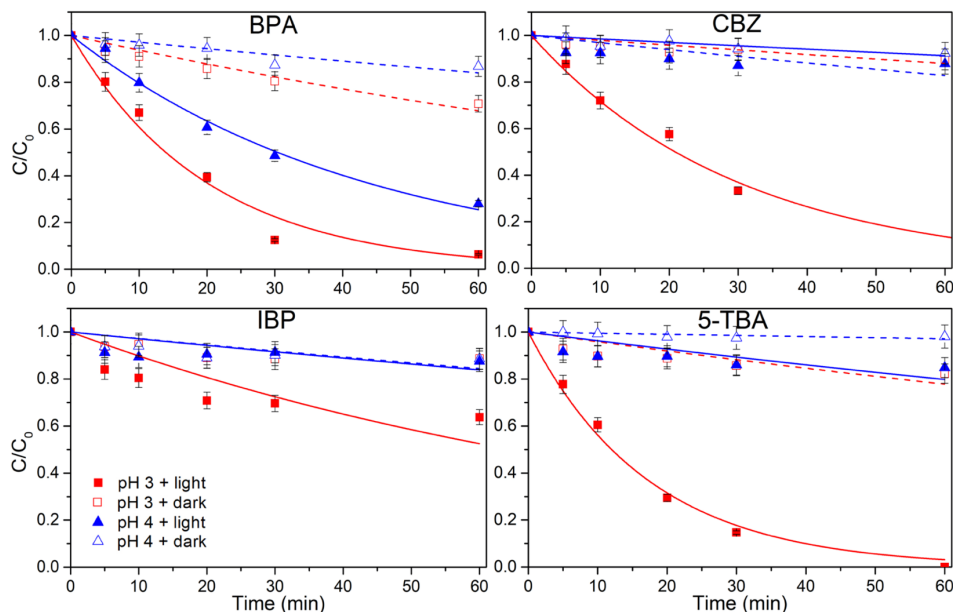


Figure 2.8. Fenton-like and photo-Fenton-like degradation of each CEC separately ($C_0^{BPA,IBP,5-TBA} = 0.2 \text{ mmol L}^{-1}$; $C_0^{CBZ} = 0.1 \text{ mmol L}^{-1}$) at pH 3 and 4, in the presence of H_2O_2 (1.0 mmol L^{-1}) and $Fe_3O_4/0.5HA$ (100 mg L^{-1})

At pH 4 a significant degradation was observed only for BPA, under irradiation, while CBZ, IBP and 5-TBA were only partially removed. The extension up to pH 4 of the reactivity of $Fe_3O_4/0.5HA$ was previously reported for 4-CP (see above): the presence of phenolic moieties seemed to promote an effective removal of the substrate. The highest reactivity toward BPA can be explained considering that BPA is, among the CECs investigated, the compound with the highest second order kinetic constant with $\cdot OH$ ($1.55 \times 10^{10} \text{ M}^{-1} \text{ s}^{-1}$ [143]), while IBP is that with the lowest one ($6.5 \times 10^9 \text{ M}^{-1} \text{ s}^{-1}$ [143]). This suggested a dominant role of the $\cdot OH$ as reactive species in the investigated process as usually reported for the (photo)Fenton processes carried out in acidic conditions [56] and in

agreement with the main transformation products identified during the 4-CP degradation.

Effect of water matrix

In order to evaluate a more representative system of a real scenario, the efficiency of $\text{Fe}_3\text{O}_4/0.5\text{HA}$ was also tested in real wastewater spiked with a CECs mixture at lower concentration ($C_0 = 20 \mu\text{M}$). The degradation profiles are shown in Figure 2.9 together with the observed kinetic constants. Despite the high concentration of organic and inorganic constituents in the wastewater samples, the obtained results showed no decrease on CECs removal efficiency comparing with results obtained in Milli-Q water (Figure 2.9a). In fact, a slight increase on degradation kinetic constants was observed, being the material able to completely abate the pollutants within 1 h of irradiation. Considering the presence of organic (mainly the dissolved organic matter) and inorganic constituents (mainly inorganic carbon ($\text{HCO}_3^-/\text{CO}_3^{2-}$), but also other reactive anions, e.g. Cl^- and NO_3^-) in wastewater sample that can compete for the reactive species, these results were rather surprising and support the possible application of this process for the abatement of recalcitrant pollutants in real wastewaters.

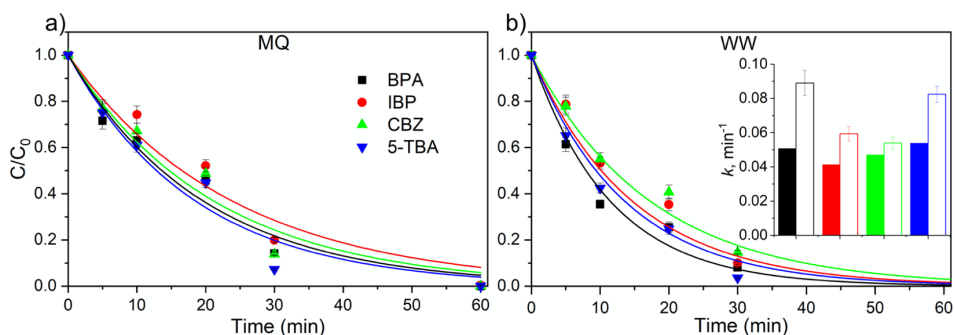


Figure 2.9. Photo-Fenton-like degradation of CEC mixture ($20 \mu\text{M}$) in a) Milli-Q water (MQ) and b) real wastewater (WW) sample at pH 3, in the presence of H_2O_2 (1.0 mmol L^{-1}) and $\text{Fe}_3\text{O}_4/0.5\text{HA}$ (100 mg L^{-1}). Inset: first-order kinetic constants of the process carried out in Milli-Q water (solid bars) and wastewater (open bars).

2.1.4 Conclusions

Humic acid coated Fe_3O_4 magnetic particles prepared *via* co-precipitation method under inert atmosphere were highly efficient to abate 4-CP in Fenton-like and photo-Fenton-like conditions and showed an enhanced activity when compared with the bare magnetite.

Thanks to XPS experiments it was possible to evidence a structure-reactivity relationship for MPs, suggesting an active role of the more defective iron species at the surface to promote faster degradations due to not only a faster photodissolution of the iron phase, but also to a higher reactivity at the catalyst surface. Although the iron ions leached into solution had a remarkable influence in the oxidation process, a relevant role can therefore be imputed to processes at the solid/liquid interface (heterogeneous reactivity).

The experiments carried out with a CECs mixture showed that $\text{Fe}_3\text{O}_4/0.5\text{HA}$ is a promising catalyst for heterogeneous (photo)-Fenton process at pH lower than 4, particularly active towards compounds with phenolic moieties also in wastewater.

This result, together with the good reusability of $\text{Fe}_3\text{O}_4/0.5\text{HA}$, see Section 2.2, opens the possibility of developing advanced tertiary treatments for the removal of CECs from urban wastewater by employing cheap and environmentally friendly materials and reagents (e.g. H_2O_2) and activating the process through the widely diffused and inexpensive solar irradiation.

2.2 Photo-Activation of Persulfate and Hydrogen Peroxide by Humic Acid Coated Magnetic Particles

Adapted from:

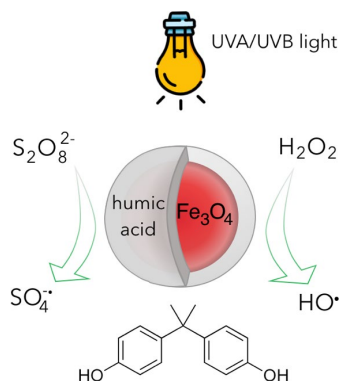


Photo-Activation of Persulfate and Hydrogen Peroxide by Humic Acid Coated Magnetic Particles for Bisphenol A Degradation

Nuno P.F Gonçalves, Marco Minella, Gilles Mailhot, Marcello Brigante,
Alessandra Bianco Prevot

Catalysis Today 361 (2021) 43–49

My direct contribution

I declare that I have prepared the material used in this work, and I have performed all the photocatalytic experiments and the identification of reactive species. All the laboratorial work was performed during my secondment at CNRS - Institut de Chimie de Clermont-Ferrand in the group of Professor Marcello Brigante.

2.2.1 Motivation

Similarly to the $\cdot\text{OH}$, the sulfate radical ($\text{SO}_4^{\bullet-}$) has a high oxidation potential ($E_0(\text{SO}_4^{\bullet-}/\text{SO}_4^{2-}) = 2.43 \text{ V vs NHE}$ [144], being investigated for oxidation of recalcitrant pollutants [49,145,146]. The activation of persulfate and peroxymonosulfate ($\text{S}_2\text{O}_8^{2-}/\text{SO}_5^{2-}$) to generate $\text{SO}_4^{\bullet-}$ can be promoted by reactions of these precursors with iron both in the dark and under irradiation [60,147], in the presence and absence of ligands [148,149]. Additionally, the persulfate is described as less subject than $\cdot\text{OH}$ to constituents of the real water samples, presenting an higher selectivity toward some pollutants [60,150]. Considering the usual low cost and quite high reactivity of the most common proposed iron-based catalysts, the activation of H_2O_2 and $\text{S}_2\text{O}_8^{2-}$ by these catalysts is raising growing interest in water treatment for emerging contaminant abatement [60,145].

In this work we investigated the use of the previous MPs coated with humic acid for the activation of persulfate. The best performing material, identified in the Section 2.1, was used in a comparative study between persulfate and hydrogen peroxide under UVA/UVB irradiation. The effect of pH, catalyst loading, oxidant agent loading was investigated using Bisphenol A (BPA) as pollutant model molecule. The contribution of the homogeneous photo-Fenton promoted by the iron released in solution was considered by following the degradation in the supernatant solution after removing the heterogeneous catalyst. The reactive species in both systems were identified by the addition of quenching agents. The catalyst recovery and reusability in consecutive cycles was performed by means of a magnetic field.

Additionally, the overall process sustainability was considered and a comparative (Life Cycle Assessment) LCA study and a comparative LCA study was performed applying $\text{Fe}_3\text{O}_4/\text{HA}$ materials for the activation of hydrogen peroxide and persulfate.

2.2.2 Materials and Methods

Materials

H₂O₂ (30% in water) was purchased from Fluka (France); bisphenol A and Na₂S₂O₈ from Sigma (France); FeCl₃·6H₂O and FeSO₄·7H₂O from Carlo Erba Reagents (Italy); humic acid sodium salts (technical, 50–60% as HA) from Aldrich-Chemie. Suspensions and standard solutions were prepared in Milli-Q water.

Humic coated magnetite particles were synthesized and characterized as reported on Chapter 2, section 2.1.2.

The Sewage Treatment Plant Water (STPW) was collected from the outflow (immediately before the last disinfection and the water discharge) of a wastewater treatment plant on NW of Italy (January 15th, 2019). Samples were used after a rough pre-filtration step, carried out through a grade qualitative filter paper (Whatman) removing large suspended solids and filtered using a hydrophilic 0.45 µm filter Sartolon Polyamide (Sartorius Biolab).

Degradation experiments under UVA/UVB irradiation

Irradiations were performed in a cylindrical Pyrex reactor, placed in a rectangular box equipped on the top with four lamps (Sankio denki G15T8E) emitting mainly in the UVA and UVB region. The emission spectrum was recorded using an optical fiber coupled with a CCD spectrophotometer (Ocean Optics USD 2000) calibrated with a Deuterium Tungsten Halogen reference lamp. A total irradiance between 265 and 400 nm of 2150 µW cm⁻² was measured (see Figure B1).

The experiments were performed at room temperature using a circulation cooling system. 50 mL of 100 mg L⁻¹ MPs suspension and 20 µM BPA at adjusted pH with H₂SO₄ were sonicated for 20 min, then the H₂O₂ or Na₂S₂O₈ solutions were added. The suspension was magnetically stirred and placed under irradiation. At defined time interval 3 mL were sampled and the reaction

immediately quenched with 200 μL of methanol. The samples were filtered using a 0.45 μm filter before the analysis.

The catalyst reusability experiments were performed by recovering the catalyst after 3h under irradiation using a magnet. The recovered catalyst was 3 times washed and then dried at room temperature before being used in the next run.

The experiments with STPW were performed on BPA-spiked solutions. STPW samples had 14.25 $\text{mg}_\text{C} \text{L}^{-1}$ of total organic carbon (TOC), 34.16 $\text{mg}_\text{C} \text{L}^{-1}$ of inorganic carbon (IC), 7.74 $\text{mg}_\text{N} \text{L}^{-1}$ of total nitrogen (TN) and pH value of 7.3.

Analysis

The concentration of BPA was measured through an ultra-performance liquid chromatography (UPLC) AQUITY (Waters, USA) equipped with photodiode array detector and by using a C18 AQUITY UPHLC BEH column (2.1 \times 100 mm, 1.7 μm). The flow rate was 0.3 mL min^{-1} and the mobile phase was a mixture water methanol (60/40, v/v). The BPA concentration was quantified at 220 nm. TOC, IC and TN were measured using a Shimadzu TOC-5000 analyzer (catalytic oxidation on Pt at 680 $^\circ\text{C}$).

The determination of Fe released in solution was evaluated by a spectrophotometric procedure as reported in the Section 2.1.2, using a Varian CARY 100 Scan double-beam UV–vis spectrophotometer, using quartz cuvettes with 1 cm path length.

2.2.3 Results and Discussion

H₂O₂ and S₂O₈²⁻ activation

In order to evaluate the role of HA coating on the H₂O₂ and S₂O₈²⁻ activation during the degradation of BPA, experiments were run by comparing the BPA degradation in the presence of both the hybrid MPs and the bare magnetite at

different pH values. In all cases the BPA disappearance followed a pseudo-first order kinetics with an exponential decay ($C/C_0 = \exp(-k \times t)$, where C and C_0 are the BPA concentration at the irradiation time t and before irradiation, k is the pseudo-first order kinetic constant). Figure 2.10a shows the BPA disappearance in the presence of H_2O_2 . It was observed an enhancement of the activity promoted by the HA coating for all pH. In detail, at pH 3 the complete abatement of BPA was observed after 2 h in the presence of MPs/HA ($k = 0.034 \pm 0.003 \text{ min}^{-1}$), while with the bare Fe_3O_4 only 80% abatement was achieved ($k = 0.015 \pm 0.001 \text{ min}^{-1}$), in agreement with results previously described [151]. A comparable tendency was observed in the presence of persulfate, as can be observed in Figure 2.10b (e.g. $\frac{k_{pH=3}^{Fe_3O_4/0.5HA}}{k_{pH=3}^{Fe_3O_4}} = 2.344 \pm 0.096$). In the presence of H_2O_2 the BPA abatement was considerably slower for pH higher than 4, while the effect on the persulfate system was less significant. In fact, even at pH 6 after 2 h under irradiation, 80% of BPA degradation was achieved using $S_2O_8^{2-}$ (despite $\sim 15\%$ with H_2O_2). The initial rates recorded in all the experiments of Figure 2.10 are reported in Table B1 (Appendix B).

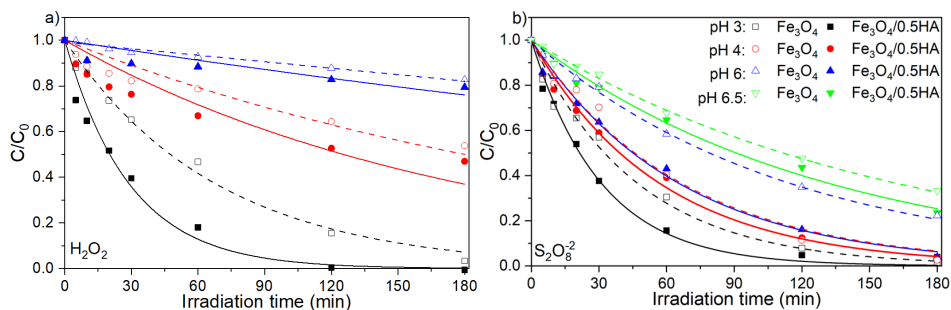


Figure 2.10. BPA photo-degradation with 1 mM H_2O_2 (a), and 1 mM of $S_2O_8^{2-}$ (b) in the presence of bare Fe_3O_4 or $Fe_3O_4/0.5HA$ (100 mg L^{-1}) at different pH. $C_0^{BPA} = 20 \text{ }\mu\text{M}$.

No significant BPA degradation was observed under direct photolysis or in the presence of $Fe_3O_4/0.5HA$ under irradiation. On the contrary, both the photolysis of persulfate and H_2O_2 in the absence of the catalyst allowed a partial degradation of BPA, faster with $S_2O_8^{2-}$ than with H_2O_2 ($\frac{k_{S_2O_8^{2-}}}{k_{H_2O_2}} = 2.47 \pm 0.08$). This

indicates that the investigated hybrid catalyst did not show any pure photocatalytic properties, while its activity was strictly related to its activation ability towards H_2O_2 and $\text{S}_2\text{O}_8^{2-}$, as shown in Figure B2.

It is well established that the pH adjustment and its subsequent neutralization, before water discharge, is responsible for an important part of the cost on the Fenton-like processes [61]. Keep the system working at circumneutral pH can be determining for the process cost-effectiveness allowing the feasibility for its application as water treatment. Considering this and in the light of possible in real scenario applications, the further persulfate experiments were performed at pH 6 while in the case of hydrogen peroxide experiments were performed at pH 3 to keep the system active (at pH 6 the H_2O_2 activation by $\text{Fe}_3\text{O}_4/0.5\text{HA}$ was negligible both in the dark and under irradiation, see Figure 2.10a).

Contribution of homogeneous catalysis

It has been reported that the contribution of homogenous (photo)-Fenton promoted by Fe(II) and Fe(III) ions released in solution by magnetite-based materials can have a not negligible effect in the abatement of organic substrates [65]. In this work the influence of irradiation on the iron release (concentration and redox speciation) was evaluated by determining the concentration of iron in solution, keeping the solution in the dark or under irradiation at pH 3, 4 and 6. Figure 2.11 shows the Fe(II) and Fe(III) concentration spectrophotometrically determined. At time zero (after the sonication period) it was observed a higher amount of Fe(II) with respect to Fe(III) in agreement with the absence of H_2O_2 - able to oxidize Fe(II) to Fe(III) - and the higher solubility of Fe(II) with respect to Fe(III) ($\text{pKsFe(OH)}_3 = 38.8$, $\text{pKsFe(OH)}_2 = 15.1$ [152]). In the dark it was not observed any increase of the released Fe(II) over time, while under irradiation the release of Fe(II) and Fe(III) (less marked, and only at pH 3) was more obvious. The photo-dissolution of the magnetite-based materials under irradiation has

been largely reported as a consequence of the formation of surface complexes which may trap e_{CB}^- and (or) h_{VB}^+ efficiently, thus enhancing the photodissolution. Spinel type oxides (as the catalyst here tested), such as γ - Fe_2O_3 (maghemite) or Fe_3O_4 , (magnetite) are known to be more easily photocorroded than hematite [153]. The solubility decrease of iron (hydr)oxides can explain the lower Fe(II) and Fe(III) ions concentration observed for the systems at higher pH in the absence of effective ligands for both Fe(II) and Fe(III).

The mechanism of the photodissolution of the catalyst is ultimately quite complex and the data here reported can only partially clarify it. The organic coating has an active role in the process especially because the carboxylic moieties at the surface are for sure effective ligands for Fe^{+2} and Fe^{+3} . Moreover, these iron complexes at the surface are not only redox active species able to react with hydrogen peroxide or persulfate, but they are also photoactive species. Note that, the spectrophotometric method used to determine the iron concentration in solution was carried out on filtered solutions and consequently is silent on the concentration and speciation of the iron complexed by organic ligands at the surface of the catalyst.

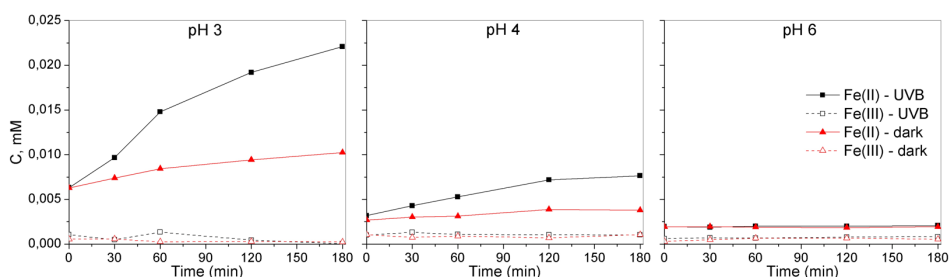


Figure 2.11. Free Fe(II) and Fe(III) ions released in solution at pH 3, 4 and 6 by $Fe_3O_4/0.5HA$ (100 mg L^{-1}) in the dark and under irradiation.

The contribution of the iron released in solution on the initial BPA degradation was evaluated as follows: BPA and $H_2O_2/S_2O_8^{2-}$ were added to the supernatant solution after removing the heterogeneous catalyst by filtration. To evaluate the effect of the iron photo-dissolution, degradation experiments were

performed with supernatant at time zero, but also with the solution after 2h under irradiation.

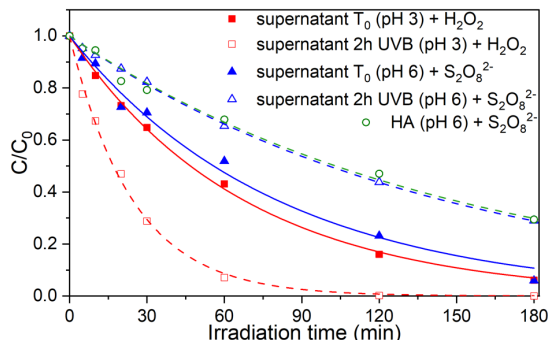


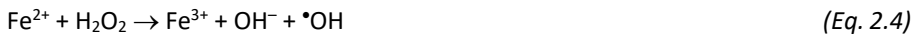
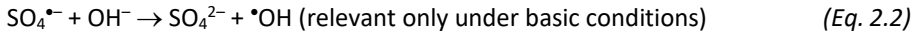
Figure 2.12. BPA photodegradation in supernatant solutions obtained at time zero and after 2 hours of irradiation in the presence of $100 \text{ mg L}^{-1} \text{ Fe}_3\text{O}_4/0.5\text{HA}$ with H_2O_2 1 mM at pH 3 and $\text{S}_2\text{O}_8^{2-}$ 1 mM at pH 6; BPA degradation with $\text{S}_2\text{O}_8^{2-}$ 1 mM and HA 0.4 mg L^{-1})

Figure 2.12 shows the BPA degradation on supernatant at pH 3 after adding H_2O_2 and on supernatant at pH 6 after $\text{S}_2\text{O}_8^{2-}$ addition. For both systems it was observed the BPA degradation in the homogenous phase. The addition of H_2O_2 to the pH 3 supernatant obtained after 2h under irradiation allows to achieve a higher BPA degradation comparing with the corresponding supernatant at t_0 . The higher concentration of iron resulted from the photo-dissolution of the catalyst. This tendency was not observed with persulfate. In fact, the supernatant at t_0 allowed to obtain higher BPA degradation than the supernatant after 2h under irradiation. The low and stable over the time concentration of iron observed at pH 6 (Figure 2.11, suggested an equal production of reactive species during the experiments with the two supernatants. The decreased rate of transformation observed with the supernatants obtained after 2 hours of irradiation, can be explained by considering the quenching effect of the HA that were partially released in solution from the organic coating, as previously reported with similar materials [75,154]. This was sustained by the negative effect observed on the BPA degradation when the direct photolysis of persulfate was carried out in solution containing HA (0.4 mg L^{-1} - the same HA amount added with 100 mg L^{-1}

of catalyst – considering the HA loading equal 0.4% w/w) which acted as efficient scavengers of reactive species.

Identification of reactive species

The reaction of H_2O_2 and $\text{S}_2\text{O}_8^{2-}$ with iron (in solution and/or at the catalyst surface, in the dark or under irradiation) can promote the formation of both $\text{SO}_4^{\bullet-}$ and $\bullet\text{OH}$ according to the following reactions:



Both $\bullet\text{OH}$ and $\text{SO}_4^{\bullet-}$ can react not only with the contaminants, but also with the oxidants (eq. 2.7 and 2.9) which, at high concentration, are able to scavenge efficiently the reactive species depressing the overall reaction rate



Furthermore, under UVA/UVB irradiation the overlap between the emission spectrum of the adopted lamps and the absorption spectra of H_2O_2 and $\text{S}_2\text{O}_8^{2-}$ can promote the photolysis of both the oxidants [155].



To understand the role of the generated reactive species involved in the investigated degradation processes, BPA photodegradation was carried out in the presence of radical scavengers (see Figure B3). Isopropanol was used due to the high reactivity with hydroxyl radical ($k_{\text{HO}^\bullet, \text{isop}} = 1.9 \times 10^9 \text{M}^{-1}\text{s}^{-1}$) [156].

With H_2O_2 we observed an almost complete inhibition of BPA degradation ($\frac{k_{H_2O_2}}{k_{isop}} = 35.0 \pm 0.12$) indicating that the degradation is mainly due to the $\bullet OH$ radicals. The BPA degradation is strongly inhibited by isopropanol also in the case of $S_2O_8^{2-}$ ($\frac{k_{S_2O_8^{2-}}}{k_{isop}} = 11.06 \pm 0.09$). However, since isopropanol is able to quench both $\bullet OH$ and $SO_4^{\bullet -}$ radicals ($k_{SO_4^{\bullet -}, isop} = 8.6 \times 10^7 M^{-1} s^{-1}$) [157], the BPA degradation was carried out also in the presence of *t*-butanol that is a more selective quenching of $\bullet OH$ ($k_{HO\bullet, t-but} = 3.1 \times 10^9 M^{-1} s^{-1}$), than of $SO_4^{\bullet -}$ ($k_{SO_4^{\bullet -}, t-but} = 8.4 \times 10^5 M^{-1} s^{-1}$) [156,157]. Figure B3 shows an only limited inhibition of the BPA degradation in the presence of *t*-butanol demonstrating that the degradation is mainly promoted by $SO_4^{\bullet -}$.

Effect of H_2O_2 and $S_2O_8^{2-}$ concentration

To elucidate the effect of H_2O_2 concentration on the catalytic system, experiments were performed by adding different H_2O_2 concentration (0.5, 1, 2, 3, 5 and 10 mM) at pH 3 (Figure 2.13a) and pH 4 (Figure 2.13b) in the presence of 100 mg L^{-1} of catalyst. The inset of Figure 4a shows a quite complex behavior for the BPA initial transformation rate at pH 3, with an increment of the BPA degradation rate up to 1 mM, then a sharp decrease and for $[H_2O_2] > 3 \text{ mM}$ a further increase. While at pH 4 the highest degradation was achieved at 2 mM, but similar rates were observed for higher concentrations (see inset of Figure 5a). This tendency can be only partially explained by the scavenging effect of H_2O_2 (eq. 9) as often reported in the literature [158,159], because the decrease of the initial rate as a consequence of the increment of the oxidant concentration can justify a bell-profile and not a profile with a maximum and a minimum as that observed at pH 3. At high concentration of H_2O_2 a further process different to the photo-Fenton one (e.g. the direct photolysis of H_2O_2 which is a first order process with respect to hydrogen peroxide, and consequently increased linearly

with the increase of the H_2O_2 concentration) might sustain the overall transformation compensating the scavenge of the $\cdot\text{OH}$, formed through the reactions 4 and 7, by H_2O_2 .

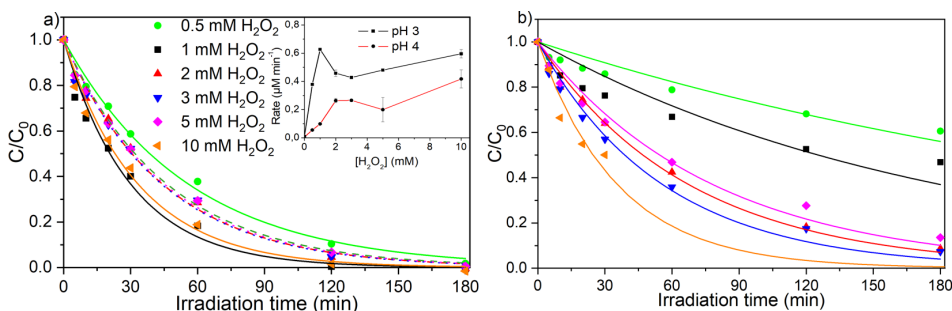


Figure 2.13. Degradation profiles of BPA under irradiation with increasing concentration of initial H_2O_2 in the presence of $\text{Fe}_3\text{O}_4/\text{HA}$ (100 mg L^{-1}) at pH 3 (a) and pH 4 (b). Inset of figure (a): initial BPA degradation rate as a function of the H_2O_2 concentration.

The BPA degradation was performed as well at different persulfate concentration (0.5, 1, 2, 3, 5 and 10 mM). Contrary of data obtained on H_2O_2 experiments, it was observed a monotonic increase of the rate rising the $\text{S}_2\text{O}_8^{2-}$ concentration (Figure 2.14a). To split the contribution of the catalyst from that of the persulfate photolysis, the same experiments were carried out in the absence of the catalyst. The comparison among the rate is reported in Figure 6b. We observed a different behavior at $[\text{S}_2\text{O}_8^{2-}]$ higher and lower than 2 mM. At $[\text{S}_2\text{O}_8^{2-}] < 2 \text{ mM}$ we recorded a positive effect of the presence of the iron-based catalyst, while at $[\text{S}_2\text{O}_8^{2-}] > 2 \text{ mM}$ the presence of $\text{Fe}_3\text{O}_4/0.5\text{HA}$ had a negative effect, being the degradation rate higher without catalyst. This trend could be attributed to a scavenger effect from the HA acid coating, competing with the generated reactive species and to the screening effect of the catalyst for the photons activating the photolysis of $\text{S}_2\text{O}_8^{2-}$ (the humic acid that can compete for the absorption of photons with the active iron-based species at the surface or in solution). The behaviour of the transformation rate with the H_2O_2 and $\text{S}_2\text{O}_8^{2-}$ concentration reported in Figure 2.13 and Figure 2.14 cannot be easily explain invoking the scavenger effect of H_2O_2 and $\text{S}_2\text{O}_8^{2-}$ only. The recorded profiles are

the results of the very complex network of reactions composing the Fenton heterogeneous process on the investigated MPs (activated by H_2O_2 or $\text{S}_2\text{O}_8^{2-}$). This complexity is well described in some previously published article [160–164].

Note that too high concentrations of $\text{S}_2\text{O}_8^{2-}$ must be avoided because the higher is the concentration of persulfate, the higher is the concentration of sulfate (the last product of the persulfate activated processes) in the final treated water. As an example, the Italian legislation imposes for the discharge of water in surface bodies a concentration of $\text{SO}_4^{2-} < 1000 \text{ mg L}^{-1}$ (10.4 mM) [165]. This value might be easily exceeded by treating the wastewater with persulfate at concentration higher than 5 mM (in this case the water should be furtherly treated after the heterogeneous photo-Fenton process to remove the excess of sulfate before the discharge). Carrying out the photo-Fenton process with H_2O_2 the same problem might be met. It is true that if H_2O_2 reacts completely the final products are environmental benign, but the need to carry out the photo-Fenton process at pH 3 and the successive phase of neutralization give very salted water that must be further treated before the discharge.

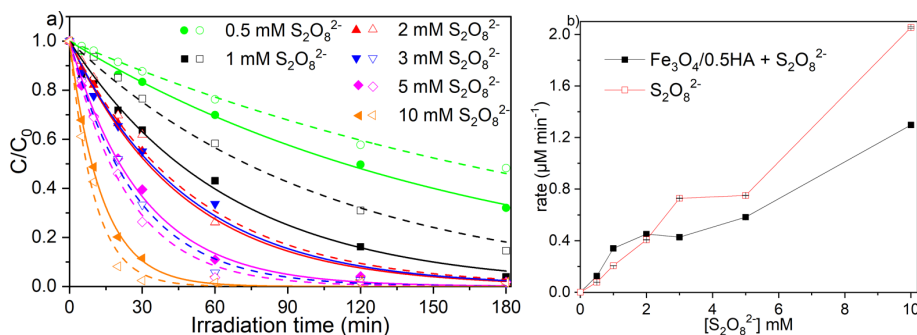


Figure 2.14. BPA degradation profiles in the presence (full symbols) and absence (empty symbols) of $\text{Fe}_3\text{O}_4/0.5\text{HA}$ (100 mg L^{-1}) at pH 6 using different $\text{S}_2\text{O}_8^{2-}$ concentrations. b) BPA initial degradation rate with and without $\text{Fe}_3\text{O}_4/0.5\text{HA}$ particles in the presence of different $\text{S}_2\text{O}_8^{2-}$ concentrations.

Catalyst recover and reuse

The catalyst reusability was tested by magnetically recovering the catalyst at the end of the BPA degradation. The catalyst was washed with water and dried

before use for the next run. Figure 2.15 shows the BPA abatement in 3 consecutive runs in the presence of H_2O_2 at pH 3 and $\text{S}_2\text{O}_8^{2-}$ at pH 6. At pH 6 in the presence of $\text{S}_2\text{O}_8^{2-}$ no decrease of activity was observed, while at pH 3 in the presence of H_2O_2 a very slight decrease on BPA abatement was observed. In both cases the tested catalyst did not show a significant deactivation/poisoning with the use.

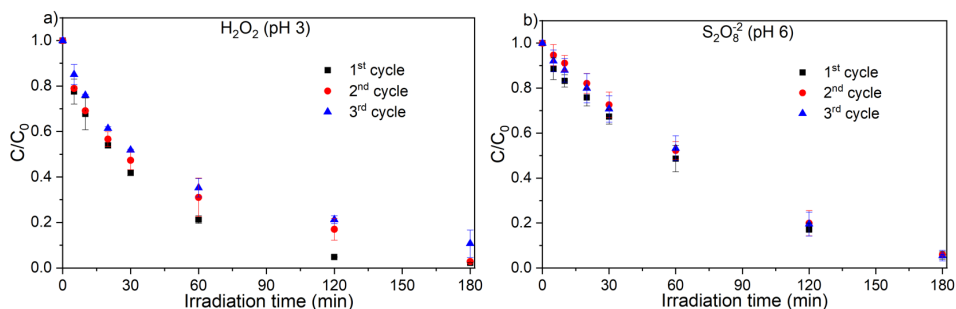


Figure 2.15. Reusability of catalyst for BPA degradation: a) 1 mM of H_2O_2 at pH 3; b) 1 mM of $\text{S}_2\text{O}_8^{2-}$ at pH 6.

Effect of water matrix composition

The influence of water matrix composition on H_2O_2 and $\text{S}_2\text{O}_8^{2-}$ based process was evaluated by comparing BPA degradation in STPW samples and in Milli-Q water. Figure 2.16 shows the BPA degradation profiles, a different behavior with H_2O_2 (pH 3) and $\text{S}_2\text{O}_8^{2-}$ (pH 6) was observed. With H_2O_2 the BPA degradation profile did not follow a first-order kinetics. The initial rate in real matrix was higher than in ultrapure water, but after 30 minutes the process slowed down giving after 3 hours a lower degradation than in ultrapure water. A hypothesis is that the presence of organic species able to act as iron ligands gave an initial higher concentration of iron in solution able to react with H_2O_2 , then the higher concentration of organic/inorganic scavengers partially block the reaction. With persulfate, the BPA degradation followed in both cases a pseudo-first order kinetics, but due to the high concentration of organic and inorganic scavengers

[166,167] in the STPW the rate was roughly 4 times lower ($\frac{k_{\text{Milli-Q}}^{\text{S}_2\text{O}_8^{2-}}}{k_{\text{STPW}}^{\text{S}_2\text{O}_8^{2-}}} = 4.43 \pm 0.10$).

The STPW sample used to simulate a real-world scenario had $2.7 \text{ mg}_C \text{ L}^{-1}$ dissolved organic carbon, $41.1 \text{ mg}_C \text{ L}^{-1}$ dissolved inorganic carbon, $\text{pH} = 7.6$ and $0.14 \mu\text{S cm}^{-1}$ conductivity. It is quite difficult on the basis of the composition of the water only, give more insights into the role that the specific components of the matrix have on modifying the rate of BPA transformation. In particular, it is possible argued that the presence of hydroxyl and sulfate radical scavengers can limit the overall degradation, as well as that the presence of high concentration of inorganic carbon (this is the case) can promote the formation of a huge amount of $\text{CO}_3^{\bullet-}/\text{HCO}_3^{\bullet-}$ radicals that are less reactive towards BPA than $^{\bullet}\text{OH}$ and $\text{SO}_4^{\bullet-}$ as it is possible conclude observing the kinetic constant of BPA with hydroxyl, sulfate and carbonate/hydrogen carbonate radicals, $k_{\text{HO}^{\bullet},\text{BPA}} = 1.70 \pm 0.21 \times 10^{10} \text{ M}^{-1} \text{ s}^{-1}$, $k_{\text{SO}_4^{\bullet-},\text{BPA}} = 1.37 \pm 0.15 \times 10^9 \text{ M}^{-1} \text{ s}^{-1}$ and $k_{\text{CO}_3^{\bullet-}/\text{HCO}_3^{\bullet-},\text{BPA}} = 3.89 \pm 0.09 \times 10^6 \text{ M}^{-1} \text{ s}^{-1}$ [168]. The role of the single species might be evaluated with specific experiments, but this is far from the scope of the actual manuscript.

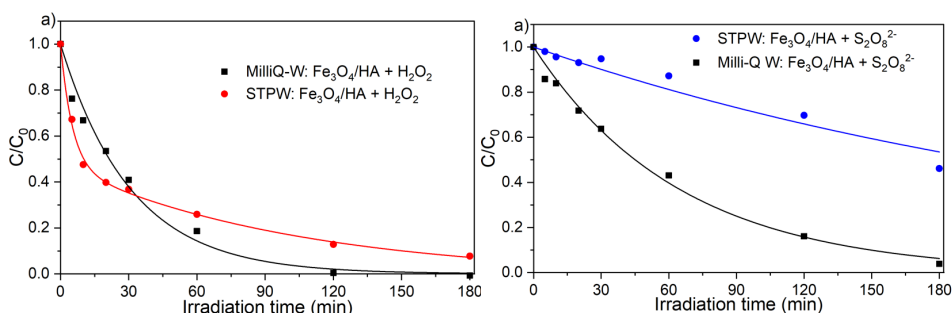


Figure 2.16. BPA degradation in STPW in the presence of 100 mg L^{-1} of catalyst: a) 1 mM of H_2O_2 at $\text{pH} 3$; b) 1 mM of $\text{S}_2\text{O}_8^{2-}$ at $\text{pH} 6$. Note that in the case of STPW with H_2O_2 the fitting curve has not a kinetic meaning, but it is reported only to help following the BPA degradation.

2.2.4 Conclusions

Coating Fe_3O_4 with HA efficiently induced higher H_2O_2 and persulfate activation for the BPA removal at different pH, comparing with the pristine magnetite. The $\text{Fe}_3\text{O}_4/0.5\text{HA}$ showed high capability to activate H_2O_2 at $\text{pH} 3$ with a substantial decrease of activity at pH higher than 4, while in the presence of

persulfate even at pH 6 the system was still able to efficiently remove BPA. Both with H_2O_2 and $\text{S}_2\text{O}_8^{2-}$, the heterogeneous photo-Fenton process here investigated was operational in real wastewater, even if with lower kinetics than in ultrapure water.

The main reactive species involved in the process catalyzed by $\text{Fe}_3\text{O}_4/0.5\text{HA}$ were $\cdot\text{OH}$ (in the presence of H_2O_2) and $\text{SO}_4^{\cdot-}$ (in the presence of $\text{S}_2\text{O}_8^{2-}$).

The recovery experiments highlighted no significant loss of activity with the reuse of the material both with H_2O_2 at pH 3 and $\text{S}_2\text{O}_8^{2-}$ at pH 6.

With H_2O_2 (at pH 3) the photo-Fenton process in the presence of $\text{Fe}_3\text{O}_4/0.5\text{HA}$ gave always better results than the “pure” photolysis of hydrogen peroxide, while with $\text{S}_2\text{O}_8^{2-}$ the presence of the catalyst gave a positive effect in comparison with the persulfate photolysis at $[\text{S}_2\text{O}_8^{2-}] < 2 \text{ mM}$ (note that $[\text{S}_2\text{O}_8^{2-}] > 5\text{mM}$ have to be avoided to prevent the production of final water with a sulfate concentration exceeding the law limits). At the same time, the photo-Fenton process at pH 3 can give after the final neutralization very salted water that must be further treated before the discharge

Chapter 3 - Development of Oxides Doped with Transition Metals and their Exploitation to Pollutants Abatement

The present chapter describes the preparation of ZnO based photocatalytic materials Fe- and Co-doped, prepared by different synthetic methods with different doping elements concentrations. Their photocatalytic activities for removal of pollutants from water are also reported.

3.1 Materials and Methods

Chemicals

The precursors and reagents used in the synthesis of new materials and in subsequent analyzes for the evaluation of their photocatalytic activity, were purchased by Sigma-Aldrich. Suspensions and standard solutions were prepared in Milli-Q water.

The real wastewater samples were provided by SMAT S.p.A. (Società Metropolitana Acque Torino, Italy) and were sampled at the wastewater treatment facility of Castiglione Torinese (Italy) on 27 October 2017. The samples used in this work were obtained from the outflow of the primary clarifier tank (hereafter, Primary sample). Real samples were used after a rough pre-filtration step, carried out through a grade 1 qualitative filter paper (Whatman) to remove large suspended solids and filtered using a hydrophilic 0.45 μm filter Sartolon Polyamid by Sartorius Biolab.

Materials synthesis

Bare and iron doped photocatalysts were prepared via sol-gel method (SG), precipitation (P) and hydrothermal (H) methods. Samples were prepared with different nominal amount of iron (0.5, 1 and 3% molar), labeled Fe(0.5%)-ZnO, Fe(1%)-ZnO and Fe(3%)-ZnO, respectively.

Bare and Cobalt doped materials were prepared via solvent (S) and hydrothermal method with different nominal amounts of cobalt (0.25, 0.5, 1, 3 and 5% molar), labelled respectively Co(0.25%)-ZnO, Co(0.5%)-ZnO, Co(1%)-ZnO, Co(3%)-ZnO, and Co(5%)-ZnO for the zinc oxide materials. The corresponding titanium dioxide materials were labelled Co(0.25%)-TiO₂, Co(0.5%)-TiO₂, Co(1%)-TiO₂, Co(3%)-TiO₂, and Co(5%)-TiO₂.

Synthesis via sol-gel (SG)

Zinc acetate is solubilized in 250 mL of deionized water; the desired stoichiometric amount of $\text{Fe}(\text{NO}_3)_3$ is added to the solution together with 5 g of citric acid. The solution is subjected to magnetic stirring and is kept for 6 hours in a hot water bath at 80 °C, in order to favor the gel formation [4]. The acidic pH favors the hydrolysis process and therefore the gelation. The beaker containing the gel is placed in an oven at 70 °C for two days, in order to promote drying and obtaining the xerogel. This phase is followed by a further heat treatment which involves calcining in a muffle at 500 °C for 2 hours.

Synthesis via precipitation (P)

The precipitation method is a simple and versatile approach for the synthesis of semiconductor materials; it is cheap, does not require complex experimental conditions [5]. The solution of the precursors, named A, is obtained by adding 2.2 g of zinc acetate dihydrate and the stoichiometric amount of FeCl_3 or $\text{Co}(\text{NO}_3)_2 \cdot 6\text{H}_2\text{O}$ to 160 mL of deionized water. 80 mL of ethanol are then added to solution A and the system is kept under magnetic stirring for 1 h in order to promote the solubilization of inorganic salts. Then, 160 mL of NaOH 1 M (solution B) are added drop by drop to the solution A. The precipitate is left to rest for two days, recovered by filtration and dried in an oven at 70 °C. The powder is finally calcined at 300 °C for 30 h [6].

Synthesis via hydrothermal method (H)

The doping agent (FeCl_3), or $\text{Co}(\text{NO}_3)_2 \cdot 6\text{H}_2\text{O}$ in the desired percentage, was added to 20 mL of $\text{Zn}(\text{NO}_3)_2 \cdot 6\text{H}_2\text{O}$ 1 M solution, and the resulted solution was kept under stirring. After complete dissolution, a solution of NaOH 4 M was added dropwise until reaching the pH value of 10. The solution was transferred to a 100 mL Teflon-lined autoclave, filled with water until complete 50 mL, and the autoclave was kept at 175 °C for 15 hours. The resulting precipitated

products were washed with water and recovered by centrifugation (6000 rpm for 10 min), repeating the procedure 2 times. After dried at 70 °C during the night, the powders were homogenized using a mortar and pestle.

The same procedure was used to obtain Co-doped TiO₂; also in this case the cobalt precursor (Co(NO₃)₂·6H₂O) was added to titanium(IV) butoxide (3.35 mL) and ethanol (50 mL). The solution was kept under continuous stirring for 10 minutes at room temperature. Then, 0.2 mL of sulfuric acid 98% and 0.2 mL of water were added at the starting solution. The thermal treatment was the same used for ZnO materials.

Synthesis via solvent method (S)

ZnO materials were synthesized dissolving 2.2 g of Zn(CH₃COO)₂ in 160 mL of water and 80 mL of ethanol. The stoichiometric amount of Co(NO₃)₂·6H₂O was added to obtain the doped samples. The mixture was kept under magnetic stirring for 1 h in order to promote the solubilization of organic salts. Then, a proper dose of NaOH 1 M was added dropwise to the solution in order to reach a pH of 10-11. The obtained gel was left to rest for two days and then dried in an oven at 70 °C. The powder was finally calcined at 300 °C for 30 h.

TiO₂ was prepared from 7.5 mL of titanium isopropoxide (97% wt) dissolved in 2-propanol (7.5 mL) and deionized water (4 mL; the desired stoichiometric amount of (Co(NO₃)₂·6H₂O) was added to the solution together with 5 g of citric acid. The solution was subjected to magnetic stirring and kept for 6 hours in a hot water bath at 80 °C, in order to favor the gel formation [105]. The acidic pH favored the hydrolysis process and therefore the gelation. The sample was placed in an oven at 70 °C for two days, in order to promote drying and obtaining the xerogel. This phase was followed by a further heat treatment which involved calcining in a muffle at 500 °C for 2 hours obtaining a light-yellow powder.

Characterization

X-rays powder diffraction (XRPD) patterns were recorded using a PANalytical PW3040/60 X'Pert PRO MPD, Lissone (MI) Italy (45kV, 40mA) with a copper K_{α} radiation source (0.15418 nm). Samples were scanned continuously in the 2θ range between 10° and 100° . The X'Pert High-Score software was used to identify the mineral phases present in the samples.

The UV-Vis absorption spectra were recorded using a Varian Cary 5000 spectrophotometer, coupled with an integration sphere for diffuse reflectance studies (DRS) and a Carywin-UV/scan software. A sample of PTFE with 100% reflectance was used as reference. The optical band gap energies were calculated applying the Tauc plot on the obtained spectra, considering that the energy dependence of the absorption coefficient for semiconductors in the region near the absorption edge is proportional to the material energy gap and dependent on the kind of transition (direct or indirect allowed).

Electron Paramagnetic Resonance (EPR) spectroscopy has been employed in order to do a pre-screening of the materials photoactivity by means *in-situ* light irradiation through an X-band CW-EPR Bruker EMX spectrometer equipped with cylindrical cavity operating at 100 kHz field modulation. The effect of UV and visible light on EPR spectra was investigated using a 1600W Xenon lamp (Oriol Instruments) equipped with an IR water filter; during the irradiation the lamp power was set at 1000W.

Photocatalytic degradation experiments

The irradiation experiments were carried out in magnetic stirred Pyrex glass cells, filled with 5 mL of model molecule (20 mg L^{-1}) and catalyst (1000 mg L^{-1} or 400 mg L^{-1}). Samples were irradiated for different times (from 5 min to 120 min) using a PHILIPS cleo 6 X 15 W TL-D Actinic BL with maximum emission wavelength at 365 nm. The UV integrated irradiance on the cells in the 290-400 nm range wavelengths was $90 \pm 2 \text{ Wm}^{-2}$ (measured with a CO.FO.MEGRA. (Milan, Italy)

power-meter). After irradiation, samples were filtered through a 0.45 μm filter and analyzed with the proper analytical technique.

Analysis

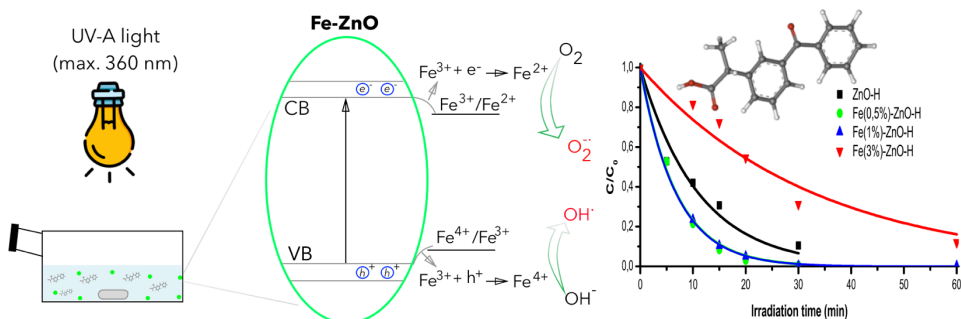
The concentration of phenol and ketoprofen were measured through a YL9300 HPLC system equipped with a YL9330 Column Compartment and a YL9150 autosampler. The column was a RP C18 column (LiChroCART®, Merck, 12.5 cm \times 0.4 cm; 5 μm packing). Phenol was analyzed using acetonitrile and phosphoric acid solution (1×10^{-2} M) at pH 2.8 (10 : 90% v/v) as eluent at a flow rate of 1 mL/min and UV detector set at 220 nm. Ketoprofen was analyzed using as eluent acetonitrile and phosphoric acid solution (1×10^{-2} M) at pH 2.8 (35: 65% v/v) at a flow rate of 1 mL/min and UV detector set at 260 nm.

Samples were analyzed by HPLC/MS Shimadzu UFLC equipped with a Nexera XR, LC-20AD XR pump and a UV-Vis detector SPD-M20A. Injection volume was 10 μL and flow rate 0.4 mL/min using a column Phenomenex Luna C18 50 \times 2 mm, 2.5 μm and a gradient mobile phase composed of acetonitrile/water was: 0 min, 5/95; 5 min 0 /100; 7 min, 0/100. A 3200 Q Trap Sciex mass spectrometer equipped with an atmospheric pressure interface and an ESI ion source was used. Samples were analyzed using ESI negative mode operating in full-scan mode between 50 and 300 m/z range.

Total organic carbon (TOC) and total nitrogen (TN) were measured using a Shimadzu TOC-5000 analyzer (catalytic oxidation on Pt at 680 °C). The calibration was performed using standards of potassium phthalate.

3.2 Iron Doped ZnO Materials for Pollutants Removal

Adapted from:



Development of oxides doped with transition metals and their exploitation to pollutants abatement

Maria Cristina Paganini, Alice Giorgini, Nuno P.F. Gonçalves, Chiara Gionco,
Alessandra Bianco Prevot, Paola Calza

Catalysis Today 328 (2019) 230–234

My direct contribution

I declare that I have prepared the doped materials described in this sub-chapter and I have performed the degradation experiments. The materials characterization was performed by Chiara Gionco and Maria Cristina Paganini from the University of Turin.

3.2.1 Motivation

As explained in Section 1.3.2, ZnO is one of the most promising semiconductors for water treatment. To overcome some of its limitations and improve its photocatalytic properties doping has been pointed as a good strategy. Among all the possible doping agents, iron, a transition metal that is easy to find and very abundant on the earth's crust. Also, zinc oxide is particularly easy to find, so the Fe/ZnO system can be a sustainable and economical photocatalyst. We assessed how the photocatalytic efficiency of the zinc oxide can be improved by introducing iron in its reticular structure. Different synthetic strategies, not expensive and easy to performed, have been investigated, aimed to achieve the development of materials with enhanced photocatalytic performances. The effect of the type of synthetic process (sol-gel, precipitation and hydrothermal methods) and of the dopant concentration (from 0.5% to 3%) on the efficiency of photocatalysis was studied using phenol as a prob molecule.

The efficiency of the most promising materials Fe-doped to remove ketoprofen, a contaminant of emerging concern, in wastewater samples were also investigated.

3.2.2 Results and Discussion

Materials characterization

Iron doped materials

Figure 3.1 shows the diffraction patterns of pure and doped samples. All the diffractograms present the reflections typical of wurtzite ZnO (ICDD 01-089-7102 reference pattern). None of the doped samples show reflections related to other phases, such as iron oxides, α -Fe₂O₃ or γ -Fe₂O₃ [169]. This means either that the iron ions entered the structure of zinc oxide substitutionally or that the iron oxide phases are too small to be detected with the XRD analysis.

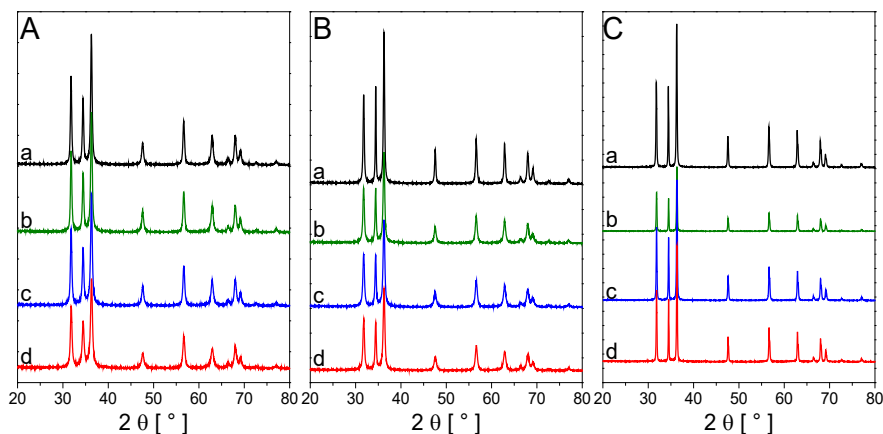


Figure 3.1. XRD patterns of bare (trace a, black) and Fe-doped ZnO with different iron contents: 0.5% (trace b, green), 1% (trace c, blue) and 3% (trace d, red). Samples were prepared via sol-gel (panel A), precipitation (panel B) and hydrothermal methods (panel C)

Table 3.1. Average size of crystallites (d), energy gap values (E_{BG}) and calculated kinetic constant (phenol 20 mg L^{-1} , catalyst 1000 mg L^{-1}) for pure and doped zinc oxide samples.

Synthesis	% dopant	d [nm] ^a	E_{BG} [eV] ^b	k , min^{-1}
SG	0	21 ± 7	3.24	0.040
	0.5	20 ± 5	3.21	0.011
	1	21 ± 5	3.23	0.005
	3	14 ± 4	3.24	0.004
P	0	37 ± 5	3.27	0.030
	0.5	19 ± 6	3.27	0.044
	1	19 ± 5	3.27	0.025
	3	18 ± 4	3.25	0.026
H	0	143 ± 30	3.28	0.058
	0.5	112 ± 17	3.27	0.171
	1	91 ± 13	3.27	0.123
	3	120 ± 14	3.25	0.035

^a as calculated from the Scherrer equation

^b as obtained from the Tauc plot

The addition of iron changes the average crystalline size of ZnO, calculated using the Debye-Scherrer equation, as reported in Figure 3.1. Indeed, the XRD peaks of the doped samples result broadened with respect to the pattern of the bare oxide. This phenomenon is quite known in literature, and it is attributable to the fact that the presence of the dopant ion prevents the growth of

crystallites, favoring instead nucleation. The hydrothermal synthesis leads to the formation of materials with a higher degree of crystallinity (average crystallite size around 100-150nm) as evidenced also by the comparison of pure ZnO samples for the different synthesis methods reported in the supporting information (Figure C1), while the sol-gel and precipitation synthesis both form crystallites with an average size around 20nm.

Figure 3.2 shows DR-UV-Vis spectra for all samples. It is clear from the spectra, and from the energy gap values calculated using the Tauc plot reported in Table 3.1, that the addition of iron does not affect dramatically the fundamental edge transition due to the excitation between the material's valence and conduction bands. On the other hand, the addition of iron leads to the formation of an additional absorption shoulder that can be related to iron states. The intensity of this band is highly dependent on the material's synthesis, the most intense being the one obtained with the precipitation method. Figure C2 reports the comparison of the DR spectra for the samples containing 3% of iron obtained with the different synthesis. Figure C2 highlight the presence of two intra-band features. The first one, centered at 420 nm, was assigned for the analogous system Fe-TiO₂, to the charge transfer between Fe³⁺ states and the oxide conduction band. This band is present in the samples prepared with the precipitation and the hydrothermal methods, while it was absent in the samples prepared through the sol-gel method. The second feature represents the main absorption in the visible region and it is centered at 500 nm. This band has been attributed in the past to "on-site" transitions (d-d transitions on the Fe³⁺ ion) or to inter-site transitions (between two Fe³⁺ ions) [170–173].

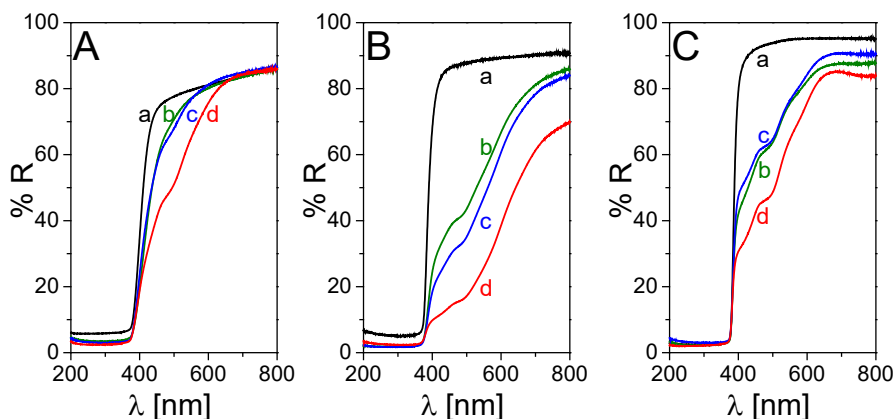


Figure 3.2. DR spectra for bare (trace a, black) and Fe-doped ZnO with different iron contents: 0.5% (trace b, green), 1% (trace c, blue) and 3% (trace d, red). Samples were prepared via sol-gel (panel A), precipitation (panel B) and hydrothermal (panel C) methods.

Photoactivity tested on a probe molecule

Influence of the synthesis method

The photocatalytic activity of all synthesized materials was evaluated by using phenol as a model molecule in Milli-Q water. Figure 3.3 shows the degradation curves obtained by irradiating the probe molecule in the presence of pristine or doped zinc oxide, at different dopant concentrations produced through hydrothermal method, while data obtained from sol-gel and precipitation methods are plotted in Figure C3 and C4, respectively.

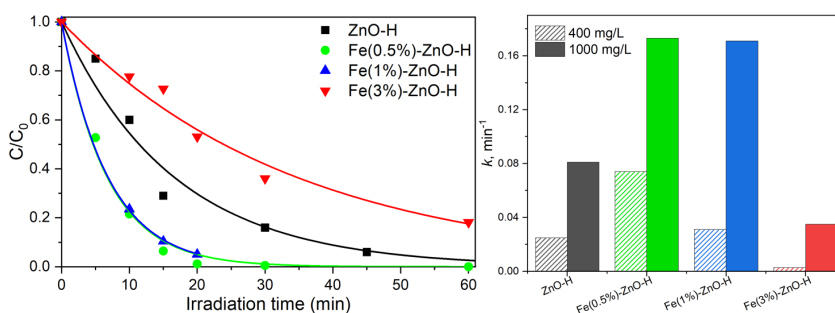


Figure 3.3. Phenol degradation (20 mg L^{-1}) under UV-A in the presence of 1000 mg L^{-1} of Fe-ZnO-H (left) and kinetic constants of phenol abatement in the presence of different catalysts at 400 and 1000 mg L^{-1} (right).

For a complete view, we report in Figure 3.3 the kinetic constants values calculated from phenol degradation curves for all synthesized materials. Materials prepared via sol-gel method exhibit a poor activity and permit to abate only a small percentage of phenol (from 20 to 40% after 2 h of irradiation, see Figure C3), while oxides produced through hydrothermal method were the most efficient.

The materials prepared *via* hydrothermal method allowed to degrade the probe molecule with kinetic constants which are greater of one order of magnitude compared to those characteristics of the precipitated powders. This phenomenon could be probably due to the higher degree of crystallinity of the former as pointed out by the XRD patterns.

Doping effect

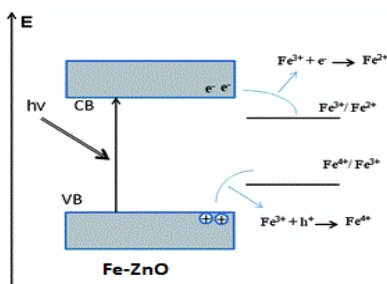
Data collected in Table 3.1 allowed to assess that iron doping induced an enhancement in the phenol degradation rate compared to pristine ZnO, with SG method only exception. Results obtained for materials prepared *via* hydrothermal or precipitation method show that ZnO doped with the lowest concentration of iron, namely 0.5%, promotes the phenol degradation with the highest kinetics, while the photoactivity is reduced as the dopant concentration increases.

In fact, the sample containing the lowest dopant concentration ensures the complete elimination of the phenol after only 30 minutes of irradiation with Fe(0.5%)-ZnO-H (see Figure 3.3) or 60 minutes with Fe(0.5%)-ZnO-P (see Figure C4). Instead, as the amount of iron increases, the performances are reduced and become lower than those of the pristine semiconductor; less than 90% of the initial phenol was eliminated in 1 h when the highest concentration of dopant is used.

For comparison purpose, the kinetic constants for all materials obtained *via* hydrothermal method are plotted in Figure 3.3, where two catalysts

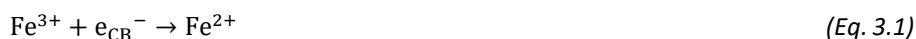
concentration (400 or 1000 mg L⁻¹) were considered. As expected, although the values of the kinetic constants are reduced by decreasing the photocatalyst concentration, the order of reactivity already observed for the materials is maintained.

To explain the reasons for such experimental evidences, it is necessary to consider the role played by the dopant within the crystalline lattice of zinc oxide. It is well-known that electron/hole recombination limits the photocatalytic efficiency and has therefore to be prevented. Iron acts as a surficial trap for the photogenerated charges generated and, therefore, prevents or in any case reduces the electrons/holes recombination [174]. The possibility for Fe³⁺ to undergo redox reactions introduces two discrete levels of energy into the oxide band gap, as shown in Scheme 3.1.



Scheme 3.1. Energetic levels for Fe-doped ZnO.

The oxide conduction band has an energy close to the redox potential of the Fe³⁺/Fe²⁺ pair and Fe³⁺ ion can, therefore, behave as a scavenger for the photogenerated electrons and be reduced to Fe²⁺. Fe²⁺ ion can then easily transfer an electron to the oxygen adsorbed on the semiconductor surface, so favoring the formation of the superoxide anion radical, as described in reactions (Eq. 3.1 and 3.2).



Fe³⁺ ion can also act as a capture center in the valence band. The resulting Fe⁴⁺ combines with the surface hydroxyl groups to produce the [•]OH radicals [13].



Therefore, the enhanced degradation of phenol obtained following iron doping could be attributed to the increased production of reactive oxygen species, described through reactions Eq. 3.1-3.4.

However, an excessive addition of dopant inhibits the degradation process. The order of photoactivity of the materials is modified for the highest concentrations of doping. In this case, pure oxide has the greatest photoactivity, attributable to an increase in electron/hole recombination with a consequent reduction in the performance of doped semiconductors [175]. In fact, a high concentration of iron reduces the degree of crystallinity of the solid and increases the fraction of reticular defects, which represent preferential centers where electron/hole recombination could occur. From the collected data it can be inferred that 3% of dopant is enough to favor charge recombination rather than charge separation. However, some studies showed that the highest photoactivity is guaranteed by the materials containing the highest doping concentrations [176].

Phenol transformation products

The evolution over time of the main transformation products (TPs) arose during phenol degradation was followed as well. The formation of catechol, hydroquinone and resorcinol occurred in all cases, in agreement with literature data [177–179], and their evolution profiles are plotted in Figure C6. Doping with the lowest percentages of iron allows the abatement of the intermediate in times shorter than those necessary for pristine oxide. The disappearance of the intermediate is already observed at 30 minutes of irradiation with ZnO doped at 0.5% and 1%. Instead, 1 h of irradiation is required for the 3% Fe-doped material. In particular, catechol maximum concentration is achieved, for all the materials, at short irradiation times (10 minutes of irradiation for pristine ZnO and ZnO

doped with the lowest concentrations of iron, and 15 minutes for ZnO doped at 3%). Similarly, to what has been observed for catechol, the disappearance kinetics of hydroquinone is slower for samples characterized by the highest doping content.

Application to emerging contaminant degradation

The best performing material, namely Fe(0.5%)-ZnO-H, was also tested toward the abatement of ketoprofen, a contaminant of emerging concern, and the degradation profiles are shown in Figure 3.4. Analyzing data in Milli-Q water, Fe(0.5%)-ZnO-H permits to achieve the complete degradation of ketoprofen in 20 min, while ZnO-H requires 45 min.

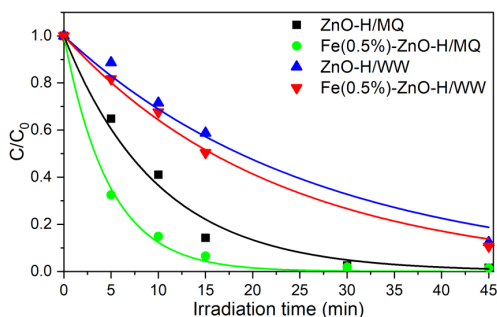


Figure 3.4. ketoprofen degradation (20 mg L^{-1}) in the presence of 1000 mg L^{-1} of catalyst in Milli-Q (MQ) water and wastewater (WW).

The effect of matrix composition was assessed as well by studying the ketoprofen degradation after added to real wastewater. Total organic carbon measures on wastewater matrix allowed to determine a concentration of organic component equal to 9.7 mg L^{-1} and inorganic carbon 68.4 mg L^{-1} . The organic nitrogen measures allowed to determine of 31.3 mg L^{-1} of total nitrogen. The high organic load, combined with the presence in the real matrix of inorganic ions, is the reason why the degradation curves go to zero more slowly than those acquired in Milli-Q water [180]. Even if rates are slightly decreased, all materials are able to completely abate the molecule within 1 h of irradiation.

The formation of transformation products (TPs) was assessed too and their evolution profiles are plotted in Figures C7. Ketoprofen transformation involved in all cases the formation of several hydroxylated derivatives, in a close analogy with TPs already detected during the treatment with titanium dioxide [181] and in surface water. In the presence of Fe(0.5%)-ZnO-H, all TPs are formed within few minutes (maximum at 5 min) and completely disappeared within 30 min, while with ZnO-H the evolution profiles are delayed and a longer irradiation time is required to achieve the complete TPs abatement.

3.2.3 Conclusions

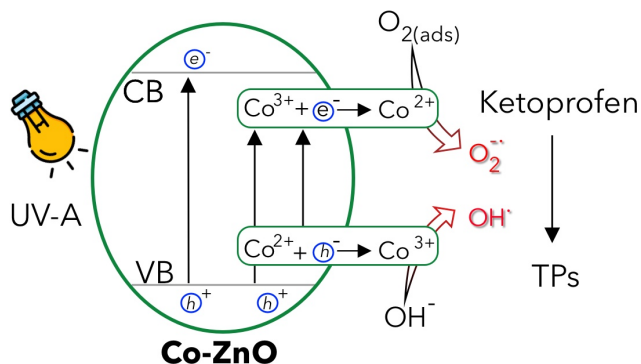
The sol-gel synthesis led to the design of materials with limited photocatalytic activity, while the most promising synthesis procedures were those obtained *via* precipitation and hydrothermal processes. Among the various strategies of investigated synthesis, the hydrothermal method proved to be the most advantageous in the development of materials characterized by excellent photocatalytic performances. The initial objective of increasing the photoactivity of zinc oxide is reached by using doping with iron at low concentrations (0.5%), for which a clear improvement is observed in the abatement of the model molecule. The transition metal ions, if present in suitable quantities, act as surface traps for the photoinduced charges and reduce e^-/h^+ recombination. Conversely, when present at high concentrations, charge recombination prevails on charge separation, so affecting (and decreasing) the degradation performance.

From the obtained results it is possible to deduce that the synthesized materials are efficient, not only in the elimination of the phenol, but also in the removal of the degradation intermediates. All the materials synthesized by hydrothermal method are able to completely degrade the aromatic products formed by the degradation of phenol (catechol, hydroquinone and resorcinol)

within 2h of irradiation. The best performing materials have also been successfully applied for the abatement of ketoprofen in real wastewater.

3.3 Cobalt Doped ZnO Materials For Pollutants Abatement

Adapted from:



The effect of cobalt doping on the efficiency of semiconductor oxides in the photocatalytic water remediation

Nuno P.F. Gonçalves, Maria Cristina Paganini, Paolo Armillotta, Erik Cerrato and Paola Calza

Journal of Environmental Chemical Engineering 7 (2019) 103475

My direct contribution

I declare that I have prepared the doped materials described in this sub-chapter as well as the degradation experiments. The materials characterization was performed by Erik Cerrato, Paolo Armillotta and Maria Cristina Paganini from the University of Turin.

3.3.1 Motivation

The cobalt doping role on different newly semiconductors oxide materials, produced through different synthetic methods, correlating the reticular structure with their photocatalytic activity for removal of pollutant from water. The Co-doping concentration effect (from 0.25 to 5%), as well as the synthesis procedure (solution and hydrothermal methods), were evaluated on the TiO_2 and ZnO photocatalytic efficiency for phenol abatement, used as pollutant model molecule due to its chemical structure.

The efficiency of the most promising material Co-doped to remove ketoprofen, a contaminant of emerging concern, in wastewater samples were also investigated.

3.3.2 Results and Discussion

Materials characterization

Figure 3.5 shows the diffractograms of pristine zinc oxide and zinc oxide doped with cobalt at different concentrations, prepared by solution (A) or hydrothermal methods (B). The XRD patterns of the synthesized samples display reflections corresponding to (1 0 1), (0 0 2), (1 0 1), (1 0 2), (1 1 0), (1 0 3), (2 0 0), (1 1 2) and (2 0 1) planes of the ZnO wurtzitic hexagonal phase. No other reflections were recorded, suggesting the high purity of the synthesized samples; in addition, the diffraction peaks are relatively sharp, indicating the good crystallinity of the materials.

The doping with cobalt does not modify the diffraction profile of zinc oxide, corroborating the hypothesis that the doping species were able to effectively enter the crystalline lattice of the solid and substitute itself with the zinc atoms. The good dispersion of the cobalt ions in the crystalline lattice of the oxide or the small fraction of dopant addition prevents observing signals referable to other crystalline phases, such as the cubic spinel form of Co_3O_4 . In fact, all the

diffraction patterns were characterized by the same reflections at the same value of 2θ . This experimental evidence suggests that, independently of the synthesis method, cobalt doping does not modify the wurtzite structure typical of zinc oxide.

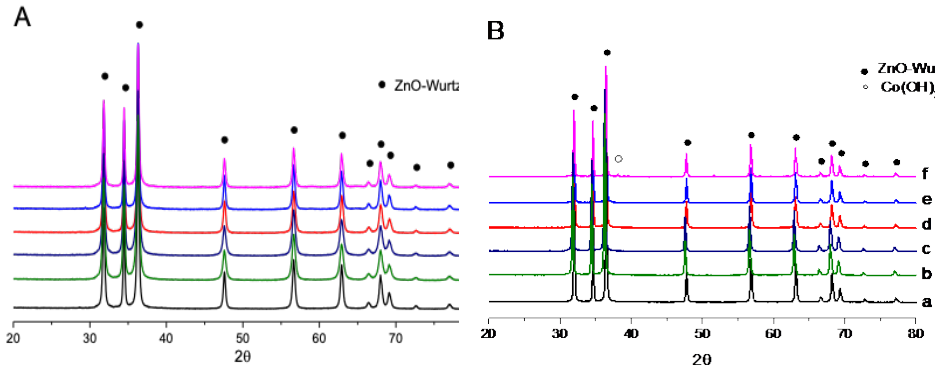


Figure 3.5. Diffratograms of bare and Co-ZnO prepared via (A) solution and (B) hydrothermal methods, a) pristine ZnO, b) Co(0.25%)-ZnO, c) Co(0.5%)-ZnO, d) Co(1%)-ZnO, e) Co(3%)-ZnO, f) Co(5%)-ZnO.

For a more in-depth analysis an enlargement of the diffraction profiles in the region $30^\circ < 2\theta < 40^\circ$ are shown in Figure D1 where the most intense reflections fall. The peaks retain their position, with a negligible displacement at greater angles as the concentration of cobalt increases. This effect can be explained by considering the very slightly different values of the ionic rays of Co^{2+} ($r_{\text{Co}^{2+}} = 0.070\text{nm}$) and of the Zn^{2+} ($r_{\text{Zn}^{2+}} = 0.074\text{nm}$). The interstitial ions, having almost the same size than those of zinc, generate a very small disorder and negligible stress in the crystalline structure of the oxide. Furthermore, the signals of pristine zinc oxide appear more intense and narrower than the reflections of cobalt-containing powders. The peaks enlargement is more evident at higher dopant concentrations. The signal amplitude is a parameter related to the degree of crystallinity of the sample; the increase in the percentage of doping inhibits, therefore, the crystallization and limits the growth of the crystallites. The Scherrer equation on XRD pattern reported below, was used to evaluate the size of the average crystals of synthesized materials [182]:

$$\tau = \frac{K\lambda}{\beta \cos\theta}$$

where τ is the mean size of the ordered crystalline domain, K is a dimensionless shape factor which varies varying the nanoparticles morphology and in this case we used a value of 0.9 which is suitable for platelet shape [183], λ is the X-ray radiation wavelength, β is line broadening at half maximum intensity (FWHM) after subtracting the instrumental line broadening which in our case were performed with a silicon single-crystal standard and θ is the Bragg angle at which we measure the reflection.

Generally, the increasing of cobalt percentage in the matrix affects the degree of crystallinity and consequently the reduction in the crystallites dimensions, but in the case of TiO_2 obtained *via* hydrothermal synthesis, this phenomenon does not occur (Table 3.2). By comparing these values, it is possible to state that the hydrothermal synthesis ensures a greater degree of crystallinity of the powders only in the case of ZnO (see Figure D1 where it is possible to compare different width). Also, in the case of TiO_2 , the XRD analysis (reveals the formation of a single phase corresponding to anatase structure. No influence of Co-doping is observable in the XRD patterns; in fact, it is not possible to identify the presence of cobalt-like phases like the spinel cobalt oxide, or cobalt hydroxide. Regardless of the synthesis procedure and the type of transition metal added, all the materials show the same diffraction profile and this is compatible with what is reported in the literature [184–186]. In the case of titania, the type of synthesis performed does not affect the degree of crystallinity of the sample and consequently the size of the nanoparticles as reported in Table 3.2.

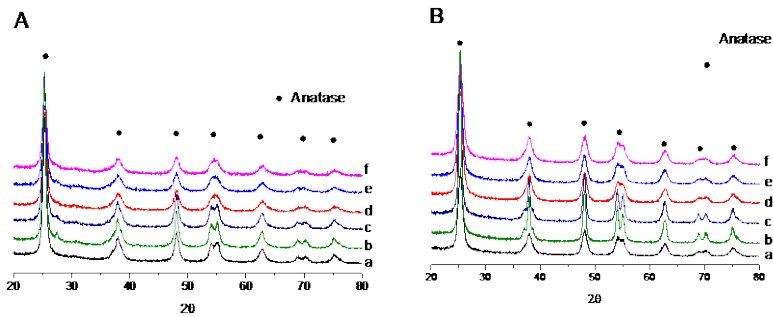


Figure 3.6. Diffractograms of bare and Co-TiO₂ prepared via (A) solution and (B) hydrothermal methods; a) bare TiO₂, b) Co(0.25%)-TiO₂, c) Co(0.5%)-TiO₂, d) Co(1%)-TiO₂, e) Co(3%)-TiO₂, f) Co(5%)-TiO₂.

Table 3.2. Average size of crystallites (*d*), for pure and doped materials.

% Co	<i>d</i> (nm) for ZnO		<i>d</i> (nm) for TiO ₂	
	S	H	S	H
0	37±5	143±30	8±2	4±1
0.25	36±6	141±20	7±2	5±2
0.5	34±5	141±17	6±2	6±2
1	32±7	140±18	6±2	5±2
3	30±6	125±14	6±2	8±2
5	35±7	116±17	6±2	4±1

Also, for TiO₂ samples an enlargement of the diffraction profiles in the region $20^\circ < 2\theta < 30^\circ$ is shown in Figure D2 where the most intense reflections fall. Both the synthesis procedures bring to the formation of pure anatase, moreover, it is possible to observe a slight enlargement of the peaks related to the doped materials respect to the pure ones. This phenomenon is particularly evident for the samples prepared *via* hydrothermal methods (see Figure D2).

In DR-UV-Vis spectra for all the samples Co-ZnO (Panel A and B) and Co-TiO₂ (Panel C and D) obtained via solution and hydrothermal methods are shown. For all the samples the type of synthesis does not modify the optical behavior of the semiconductor. For all the ZnO samples the band gap (calculated with the Tauc plot method) is around 3.3 eV while for titania is slightly higher about 3.4 eV. The EBG values present once again that the addition of the doping agent has no effect in defining the extent of the solid bandwidth. The presence of cobalt in the

crystalline oxide lattice is confirmed by the presence in the spectrum of characteristic bands related to the d-d transitions. In the first two panels (A and B) related to the ZnO material the presence of well-defined bands centered at 554 nm, 587 nm and 635 nm are assigned to the d-d transitions of Co^{2+} involving crystal fields levels in a tetrahedral crystal symmetry and can be ascribed to the $(F) \rightarrow {}^2E(G)$, ${}^4A_2(F) \rightarrow {}^4T_1(P)$ and ${}^4A_2(F) \rightarrow {}^2A_1(G)$ transitions respectively, where A, E and T are generally used to indicate intermediate energy bands [187–190]. These results support the fact that high spin tetrahedrally coordinated Co^{2+} ions ($3d^7$, $S=3/2$) can replace Zn^{2+} sites in the ZnO structure. With regard to these absorption bands, there is a substantial difference, especially in the intensity of these bands, for the different samples. In detail, different trends are observed for the four panels. In the case of Co-ZnO by solution method (A) the most evident aspect is the low reflectance value, the sample is in fact colored (green) and quite dark. The d-d transitions are observed but are partially shielded by the low reflectance value. In the case of ZnO synthesized by the hydrothermal way (B) the situation is similar: indeed, again the sample with the lowest reflectance value is the one with the highest concentration of dopant, in any case, the d-d transitions are perfectly observable and well resolved. The situation for TiO_2 is diametrically opposed. The sample synthesized by solution method presents the absorptions due to the d-d well evident and increasing transitions as a function of the percentage of dopant (C) whereas in the case of samples synthesized by hydrothermal method (D) only the poorly defined and not resolved absorption shoulders can be observed. Also, the region of absorption is slightly different respect to the case of ZnO, in fact, the titania doped samples are yellow if obtained *via* hydrothermal way and pale blue if prepared *via* solution synthesis.

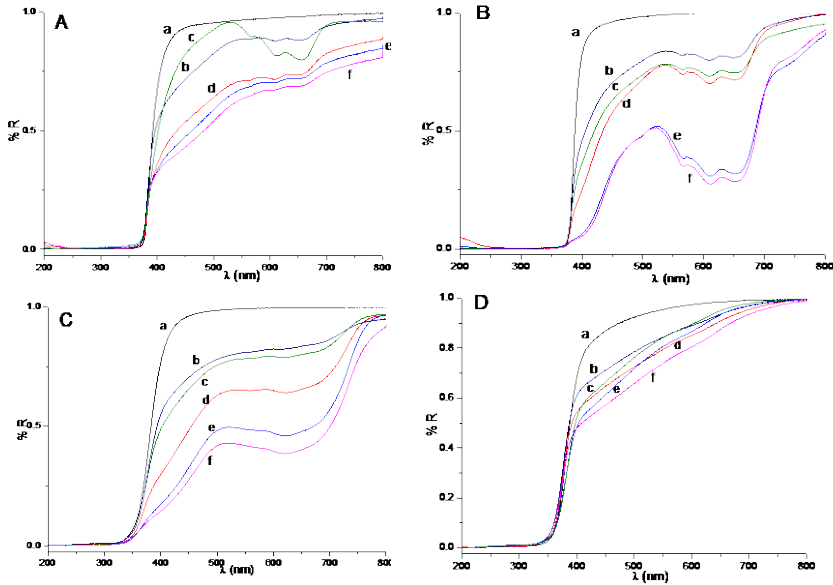


Figure 3.7. DRS-UV-Vis Reflectance spectra of A) Co-ZnO via solution synthesis, B) Co-ZnO via hydrothermal synthesis, C) Co-TiO₂ via solution synthesis, D) Co-TiO₂ via hydrothermal synthesis. a) bare ZnO, b) Co(0.25%)-ZnO, c) Co(0.5%)-ZnO, d) Co(1%)-ZnO, e) Co(3%)-ZnO, f) Co(5%)-ZnO.

To understand the nature of the defects generated by the introduction of Co ions into the lattice of ZnO and TiO₂ matrices we analysed the samples with the electron paramagnetic resonance technique (EPR). The pristine oxides do not present any signals, at low magnetic field, due to paramagnetic species, this means that all the bare materials are stoichiometric and without defects. In the case of doped samples, it is possible to observe in Figure 3.7A and B that the two oxides behave differently. Co-doped ZnO (Figure 3.7A) presents a huge anisotropic signal: the spectrum is characterized by a strong peak centered at $g_{\perp}=4.5038$ and $g_{//}=2.314$ assigned to the a d^7 high spin configuration of cobalt (II) ions located in tetrahedral coordination, [184,185] replacing Zn²⁺ sites in the wurtzite structure. The presence of g_{\perp} and $g_{//}$ values suggest an axially distorted symmetry of the dopant into the ZnO matrix in accordance with the XRD patterns.

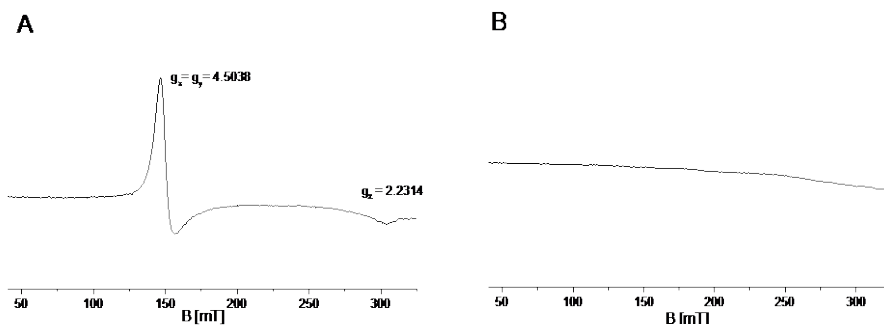


Figure 3.8. EPR spectra of A) Co(1%)-ZnO via solution synthesis and B) Co(1%)-TiO₂ via solution synthesis.

The signals increase with the cobalt loading (data shown in the Appendix D, Figure D4). Moreover, the lines with a g value of about 1.96 associated to shallow donors or core-shell vacancies originating from zinc, and always present in any ZnO sample, were not detected [186,187,191] (see Figure 3.8). Another difference between doped and undoped materials is the fact in the doped ones, a consistent decrease in the signal intensities, due to native paramagnetic species is observed, as already reported by previous studies [192]. This behaviour can be explained due to cobalt in the lattice of ZnO stabilize the hexagonal structure of zinc oxide, limiting the formation of paramagnetic defects responsible for the signal around $g \sim 1.96$, such as the interstitial ions Zn⁺.

In the case of TiO₂ no signal related to the presence of Co²⁺ can be observed in the same region of low magnetic field, even increasing the cobalt loading (Figure 3.7B). Ti ions in titanium dioxides presents an octahedral coordination, with tetragonal distortion; according to Liu [190] when Co ions replace Ti ions into the lattice, the charge balance and the different sizes of ionic radii of Co²⁺ (octahedral - 0.745 Å) and Ti⁴⁺ (octahedral - 0.605 Å) could easily lead to lattice distortion with the formation of defects that would reduce the stability and the crystallinity. Thus, cobalt doping could hinder the grain growth of the catalysts and reduce the particle sizes. Also, the reduced crystallinity would promote phase transformation, owing to the increased number of oxygen vacancies in the TiO₂ lattice created by replacing the Ti⁴⁺ sites with Co²⁺ for charge compensation.

To preserve the charge balance, the formation of Ti^{3+} species is expected. Thus, cobalt doping should enhance the concentration of Ti^{3+} and oxygen vacancy in the lattice. The absence of this signal can be interpreted as the non-formation of the paramagnetic species due to the presence of high spin Co^{2+} in d^7 configuration. The two spectra presented in Figure 3.9 are related to undoped titania (orange) and cobalt doped titania (black). The signal of Ti^{3+} species is present only in the case of undoped TiO_2 and in the $Co-TiO_2$ sample it disappears; this means that probably cobalt does not enter into the titania lattice in substitutional position and it is present in a non-paramagnetic species as Co^{3+} . Both oxides are able to trap cobalt ions in some way, the samples are colored and different spectroscopic techniques revealed the cobalt presence but different results were obtained in the case of the two oxides, at least in terms of the nature of the defects. This different behaviour can play a role in the different photoactivity of the two samples that we will present in the next section.

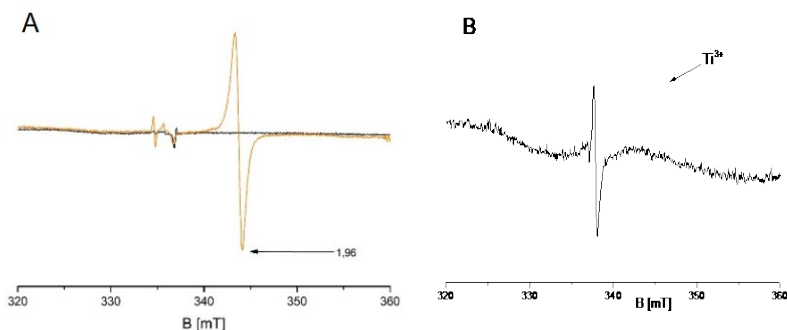


Figure 3.9. Comparison of bare and cobalt doped Oxides. A) bare ZnO (orange) and Co(1%)-ZnO (black) via solution synthesis; B) bare TiO_2 (orange) and Co(1%)- TiO_2 (Black) via solution synthesis.

Photocatalytic Degradation with a Pollutant Model Molecule

Cobalt doped TiO_2

Figure 3.10 shows the phenol degradation obtained under irradiation in the presence of the titanium dioxide materials doped with different cobalt concentrations prepared by the solution and hydrothermal methods compared with the respective pristine titanium dioxide material. It is possible to observe a

higher activity for the materials prepared though the hydrothermal method when compared with the corresponding materials prepared by solution method.

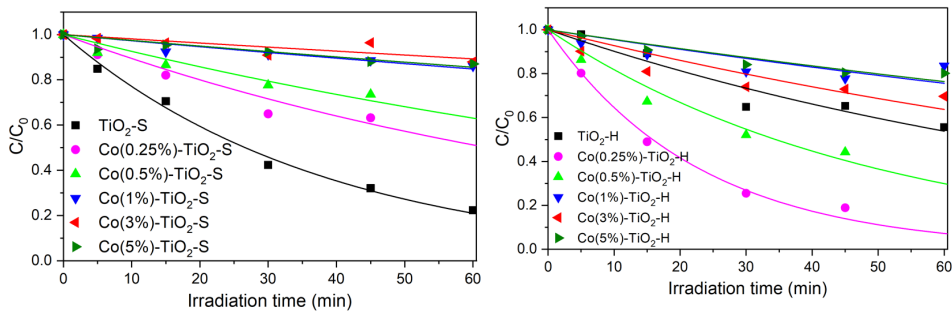


Figure 3.10. Phenol degradation over time (20 mg L^{-1}) under UVA irradiation in the presence of (1000 mg L^{-1}) Co-doped TiO_2 prepared by solution (left) and hydrothermal method (right).

Among Co- TiO_2 materials prepared by hydrothermal, those with lower cobalt concentration, namely 0.25% and 0.5% allow to achieve faster phenol degradation than the pristine TiO_2 . While increasing the dopant amount seems to be detrimental in the photoactivity process, as evidenced on kinetic constant values presented on Table 3.3. This behavior can be explained in terms of population of intraband gap states in the band gap of TiO_2 . It is well known from the literature [193,194] that not always the doping increases the photoactivity of the bare material, it depends on the formation of recombination center into the lattice system and it is strictly related to the concentration of dopants. Most often a very low amount of extra ions leads to an increase of photocatalytic activity while an excess of dopants is detrimental. The reason, once again is related to the formation of recombination centers that instead of helping the charge separation, brings to a faster recombination of holes and electrons. The problem of extending the spectral sensitivity of photoactive materials to visible light became one of the major challenges in applied photocatalysis and photo-electrochemistry. The simplest way to extend the spectral sensitivity ought to be the chemical modification of the materials through doping with metal cations that thus displayed additional absorption bands in the extrinsic spectral region

at wavelengths longer than the absorption edge. However, such spectral extension of light absorption typically gives no improvement in integral activity of photocatalysts, since metal doping resulted in either formation of non-active extrinsic absorption or creation of additional centers of charge carrier recombination. It depends on the coordination environment of the dopant and on its ability to modify its oxidation number. This is the case of high concentration of cobalt (II) doping TiO_2 .

Cobalt doped ZnO

Figure 3.11 shows the phenol degradation under irradiation in the presence of the Co-doped ZnO materials with different cobalt amounts prepared by the solution and hydrothermal methods comparing with the pristine zinc oxide. It is possible to observe a lower activity for the materials prepared through the solution method when compared with the corresponding obtained by hydrothermal method. In fact, the most active material prepared by solution method needs more than 1h of irradiation to completely abate the model molecule, while those prepared by hydrothermal method required only 40 min. This phenomenon could be probably due to the higher degree of crystallinity of the former as pointed out by the XRD patterns. Moreover, the low calcination temperature, used for the synthesis of the ZnO obtained *via* solution process, does not allow a complete cleaning of the surface from the precursor. Chemically adsorbed species on the surface of the prepared material can affect the reactivity of active sites and their interaction with the pollutants.

Results obtained for the materials prepared by hydrothermal method show that cobalt doping with low concentrations induce a slight enhancement on phenol degradation when compared with the pristine ZnO, while the photoactivity is reduced as the dopant concentration increases. Actually, samples doped with 0.25%, 0.5% and 1% allow achieving the complete phenol elimination in less than 45 minutes under irradiation while only 80% of the initial

concentration is reduced in the presence of the material doped with 3%. For the sample prepared with the highest doping amount, namely 5%, no notably phenol degradation was observed.

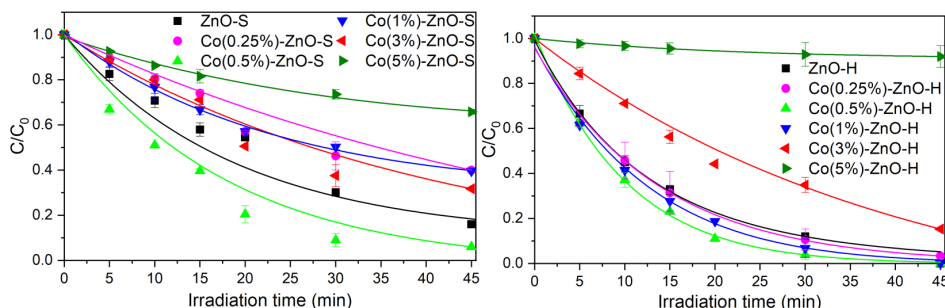


Figure 3.11. Phenol degradation over time (20 mg L^{-1}) under UVA irradiation in the presence of (1000 mg L^{-1}) Co-doped ZnO prepared by solution (left) and by hydrothermal method (right).

Table 3.3. Kinetic constant calculated for bare and doped materials produced through the solution and hydrothermal methods.

Material	k, min^{-1}					
	0%	0.25%	0.5%	1%	3%	5%
TiO ₂ -S	0.025	0.008	0.005	0.003	0.002	0.002
TiO ₂ -H	0.010	0.028	0.013	0.006	0.001	0.005
ZnO-S	0.038	0.020	0.060	0.021	0.028	0.009
ZnO-H	0.075	0.075	0.113	0.088	0.041	0.002

As shown in Table 3.3, the cobalt doped ZnO materials prepared via hydrothermal synthesis exhibit a higher phenol degradation kinetics constant than the corresponding samples obtained by solution synthesis. These results can be explained considering that the two synthesis lead to a different sample morphology. Hydrothermal way generates more crystalline material with bigger crystals (in the case of ZnO). The photogenerated charge can be trapped by the cobalt ions, preventing the charges recombination leading to a higher charge transfer. The photogenerated charge can be trapped by the cobalt ions, preventing the charges recombination leading to a higher charge transfer [195]. According to the mechanism proposed by Ba-Abbad et al., the photocatalytic degradation ability of cobalt doped ZnO can be ascribed to the formation of

reactive species in solutions like $\bullet\text{OH}$ radicals and O_2^- due to the conversion under irradiation of Co^{2+} into Co^{3+} . The Co^{3+} ion is poorly stable and then it is easily converted into Co^{2+} [106]. This mechanism is working only with an optimal concentration of dopants, if the amount of cobalt is too high, the cobalt itself acts as recombination center for the charges.

However, the photo-efficiency for the materials containing high doping amounts, namely Co(3%)-ZnO-H and Co(5%)-ZnO-H, is reduced probably due to sufficiently high cobalt quantity to reduce the degree of crystallinity making the recombination between charges become prevalent with respect to the charge separation, which instead would have guaranteed a better functioning of the material. These results contrast with those reported by Yildirim *et al.*, where raising the cobalt doping concentration in ZnO materials leads to a faster methylene blue degradation under visible light irradiation [196].

Phenol transformation products

The principal phenol transformation products (TPs) were followed as well, and are shown in Figure D3. The phenol TPs were identified as catechol, hydroquinone and resorcinol in agreement with those reported in the presence of TiO_2 [176,177]. As observed for parent compound, the materials prepared with low concentration of cobalt allow its abatement in shorter times than those required for the pristine ZnO and Co(3%)-ZnO-H. After 45 min of irradiation, the 0.5% and 1% doped materials allow almost the complete disappearance of hydroquinone, while the pristine ZnO and 3% dopes requires 1 h of irradiation. The disappearance of resorcinol was observed with comparable slower evolution for the 3% doped ZnO.

Photocatalytic Degradation with a CEC

a) The best performing material, namely Co(0.5%)-ZnO-H, was also tested on the ketoprofen degradation, that has been detected in natural waters and is

reported as a contaminant of emerging concern [197,198]. Also, the ketoprofen mineralization was evaluated by determining the concentration of TOC. The degradation profiles in Milli-Q water shown in Figure 3.12A allow to observe a similar ketoprofen degradation for both doped and pristine zinc oxide. However, the doped material allows to obtain a fast ketoprofen mineralization as shown in Figure 3.12B. In fact, Co(0.5%)-ZnO-H is able to reduce $\sim 80\%$ of TOC after 1 h under irradiation while less than 60% was observed for the bare material in the same period.

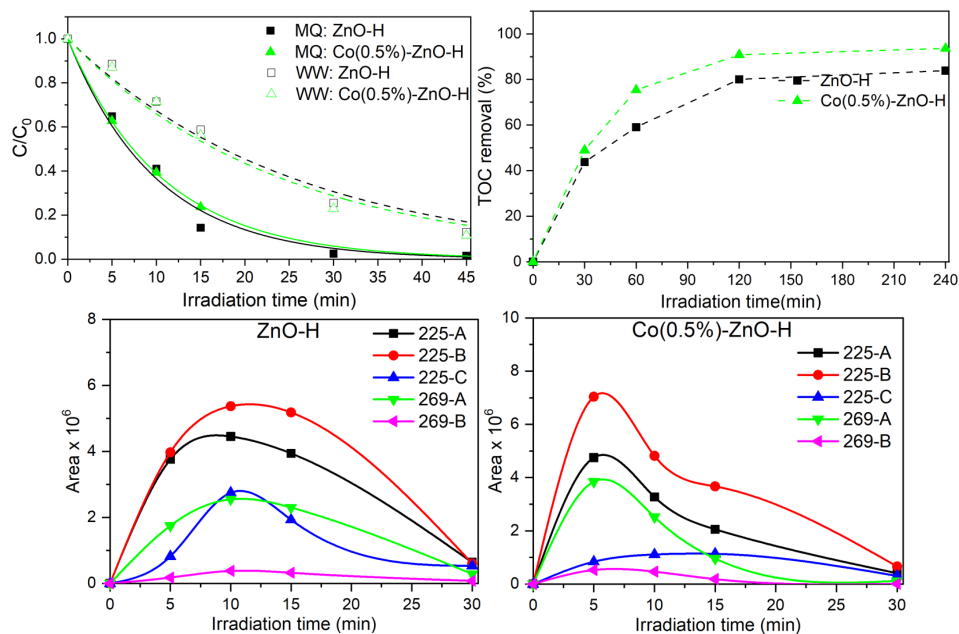


Figure 3.12. A) Ketoprofen degradation over time (20 mg L^{-1}) under UVA irradiation in the presence of (1000 mg L^{-1}) Co(0.5%)-ZnO-H and ZnO-H in Milli-Q water (MQ) and in real wastewater sample (WW). B) TOC removal in during ketoprofen degradation in the presence of ZnO-H and Co(0.5%)-ZnO-H in Milli-Q water. C) Ketoprofen transformation products over time observed in the presence of ZnO-H and Co(0.5%)-ZnO-H.

The evolution profiles of the TPs identified by LC/MS are plotted in Figure 3.12C. The TPs present a faster fade with Co-doped ZnO when compared with the bare material. In fact, the TPs maximum concentration is achieved in just 5 minutes of irradiation for the doped material while longer irradiation times are required for the bare ZnO. The observed ketoprofen TPs were the same

described on experiments performed with TiO_2 as shown in Table D1 [119,180,181].

To study the complexity effect of water matrix composition the ketoprofen degradation was also performed in spiked a real wastewater sample, Figure 3.12. The reducing on the degradation efficiency can be attributed to the presence of the inorganic water constitutes and organic matter [167]. Even though, both materials were able to complete abate the pollutant in 1 h of irradiation.

3.3.3 Conclusions

Synthesis of cobalt doped ZnO and TiO_2 following different synthetic strategies, namely solution and hydrothermal, led to the materials with distinct morphology and photocatalytic properties. The TiO_2 doped with low amounts (0.25% and 0.5%) prepared by hydrothermal method leads to an enhancement on the phenol degradation comparing to the pristine material. However, if prepared by solution method an inhibition on the photocatalytic activity was observed.

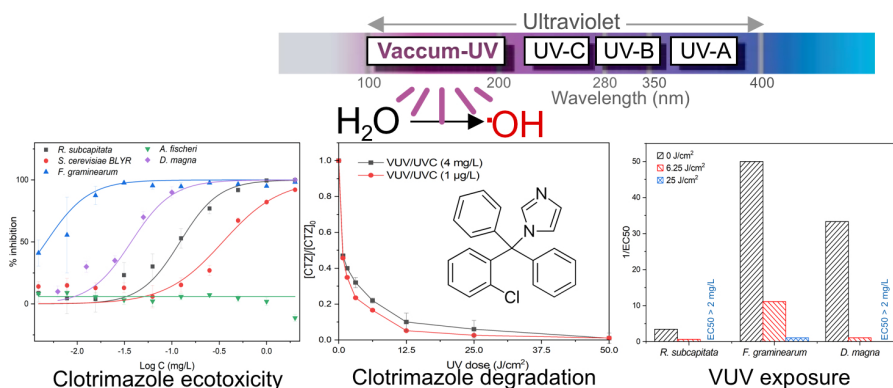
The hydrothermal method proved to be the most advantageous to prepare Co-doped ZnO materials for photocatalytic applications. Doping concentration presents a clear contribution on the material performance, being the one prepared by the addition of 0.5% the most effective on the pollutant model molecule removal. The cobalt ions on ZnO lattice, if in appropriate quantities can act as a trap for the photoproduced charges reducing the electron/hole recombination. The best performing material was also able to remove ketoprofen in real a wastewater sample, proving to be more efficient on ketoprofen mineralization.

Chapter 4 - Vacuum-UV for Pollutants Removal and Ecotoxicity Mitigation

The present chapter describes the use of Vacuum-UV (combined 185 nm and 254 nm) irradiation and monochromatic UVC (254 nm) irradiation for the removal of the widely used antifungal agent clotrimazole from water. The kinetics, degradation mechanism and ecotoxicity mitigation to test organism are also reported.

4.1 Antifungal Clotrimazole Removal by Vacuum UV Irradiation – Toxicity Attenuation

Adapted from:



Degradation of the antifungal pharmaceutical clotrimazole by UVC and Vacuum UV irradiation: kinetics, transformation products and attenuation of toxicity

Nuno P.F. Gonçalves, Oihane del Puerto, Claudio Medana, Paola Calza and

Peter Roslev

Journal of Hazardous Materials (*submitted*)

My direct contribution

I declare that I have performed all the VUV/UVC degradation experiments and analysis described in this sub-chapter as well as toxicological experiments with the standard compounds and the samples after treatment. The elucidation of the clotrimazole degradation pathways was performed in the group of Professor Claudio Medana, University of Turin. All experiments were performed during my secondment at Aalborg University in the group of Professor Peter Roslev.

4.1.1 Motivation

Azole fungicides are active ingredients used in pharmaceutical and personal care products for the treatment of human mycosis and are also used in agriculture against fungal infections. As a consequence of the extensive use over the past years, these compounds have emerged as a new class of environmental pollutants [23,199]. Azoles fungicides are usually moderately lipophilic and relatively persistent with typical half-lives of weeks to months, and are not entirely removed by traditional wastewater treatment plants (WWTPs) [200]. Consequently, WWTPs act as a constant source of azoles into the natural environment where they may have adverse effects on non-target organisms.

Azoles are cyclic molecules and can be classified into triazoles (three nitrogen atoms) or imidazoles (two nitrogen atoms). Clotrimazole is an imidazole antifungal agent that is widely used, to treat different types of skin fungus infections and oral/vaginal candidiasis. Result of the topical application in the form of a cream is easily released into urban wastewater after use in personal hygiene. For example, Roberts et al., investigating the presence of pharmaceuticals in Tyne River (UK) reported the presence of clotrimazole in all samples with an average concentration of 21 ng/L [201]. Despite the high persistence, with a half-life of more than 60 days, and significant frequency of detection in aqueous environment [19], questions remains about the potential harmful impacts [200,202,203]. Moreover, as discussed in Section 1.2.1, fungicides are reported as harmful to several non-target organisms and with potential effects to human wealth.

In this study, we investigated the effect of VUV based processes (simultaneous VUV and UVC irradiation) of clotrimazole in water on degradation, occurrence of transformation products and changes in ecotoxicity. A specific aim was to determine to what degree UV irradiation could facilitate direct or indirect photolysis and thereby attenuate toxicity of clotrimazole to different aquatic test organisms. Changes in toxic responses were compared before and after UVC and

VUV irradiation using a battery of organisms that included *Aliivibrio fischeri*, *Raphidocelis subcapitata*, *Saccharomyces cerevisiae*, *Fusarium graminearum* and *Daphnia magna*. Organisms from different trophic levels were included to better assess biological effects of all bioactive compounds in samples with clotrimazole after UV treatment including transformation products. To the best of our knowledge, this is the first study comparing UV mediated photolysis and changes in ecotoxicity of clotrimazole after VUV treatment.

4.1.2 Materials and Methods

Chemicals

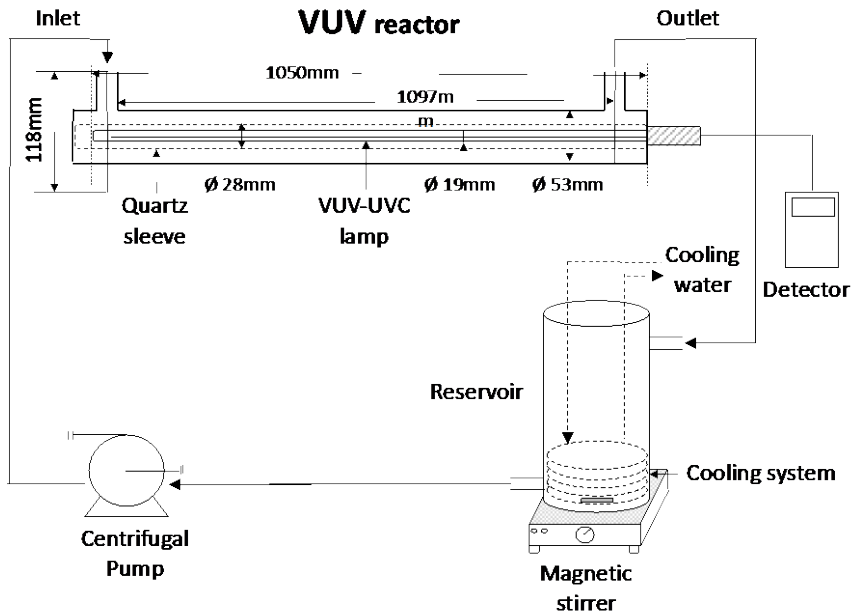
Clotrimazole (CAS 23593-75-1) was obtained from Sigma-Aldrich, Italy (Milan) while the degradation product (2-chlorophenyl)bisphenylmethanol (CAS 66774-02-5) was obtained from LGC Standards, Italy. Stock solutions were prepared in autoclaved distilled deionized water and stored in the dark at 5 °C.

Water was collected at Aalborg Municipality, Denmark. The source water in Aalborg Municipality is hard groundwater (12°dH) abstracted directly from chalk aquifers. No water treatment or disinfection is employed by the municipality before distribution of the drinking water to the consumers. The drinking water is naturally nutrient poor with a concentration of non-volatile organic carbon (NVOC), NO₃⁻, NH₃/NH₄⁺, NO₂⁻, and total P of 0.99 mg/L, 1.3 mg/L, 0.007 mg/L, <0.001 mg/L, and 0.01 mg/L, respectively. The water temperature, pH and turbidity were 8.8 °C, 7.6 and <0.13 FTU, respectively.

Vacuum UV irradiation (VUV/UVC)

The effect of vacuum UV irradiation of clotrimazole in water was investigated in a continuous-flow VUV photoreactor from ULTRAAQUA A/S (Aalborg, Denmark). The VUV photoreactor consisted of a tubular stainless-steel reactor with an inner diameter of 53 mm, a length of 1097 mm and a reactor volume of 1.7 L (Scheme 4.1). The photoreactor was connected to a 2.3 L stainless steel

reservoir and a diaphragm pump (Siebec, pompe M7) operated at 2.0 – 2.2 L/min for recirculation. The reservoir was equipped with a magnetic stir bar to facilitate mixing, and a stainless-steel cooling spiral operated at 10 °C to prevent heating. The average retention time and photoreactor passages as a function of flowrate were calculated using tracer studies with Safranin O (1 mg/L).



Scheme 4.1. Schematic representation of the VUV reactor system.

The photoreactor was equipped with a low-pressure high output amalgam VUV Hg lamp with a 19 mm diameter, and a length of 1050 mm (UltraTherm 200 W LPHO TOC UV, ULTRAAQUA A/S, Denmark). The UV lamp simultaneously emitted UVC (254 nm) and VUV (185 nm) at a radiation flux of 56W and 14W, respectively (4:1 ratio). The UVC/VUV lamp was located inside a high purity 28 mm diameter quartz tube transparent to both wavelengths. The theoretical thickness of the water film around the quartz sheath was 12.5 mm. The reactor was equipped with an UVC sensor and the maximum irradiance in drinking water was 360 W m⁻² for UVC corresponding to 90 W m⁻² of VUV.

VUV irradiation experiments were conducted by loading the photoreactor and reservoir with a total of 4 L of water spiked with clotrimazole with different nominal concentrations (1 $\mu\text{g/L}$ to 4 mg/L). The water was recirculated for 64 min and 10 mL samples were collected at the outlet of the photoreactor before turning on the VUV lamp (0 min), and at 1, 2, 4, 8, 16, 32 and 64 min after turning on the UV lamp (“post VUV”) corresponding to 0, 0.78, 1.56, 3.12, 6.25, 12.5, 25, 50 J/cm^2 dose exposure.

UVC irradiation

The effect of UVC irradiation of clotrimazole in water was investigated to compare results from combined VUV/UVC irradiation (see above) with effect of UVC irradiation alone (no VUV). Stock solutions of clotrimazole (4 mg/L) were exposed to UVC irradiation in 10 mm 3.5 mL quartz cuvettes (Science Outlet Optical Quartz QS10 and Hellma Precision Quartz Suprasil QS10) using an 8W UVP 3UV lamp (Analytic Jena, USA). Irradiation intensity was measured using an Extech SDL470 Light meter equipped with an UVC sensor. The UVC irradiation intensity at 10 cm distance from the UVP 3UV lamp was 60 $\mu\text{W/cm}^2/\text{sec}$. UVC doses (J/cm^2) were calculated from the measured UV irradiation intensity ($\mu\text{W/cm}^2/\text{sec}$) and the exposure time (sec). The UV exposure doses were varied by changing the exposure times.

Detection of active oxygen species

The formation of H_2O_2 in aqueous samples after VUV treatment was assessed by spectrophotometry using the vanadate method in which a peroxo complex is measured as absorbance at 450 nm [204].

Clotrimazole degradation and occurrence of transformation products

The concentration of clotrimazole over time was measured by HPLC with UV detection at 230 nm (Summit - Dionex Corporation). The HPLC was equipped

with a Luna 5 μ C18 100 Å (250 × 4.60 mm) column and acetonitrile/water (50:50 v:v) was used as mobile phase at a flow of 1 mL/min.

Non-target liquid chromatography-high resolution mass spectrometry analysis (LC-HRMS) of water samples with clotrimazole was performed before and after UV exposure to identify transformation products. Analyses were carried out using an Ultimate 3000 High-Pressure Liquid Chromatography coupled through an ESI source to an LTQ-Orbitrap mass spectrometer (Thermo Scientific). Chromatographic separation was achieved using a reversed-phase C18 column (Phenomenex Luna, 150 × 2 mm, 3 μ m, 110 Å; Phenomenex, Italy) by injecting a 10 μ L sample volume at a mobile phase consisted of a mixture of 0.1 mM formic acid (eluent A) and acetonitrile (eluent B). The gradient profile started with 5% B, increased up to 100% B in 40 minutes and to 100% A in 10 minutes. Samples were ionized in both positive and negative ionization modes. The LC effluent was delivered to the ESI ion source using Nitrogen as sheath and auxiliary gas with the following parameters: sheath gas 34 arbitrary unit (arb), auxiliary gas 15 arb, capillary voltage 4.48 kV, and capillary temperature of 270 °C. Full mass spectra were acquired in positive ion mode with a resolution of 30.000. Data analysis was performed using the MZmine 2.53 for peak alignment, peak grouping, background noise and retention time correction, and the METLIN database was used to identify the transformation products.

Samples at initial concentration of 1 μ g/L were preconcentrated before analysis using a freeze-dryer (LABOGENE – CoolSafe 55-110). After drying 15 mL of the sample, the reconstituted with 500 μ L of acetonitrile (final pre-concentration factor of 30) for the LC-HRMS analysis.

Total organic carbon (TOC) was measured using a Shimadzu TOC-5000 analyzer with catalytic oxidation on Pt at 680 °C. The calibration was performed using standards of potassium phthalate.

Toxicity Tests

*Toxicity test with the luminescent bacterium *Aliivibrio fischeri**

Toxicity screening of samples with clotrimazole and (2-chlorophenyl)bisphenylmethanol were examined in a standard inhibition tests with the luminescent bacterium *Aliivibrio fischeri* [205]. *A. fischeri* DSM 7151 was incubated in white 96-well plates (CulturPlate, Perkin Elmer) with serial 2-fold dilutions of clotrimazole and (2-chlorophenyl)bisphenylmethanol resulting in 10 different nominal concentrations and 4 replicates of each dilution series. Changes in bioluminescence was quantified after 30 min using a Victor X2 Multilabel Plate Reader (Perkin Elmer). The toxicity to *A. fischeri* was examined before and after exposure of aqueous solutions of clotrimazole and (2-chlorophenyl)bisphenylmethanol to different UV irradiation regimes.

*Toxicity test with the luminescent yeast *Saccharomyces cerevisiae* BLYR*

The toxicity of clotrimazole and (2-chlorophenyl)bisphenylmethanol to a single-celled yeast was examined in an inhibition test with the bioluminescent yeast reporter strain *Saccharomyces cerevisiae* BLYR (490 Biotech, USA). This yeast strain produces light continuously by constitutive expression of the luxCDABE genes from *Photobacterium luminescens* and the frp gene from *Vibrio harveyi* [206]. We used this engineered yeast to develop a bioassay in which the endpoint was inhibition of luminescence after growth for 72 h.

S. cerevisiae BLYR was grown for 24-48 h at 25 °C in YMM medium [207] until luminescence was detectable. The culture was then diluted 1:100 in YMM medium and used as inoculum in the bioassays. 2-fold dilutions of clotrimazole were prepared in 96-well white microplates (CulturPlate, Perkin Elmer) by serially diluting 150 µL of an aqueous solution with the chemical in 150 µL YMM medium. After dilution of clotrimazole, 150µL of 1:100 diluted *S. cerevisiae* BLYR culture was added to each well resulting in a final liquid volume of 300 µL in each well. Sealed plates were incubated with shaking for 72h ± 2 h at 25 °C. Changes

in bioluminescence was then quantified using a Victor X2 Multilabel Plate Reader (Perkin Elmer). The bioassay with *S. cerevisiae* BLYR included four replicates of blanks (medium only), controls (no clotrimazole), and each of the 10 clotrimazole concentrations. The toxicity of clotrimazole to *S. cerevisiae* BLYR was examined before and after exposure of aqueous solutions of the chemical to different UV irradiation regimes.

Toxicity test with the fungus Fusarium graminearum

The toxicity of clotrimazole and (2-chlorophenyl)bisphenylmethanol to a filamentous fungus was examined in an inhibition test with the plant pathogen *Fusarium graminearum*. We used this fungal strain to develop a Fusarium Toxicity assay (FUTOX) in which the endpoint was inhibition of enzyme activity after growth for 72 h. *F. graminearum* was cultivated at 25 °C in a Fusarium Minimal Medium (FMM) with the following composition (g/L): 0.12 Na₂SO₄; 0.05 MgSO₄* 7H₂O; 0.008 CaCl₂*2H₂O; 0.268 NH₄Cl; 5.0 KNO₃; 1.14 Na₂HPO₂; 0.272 KH₂PO₄; 0.5 Yeast extract; 1.0 Proteose peptone; 10.0 Glucose; 10.0 Maltose. The medium was supplemented with the following trace elements (mg/L): 1.39 FeSO₄*7H₂O; 0.054 ZnCl₂; 0.068 CuCl₂*2H₂O; 0.021 NaBr; 0.024 Na₂MoO₂*2H₂O; 0.079 MnCl₂*4H₂O; 0.033 KI; 0.025 H₃BO₃; 0.048 CoCl₂*6H₂O; 0.048 NiCl₂*6H₂O.

2-fold dilutions of clotrimazole and (2-chlorophenyl)bisphenylmethanol were prepared in 96-well black microplates (CulturPlate, Perkin Elmer) by serially diluting 150 µL of an aqueous solution with the chemical in 150 µL FMM medium. After diluting the chemical, 150µL of diluted *F. graminearum* culture was added to each well resulting in a final liquid volume of 300 µL in each well. The *F. graminearum* culture used as inoculum in the FUTOX assay consisted of a 72-96 h old culture in FMM diluted to A600 = 0.01 in FMM.

Sealed plates were incubated with shaking for 72h ± 2 h at 25 °C. Activity of chitinase (1→4)-2-acetamido-2-deoxy-β-D-glucan glycanohydrolase) in *F. graminearum* was measured by adding 30 µL of the fluorescent substrate 4-

methylumbelliferyl N-acetyl- β -D-glucosaminide (4-Methylumbelliferyl 2-Acetamido-2-deoxy- β -D-glucopyranoside). The fluorescent chitinase substrate was added to each well from a concentrated stock solution in dimethyl sulfoxide to obtain a final concentration of 10 μ M. After 60 and 120 min incubation at 25 °C, fluorescence was quantified in each well using a Victor X2 Multilabel Plate Reader with a 355 nm excitation and 460 nm emission filter (Perkin Elmer). The bioassay with *F. graminearum* included eight replicates of blanks (medium only), controls (no compound), and each of the 10 pollutant concentrations. The toxicity of clotrimazole and (2-chlorophenyl)bisphenylmethanol to *F. graminearum* was examined before and after exposure of aqueous solutions of the chemicals to different UV irradiation regimes.

Toxicity test with the green microalga Raphidocelis subcapitata

The toxicity of clotrimazole and (2-chlorophenyl)bisphenylmethanol to phytoplankton was examined in an inhibition tests with the unicellular green microalgae *Raphidocelis subcapitata* (formerly *Selenastrum capricornutum* and *Pseudokirchneriella subcapitata* [208]). *R. subcapitata* (MicroBioTests Inc.) was cultivated in alga test medium at 23 ± 2 °C and continuous illumination at 6500 lux (ISO 8692, 2012).

2-fold dilutions of clotrimazole and (2-chlorophenyl)bisphenylmethanol were prepared in 96-well clear Nunclon microplates (Thermo Scientific) by serially diluting 150 μ L of an aqueous solution with the chemical in 150 μ L alga test medium. After dilution, 150 μ L of diluted *R. subcapitata* culture (1:50) was added to each well resulting in a final liquid volume of 300 μ L in each well. Plates were incubated for 72 h at 23 °C on a shaker at 70 rpm with continuous illumination (6500 lux). Growth was measured after 0, 24 h, 48 h and 72 h as absorbance at 450 nm using a Thermo Multiskan Plate Reader (Thermo Scientific).

The bioassay with *R. subcapitata* included eight replicates of blanks (medium only), controls (no compounds), and each of the 10 pollutants concentrations. The toxicity of clotrimazole and (2-chlorophenyl)bisphenylmethanol to *R. subcapitata* was examined before and after exposure of aqueous solutions of the chemicals to different UV irradiation regimes.

Toxicity test with the crustacean Daphnia magna

The toxicity of clotrimazole and (2-chlorophenyl)bisphenylmethanol to zooplankton was examined in inhibition tests with the crustacean *D. magna* (ISO 6341, 2012). The toxicological endpoint was inhibition of mobility determined by visual inspection of the animals [209]. *D. magna* STRAUS was cultivated from a laboratory clone originating from pure-culture ephippia. Each treatment consisted of 20 juvenile animals distributed among 4 glass vials with 5 animals and 20 mL freshwater medium in each 30 mL vial. The mobility of each animal was determined after 24 h and 48 h (ISO 6341, 2012).

Data analysis and statistics

The toxic response measured for all endpoints were expressed as inhibition (I) relative to control samples: $I = 1 - (R_i / R_c)$, where R_i and R_c are responses measured for inhibited and control samples, respectively. Control samples included water samples with UV exposure without drug to assess any toxicity associated with active oxygen species generated during irradiation. Concentration-response curves were fitted using iterative non-linear regression:

$$Response = A1 + \frac{A2 - A1}{1 + 10^{(Logx0 - x)p}} \quad (4.1)$$

where A1 is the bottom asymptote, A2 is the top asymptote, EC50 is the median effective concentration (mg/L), and p is a model parameter representing the slope of the curve. Iterative non-linear regressions and calculation of 95% confidence limits for EC50 values were performed using Origin 2019b (9.65).

4.1.3 Results

VUV/UVC and UVC degradation of clotrimazole

Clotrimazole removal during simultaneous VUV and UVC irradiation (hereafter referred to as VUV/UVC) was investigated over time and UV dose, Figure 4.1. A fast removal was observed within the initial 8 min of VUV/UVC irradiation for both 4 mg/L and 1 $\mu\text{g/L}$, and the degradation appeared to follow first order kinetics, with a half-life of less than 1 min (0.78 J/cm^2) for both concentrations. About 95% drug removal was observed after 32 min for 4 mg/L and 97% removal for 1 $\mu\text{g/L}$ in the same irradiation dose (25 J/cm^2). Hence, a faster drug removal was observed at trace levels (1 $\mu\text{g/L}$) compared to those observed at 4 mg/L (Figure 4.1a). Similarly, the TOC analysis showed a fast initial removal with 42% degradation after 4 min, and subsequent slower removal with time resulting in 92% degradation after 64 min (Figure 4.1). The effect of monochromatic UVC (254 nm) on clotrimazole removal was also investigated, as shown in Figure 4.1b. Exposure of 4 mg/L clotrimazole to 5 J/cm^2 removed more than 75% of the drug while 40 J/cm^2 resulted in >99% removal.

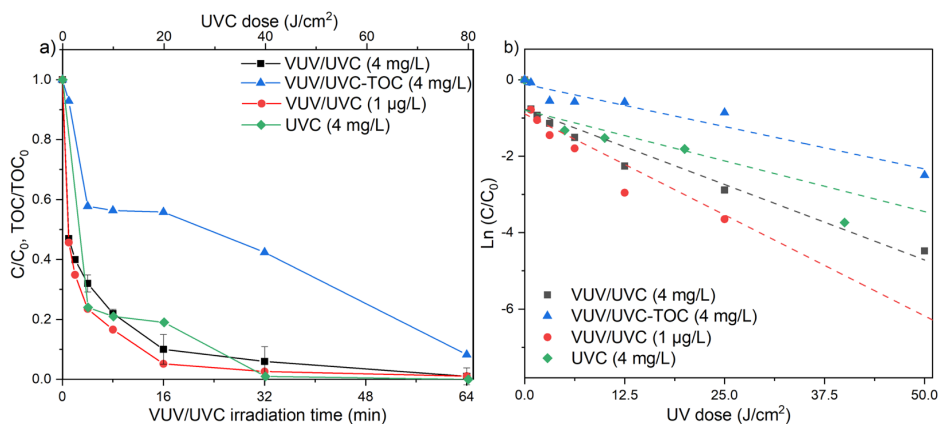


Figure 4.1. Clotrimazole degradation ($C_0 = 4 \text{ mg/L}$ and $C_0 = 1 \mu\text{g/L}$) and TOC removal ($C_0 = 4 \text{ mg/L}$) as a function of VUV/UVC irradiation time (Panel a). $\text{Ln}(C/C_0)$ values for clotrimazole and TOC removal as function of UV dose for VUV/UVC irradiation and monochromatic UVC ($C_0 = 4 \text{ mg/L}$) (Panel b).

Identification of clotrimazole transformation products

Samples were analysed by liquid chromatography high-resolution mass spectrometry (LC-HRMS) to identify aqueous clotrimazole transformation products after exposure to VUV/UVC and UVC irradiation. As summarized in Table 4.1, a total of 7 transformation products of clotrimazole ($C_{22}H_{17}ClN_2$) were identified after VUV/UVC treatment, resulting mainly from the hydroxyl group addition to the clotrimazole molecule and/or loss of the imidazole group. In detail, 3 isomers of the drug monohydroxylation in the phenyl ring were detected (TP2, TP3, TP4: $C_{22}H_{17}ClN_2O$).

Table 4.1. Transformation products identified by LC-HRMS analysis after VUV/UVC and UVC irradiation of aqueous clotrimazole.

Compound	r.t. (min)	Empirical formula	m/z [M+H] ⁺	Δ (ppm)
Clotrimazole	14.6	$C_{22}H_{17}ClN_2$	345.1158	1.61
TP1	18.9	$C_{19}H_{13}ClO$	293.0728	-0.55
TP2	10.9	$C_{22}H_{17}ClN_2O$	361.1109	-1.57
TP3	13.5			
TP4	14.3			
TP5 ^{a)}	14.7			
TP6	14.4	$C_{20}H_{17}ClN_2$	321.1160	0.70
TP7 ^{b)}	13.4	$C_{13}H_9ClO$	217.0415	-0.55
TP8	5.1	$C_3H_4N_2$	69.0442	0.56

^{a)}not observed after VUV irradiation; ^{b)}not observed after UVC irradiation

The hydroxylation of the imidazole ring led to the subsequent ring opening (TP6: $C_{20}H_{17}ClN_2$), while the loss of imidazole group was followed by the hydroxylation in the tertiary carbon (TP1: $C_{19}H_{13}ClO$). The last one was confirmed by the commercial standard. Additionally, further oxidation resulted in loss of one phenyl ring (TP7: $C_{13}H_9ClO$). From the profile over time of the identified photoproducts (Figure 4.2), a maximum relative abundance of TPs (TP1, TP2, TP3, TP4 and TP6) was observed at 6.25 J/cm² VUV irradiation followed by a disappearance with extended exposure time and UV dose (Figure 4.2). Under

monochromatic UVC irradiation, a similar degradation pathway was observed with formation of also a total of 7 photoproducts. However, one more isomer resulting from the drug monohydroxylation was formed after UVC (TP5) whereas the product TP7 detected after VUV/UVC was not observed under UVC (Table 4.1).

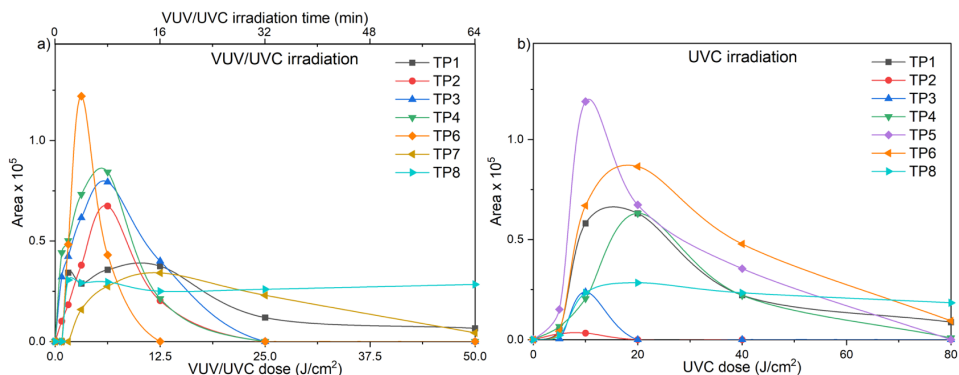


Figure 4.2. Profile of clotrimazole transformation products under a) VUV irradiation and b) UVC irradiation.

Selection of test organisms

Initial experiments were conducted to identify test organisms responsive to clotrimazole exposure (Figure 4.3). Clotrimazole showed no effect on the traditional test organism *A. fischeri* at the investigated concentration range (2.0 - 0.004 mg/L), and it was not possible to estimate a median effective concentration (EC₅₀). On the contrary, inhibition was observed for the yeast *S. cerevisiae* BLYR, the green microalgae *R. subcapitata*, the crustacean *D. magna* and the fungus *F. graminearum* with EC₅₀ values of 0.39 mg/L, 0.15 mg/L, 0.04 mg/L and 0.01 mg/L, respectively. Considering that the greatest inhibition was observed for *R. subcapitata*, *D. magna* and *F. graminearum*, these test organisms were selected for subsequent experiments in which changes in ecotoxicity was examined after UV treatment of aqueous clotrimazole.

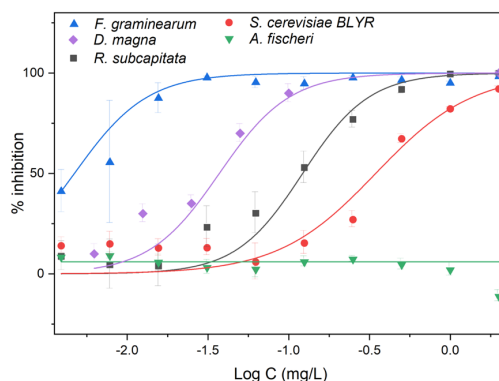


Figure 4.3. Toxicity of clotrimazole to different test organisms measured as concentration-response curves. Data points represent mean \pm standard error.

Toxicity of clotrimazole photoproduct: (2-chlorophenyl)bisphenylmethanol

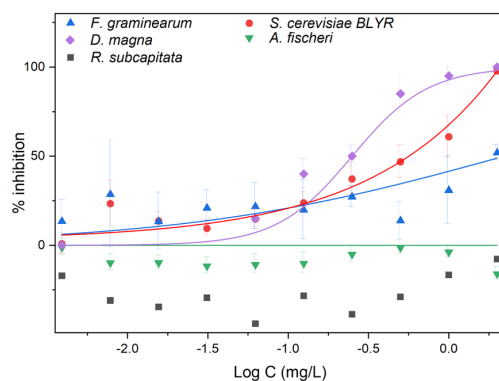


Figure 4.4. Toxicity of (2-chlorophenyl)bisphenylmethanol (TP1) to different test organisms measured as concentration-response curves. Data points represent mean \pm standard error.

(2-chlorophenyl)bisphenylmethanol was identified as a transformation product during degradation of clotrimazole under UVC and VUV/UVC (Table 4.1). As previously observed for clotrimazole, TP1 showed no effect on *A. fischeri* at the investigated concentration range (0.004 – 2.0 mg/L), but also the green microalgae *R. subcapitata* was not inhibited by this photoproduct (Figure 4.4). On the contrary, inhibitory effects were observed for the yeast *S. cerevisiae* BLYR, the crustacean *D. magna* and the fungus *F. graminearum* with EC50 of 0.44 mg/L, 0.25 mg/L, and 1.90 mg/L, respectively. However, it should be noted that TP1 was much less toxic compared to the parent compound clotrimazole with higher

EC50 values for the test organisms. Especially the fungus *F. graminearum* was less susceptible to TP1 and this compound appeared 190 times less toxic than clotrimazole as indicated by a much greater EC50 value.

Effect of VUV/UVC and UVC irradiation on clotrimazole toxicity

The effect of VUV/UVC and monochromatic UVC irradiation on clotrimazole toxicity was investigated using *R. subcapitata*, *D. magna* and *F. graminearum* as test organisms as shown in Figure 4.5 and Figure 4.6. To investigate the impact of the drug disappearance as well as the formation of transformation products towards the test organisms after VUV/UVC, samples collected before irradiation (0 J/cm²) were compared with samples irradiated with 6.25 J/cm² where several TPs were present at high relative abundance (figure 4.2), and samples irradiated with 25 J/cm² which was the dose resulting in 95% drug removal.

Exposure of aqueous clotrimazole to different UV doses had a substantial impact on the toxicity to the test organisms as shown in Figure 4.5 and Table 4.2. Changes in growth of *R. subcapitata* after VUV/UVC irradiation demonstrated a noticeable decrease in aqueous clotrimazole toxicity after 6.25 J/cm² leading to a 6-fold increase of the EC50 value from 0.29 mg/L to 1.63 mg/L. Furthermore, 25 J/cm² VUV/UVC irradiation led to an additional decrease in clotrimazole toxicity with no or low observed inhibitory effect on the growth of the green microalga at nominal concentrations up to 2.0 mg/L (Figure 4.5a). As a result of the low inhibition after VUV/UVC, it was no longer possible to estimate an EC50 value (Table 4.2). Similarly, clear decreases in inhibitory effects of clotrimazole to the fungus *F. graminearum* was observed after VUV/UVC irradiation with 6.25 J/cm² and 25 J/cm², causing a fivefold (EC = 0.09 mg/L) and 47-fold (EC = 0.94 mg/L) decrease in aqueous clotrimazole toxicity, respectively (Figure 4.5b and Table 4.2). For the crustacean *D. magna*, sample exposed to 6.25 J/cm² showed a 31-fold decrease in toxicity with EC50 values increasing from to 0.03 mg/L to 0.94 mg/L (Figure 4.5c and Table 4.2). Interestingly, no inhibitory effect of

aqueous clotrimazole to *D. magna* could be detected after VUV irradiation with 25 J/cm² (Figure 4c). To further illustrate the relationship between VUV/UVC treatment and decreases in toxicity, Figure 4.5d shows how different UV doses promoted an attenuation of toxicity (1/EC50) of aqueous clotrimazole to all the test organism.

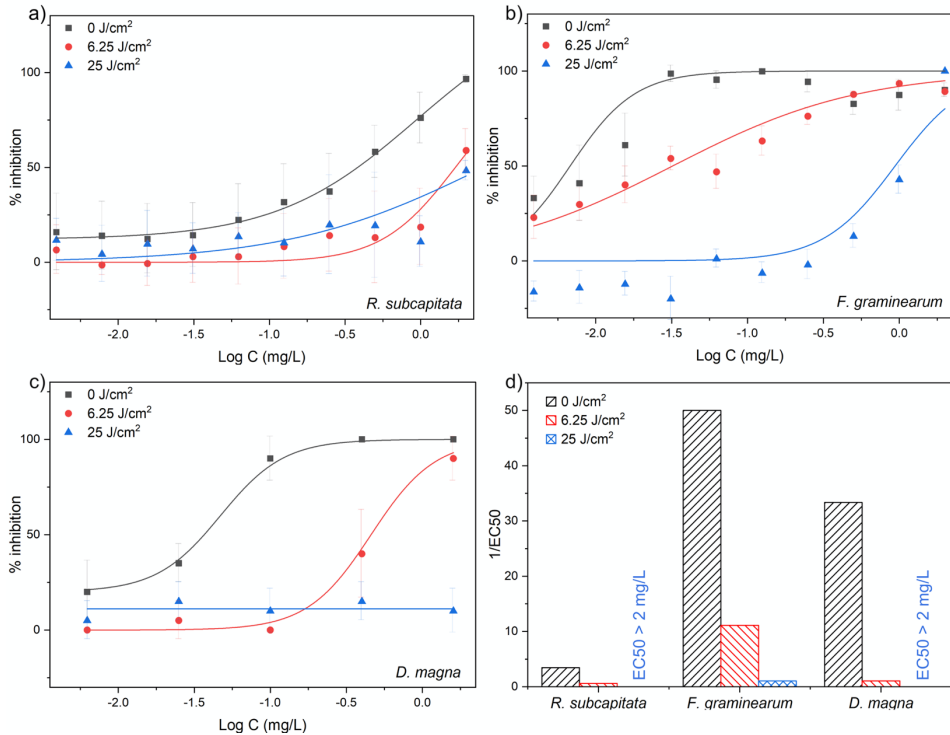


Figure 4.5. Effect of VUV/UVC irradiation of aqueous clotrimazole on the toxicity to *R. subcapitata* (a), *F. graminearum* (b) and *D. magna* (c). Data points represent mean \pm standard error. Panel d) shows the 1/EC50 value in function of VUV/UVC dose for the test organisms.

The effects of VUV/UVC irradiation on toxicity of aqueous clotrimazole was compared with the effects of monochromatic UVC irradiation (Figure 4.6). UVC irradiations led to a decrease in clotrimazole toxicity to *R. subcapitata* and *F. graminearum* as shown in Figure 4.6. As shown in Figure 4.1, an irradiation with 40 J/cm² UVC resulted in almost complete clotrimazole removal and this treatment subsequently decreased the apparent toxicity twofold to the green microalgae *R. subcapitata* as indicated by a change in EC50 from 0.29 mg/L to

0.66 mg/L (Figure 4.6a and Table 4.2). Similarly, 40 J/cm² UVC decreased the drug growth inhibitory effect to *F. graminearum* (Figure 4.6b), and for this test organism the EC₅₀ increased 62-fold (Table 4.2).

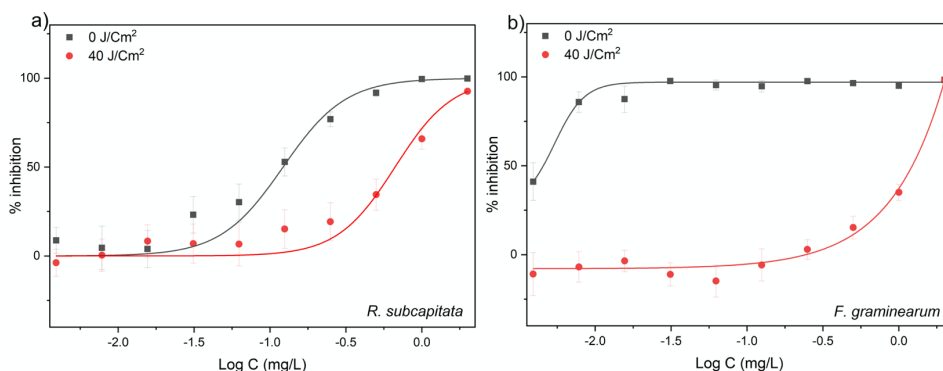


Figure 4.6. Effect of monochromatic UVC irradiation of aqueous clotrimazole on the toxicity to *R. subcapitata* (a) and *F. graminearum* (b). Data points represent mean \pm standard error.

Table 4.2. Median effective concentration (EC₅₀) for the test organisms before and after exposure of clotrimazole to VUV/UVC and UVC at different doses.

Test organism	EC ₅₀ (mg/L)				
	Before UV	VUV/UVC dose		UVC dose	
		6.25 J/cm ²	25 J/cm ²	5 J/cm ²	40 J/cm ²
<i>R. subcapitata</i>	0.29	1.63	> 2.0	0.19	0.66
<i>F. graminearum</i>	0.02	0.09	0.94	0.25	1.23
<i>D. magna</i>	0.03	0.94	> 2.0	ND	ND

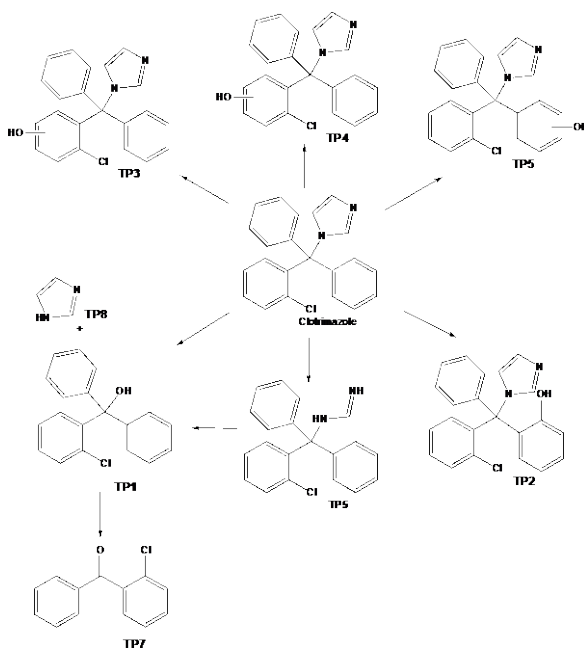
ND: not determined

4.1.4 Discussion

UV based AOPs allow the removal of micropollutants by both, direct and indirect photolysis [210,211]. Direct photolysis involves light absorption by the pollutant with subsequent transformation, while during indirect photolysis the degradation is mediated by generated reactive species. The use of the VUV processes with radiation below 200 nm promotes the photolysis of water allowing the in situ generation of reactive oxygen species such as hydroxyl radical ($\cdot\text{OH}$), superoxide anion ($\cdot\text{O}_2^-$) and hydrogen peroxide (H_2O_2), that can lead the indirect photolysis of organic pollutants. Moreover, the VUV lamps used in the

present study are characterized by combined radiation at 185 nm and 254 nm (UVC), and the latter wavelength can also contribute to pollutant degradation by direct photolysis if absorbed by the molecule. In addition, UVC has a greater transmission in water compared to VUV at 185 nm which can facilitate chemical reactions further from the lamp surface.

VUV/UVC irradiation (combined 185 nm and 254 nm) showed high efficiency removing aqueous clotrimazole with more than 50% abatement in just one 1 min of exposure (0.78 J/cm^2) followed by a slower removal over exposition time with a non-linear degradation (Figure 4.1). Clotrimazole degradation during UV photolysis investigated by LC-HRMS pointed to a pathway that resulted mainly from hydroxyl group addition in the phenyl ring and/or imidazole moiety with further oxidation reactions resulting in the loss of the phenyl ring as shown in Scheme 4.2. Clotrimazole has an unsubstituted imidazole moiety, which is probably why the ring opening or loss of imidazole moiety was the main route of drug degradation leading to the formation of (2-chlorophenyl)bisphenylmethanol (TP1), as previously reported for clotrimazole stability studies in the presence of photocatalysts [212]. The observed TPs matched with those previously described during the photocatalytic degradation using semiconductors catalysts under UVA irradiation [212]. However, the higher number of TPs reported in the photocatalytic system resulted mainly from the drug multihydroxylation and can be explained by the higher ability to generate hydroxyl radicals relatively to the UV based AOPs, yet the latter does not require the addition of chemicals or catalysts.



Scheme 4.2. Degradation pathways of clotrimazole under UV irradiation.

As previously reported, H_2O_2 is one of the products formed during VUV/UVC treatment of water [117]. In our study, we detected H_2O_2 during VUV/UVC irradiation of water in the absence of clotrimazole and the concentration increased with increasing irradiation time up to $19.7 \mu\text{M}$ after 64 min (Figure 4.7). H_2O_2 is generally toxic to many organisms, however, the trace levels observed in the present study did not show any detectable inhibitory effects towards the test organisms (data not shown).

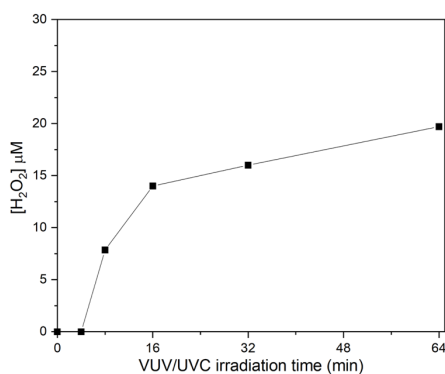


Figure 4.7. Concentration of H_2O_2 over VUV irradiation in the absence of clotrimazole.

The substantial decrease in the inhibition of the green microalgae *R. subcapitata*, the crustacean *D. magna* and the fungus *F. graminearum* after exposing aqueous clotrimazole to 25 J/cm² can be explained by the 95% drug removal and generation of apparently less toxic transformation products (Figure 4). The meaningful degradation profile observed under monochromatic UVC irradiation can be explained mainly by the drug direct photolysis due to their absorbance at 254 nm [213]. While the almost complete drug removal observed after exposing aqueous clotrimazole to 40 J/cm² support the decrease on toxicity towards the green microalgae *R. subcapitata* and the fungus *F. graminearum*. Comparable decreases in ecotoxicity after UVC irradiation has recently been observed for the herbicide glyphosate where UV doses of 20 J/cm² resulted in a 2-23 times decrease in toxicity to different test organisms [214].

Organisms from different trophic levels have been reported to be adversely impacted by the clotrimazole molecule [199,201,203]. However, to the best of our knowledge the environmental fate of clotrimazole including occurrence of degradation products is still not known. Due to substantial lipophilicity and environmental persistence, clotrimazole is frequently detected in WWTPs sewage sludge used for soil amendment to promote agricultural crops [199,215]. Sabourin et al., 2011 investigating the antifungal fate in the agricultural soil reported the identification of only (2-chlorophenyl)bisphenylmethanol as a degradation product. Moreover, this compound is of particular interest because it can also reach the environment resulted from the drug metabolization once it is reported as a metabolite observed in human urine and faeces [216,217]. In the present study, (2-chlorophenyl)bisphenylmethanol (TP1) was observed as a major transient transformation product after VUV/UVC treatment of water containing clotrimazole. The relatively low inhibitory effect of this photoproduct to our test organisms suggested less toxic properties compared to the clotrimazole parent molecule (Figure 4.4). The inferior effect can be attributed to the absence of the imidazole moiety which is likely the active functional group,

in relation to fungi, algae and crustaceans [203,218]. Hence, the VUV/UVC treatment generally appeared to generate some less bioactive transformation products with lower toxicity that may subsequently be biodegraded in the environment or perhaps mineralized by further VUV/UVC treatment.

4.1.5 Conclusions

Our results suggest that non-invasive VUV/UVC can efficiently remove the persistent pollutant clotrimazole via direct and indirect photolysis and consequently decrease the overall toxicity throughout the formation of less toxic intermediates. Moreover, VUV proved to efficient remove the antifungal agent even at trace levels offering an attractive solution for water remediation without the addition of chemicals or catalysts.

Chapter 5 - Elucidation of Degradation Pathways of CECs

In this Chapter is reported the elucidation of the environmental degradation pathways of two CECs: Maprotiline and Aliskiren. These two drugs selected as compound of potential interest were investigated based to potential risk and the lack of information about their environmental fate. Environmental conditions were simulated by spiking river water at environmental concentrations ($\mu\text{g/L}$) and the photoproducts elucidated by HPLC-HRMS. Their presence in the environment were assessed by retrospective analysis.

5.1 Chemical Selection Approach

Maprotiline and Aliskiren were selected as compounds of potential interest for further monitoring activities as a result of the application of the NORMAN prioritization scheme. This scheme was designed by NORMAN to deal with less-investigated substances for which knowledge gaps are identified (e.g. insufficient information on the exposure levels and/or adverse effects, or inadequate performance of the analytical methods for their measurement in the environment) [219]. The concept involves the application of a decision tree, which allows the allocation of substances into six main action categories, based on the identified knowledge gaps and actions needed to address them. The priority within each category is then evaluated on the basis of specific occurrence, hazard (e.g. persistence, bioaccumulation, mobility, endocrine disruption potential) and risk indicators. This workflow, originally designed to work with target monitoring data, is currently exploring the automatic query of non-target screening (NTS) mass spectral information archived in the Digital Sample Freezing Platform (DSFP).

Maprotiline and aliskiren were identified as compounds of potential interest further to a suspect screening test carried out for a list of more than 40,000 substances (present at the time of the study in the SusDat database, 5th September 2019) on 46 composite effluent wastewater samples collected from Danube river basin (August 2017) [12] and from a national wastewater effluent campaign in Germany (May 2018) [220] archived in DSFP. Considering mass accuracy, plausibility of the chromatographic retention time (RT), isotopic pattern fit, number of experimental and predicted fragments, and % similarity of experimental and library spectra as criteria supporting the tentative identification of the suspects, maprotiline was elucidated at level 2A (probable structure by library spectrum match) as compared to other substances for which actions to improve the elucidation of the structure are needed before implementation of further monitoring effort.

In line with the purposes of the prioritization methodology (worst-case scenario approach), the lowest Provisional No Effect Concentration (PNEC) values were used – representing the most conservative ecotoxicological threshold values for the investigated suspect compounds.

Substances were ranked based on three indicators: (i) Frequency of Appearance (FoA), calculated as percentage of sites where the substance was detected above the limit of detection (LOD); (ii) Frequency of PNEC exceedance (FoE), calculated as percentage of sites where the substance was detected above the PNEC, and (iii) extent of PNEC exceedance (EoE), calculated as the 95th percentile (MEC95) of the substance's maximum observed concentration at each site divided by the PNEC. No PNEC value based on experimental data was available for both pollutants and therefore a predicted PNECs (P-PNECs) were derived by QSTR models [221]. P-PNECs values of 0.300 $\mu\text{g L}^{-1}$ and 0.041 $\mu\text{g L}^{-1}$ were predicted for maprotiline and aliskiren, respectively. Maprotiline and aliskiren were prioritized and allocated to the group of compounds with “Sufficient frequency of appearance (FoA)”, that is FoA (sites with positive detection) $\geq 20\%$. In the case of maprotiline: 67% of the investigated wastewater treatment stations, with 17% of the sites exceeding the predicted PNEC value. While for aliskiren: 42.6% of the investigated wastewater treatment stations, with 36.5% of the sites exceeding the predicted PNEC value.

5.1.1 Materials and Methods

Chemicals

Maprotiline hydrochloride (CAS: 10347-81-6), whose structure with the numbering of carbons atoms is shown in Figure 5.1, was purchased from Sigma-Aldrich (Milan, Italy). In order to avoid possible interference from ions adsorbed on the photocatalyst, TiO_2 (Evonik P25, Frankfurt, Germany) was irradiated and washed with distilled water, until there were no detectable signals due to

chloride, sulfate and sodium ions. All the chemical reagents were used as received. Suspensions and standard solutions were prepared in Milli-Q water.

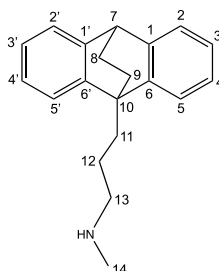


Figure 5.1. Numbering of maprotiline carbon atoms.

The river water sample used for maprotiline experiments was collected from the River Po, Torino Italy, (45°02'40.4"N 7°41'02.1"E) on September 30th 2019. Samples were used after a rough pre-filtration step, carried out through a grade qualitative filter paper (Whatman) removing large suspended solids and filtered using a hydrophilic 0.45 μm filter Sartolon Polyamide (Sartorius Biolab). River water samples had 1.83 mg L^{-1} of total organic carbon (TOC), 44.81 mg L^{-1} of inorganic carbon (IC), and 3.85 mg L^{-1} of total nitrogen (TN) and pH = 8.2. The potential presence of Maprotiline, identified TPs and the described metabolites in the explored river water sample were investigated by HPLC-HRMS before spiking and they were below the detection limit.

Aliskiren (CAS: 173334-57-1), structure with the numbering of carbons atoms is shown in Figure 5.2, was purchased from Sigma-Aldrich (Milan, Italy). Humic acid sodium salts (technical, 50–60% as HA) from Aldrich-Chemie (Milan, Italy). Sodium nitrate (analysis grade) was purchase from Merck, KGaA. All the chemical reagents were used as received. Suspensions and standard solutions were prepared in ultrapure water.

The river water sample used for aliskiren experiments was collected from the River Po, Torino Italy, (45°02'40.4"N 7°41'02.1"E) on September, 14th 2020. Samples were used after a rough pre-filtration step, carried out through a grade

qualitative filter paper (Whatman) removing large suspended solids and filtered using a hydrophilic 0.45 μm filter Sartolon Polyamide (Sartorius Biolab). River water samples had 1.92 mg L^{-1} of total organic carbon (TOC), 44.60 mg L^{-1} of inorganic carbon (IC), 3.940 mg L^{-1} of total nitrogen (TN) and a pH= 8.2. Aliskiren and its identified TPs and the described metabolites were below the detection limit in the investigated river water sample.

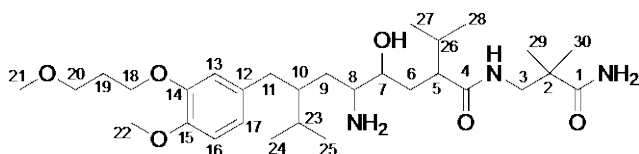


Figure 5.2. Numbering of aliskiren carbon atoms.

Maprotiline degradation experiments

Maprotiline photocatalytic degradation was carried out in ultrapure water in Pyrex glass cells (2.3 cm height \times 4.0 cm diameter), filled with 5 mL of maprotiline (20 mg L^{-1}) and TiO_2 (500 mg L^{-1}) suspension kept under magnetic stirring under irradiation for times ranging from 1 min to 60 min. After irradiation, the photocatalyst was removed using a 0.45 μm Sartolon Polyamide (Sartorius Biolab) filter before analysis. The photolysis experiments were performed in the same conditions without the catalyst addition.

Photolysis experiments in river water sample were performed on a 200 mL water volume spiked with 10 $\mu\text{g L}^{-1}$ of maprotiline divided into three Pyrex glass cells (7.5 cm height \times 9.5 cm diameter). Samples were irradiated for times ranging from 1 h to 72 h. The irradiation was carried out using a PHILIPS cleo 6 X 15 W TL-D Actinic BL with maximum emission wavelength at 365 nm. The UV integrated irradiance on the cells in the 290-400 nm wavelength range was $90 \pm 2 \text{ Wm}^{-2}$ (measured with a CO.FO.MEGRA (Milan, Italy) power-meter). To control the effect of water sample constituents on maprotiline fate, spiked water samples (10 $\mu\text{g L}^{-1}$) were kept in the dark collecting samples over time (0, 16, 24, 48 and 72 hours). Samples were then freeze-dried (LABOGENE – CoolSafe 55-

110). The obtained powder was dissolved into 10 mL of a 50:50 (v/v) methanol: acetonitrile mixture, which was filtered with a 0.22 μm polypropylene filter (ThermoFisher Scientific). The sample was dried under a gentle nitrogen stream at room temperature, then reconstituted with 200 μL of acetonitrile (final pre-concentration factor of 1000) for the LC-HR-MS analysis.

Aliskiren degradation experiments

Photolysis experiments in ultrapure and river water sample were performed on a 200 mL water volume spiked with 5 $\mu\text{g L}^{-1}$ of aliskiren divided into three Pyrex glass cells (7.5 cm height \times 9.5 cm diameter). Samples were irradiated for times ranging from 1 h to 72 h in a sunlight simulator (Solarbox, CO.FO.Me.Gra, Milan) equipped with a xenon lamp (1500 W) with a cut-off filter at below 340 nm. On top of the suspensions the irradiance was 18 W m^{-2} in the 295–400 nm range (similar to the natural sunlight UV irradiance at middle European latitude in sunny days) [22]. Dark experiments were conducted in the same conditions protecting the samples from light over time. Degradation experiments in the presence of humic acid and nitrate were performed with a final concentration of 2 mg L^{-1} of both. Samples were then freeze-dried (LABOGENE – CoolSafe 55-110). The obtained powder was dissolved into 10 mL of a 50:50 (v/v) methanol: acetonitrile mixture which was filtered with a 0.22 μm polypropylene filter (ThermoFisher Scientific). Sample were dried under a gentle nitrogen stream at room temperature and reconstituted with 200 μL of acetonitrile (final pre-concentration factor of 1000) before the LC-HRMS analysis.

Analytical procedures

The identification of maprotiline and aliskiren TPs in ultrapure water and in river water samples was performed using an Ultimate 3000 High Pressure Liquid Chromatography coupled with an LTQ-orbitrap mass spectrometer (Thermo Scientific, Bremen, Germany) operated in ESI mode. The chromatographic

separation was achieved with a reverse phase C18 column (Gemini NX C18, 150 × 2 mm, 3 μm, 110 Å; Phenomenex, Castel Maggiore, BO, Italy) using 20 mM aqueous formic acid (eluent A) and acetonitrile (eluent B). Gradient separation ramp started with 5% B, increased up to 40% B in 18 minutes and to 100% in 5 minutes; then the column was reconditioned. The flow was 0.2 mL/min and injection volume 20 μL.

For the ESI ion source used nitrogen as both sheath and auxiliary gas. Source parameters were set as followed: sheath gas 30 arbitrary unit (arb), auxiliary gas 25 arb, capillary voltage 4.0 kV and capillary temperature 275 °C. Full mass spectra were acquired in positive ion mode on m/z range between 50 and 500 Th, with a resolution of 30.000. MS^n spectra were acquired on the range between ion trap cut-off and precursor ion m/z values. Accuracy on recorded m/z (versus calculated) was ±0.001 Th (without internal calibration).

For the structural elucidation of Maprotiline TPs, collision-induced dissociation (CID) experiments were performed on an Acquity HPLC system (Water Technologies, Guyancourt, France) coupled with a Bruker SolarixXR FT-ICR 9.4 T MS instrument (Bruker Daltonics, Bremen, Germany). For the chromatographic separation, an Agilent Pursuit XR_sULTRA C18 (length 50 mm, diameter 2 mm, particle size 2.8 μm) column was used with an Agilent HPLC MetaGuard (Pursuit XR_s C18, 3 μm, 2,0 mm) guard column (Agilent Technologies, Les Ulis, France). The flow was set to 0.2 mL/min, the total run time was 22 minutes with an acquisition time of 15 minutes. Gradient flow was used with solvent A being water with 0.1% formic acid and solvent B being acetonitrile with 0.1% formic acid. The LC method consisted of holding 95% of solvent A and 5% of solvent B for 3 minutes, after which a gradient of 9 minutes was applied, until the ratio of the two solvents reached 50-50%. The ratio of solvent A was promptly decreased to 5% and kept at this ratio until 17.1 min total run time, after it was reset to the initial 95%. After every measurement, 5 minutes were let for equilibration and washing using the latter solvent ratio. The injection

volumes were 2 μL and 10 μL for LC-MS and LC-MSⁿ experiments, respectively. The autosampler (Water Technologies, Guyancourt, France) was kept at 4 °C for better preservation. Each sample was prepared before analysis by adding 10% volume of a mixture acetonitrile/formic acid (0.1%). Electrospray ionization was used as the ion source in positive mode with a sample flow of 0.2 mL/min. The capillary voltage was 4000 V and the spray shield was set at -500 V. Nitrogen was used as nebulizer gas (1 bar) and drying gas (8 L/min, 250 °C). The detection range was 57.7 – 1000 m/z , in broadband mode, with a data acquisition size of 4 Mpts and a data reduction of noise of 97%. For MS² experiments, isolation was carried out with a 1 m/z window and CID experiments were performed with collision energies of 5, 10, 15 and 20 V. Preliminary in-cell experiments were performed to assess the optimal parameters (isolation window, quadrupole voltage, and collision energy) for the MS³ experiments. The Bruker Data Analysis software was used for data processing.

Total organic carbon (TOC) was measured using a Shimadzu TOC-5000 analyzer (catalytic oxidation on Pt at 680 °C). The calibration was performed using standards of potassium phthalate.

Inorganic ions (NO_3^- , NO_2^- and NH_4^+) generated during maprotiline degradation were identified by ion chromatography analysis using a Dionex chromatograph equipped with a Dionex 40 ED pump and a Dionex 40 ED conductimetric detector. For nitrate anions, a Dionex Ion Pac AS9-HC 4 \times 250 mm column, and Ion Pac ASRS-ULTRA 4 mm conductivity suppressor were used while ammonium cations were analyzed using a Dionex Ion Pac CS12A 4 \times 250 mm column, and an Ion Pac CSRS-ULTRA 4 mm conductivity suppressor, using 10 mM NaHCO_3 and 4 mM K_2CO_3 as eluent at 1 mL/min.

Retrospective suspected screening

The retrospective suspected analysis was performed accordingly to the workflow previously described [222]. The occurrence of maprotiline and the

elucidated TPs were investigated in 130 digitally achieved chromatograms (58 wastewater and 72 river water samples). 34 wastewater samples from the river basins of Germany (Danube, Rhine, Ems, Weser, Elbe, Odra, Meuse, Eider, Trave, Peene) [220] and 24 additional wastewater samples from Danube River basin (12 countries) [12] and surface water samples from Danube, Dniester [223] and Donets were investigated, as described in Table E5 (see Appendix E).

The occurrence of aliskiren drug and the five elucidated TPs through retrospective suspect screening was investigated in a total of 754 environmental samples. For each batch of samples at least one procedural blank sample was included for quality assurance (in total 37 procedural blanks). Most of the samples were collected in national and international monitoring campaigns such as joint Danube survey 4 (JDS4) [12,224], river monitoring campaigns (e.g. Donets/Dniester/Dnieper) [223], monitoring of the Black Sea (EMBLAS-II) [225], monitoring of top predators and their prey from specimen banks in context of LIFE APEX among others. The search was based on the combination of exact mass and the predicted retention time window in the chromatogram [222]. The information was supplemented by the isotopic fit check (if available) and the presence of at least two qualifier fragment ions.

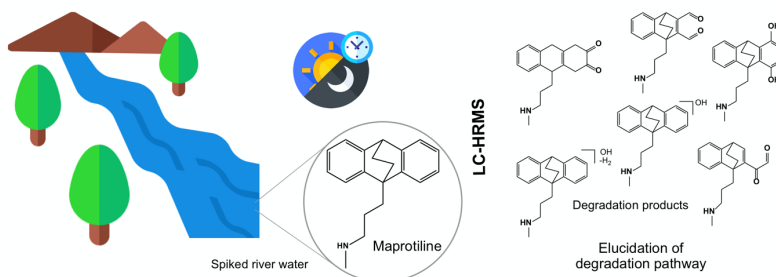
Toxicity

The acute toxicity of maprotiline and TPs (20 mgL^{-1}) degradation in Milli-Q water in the presence of TiO_2 (500 mgL^{-1}) was evaluated for samples after different irradiation times using a Microtox Model 500 toxicity analyzer (Milan, Italy). The analyses were performed evaluating the bioluminescence inhibition assay in the marine bacterium *Vibrio fischeri* by monitoring changes in the natural emission of the luminescent bacteria. Freeze-dried bacteria, reconstitution solution, diluent (2% NaCl) and an adjustment solution (non-toxic 22% NaCl) were obtained from Azur (Milan, Italy). Samples were tested in a medium containing 2% NaCl, and the luminescence was recorded after 5, 15 and

30 min of incubation at 15 °C. The luminescence inhibition percentage was determined by comparing with a non-toxic control solution.

5.2 Elucidation of Maprotiline Degradation Pathways

Adapted from:



Study of the photoinduced transformations of maprotiline in river water using liquid chromatography high-resolution mass spectrometry

Nuno P.F. Gonçalves, Zsuzsanna Varga, Stéphane Bouchonnet, Valeria Dulio, Nikiforos Alygizakis, Federica Dal Bello, Claudio Medana, Paola Calza

Science of the Total Environment 755 (2021) 143556

My direct contribution

I declare that have performed all the degradation experiments described in this sub-chapter, the elucidation of the maprotiline degradation pathways as well as the toxicity tests. The chemical selection approach and the retrospective analysis was performed by Valeria Dulio and Nikiforos Alygizakis, respectively. LC-HRMS analysis were performed in the group of Claudio Medana, University of Turin. CDI experiments were performed during my secondment at CNRS - Ecole Polytechnique, Institut Polytechnique de Paris in the group of Professor Stéphane Bouchonnet.

5.2.1 Motivation

Maprotiline is a tetracyclic antidepressant drug approved in many countries, with a daily usual dosage of 150 to 225 mg used to treat depression associated with agitation or anxiety [226]. As a consequence of its wrong disposal and excretion in its unmetabolized form (3-4%), [227], like many other drugs, maprotiline drug has been reported in influent and effluent of wastewater treatment plants as well as in surface waters, usually at ng/L up to few µg/L concentration [35,228,229]. Despite hazard and risk indicators and its frequent environmental occurrence, there is no information about the maprotiline environmental fate, its degradation pathway neither toxicity of its degradation products.

The maprotiline environmental fate was investigated in river water by initially performing a laboratory simulation to identify the degradation products by HPLC-HRMS and then search for them under natural conditions. For easier identification of the degradation products, maprotiline degradation experiments were firstly performed at high concentration in ultrapure water using TiO₂ as a benchmark photocatalyst. Subsequently, experiments were performed in spiked river water, at concentration similar to those described in natural waters, for the elucidation of the drug environmental fate. Toxicity was estimated as well and preliminary bioassays were performed on the generated degradation species.

5.2.2 Results and Discussion

Maprotiline degradation in ultrapure water

The direct photolysis of maprotiline in the considered time window (1 h) is negligible. The most likely reason is the fact that the molecule does not absorb radiations above 280 nm [230], while the sunlight irradiance below 300 nm is extremely limited [231]. To hasten the degradation process and generate degradation products, the drug degradation was firstly performed at high

concentration (for easier identification) in ultrapure water using TiO_2 as photocatalyst. Figure 5.3 shows the maprotiline degradation in the presence of the heterogeneous photocatalyst activated under UVA irradiation. In the presence of the photocatalyst, the complete maprotiline removal was achieved after only 15 minutes, while the total organic carbon (TOC) measurements showed more than 85% of the pollutant mineralization in just 30 min under irradiation and > 95% after 1 h. This trend is in agreement with the ammonium and nitrate concentrations monitored during the degradation, as shown in Figure 5.3. The ammonium ion (73%) release was observed in a significantly higher amount than that of nitrate (15%) within 1 h of irradiation, as previously observed [232].

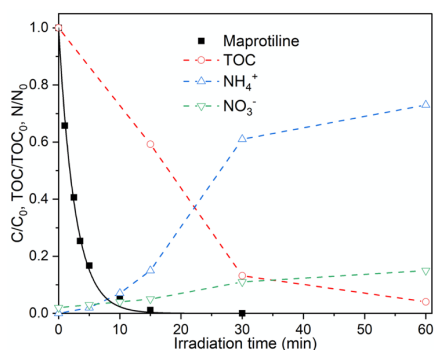


Figure 5.3. Maprotiline degradation (black line) and mineralization (colored lines) in the presence of TiO_2 (500 mg L^{-1}).

All samples were analyzed by HPLC-HRMS for the identification of maprotiline degradation products. The m/z ratios, proposed elemental compositions, as well as fragment ions and retention times are presented in Table 5.1. In total, 32 degradation products were formed, many of them in the form of several isomeric species as summarized in Table 5.1. The formation of degradation products and their evolution over irradiation time are shown in Figure E1. For all degradation products, complete removal was observed after less than 30 minutes of irradiation, in agreement with the high percentage of mineralization (86%) obtained within the same experimental time.

Table 5.1. Summary of $[M+H]^+$ ions and main product ions from CID experiments.

Compound	$[M+H]^+$	Empirical Formula	r.t. (min)	MS ²			Theoretical m/z
				m/z	Empirical formula	Δ (ppm)	
Maprotiline	278.1911	C ₂₀ H ₂₄ N	12.5	278.1943	C ₂₀ H ₂₄ N (16)	0.45	278.1903
				250.1594	C ₁₈ H ₂₀ N (100)	-0.66	250.1590
				247.1489	C ₁₉ H ₁₉ (1)	0.91	247.1482
				219.1173	C ₁₇ H ₁₅ (66)	-0.48	219.1168
				191.0850	C ₁₅ H ₁₁ (13)	-5.26	191.0855
				169.1013	C ₁₃ H ₁₃ (8)	-2.76	169.1012
294-A	294.1858	C ₂₀ H ₂₄ NO	9.0	294.1871	C ₂₀ H ₂₄ NO (8)	-6.4	294.1852
				266.1556	C ₁₈ H ₂₀ NO (100)	-6.2	266.1539
				235.1132	C ₁₇ H ₁₅ O (42)	-6.3	235.1117
				217.1026	C ₁₇ H ₁₃ (35)	-6.4	217.1012
				207.0818	C ₁₅ H ₁₁ O (55)	-6.4	207.0804
				191.0868	C ₁₅ H ₁₁ (25)	-6.4	191.0855
				157.0658	C ₁₁ H ₉ O (6)	-6.5	157.0648
				117.0706	C ₉ H ₉ (6)	-6.4	117.0699
294-B			9.7	91.0548	C ₇ H ₇ (10)	-6.3	91.0542
				276.1765	C ₂₀ H ₂₂ N (100)	-6.5	276.1747
				250.1606	C ₁₈ H ₂₀ N (59)	-6.3	250.1590
				245.1340	C ₁₉ H ₁₇ (31)	-6.0	245.1325
				219.1182	C ₁₇ H ₁₅ (78)	-6.4	219.1168
				217.1026	C ₁₇ H ₁₃ (40)	-6.4	217.1012
				191.0868	C ₁₅ H ₁₁ (6)	-6.4	191.0855
				141.0708	C ₁₁ H ₉ (7)	-6.8	141.0699
				129.0707	C ₁₀ H ₉ (30)	-6.6	129.0699

		91.0548	C ₇ H ₇ (21)	-6.3	91.0542
294-C	10.0	294.1871	C ₂₀ H ₂₄ NO (5)	-6.4	294.1852
		266.1556	C ₁₈ H ₂₀ NO (54)	-6.3	266.1539
		235.1132	C ₁₇ H ₁₅ O (100)	-6.3	235.1117
		209.0974	C ₁₅ H ₁₃ O (3)	-6.4	209.0961
		207.0818	C ₁₅ H ₁₁ O (21)	-6.4	207.0804
		185.0973	C ₁₃ H ₁₃ O (20)	-6.5	185.0961
		169.1023	C ₁₃ H ₁₃ (8)	-6.4	169.1012
		147.0814	C ₁₀ H ₁₁ O (6)	-6.3	147.0804
		143.0865	C ₁₁ H ₁₁ (7)	-6.7	143.0855
		133.0657	C ₉ H ₉ O (14)	-6.5	133.0648
		117.0706	C ₉ H ₉ (15)	-6.4	117.0699
		107.0498	C ₇ H ₇ O (9)	-6.2	107.0491
				91.0548	C ₇ H ₇ (5)
294-D	10.5	294.1871	C ₂₀ H ₂₄ NO (16)	-6.2	294.1852
		266.1556	C ₁₈ H ₂₀ NO (59)	-6.2	266.1539
		263.1447	C ₁₉ H ₁₉ O (9)	-6.3	263.1430
		245.1340	C ₁₉ H ₁₇ (9)	-6.4	245.1325
		235.1132	C ₁₇ H ₁₅ O (100)	-6.3	235.1117
		221.0975	C ₁₆ H ₁₃ O (19)	-6.4	221.0961
		217.1026	C ₁₇ H ₁₃ (14)	-6.4	217.1012
		209.0974	C ₁₅ H ₁₃ O (11)	-6.4	209.0961
		207.0818	C ₁₅ H ₁₁ O (16)	-6.5	207.0804
		185.0973	C ₁₃ H ₁₃ O (19)	-6.5	185.0961
		169.1023	C ₁₃ H ₁₃ (51)	-6.5	169.1012
		143.0865	C ₁₁ H ₁₁ (32)	-6.5	143.0855
		141.0708	C ₁₁ H ₉ (40)	-6.5	141.0699

				133.0657	C ₉ H ₉ O (24)	-6.5	133.0648
				129.0707	C ₁₀ H ₉ (15)	-6.5	129.0699
				117.0706	C ₉ H ₉ (16)	-6.5	117.0699
				107.0498	C ₇ H ₇ O (24)	-6.4	107.0491
				91.0548	C ₇ H ₇ (5)	-6.3	91.0542
294-E			11.3	294.1871	C ₂₀ H ₂₄ NO (11)	-6.2	294.1852
				276.1764	C ₂₀ H ₂₂ N (6)	-6.3	276.1747
				266.1556	C ₁₈ H ₂₀ NO (98)	-6.2	266.1539
				235.1132	C ₁₇ H ₁₅ O (100)	-6.3	235.1117
				217.1026	C ₁₇ H ₁₃ (11)	-6.4	217.1012
				207.0818	C ₁₅ H ₁₁ O (72)	-6.4	207.0804
				185.0973	C ₁₃ H ₁₃ O (26)	-6.5	185.0961
				169.1023	C ₁₃ H ₁₃ (19)	-6.5	169.1012
				157.0658	C ₁₁ H ₉ O (13)	-6.5	157.0648
				141.0708	C ₁₁ H ₉ (19)	-6.5	141.0699
				133.0657	C ₉ H ₉ O (21)	-6.5	133.0648
				117.0706	C ₉ H ₉ (23)	-6.5	117.0699
				107.0498	C ₇ H ₇ O (17)	-6.4	107.0491
				91.0548	C ₇ H ₇ (7)	-6.3	91.0542
310-A	310.1807	C ₂₀ H ₂₄ NO ₂	8.4	310.1820	C ₂₀ H ₂₄ NO ₂ (100)	-6.1	310.1802
				292.1714	C ₂₀ H ₂₂ NO (63)	-6.2	292.1696
				279.1397	C ₁₉ H ₁₉ O ₂ (67)	-6.2	279.1380
				261.1290	C ₁₉ H ₁₇ O (31)	-6.3	261.1274
				217.1026	C ₁₇ H ₁₃ (70)	-6.4	217.1012
				191.0867	C ₁₅ H ₁₁ (81)	-6.5	191.0855
				185.0973	C ₁₃ H ₁₃ O (34)	-6.5	185.0961
				159.0815	C ₁₁ H ₁₁ O (15)	-6.5	159.0804

310-B	9.0	133.0657	C ₉ H ₉ O (9)	-6.5	133.0648
		310.1820	C ₂₀ H ₂₄ NO ₂ (45)	-6.1	310.1802
		292.1714	C ₂₀ H ₂₂ NO (86)	-6.1	292.1696
		266.1556	C ₁₈ H ₂₀ NO (15)	-6.3	266.1539
		261.1290	C ₁₉ H ₁₇ O (100)	-6.3	261.1274
		233.0976	C ₁₇ H ₁₃ O (45)	-6.4	233.0961
		207.0818	C ₁₅ H ₁₁ O (21)	-6.5	207.0804
		169.1023	C ₁₃ H ₁₃ (53)	-6.5	169.1012
		141.0708	C ₁₁ H ₉ (20)	-6.5	141.0699
		123.0449	C ₇ H ₇ O ₂ (14)	-6.5	123.0441
310-C	9.4	89.0603	C ₄ H ₉ O ₂ (9)	-6.2	89.0597
		310.1820	C ₂₀ H ₂₄ NO ₂ (99)	-6.1	310.1802
		282.1506	C ₁₈ H ₂₀ NO ₂ (100)	-6.2	282.1489
		279.1397	C ₁₉ H ₁₉ O ₂ (23)	-6.2	279.1380
		251.1082	C ₁₇ H ₁₅ O ₂ (39)	-6.3	251.1067
		185.0973	C ₁₃ H ₁₃ O (80)	-6.5	185.0961
		159.0815	C ₁₁ H ₁₁ O (21)	-6.5	159.0804
		145.0657	C ₁₀ H ₉ O (8)	-6.6	145.0648
		133.0657	C ₉ H ₉ O (17)	-6.5	133.0648
		107.0498	C ₇ H ₇ O (10)	-6.4	107.0491
310-D	10.1	310.1820	C ₂₀ H ₂₄ NO ₂ (96)	-6.1	310.1802
		282.1506	C ₁₈ H ₂₀ NO ₂ (100)	-6.2	282.1489
		251.1082	C ₁₇ H ₁₅ O ₂ (27)	-6.3	251.1067
		233.0976	C ₁₇ H ₁₃ O (8)	-6.3	233.0961
		201.0923	C ₁₃ H ₁₃ O ₂ (11)	-6.4	201.0910
		169.1023	C ₁₃ H ₁₃ (65)	-6.5	169.1012
		143.0865	C ₁₁ H ₁₁ (14)	-6.5	143.0855

				141.0708	C ₁₁ H ₉ (16)	-6.5	141.0699
310-E			10.6	310.1821	C ₂₀ H ₂₄ NO ₂ (50)	-6.1	310.1802
				292.1714	C ₂₀ H ₂₂ NO (100)	-6.1	292.1696
				280.1349	C ₁₈ H ₁₈ NO ₂ (26)	-6.2	280.1332
				233.0976	C ₁₇ H ₁₃ O (24)	-6.5	233.0961
310-F			11.3	101.0604	C ₅ H ₉ O ₂ (14)	-6.5	101.0597
				310.1820	C ₂₀ H ₂₄ NO ₂ (4)	-6.1	310.1802
				250.1606	C ₁₈ H ₂₀ N (100)	-6.2	250.1590
				217.1026	C ₁₇ H ₁₃ (23)	-6.4	217.1012
				191.0868	C ₁₅ H ₁₁ (42)	-6.5	191.0855
326-A	326.1757	C ₂₀ H ₂₄ NO ₃	7.2	326.1770	C ₂₀ H ₂₄ NO ₃ (100)	-6.0	326.1751
				308.1664	C ₂₀ H ₂₂ NO ₂ (42)	-6.2	308.1645
				298.1456	C ₁₈ H ₂₀ NO ₃ (23)	-6.0	298.1438
				185.0973	C ₁₃ H ₁₃ O (8)	-6.5	185.0961
				89.0603	C ₄ H ₉ O ₂ (2)	-6.2	89.05971
326-B			8.4	326.1770	C ₂₀ H ₂₄ NO ₃ (99)	-6.0	326.1751
				308.1664	C ₂₀ H ₂₂ NO ₂ (37)	-6.0	308.1645
				298.1456	C ₁₈ H ₂₀ NO ₃ (100)	-6.0	298.1438
				267.1032	C ₂₀ H ₁₃ N (23)	3.8	267.1043
				191.0867	C ₁₅ H ₁₁ (23)	-6.4	191.0855
326-C			9.3	185.0973	C ₁₃ H ₁₃ O (62)	-6.4	185.0961
				326.1770	C ₂₀ H ₂₄ NO ₃ (21)	-5.9	326.1751
				308.1664	C ₂₀ H ₂₂ NO ₂ (55)	-6.0	308.1645
				298.1456	C ₁₈ H ₂₀ NO ₃ (59)	-6.0	298.1438
				280.1349	C ₁₈ H ₁₈ NO ₂ (100)	-6.1	280.1332
				267.1032	C ₂₀ H ₁₃ N (25)	3.9	267.1043
				249.0926	C ₁₇ H ₁₃ O ₂ (86)	-6.2	249.0910

342-A	342.1707	C ₂₀ H ₂₄ NO ₄	6.5	342.1720	C ₂₀ H ₂₄ NO ₄ (75)	-5.9	342.1700
				324.1613	C ₂₀ H ₂₂ NO ₃ (54)	-5.9	324.1594
				275.1084	C ₁₉ H ₁₅ O ₂ (53)	-6.2	275.1067
				247.0769	C ₁₇ H ₁₁ O ₂ (100)	-6.3	247.0754
				183.0816	C ₁₃ H ₁₁ O (47)	-6.4	183.0804
342-B			7.1	342.1730	C ₂₀ H ₂₄ NO ₄ (100)	-5.9	342.1700
				324.1613	C ₂₀ H ₂₂ NO ₃ (47)	-5.9	324.1594
				306.1507	C ₂₀ H ₂₀ NO ₂ (37)	-6.0	306.1489
				216.1397	C ₁₄ H ₁₈ NO (51)	-6.3	216.1383
				185.0973	C ₁₃ H ₁₃ O (57)	-6.4	185.0961
				167.0866	C ₁₃ H ₁₁ (46)	-6.5	167.0855
				157.0658	C ₁₁ H ₉ O (50)	-6.5	157.0648
342-C			7.5	342.1720	C ₂₀ H ₂₄ NO ₄ (100)	-5.8	342.1700
				324.1614	C ₂₀ H ₂₂ NO ₃ (36)	-6.0	324.1594
				296.1663	C ₁₉ H ₂₂ NO ₂ (48)	-6.1	296.1645
				240.1398	C ₁₆ H ₁₈ NO (16)	-6.3	240.1383
				133.0868	C ₆ H ₁₃ O ₃ (22)	-6.4	133.0859
				89.0603	C ₄ H ₉ O ₂ (17)	-6.1	89.0597
342-D			8.5	342.1720	C ₂₀ H ₂₄ NO ₄ (100)	-5.8	342.1700
				324.1614	C ₂₀ H ₂₂ NO ₃ (30)	-6.0	324.1594
				296.1663	C ₁₉ H ₂₂ NO ₂ (22)	-6.1	296.1645
				240.1398	C ₁₆ H ₁₈ NO (16)	-6.3	240.1383
				212.1447	C ₁₅ H ₁₈ N (8)	-6.4	212.1434
292-A	292.1701	C ₂₀ H ₂₂ NO	9.4	292.1714	C ₂₀ H ₂₂ NO (31)	-6.3	292.1696
				250.1606	C ₁₈ H ₂₀ N (14)	-6.3	250.1590
				217.1026	C ₁₇ H ₁₃ (94)	-6.3	217.1012
				191.0868	C ₁₅ H ₁₁ (100)	-6.5	191.0855

292-B			9.9	292.1714	C ₂₀ H ₂₂ NO (100)	-6.1	292.1696
				250.1606	C ₁₈ H ₂₀ N (11)	-6.3	250.1590
				219.1182	C ₁₇ H ₁₅ (12)	-6.1	219.1168
				191.0867	C ₁₅ H ₁₁ (13)	-6.3	191.0855
292-C			10.7	292.1714	C ₂₀ H ₂₂ NO (67)	-6.1	292.1696
				250.1606	C ₁₈ H ₂₀ N (58)	-6.2	250.1590
				243.1183	C ₁₉ H ₁₅ (23)	-6.2	243.1168
				219.1182	C ₁₇ H ₁₅ (100)	-6.3	219.1168
				191.0867	C ₁₅ H ₁₁ (22)	-6.4	191.0855
292-D			11.3	292.1713	C ₂₀ H ₂₂ NO (27)	-6.0	292.1696
				243.1183	C ₁₉ H ₁₅ (20)	-6.2	243.1168
				217.1026	C ₁₇ H ₁₃ (31)	-6.3	217.1012
				191.0868	C ₁₅ H ₁₁ (100)	-6.4	191.0855
292-E			11.6	292.1714	C ₂₀ H ₂₂ NO (36)	-6.3	292.1696
				246.1292	C ₁₈ H ₁₆ N (66)	-6.0	246.1277
				183.0816	C ₁₃ H ₁₁ O (100)	-6.4	183.0804
308-A	308.1651	C ₂₀ H ₂₂ NO ₂	7.5	308.1664	C ₂₀ H ₂₂ NO ₂ (3)	-6.2	308.1645
				233.0976	C ₁₇ H ₁₃ O (100)	-6.3	233.0961
				215.0869	C ₁₇ H ₁₁ (28)	-6.4	215.0855
				207.0818	C ₁₅ H ₁₁ O (16)	-6.4	207.0804
				203.0868	C ₁₆ H ₁₁ (9)	-6.4	203.0855
308-B			8.4	308.1664	C ₂₀ H ₂₂ NO ₂ (86)	-6.0	308.1645
				265.1478	C ₁₈ H ₁₉ NO (25)	-6.2	265.1461
				233.0976	C ₁₇ H ₁₃ O (91)	-6.3	233.0961
				215.0869	C ₁₇ H ₁₁ (18)	-6.3	215.0855
				207.0818	C ₁₅ H ₁₁ O (100)	-6.4	207.0804
				178.0789	C ₁₄ H ₁₀ (24)	-6.4	178.0777

308-C			9.6	308.1663	C ₂₀ H ₂₂ NO ₂ (14)	-5.9	308.1645
				280.1349	C ₁₈ H ₁₈ NO ₂ (100)	-6.1	280.1332
324	324.1599	C ₂₀ H ₂₂ NO ₃	6.7	324.1614	C ₂₀ H ₂₂ NO ₃ (57)	-6.0	324.1594
				306.1507	C ₂₀ H ₂₀ NO ₂ (25)	-6.0	306.1489
				247.1371	C ₁₈ H ₁₇ N (100)	-6.3	247.1356
				233.0976	C ₁₇ H ₁₃ O (52)	-6.4	233.0961
				207.0818	C ₁₅ H ₁₁ O (13)	-6.4	207.0804
				191.0867	C ₁₅ H ₁₁ (17)	-6.3	191.0855
284-A	284.1650	C ₁₈ H ₂₂ NO	8.0	284.1662	C ₁₈ H ₂₂ NO ₂ (100)	-6.1	284.1645
				266.1557	C ₁₈ H ₂₀ NO (3)	-6.1	266.1539
				253.1239	C ₁₇ H ₁₇ O ₂ (6)	-6.3	253.1223
				225.1288	C ₁₆ H ₁₇ O (3)	-6.4	225.1274
				207.1182	C ₁₆ H ₁₅ (4)	-6.4	207.1168
284-B			9.1	284.1664	C ₁₈ H ₂₂ NO ₂ (100)	-6.5	284.1645
				89.0603	C ₄ H ₉ O ₂ (5)	-6.2	89.0597
284-C			9.5	284.1662	C ₁₈ H ₂₂ NO ₂ (100)	-6.1	284.1645
				256.1348	C ₁₆ H ₁₈ NO ₂ (15)	-6.2	256.1332
				225.0924	C ₁₅ H ₁₃ O ₂ (7)	-6.3	225.0910
234	234.1492	C ₁₄ H ₂₀ NO ₂	5.4	216.1396	C ₁₄ H ₁₈ NO (21)	-6.0	216.1383
				185.0972	C ₁₃ H ₁₃ O (53)	-6.1	185.0961
				167.0866	C ₁₃ H ₁₁ (100)	-6.2	167.0855
				157.0658	C ₁₁ H ₉ O (27)	-6.1	157.0648
				141.0707	C ₁₁ H ₉ (14)	-6.1	141.0699
				129.0707	C ₁₀ H ₉ (26)	-6.1	129.0699
258	258.1493	C ₁₆ H ₂₀ NO ₂	7.3	258.1505	C ₁₆ H ₂₀ NO ₂ (100)	-6.2	258.1489
				240.1398	C ₁₆ H ₁₈ NO (4)	-6.3	240.1383
				212.1447	C ₁₅ H ₁₈ N (4)	-6.4	212.1434

Among the identified TPs, 18 resulted from the drug hydroxylation. Species with m/z 294.1858, 310.1806, 326.1755 and 342.1709 matches with formulae corresponding to mono-, di, tri- and tetrahydroxy derivative isomers. The main drug degradation products were those involving monohydroxylation (m/z 294, see Figure E2), and in particular the isomers 294-D and 294-E, which exhibited maximum intensity within 5 min, as shown in Figure E1. The species resulting from the addition of the second (m/z 310), third (m/z 326) and fourth (m/z 342) hydroxyl groups showed similar evolution profiles over time. Additionally, 9 degradation products resulting from the drug oxidation were identified. Species with m/z 292.1709, 308.1648, 324.1609 match formulae corresponding to dehydrogenation of mono-, di- and trihydroxy derivatives, respectively. It can be reasonably assumed that these TPs are a result of H_2 elimination from the corresponding species determined with m/z 294, 310 and 326. The TPs with m/z 308 showed a fast formation (maximum intensity at 5 min) but a longer persistence, nevertheless they were also completely removed within 30 min. A similar evolution over time was observed for the 3 isomeric species with m/z 284.1647 matching with the formula $C_{18}H_{22}NO_2^+$. Additionally, two species at m/z 258.1503 and 234.1505 ions were observed, matching respectively with the formulae $C_{16}H_{20}NO_2^+$ and $C_{14}H_{20}NO_2^+$, and both species presented the maximum intensity at 5 minutes and complete disappearance in 30 min. Furthermore, it could be noted a progressively lower abundance of TPs formed from the addition of multiple hydroxyl groups. Also, the species with m/z 284.1647, 258.1503 and 234.1505 were the lowest abundant TPs.

The potential acute toxicity of maprotiline and its TPs was assessed by using the *Vibrio fischeri* assay and the results are plotted in Figure 5.4. At time zero, the inhibition percentage related to maprotiline is low (12%) and, despite a slight increase in the first stage of degradation, then it decreases, so suggesting that the drug proceeds through the formation of slightly toxic compounds. The sample at 30 minutes shown no inhibition that can be explained by the complete removal of the identified TPs and the almost complete mineralization.

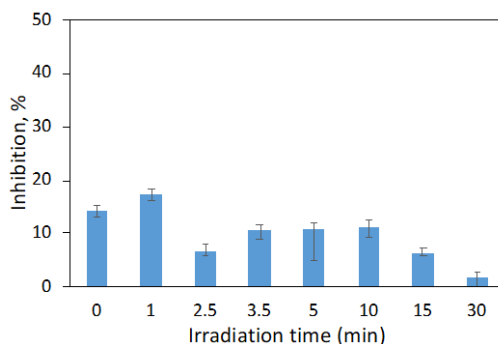


Figure 5.4. Inhibition effect on *vibrio fischeri* bioluminescence in the presence of TPs resulting from maprotiline photocatalytic degradation as a function of irradiation time. error bars correspond to standard deviations ($n=3$).

Structural elucidation of maprotiline main degradation products

Aiming at TPs structural elucidation, the maprotiline fragmentation pathway was firstly investigated by CID experiments, ascertaining the most likely losses from the protonated molecule. The maprotiline MH^+ (m/z 278.1910) MS^2 fragmentation pathways are presented in Figure 5.5 and was suggested based on the 5 observed product ions (see Table 5.1).

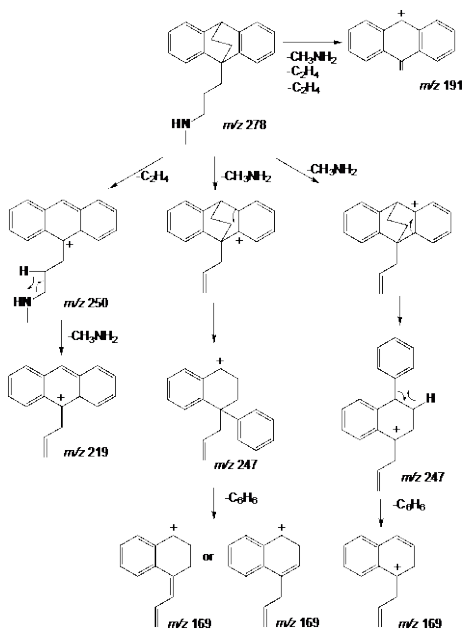


Figure 5.5. Suggested fragmentation pathways for protonated maprotiline in CID experiments.

Table 5.2. Ions detected in CDI experiments for maprotiline main degradation products.

<i>m/z</i>	Ion formula	294				
		A	B	C	D	E
294.1852	C ₂₀ H ₂₄ NO ⁺	+		+	+	+
276.1747	C ₂₀ H ₂₂ N ⁺	+	+		+	
266.1539	C ₁₈ H ₂₀ NO ⁺	+		+	+	+
263.1447	C ₁₉ H ₁₉ O ⁺				+	
250.1606*	C ₁₈ H ₂₀ N ⁺		+			
245.1341	C ₁₉ H ₁₇ ⁺		+		+	
235.1132	C ₁₅ H ₁₅ O ⁺	+		+	+	+
219.1182*	C ₁₇ H ₁₅ ⁺		+			
207.0804	C ₁₅ H ₁₁ O ⁺	+		+	+	+
191.0868*	C ₁₅ H ₁₁ ⁺		+			
185.0973	C ₁₃ H ₁₃ O ⁺	+		+	+	+
169.1023*	C ₁₃ H ₁₃ ⁺	+		+	+	+
157.0658	C ₁₁ H ₉ O ⁺					+

<i>m/z</i>	Ion formula	292				
		A	B	C	D	E
292.1713	C ₂₀ H ₂₄ NO ⁺	+	+	+	+	+
250.1605*	C ₁₈ H ₂₀ N ⁺	+	+	+	+	
246.1292	C ₁₈ H ₁₆ N ⁺					+
243.1183	C ₁₅ H ₁₅ O ⁺			+	+	
219.1182*	C ₁₇ H ₁₅ ⁺	+	+	+	+	
217.1025	C ₁₅ H ₁₁ O ⁺	+	+	+	+	
191.0867*	C ₁₅ H ₁₁ ⁺	+	+	+	+	
183.0816	C ₁₃ H ₁₃ O ⁺					+

*product ions observed also in the maprotiline fragmentation.

Five photoproducts with *m/z* 294 were detected with retention times between 9.0 and 11.3 minutes and, based on their empirical formula, were attributed to hydroxylated maprotiline. If one considers that these photoproducts result from hydroxyl addition onto an aromatic ring, as usually reported when photochemistry occurs in water matrix, the main dissociations of oxidized maprotiline are expected to be those displayed in Figure 5.6. It is to be noted that water loss from the protonated molecule is not informative considering that protonation of a hydroxyl group can lead to water elimination whatever its location on the ion [233].

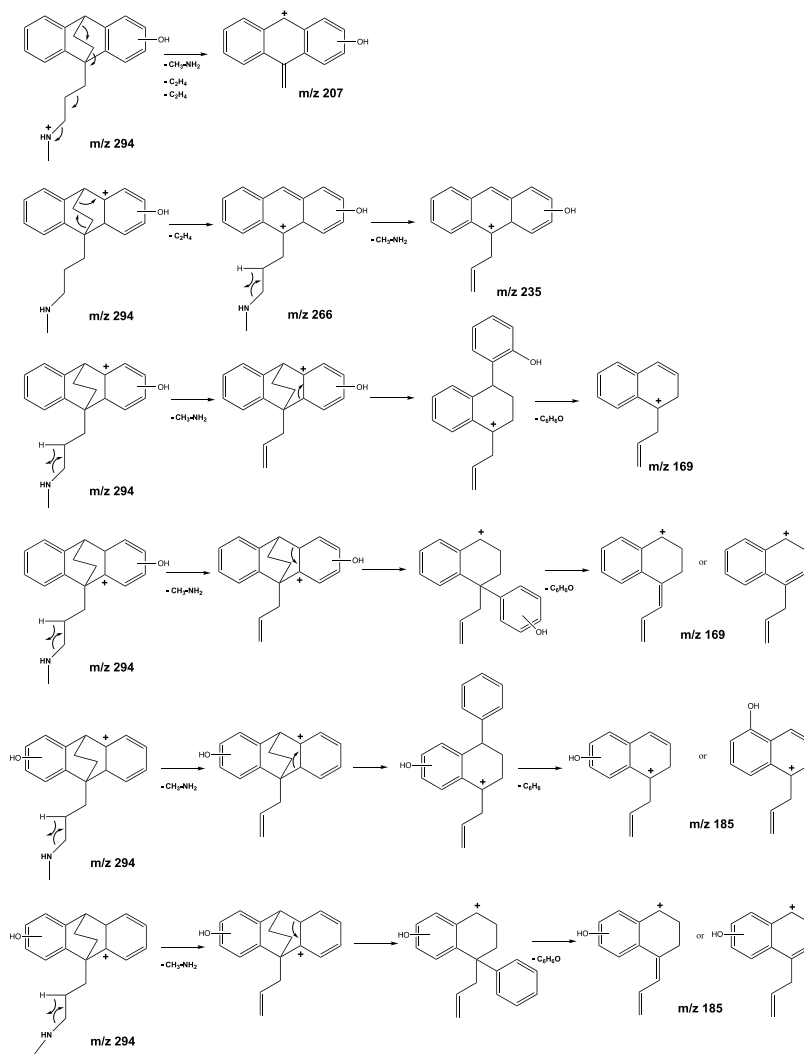


Figure 5.6. Suggested dissociation pathways for photoproducts resulting from hydroxylation of maprotiline on an aromatic ring.

The main ions observed in CID experiments on m/z 294 are those described in Figure 5.6, and are common for the photoproducts 294-A, 294-C, 294-D and 294-E (see Table 5.2) but not for 294-B, for which CID decomposition pathways are different. The protonated structure of the compound 294-D displays specific ions (m/z 263 and m/z 245), which allow to determine the position of the hydroxyl group according to the mechanism displayed in Figure E2. In the same way, the specific ion at m/z 157 allowed structural determination of the

compound 294-E (see Figure E4). The CID mass spectra of the photoproducts 294-A and 294-C are the same and do not allow to discriminate between the compound resulting from hydroxyl addition on the carbon atom 3 or onto the carbon atom 4 (see Figure 5.1). The structures were suggested based on their relative retention times, in comparison with those of the elucidated structures. In the case of the photoproduct 294-B, CID experiments provided common ions with those resulting from CID of protonated maprotiline: m/z 276, m/z 250, m/z 219 and m/z 191, which show evidence that hydroxylation of this compound occurred on the bridge, i.e., on C8 or C9. The CID pathways depicted in Figure E5 demonstrate that it is not possible to establish whether the hydroxylation took place on carbon 8 or 9 since the CID mechanism begins by a water elimination that leads to the same ion in both cases. One should have expected hydroxylation to occur onto C7 because cleavage of the C7-H bond would have led to a very stable carbocation but the resulting compound would not have been able to undergo the subsequent losses of H₂O and C₂H₂ reported in Table 5.2 for the corresponding ion. Additional experiments (see below) allowed to establish that hydroxylation took place on C9.

Five photoproducts with a pseudo molecular ion at m/z 292 were detected with retention times between 9.4 and 11.6 minutes; in terms of molecular formulae, they result from the addition of one oxygen atom and the removal of two hydrogen atoms on maprotiline. It can be reasonably assumed that these five photoproducts result from H₂ elimination from the five photoproducts with a pseudo molecular ion at m/z 294. Dehydrogenation is possible to create a double bond between C7 and C8 or C8 and C9, the first hypothesis leading to a more stable species regarding mesomeric effects. This is confirmed by CID mechanisms. Considering for example the molecule 292-B, the formation of ions at m/z 250 and m/z 119 from MH⁺ is only possible if the new double bond created is located between C7 and C8 (see Figure E6). Based on these considerations, the four ions at m/z 292 that dissociate to provide ions at m/z 250, m/z 243, m/z 219

and m/z 191 were assumed to result from the formation of a double bond between carbon atoms C7 and C8 from the photoproducts with MH^+ ions at m/z 294. The photoproduct 292-E displays a different CID pathway with product ions at m/z 246 and m/z 183, which show that in this case the double bond was created on the alkyl chain. It has been assumed to be formed between C12 and C13 because: *i*) it is thus conjugated with the free doublet of the nitrogen atom, *ii*) this localization allows the C_2H_4 elimination depicted in Figure E7. Localization of the hydroxyl group on C9 permits to explain the same mechanism. This last conclusion allowed assigning the structure of the 294-B as displayed in Figure E8.

Considering the molecular symmetry of maprotiline and the fact that water loss induced by CID does not allow to attribute the exact position of the hydroxyl group, it was not always possible to accurately elucidate the structures of the multi hydroxylated species. However, it is reasonable to assume that the second, third and fourth consequent hydroxylations took place on the aromatic ring or the ethylene bridge of species with molecular ions at m/z 294 and 292.

Six products with MH^+ at m/z 310 resulting from the dihydroxylation of maprotiline were detected between 8.4 and 11.3 minutes. As suggested above, it can be expected that these substances resulted from the hydroxyl addition to the generated monohydroxylated species m/z 294. Table E1 summarizes the common ions observed in CID experiments of different isomers and the main dissociation pathways are shown in Figure E9. In the case of the photoproduct 310-F, CID experiments provided common ions with those resulting from CID of protonated maprotiline: m/z 250 and m/z 191, which show evidence that hydroxylation of this compound occurred on the bridge, i.e., on C9 and C8 (Figure E10). The CID experiments of the photoproduct 310-E provided the ions m/z 280 and 101, allowing to postulate the hydroxyl group addition in the C2 and C5 (Figure E11). As evidenced in Figure E1, this was the most abundant dihydroxylated compound, what can be explained the probability of the second hydroxyl group addition in the most abundant photoproducts, also formed from

the hydroxylation in the C2 (294-E) and C5 (294-D), besides the ortho/para director effect. However, this structure could not be demonstrated due to the lack of product ions. The CID experiments of 310-A, 310-C and 310-D do not permit to elucidate the structure of the isomer. However, the generated ion at m/z 251 from 310-C and 310-D species allowed to confirm that the hydroxylation does not occurred on the bridge, i.e., on C8 and C9, while the ion m/z 201 from 310-D endorsed to ascertain the dihydroxylation in the same aromatic ring (Figure E9). The ion m/z 266 obtained from CID experiments of compound 310-B evidenced the hydroxyl addition to the bridge, i.e., on C9 if considering this species to result from the hydroxyl group addition to the 294-B. The formation of ions m/z 123 and 89 allowed to postulate the hydroxyl group addition on C11, as suggested in Figure E12. However, the formed ions do not allow demonstrating the suggested structure.

Additionally, three compounds with MH^+ at m/z 284 were detected with retention times between 8.0 and 9.5 minutes; they result from ethylene loss and hydroxylation with ring-opening. In the case of 284-A, CID experiments lead to the formation of the fragment at m/z 225 through consecutive losses of methylamine and carbon monoxide. The compound 284-C generated the product ion at m/z 256 from the loss of ethylene bridge and at m/z 225 through the loss of methylamine. The structures were postulated based on these eliminations (Figure E13 and E14) but the lack of other product ions does not allow their conclusive elucidation. The 284-B generated a single ion at m/z 89, allowing to speculate the oxygen addition on C3 and C4 with the loss of the ethylene bridge, as proposed in Figure E15.

A compound with MH^+ at m/z 258 ($C_{16}H_{20}NO_2^+$) elutes at 7.3 min. The fact that no other isobaric species are detected suggests that it does not result from further oxidation of one the aforementioned hydroxylated species. Only two product ions are detected in CID experiments and correspond to subsequent losses of water and carbon monoxide, which is typical of protonated carboxylic

acids. That is why the structure displayed in Figure E16 is that of a carboxylic acid. Opening of an aromatic ring with the formation of a carboxylic acid is quite frequent in photochemistry [234]. Unfortunately, the structure postulated in Figure E16 was not demonstrated due to the lack of product ions in CID experiments; although its high polarity is in agreement with relatively short retention time.

Simulated and real environmental conditions

The environmental fate of the drug was investigated in natural river water by searching for the TPs detected in the photocatalytic simulation, but also for potential new TPs not observed before. For such, a river water sample was spiked with maprotiline ($10 \mu\text{g L}^{-1}$) at a concentration similar to those previously reported in the environment [35]. It should be pointed out that, as detailed in experimental part, the samples were pre-concentrated by freeze-drying before analysis. During degradation experiments, the pH value was measured and compared the initial pH with that measured at the end of the degradation no significant change over time was observed ($\Delta\text{pH} \leq 0.1$).

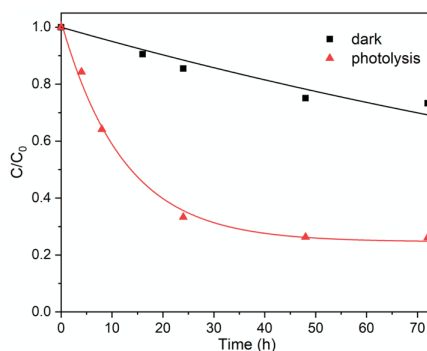


Figure 5.7. Maprotiline ($10 \mu\text{g L}^{-1}$) removal over time in a river water sample, in the dark and under UVA irradiation.

As evidenced in Figure 5.7, experiments performed in the dark showed around 20% of maprotiline removal within 72 h, so implying a limited effect of the biotic components on drug fate. In the dark, the drug degradation leads to

the formation of the byproducts 294-D and 284-C, observed after 24 h and 16 h, respectively, and still present after 72 h, as shown in Figure 5.8a. The monohydroxylated species matches with one of the most abundant TPs observed in ultrapure water, while the species with m/z 284, was previously observed in low abundance.

Under irradiation, the maprotiline degradation kinetic increased following a pseudo first-order decay until 24 h, achieving 65% of drug removal (Figure 5.7), while the appearance of TPs is also favored compared to dark conditions. In detail, 12 out of the 32 TPs previously identified (see Table 5.3) were found in spiked river water and all were still present after 72 h irradiation. All the 5 isomeric forms of the monohydroxylated species (MH^+ at m/z 294) were observed, 294-C, 294-D and 294-E in significantly larger amounts (Figure 5.8). It is interesting to note the slower formation of 294-B, the only isomer resulting from hydroxylation on the bridge and not on an aromatic ring. From the literature, it is possible to realize that besides maprotiline degradation, the species 294-A (2-hydroxymaprotiline) and 294-C (3-hydroxymaprotiline) can reach the environment also from drug metabolism; hydroxylated products represent 4-8% of the dose being excreted in human urine, with 3-hydroxymaprotiline and the corresponding *N*-demethylated specie reported as major human metabolites [227]. Additionally, the study identifies metabolites resulting from hydroxylation on the C8 atom (ethylene bridge) and the corresponding demethylation product, besides the metabolite resulted from the di-hydroxylation in C3 and C4.

The species 292-B, 292-C and 292-D, issued from dehydrogenation of the most abundant 294 isomers, (with the formation of a double bond between atoms C7 and C8) show distinct evolutions over time. 292-C showed its maximum intensity at 4 h and was completely removed within 48 h, 292-D reached its maximum intensity at 48 h and was still present at 72 h, while 292-B appeared after 24 h and decreased until the end of the experiment.

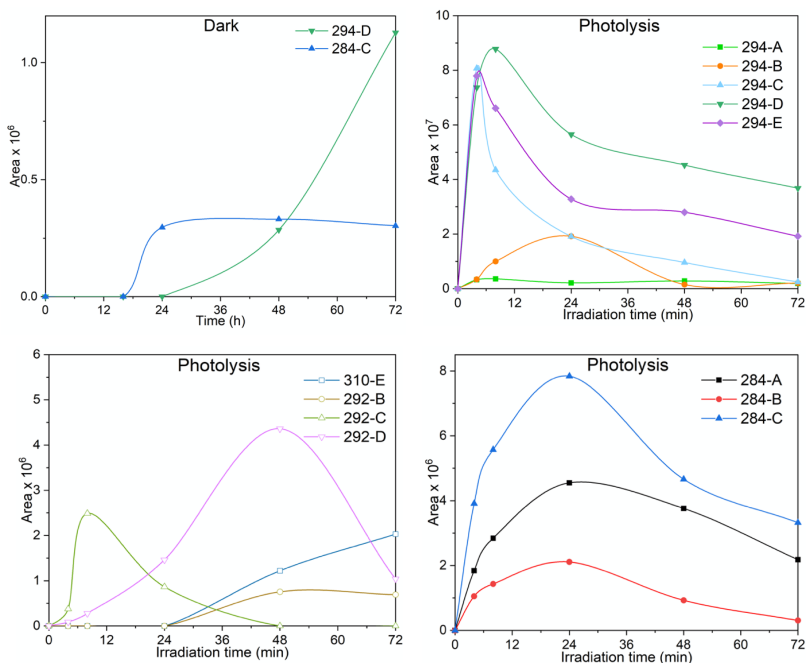


Figure 5.8. Profile over time of maprotiline degradation products observed in a river water sample over time: a) in the dark; b, c and d) under irradiation.

Only one species formed by the addition of more than one hydroxyl group was detected. Resulting from the addition of two hydroxyl groups, the compound 310-E was formed after 24 h irradiation with increasing abundance until the end of the experiment. As stated above, this compound was the most abundant dihydroxylated observed in photocatalytic experiments in ultrapure water and resulted from a second hydroxyl group addition into the most abundant monohydroxylated species (294-D and 294-E).

Additionally, the 3 species at m/z 284 resulting from the ring-opening were also formed with maximum intensity at 24 h, showing a slow degradation profile and still present at the end of the experiment. One could argue that the species MH^+ at m/z 284 resulted from the degradation through ring-opening of the dihydroxylated compounds (MH^+ at m/z 310), particularly the 284-A resulting from the degradation of the compound 310-E. However, as evidenced in Figure 5.8, the species MH^+ at m/z 284 are formed at the early steps of maprotiline.

degradation, while the compound 310-E was observed only after 24h, so implying that ring-opening pathway occurs from maprotiline molecule. Figure 5.9 displays the proposed maprotiline degradation pathways in river water

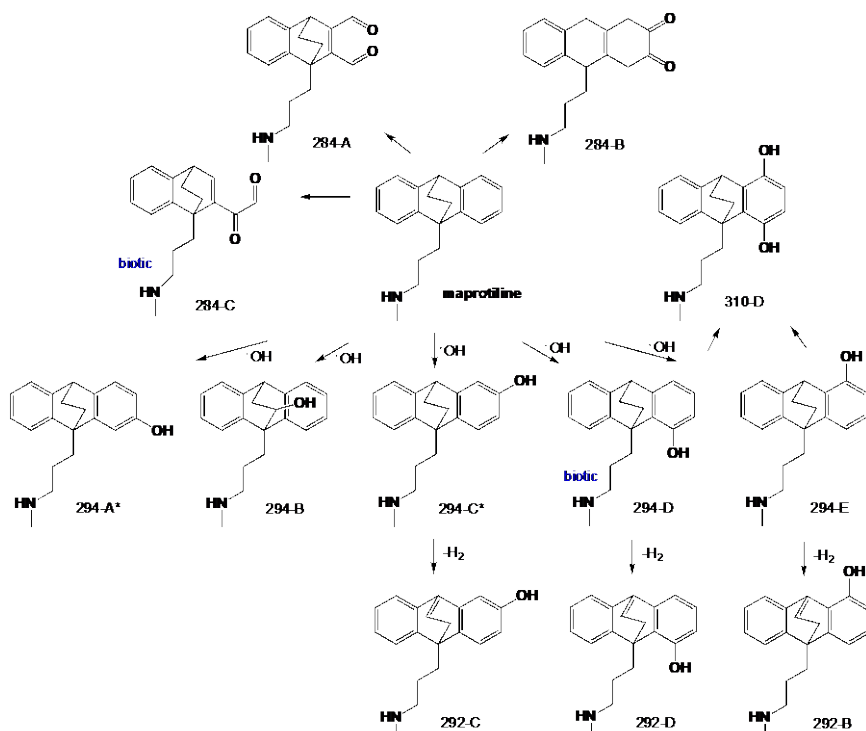


Figure 5.9. Proposed maprotiline degradation pathways in river water in the dark (biotic) and under irradiation (abiotic) *indicated TPs also resulted from human metabolic transformation.

All the TPs observed in river water experiments matched with those previously identified in the photocatalytic experiments performed in ultrapure water, as previously observed for other pollutants [235,236].

Additionally, the faster photodegradation rate observed in river water experiments relative to the degradation in ultrapure water indicated that indirect photolysis played an important role in the drug removal. Faster photodegradation of organic pollutants in wastewater has been reported by other authors [237–239], while nitrate and dissolved organic matter have been

identified as photosensitizers responsible for the generation of reactive species [238,240,241].

Table 5.3. Maprotiline TPs observed in degradation experiments in river water (dark and under irradiation); and retrospective analysis in digitally archived wastewater and river water samples. Results are expressed as percentage of frequency of appearance (FoA). (+) Observed, (N.D.) non detected.

Compounds	Degradation experiments		Retrospective analysis	
	Dark	Photolysis	FoA treated waste water (n=58)	FoA river water (n=72)
Maprotiline			65.5	1.4
294-A	N.D.	+	15.5	N.D.
294-B	N.D.	+	6.9	N.D.
294-C	N.D.	+	17.2	N.D.
294-D	+	+	N.D.	N.D.
294-E	N.D.	+	N.D.	N.D.
310-A	N.D.	N.D.	N.D.	N.D.
310-B	N.D.	N.D.	N.D.	N.D.
310-C	N.D.	N.D.	N.D.	N.D.
310-D	N.D.	N.D.	N.D.	N.D.
310-E	N.D.	N.D.	N.D.	N.D.
310-F	N.D.	N.D.	N.D.	N.D.
326-A	N.D.	N.D.	N.D.	N.D.
326-B	N.D.	N.D.	3.4	N.D.
326-C	N.D.	N.D.	5.2	2.8
342-A	N.D.	N.D.	13.8	N.D.
342-B	N.D.	N.D.	5.2	N.D.
342-C	N.D.	N.D.	12.1	N.D.
342-D	N.D.	N.D.	N.D.	N.D.
292-A	N.D.	N.D.	N.D.	N.D.
292-B	N.D.	+	1.7	N.D.
292-C	N.D.	+	1.7	N.D.
292-D	N.D.	+	N.D.	N.D.
292-E	N.D.	N.D.	N.D.	N.D.
308-A	N.D.	N.D.	1.7	N.D.
308-B	N.D.	N.D.	56.9	2.8
308-C	N.D.	N.D.	19.0	N.D.
324	N.D.	N.D.	1.7	N.D.
284-A	N.D.	+	N.D.	N.D.
284-B	N.D.	+	N.D.	N.D.
284-C	+	+	1.7	N.D.
234	N.D.	N.D.	1.7	1.4
258	N.D.	N.D.	N.D.	N.D.

The results of the retrospective suspect screening presented in Table 5.3 indicate that the elucidated TPs by laboratory-scale experiments are formed in real waters. 16 TPs were detected in at least one effluent wastewater sample with maprotiline 308-B showing the highest frequency of appearance (FoA 56.9%). This fact creates concerns about the toxicity of the formed chemical mixture in wastewaters. Despite the formation and the detection of numerous TPs in real wastewater, most of the TPs remained undetectable in river water samples. Maprotiline and three TPs (308-B, 326-C, Maprotiline 234) were the only TPs that were scarcely detected in river waters (FoA below 2.8%), which indicates that the substance is further degraded in the environment and the concentration of the substance and its TPs becomes lower than the limit of the detection of the applied sample preparation and instrumental methods.

5.2.3 Conclusions

The degradation of maprotiline in spiked river water led to the formation of twelve TPs, structurally elucidated through LC/HR-MS. The degradation pathways in natural water were proposed for the first time, which results from monohydroxylation in several positional isomers and the corresponding dehydrogenated molecules, besides dihydroxylation and ring-opening. Some of these TPs, 2-hydroxymaprotiline and 3-hydroxymaprotiline matched with described maprotiline metabolites, that can be released in the environment by drug excretion.

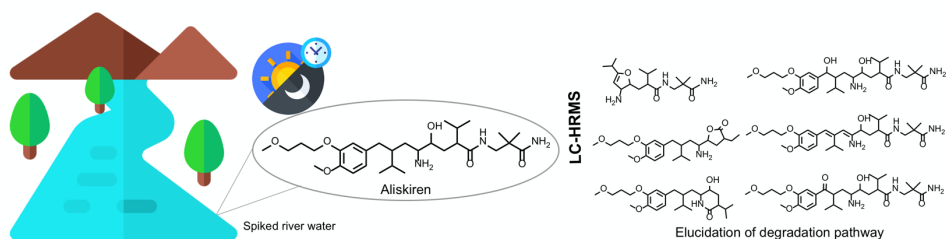
Moreover, photocatalytic experiments led to the formation of a higher number of TPs, mostly resulting from similar chemical transformation in multiple positions.

Additionally, retrospective suspect screening of wastewater effluents and river water samples indicate that the elucidated TPs by laboratory-scale experiments are formed in real waters.

Vibrio fischeri Microtox assay allowed to estimate that maprotiline photocatalytic degradation leads to the formation of slightly more toxic TPs than the parent compound. Therefore, future research should focus on evaluating the toxicity of the formed TPs in wastewater treatment plants.

5.3 Elucidation of Aliskiren Degradation Pathways

Adapted from:



Elucidation of the photoinduced transformations of Aliskiren in river water using liquid chromatography high-resolution mass spectrometry

Nuno P.F. Gonçalves, Lucia Iezzi, Masho H. Belay, Valeria Dulio, Nikiforos Alygizakis, Federica Dal Bello, Claudio Medana, Paola Calza

Science of the Total Environment (*submitted*)

My direct contribution

I declare that I have performed all the degradation experiments and elucidation of the aliskiren degradation pathways described in this sub-chapter. The chemical selection approach and the retrospective analysis was performed by Valeria Dulio and Nikiforos Alygizakis, respectively. LC-HRMS analysis were performed in the group of Claudio Medana, University of Turin.

5.3.1 Motivation

Among pharmaceuticals, antihypertensive drugs are pointed as one of the most frequently detected drug classes in the environment [242,243], representing 12% of total therapeutics [244]. Aliskiren is a direct renin inhibitor used in the treatment of hypertension [245], widely used since 2009 as a monotherapy or as the principal component of as many as 8 aliskiren-based drug combinations [245,246], with a daily prescription of 150 - 300 mg, and it is mainly eliminated in unmetabolized form ($79.8 \pm 3.0\%$) [247]. As a result, aliskiren is one of those CECs continuously released in water that has been detected in the aquatic environments [248].

Once entered the aquatic environment, pollutants may undergo several transformations such as hydrolysis, microbial degradation, interactions with dissolved organic matter, and sunlight photodegradation. Thus, it is important to study the pollutants environmental fate and the formation of their transformation products and ecotoxicological properties. Photodegradation reactions in surface waters comprise direct and indirect photolysis. Direct photolysis involves sunlight absorption by the pollutant with its transformation, while during indirect photolysis photoactive compounds absorbed sunlight. In the last, dissolved organic matter (DOM), nitrite and nitrate can generate reactive species, such as the hydroxyl radical ($\cdot\text{OH}$), singlet oxygen ($^1\text{O}_2$) and DOM triplet states (^3DOM), which can react with pollutants [21,22].

The aliskiren photoinduced transformation of aliskiren in aqueous environment was investigated for the first time by identifying its transformation products *via* LC-HRMS. River water spiked with aliskiren at ppb level was exposed to simulated sunlight simulator for assessing sunlight-induced photolysis. The contribution of direct and indirect photolysis was then unraveled by exposing aliskiren to irradiation in ultrapure water or in the presence of humic acid substances and nitrate.

5.3.2 Results and Discussion

The photoinduced degradation of aliskiren was investigated by exposing ultrapure or river water spiked solutions ($5\mu\text{g L}^{-1}$) to simulated sunlight in order to establish the occurrence of direct and indirect photolysis. Figure 5.10a shows that a faster removal occurred in ultrapure water rather than in river water sample, indicating that direct photolysis played an important role in the drug degradation. In particular, aliskiren exhibited a half-life of 24h in river water, five times lower than in ultrapure water (half-life = 5h) [249]. The decrease rate observed in river water may be due to a scavenging effect played by one or more components of river water, thus hindering the light absorption or quenching the reactive species [241].

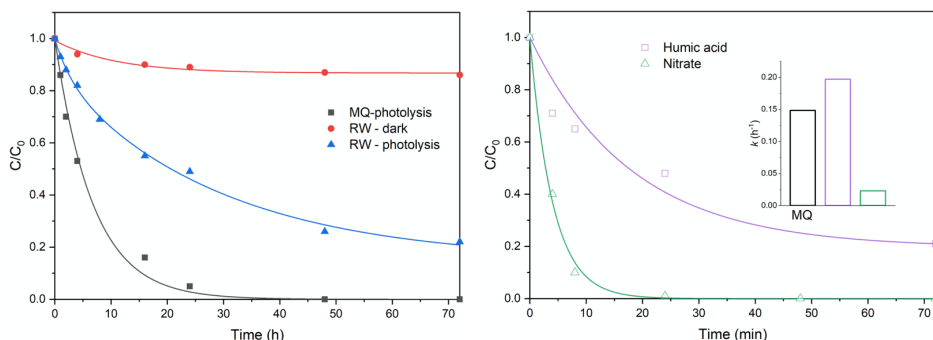
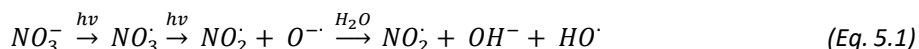


Figure 5.10. Degradation of aliskiren, a) in ultrapure water (black line) and river water (blue line) under irradiation and in the absence of light (red line); b) in the presence of humic acid and nitrate. Inset: first-order kinetic constants.

It is well-known that dissolved organic matter (DOM) and nitrate act as the main photosensitizer responsible for the formation of reactive species mediating the indirect photolysis [236,241,250,251]. For such, we investigated their influence on the photodegradation of aliskiren by performing experiments in Milli-Q water in the presence of nitrate or humic acids. The effect of nitrate on the degradation was established by adding 2 mg L^{-1} to ultrapure water, a concentration in the range of those reported for the river water sample under investigation ($1.8 - 10\text{ mg L}^{-1}$) [252] and results are shown in Figure 2b. The enhanced drug removal can be attributed to the production of $\cdot\text{OH}$ radicals.

Hydroxyl radicals can in fact be formed by the absorption of radiation below 350 nm from nitrate in water [251], accordingly to the following equation:



Similarly, the role of DOM was investigated by adding humic acids (2 mg L⁻¹) to ultrapure water, in the concentration similar to the observed for the river water sample (Section 5.1.1) and is reported in Figure 5.10b. DOM addition promotes an inhibitory effect on aliskiren degradation, reasonably due to the combination of a scavenging effect on the radical species produced [253] and by a competition on the available photons [254]. DOM is known to induce a controversial effect on the organics removal that is function of the kind of pollutants. Our results are in agreement with the data reported by Martínez-Zapata *et al.*, [255] that evidenced an inhibitory effect on the triclosan by the light screening effect of humic acids. Similarly, Chiron *et al.*, [256] reported a faster carbamazepine degradation in Milli-Q water in the presence of nitrate coupled with a slower removal rate in artificial river water with the same nitrate concentration. This effect was attributed to the scavenging effect of *OH species by the DOM. However, the presence of DOM may also promote the pollutant abatement as observed by Wang *et al.* [237]. In wastewater, HA enhanced the removal of caffeine, sulfamethoxazole and diuron, but hindered the degradation of carbamazepine, simazine, triclosan and 2,4-D. Conversely, the degradation of aliskiren is negligible under dark conditions.

Elucidation of aliskiren degradation pathways

All samples were analyzed by LC-HRMS in ESI positive mode after a pre-concentration step of the sample (Section 5.1.1) aimed to identify the aliskiren transformation products (TPs). A total of 6 transformation products were identified and are collected in Table 5.4, together with their *m/z* ratios, elemental compositions, retention times and product ions.

Table 5.4. Summary of $[M+H]^+$ ions and main product ions from CID experiments.

Compound	$[M+H]^+$	Empirical Formula	RDB	Δ (ppm)	r.t. (min)	m/z	MS ²			m/z	MS ³		
							Empirical formula	loss	Δ (ppm)		Empirical formula	loss	Δ (ppm)
Aliskiren	552.4015	C ₃₀ H ₅₄ O ₆ N ₃	5.5	0.45	15.3	534.3898	C ₃₀ H ₅₂ O ₅ N ₃	H ₂ O	-1.53	517.3642	C ₃₀ H ₄₉ O ₅ N ₂ (15)	NH ₃	1.18
										500.3369	C ₃₀ H ₄₆ O ₅ N (25)	(NH ₃) ₂	-0.4
										418.2941	C ₂₅ H ₄₀ O ₄ N (100)	C ₅ H ₁₂ ON ₂	-2.49
										401.2696	C ₂₅ H ₃₇ O ₄ (8)	C ₅ H ₁₅ ON ₃	2.42
										436.3033	C ₂₅ H ₄₂ O ₅ N	C ₅ H ₁₂ ON ₂	-2.10
										419.2811	C ₂₅ H ₃₉ O ₅ (100)	NH ₃	-1.88
										418.2970	C ₂₅ H ₄₀ O ₄ N (45)	H ₂ O	-2.07
TP1	340.2601	C ₁₈ H ₃₄ O ₃ N ₃	3.5	0.30	9.3	323.233	C ₁₈ H ₃₁ O ₃ N ₂ (65)	NH ₃	1.95	306.207	C ₁₈ H ₂₈ O ₃ N (100)	(NH ₃) ₂	2.22
TP2	436.3061	C ₂₅ H ₄₂ O ₅ N	5.5	0.18	16.2	419.2795	C ₂₅ H ₃₉ O ₅ (100)	NH ₃	-0.50	401.2692	C ₂₅ H ₃₇ O ₄ (100)	H ₂ O	1.41
										387.2534	C ₂₄ H ₃₅ O ₄ (5)	CH ₃ OH	-0.30
										369.2432	C ₂₄ H ₃₃ O ₃ (9)	CH ₆ O ₂	1.92
										346.2383	C ₂₁ H ₃₂ O ₃ N (60)	C ₄ H ₁₀ O ₂	0.09
										222.1857	C ₁₄ H ₂₄ ON (100)	C ₇ H ₆ O	2.20
TP3					16.7	419.2795	C ₂₅ H ₃₉ O ₅ (100)	NH ₃	-0.50	401.2692	C ₂₅ H ₃₇ O ₄ (100)	H ₂ O	1.41
										387.2534	C ₂₄ H ₃₅ O ₄ (5)	CH ₃ OH	-0.30
										369.2432	C ₂₄ H ₃₃ O ₃ (9)	CH ₆ O ₂	1.92
										346.2383	C ₂₁ H ₃₂ O ₃ N (58)	C ₄ H ₁₀ O ₂	0.09
										222.1857	C ₁₄ H ₂₄ ON (100)	C ₇ H ₆ O	2.20
TP4	548.3701	C ₃₀ H ₅₀ O ₆ N ₃	7.5	0.18	13.5	530.3591	C ₃₀ H ₄₈ O ₅ N ₃ (28)	H ₂ O	-0.61	513.33234	C ₃₀ H ₄₅ O ₅ N ₂ (70)	NH ₃	0.080
										496.30585	C ₃₀ H ₄₄ O ₅ N (100)	H ₃ N ₂	0.20
										414.2644	C ₂₅ H ₃₆ O ₄ N (25)	C ₅ H ₁₂ ON ₂	-0.15

						432.2748	C ₂₅ H ₃₈ O ₅ N (100)	C ₅ H ₁₂ ON ₂	-0.57	414.2644	C ₂₅ H ₃₆ O ₄ N (100)	H ₂ O	-0.15
										400.2486	C ₂₄ H ₃₄ O ₄ N (93)	CH ₄ O	0.96
										360.2176	C ₂₁ H ₃₀ O ₄ N (27)	C ₄ H ₈ O	0.29
						414.2644	C ₂₅ H ₃₆ O ₄ N (18)	C ₅ H ₁₄ O ₂ N ₂	-0.15	382.2382	C ₂₄ H ₃₂ O ₃ N (100)	CH ₄ O	1.44
										342.2070	C ₂₁ H ₂₈ O ₃ N (11)	C ₄ H ₈ O	1.93
										218.1544	C ₁₄ H ₂₀ ON (4)	C ₁₁ H ₁₆ O ₃	2.11
TP5	566.3805	C ₃₀ H ₅₂ O ₇ N ₃	6.5	0.59	13.7	548.3697	C ₃₀ H ₅₀ O ₆ N ₃ (85)	H ₂ O	-0.62	531.3427	C ₃₀ H ₄₇ O ₆ N ₂ (81)	NH ₃	0.289
										514.3162	C ₃₀ H ₄₄ O ₆ N (46)	(NH ₃) ₂	0.3
										432.2746	C ₂₅ H ₃₈ O ₅ N (100)	C ₅ H ₁₂ ON ₂	0.42
										400.2487	C ₂₄ H ₃₄ O ₄ N (3)	C ₆ H ₁₆ O ₂ N ₂	-0.23
										360.2173	C ₂₁ H ₃₀ O ₄ (10)	C ₉ H ₂₀ O ₂ N ₂	-0.04
										236.1650	C ₁₄ H ₂₂ O ₂ N (32)	C ₁₆ H ₂₈ O ₄ N ₂	-0.31
						450.2853	C ₂₅ H ₄₀ O ₆ N (100)	C ₅ H ₁₂ ON ₂	-0.69				
						432.2745	C ₂₅ H ₃₈ O ₅ N (15)	C ₅ H ₁₄ O ₂ N ₂	0.42				
TP6	568.3962	C ₃₀ H ₅₄ O ₇ N ₃	5.5	0.76	14.3	550.3864	C ₃₀ H ₅₂ O ₆ N ₃ (100)	H ₂ O	-1.05	532.3746	C ₃₀ H ₅₀ O ₅ N (100)	H ₂ O	1.27
										516.3323	C ₃₀ H ₄₆ O ₆ N (21)	(NH ₃) ₂	-0.90
										434.2906	C ₂₅ H ₄₀ O ₅ N (72)	C ₅ H ₁₂ ON ₂	-0.20
						452.3009	C ₂₅ H ₄₂ O ₆ N (60)	C ₅ H ₁₂ ON ₂	0.45	434.2906	C ₂₅ H ₄₀ O ₅ N (100)	H ₂ O	-0.20
						434.2906	C ₂₅ H ₄₀ O ₅ N (33)	C ₅ H ₁₄ O ₂ N ₂	-0.20	417.2640	C ₂₅ H ₃₇ O ₅ (26)	NH ₃	-0.29
										399.2534	C ₂₅ H ₃₅ O ₄ (13)	H ₇ O ₂ N	-0.27
										402.2644	C ₂₄ H ₃₆ O ₄ N (17)	CH ₃ OH	1.21
										362.2331	C ₂₁ H ₃₂ O ₄ N (12)	C ₄ H ₈ O	-0.04
										238.1808	C ₁₄ H ₂₄ O ₂ N (17)	C ₉ H ₁₆ O ₃	-0.44

The putative elemental composition of photoproducts was deduced by the means of Xcalibur software [2.1.0sp1.1160], on the basis of mass accuracy (<5 ppm) and RDB (ring double bond) index. We searched for potential transformation products on the basis of possible modifications reported in literature [257], giving known $\Delta m/z$ differences. A customized searching list was built by software implementation. Identification level [ES] following the Shymanski rules [258] was assigned as level 3 for all identified TPs.

The profile over time for the formed TPs in the different experimental conditions are reported in Figure F1. Two TPs were detected in the river water sample kept in the dark (namely the species TP3 and TP5), both showing a delayed formation; this is in line with the marked slowed removal observed in the dark (see Figure 5.10a). Under irradiation, six intermediates were detected in ultrapure water, all showing the maximum intensity at short times, with TP1 only exception. Five TPs were detected in river water, all showing a disappearance slower than in Milli-Q water; in fact, some TPs are still present at the end of the explored time window (72 h). It is also worth pointing out that only one isomer of the photoproduct at m/z 436 was observed in river water (TP3), while two isomers were formed in Milli-Q water, as shown Table 5.5.

Table 5.5. Summary of aliskiren photoproducts observed in ultrapure water (MQ), river water (RW) in the dark and under irradiation, also in the presence of nitrate and humic acid; (+) observed, (N.D.) non detected.

Compound	Degradation conditions				
	MQ	RW - photolysis	RW - dark	Nitrate	Humic acid
TP1	+	+	N.D.	+	+
TP2	+	N.D.	N.D.	+	N.D.
TP3	+	+	+	+	+
TP4	+	+	N.D.	+	+
TP5	+	+	+	+	N.D.
TP6	+	+	N.D.	+	N.D.

As evidenced in Table 5.5, all the detected TPs were also formed in the presence of nitrate, while only 3 of them were observed in the presence of HA. This can be explained by the differences in the drug removal rate but also by the different reactive species involved in the processes. Moreover, as evidenced in Figure F1, the nitrate mediated degradation promoted a maximum intensity of intermediated at initial times, in agreement with the fast drug removal. However longer disappearance of TPs was observed comparing these experiments with the one in ultrapure water. This may be due to the nitrate consumption and the fact that $\cdot\text{OH}$ formation is proportional to the nitrate concentration, as shown in Equation 5.1.

Structural elucidation of aliskiren degradation products

Aiming at photoproducts structural elucidation, the aliskiren fragmentation pathways were firstly investigated by collision-induced dissociation experiments, ascertaining the most likely losses from the protonated molecule. Figure 5.11 shows the suggested aliskiren MH^+ (m/z 552.4015) fragmentation pathways based on MS^2 and MS^3 spectra analysis (see Table 5.4). The drug fragmented into the products ions at m/z 534 and 436 through the loss of water and $\text{C}_5\text{H}_{12}\text{N}_2\text{O}$, respectively. MS^3 spectrum from the precursor ion at m/z 534 produces three ions: the ions with m/z 517 and 500 through the loss of one (or two) NH_3 molecules, and the product ion at m/z 418 from the loss of $\text{C}_5\text{H}_{12}\text{N}_2\text{O}$. MS^3 performed on the ion at m/z 436 fragmented into the ions with m/z 418 and 419 by involving the loss of H_2O and NH_3 , respectively. Both ions fragmented to give m/z 401 upon loss of NH_3 and H_2O . The observed fragmentation pathways is in agreement with the previous for the aliskiren molecule [259].

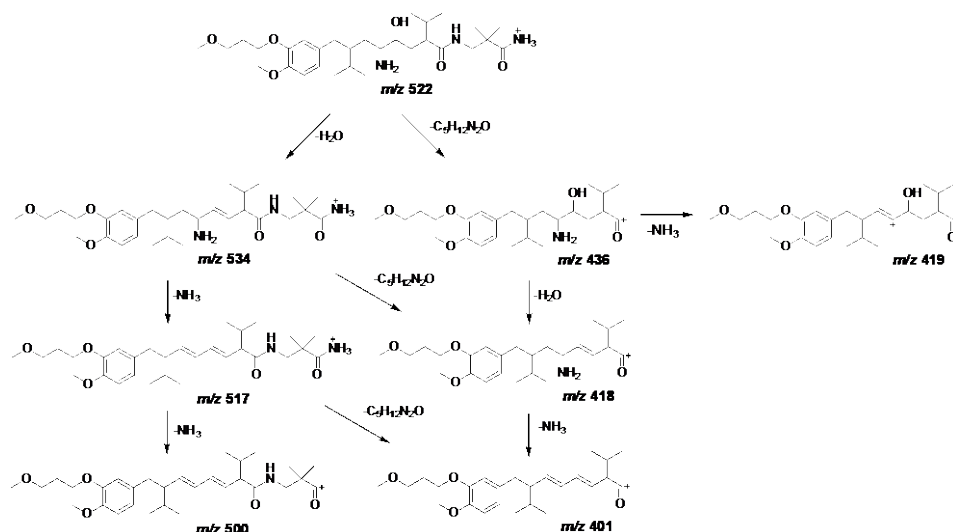


Figure 5.11. Suggested fragmentation pathways for the protonated aliskiren in CID experiments.

A compound with m/z 568.3962 and protonated molecular formula $\text{C}_{30}\text{H}_{54}\text{O}_7\text{N}_3^+$ resulted from the monohydroxylation of the parent molecule and is labelled TP6 (see Figure F2). The precursor ion fragments into m/z 550, 452 and 434 by water loss, loss of $\text{C}_5\text{H}_{12}\text{N}_2\text{O}$ (as observed in parent compound fragmentation) and subsequent H_2O loss, respectively. MS^3 fragmentation performed on ion m/z 434 brings to the formation of the structural diagnostic ion at m/z 238, that allowed to confine the hydroxylation in C11 or into the aromatic ring. However, information is not enough to attribute a unique structure.

TP5 with m/z 566.3805 and protonated molecular formula $\text{C}_{30}\text{H}_{52}\text{O}_7\text{N}_3^+$ resulted from TP6 through the oxidation of an alcoholic group into a carbonyl group. Interestingly, TP5 show the same fragmentation pathways described for TP6. In this case, the product ion at m/z 236 allowed to postulate the oxygen addition in the C11 and to exclude an involvement of the aromatic ring, as shown in the Figure F3. Therefore, it is reasonable to assess that TP6 holds the OH group on the same carbon.

The transformation product TP4 with m/z 548.3701 and empirical formula $C_{30}H_{50}O_6N_3^+$ resulted from TP5 through the removal of a molecule of water. Dehydrogenation could lead to a double bond between C8 and C9 or between C10 and C11, leading in both cases to stable species. However, the presence of the same fragmentation pathways proposed for TP5 (and TP6) allows proposing the formation of a double bond in C10-C11. Again, the formation of the structural diagnostic ion at m/z 218 supports this hypothesis (see Figure S5).

The degradation product TP1 with the accurate protonated mass m/z 340.2601 matched with the empirical formula $C_{18}H_{34}O_3N_3^+$ and its formation involved the breakage of the molecule with the loss of the aromatic ring, the cleavage of carbon atom 10 and 11 (see Figure 5.2) and a further cyclization. As shown in Figure S6, the molecular ion fragmented into the ions at m/z 323 and 306 with the loss one and two molecules of NH_3 . TP1 could result from the photoproduct TP6 with the hydroxyl group addition in the atom C10 (see above).

Additionally, two isomeric forms were found for the ions at m/z 436.3061 matching with the formula $C_{25}H_{42}O_5N^+$ attributed to the cleavage of the amide bond followed by water loss and subsequent cyclization to a lactone for TP2 (Figure F6) or to lactam for TP3 (Figure F7). TP2 protonated structure fragmented to form two main the product ions: the first one at m/z 346 was originated by the loss of H_2O and tetrahydrofuran C_4H_6O and the second m/z 419 from the NH_3 loss. The latter fragmented to m/z 387 by the loss of methanol and subsequently to m/z 369 by water loss. Despite structural differences, the TP3 shown similar fragmentation product ions as shown in Figure F7. These two isomers were previously identified and structurally characterized during stress degradation condition of the drug molecule [259] and were here distinguished based on the compound polarity. Moreover, TP2 was also reported as an aliskiren human metabolite eliminated by urine and feces [247].

Based on the TPs characterized above, we can tentatively propose the degradation pathways displayed in Figure 5.12 as the possible photoinduced transformation occurring in river water.

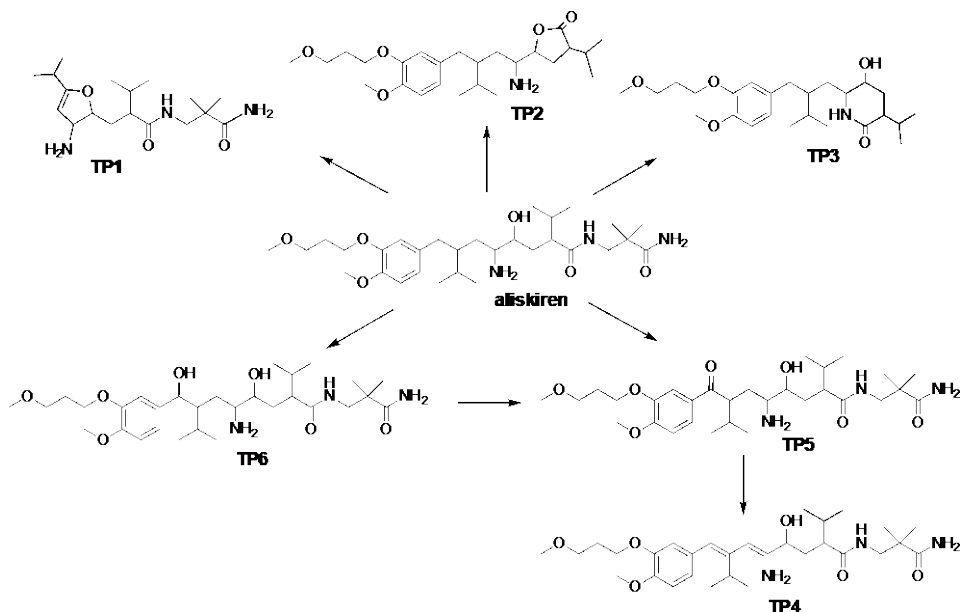


Figure 5.12. Suggested of aliskiren photodegradation pathways.

Retrospective analysis

The results of the screening as regards frequency of appearance (FoA) are presented in Table 5.6. Two out of the screened TPs were detected in the samples, while three TPs (TP2, TP4 and TP5) were not detected in any sample. The highest FoA was observed for wastewater (either influent or effluent). More specifically, aliskiren's highest FoA (43%) was observed in effluent wastewater, TP1's highest FoA (32%) was observed in influent wastewater and TP3's highest FoA (32%) was observed in influent wastewater. Aliskiren was detected only in wastewater (influent and effluent), whereas TP1 and TP3 were also detected in other matrices, what can suggest the drug degradation through the formation of TPs with higher persistence. Both TPs were detected in surface waters (river and seawater), in fresh water sediments and in biota. However, TP3 was detected sporadically at samples other than wastewater, having FoA below 6% for all

investigated matrices. Overall, the TP1 proved to have the most wide-spread occurrence. Therefore, TP1 was detected in surface water (FoA 23%) and in sediments (FoA 19%). None of the compounds were detected in groundwater samples. The detection of TP1 and TP3 in various matrices even at low detection rates, highlights the importance of transformation mechanisms that take place in the environment. These mechanisms may yield TPs of unknown behavior and toxicity.

Table 5.6. Frequency of appearance (FoA; ranged between 0-1) of aliskiren and its TPs in various environmental samples. Substances that were not detected are marked as “N.D.”

Environmental Matrix	Nº of screened samples	Aliskiren	TP1	TP2	TP3	TP4	TP5
Influent wastewater	120	0.22	0.32	N.D.	0.32	N.D.	N.D.
Effluent wastewater	126	0.43	0.06	N.D.	0.22	N.D.	N.D.
River	78	N.D.	0.23	N.D.	0.01	N.D.	N.D.
Seawater	105	N.D.	0.21	N.D.	0.02	N.D.	N.D.
Groundwater	7	N.D.	N.D.	N.D.	N.D.	N.D.	N.D.
Biota coastal	101	N.D.	0.09	N.D.	0.02	N.D.	N.D.
Biota river	71	N.D.	N.D.	N.D.	0.03	N.D.	N.D.
Biota terrestrial	52	N.D.	N.D.	N.D.	N.D.	N.D.	N.D.
Biota marine	62	N.D.	0.02	N.D.	0.07	N.D.	N.D.
Sediment river and marine	32	N.D.	0.19	N.D.	0.09	N.D.	N.D.

5.3.3 Conclusions

The degradation pathways of aliskiren in natural water were elucidated by spiking river water at low concentrations, with formation of 6 photoproducts, structurally elucidated through LC-HRMS. The drug transformation was resulted of monohydroxylation, oxidation and loss of molecule moieties with subsequent transformations.

Additionally, under sunlight simulator it was shown that nitrate at environmental concentrations can promote a faster degradation of aliskiren while humic substances had a negative impact.

Retrospective suspect screening in different samples indicated that the elucidated TPs by laboratory-scale experiments are formed in real waters raising questions about their potential harmful impacts.

Chapter 6 - General Conclusions

The main goals of this PhD project were successfully achieved by the preparation and testing new catalysts for water remediation as well as the elucidation of degradation pathways of CECs.

Initially, Fe₃O₄ magnetic particles coated with humic acid were prepared via co-precipitation method under anoxic conditions to be used as heterogeneous photo-Fenton catalyst. Humic acid proved to considerably enhance the material efficiency to remove 4-chlorophenol through the activation of hydrogen peroxide when in the dark or under simulated sunlight irradiation. The materials characterization evidenced the role of the defective iron species at the surface of the materials for faster degradations through the iron photodissolution but also due to higher surface activity. The best performing material showed also interesting results for the removal of a mixture of CECs in complex wastewater samples under irradiation at pH lower than 4.

Moreover, coating magnetite with humic showed higher efficiency removing bisphenol A in the presence of persulfate under UVA/UVB irradiation, when compared with the pristine material. The catalyst efficiency to activate hydrogen peroxide was substantially compromised at pH above 4, while in the presence of persulfate the system was still active at pH 6. These results together with the

catalyst recovery and reusability suggest promising properties of magnetite when stabilized with humic substances as heterogeneous photo-Fenton catalyst for water remediation.

Additionally, we prepared semiconductors doped with transition metals (Fe and Co) to overcome some disadvantages of pristine ZnO materials when applied as photocatalyst for water remediation. Among the different synthetic methods, hydrothermal allowed the preparation of catalyst more effective removing phenol, explained by a higher degree of crystallinity. When added in proper amounts, iron and cobalt clearly improved the pollutant removal, acting as a trap of the photoinduced charges (e^-/h^+). These materials also showed interesting properties for the removal of CECs in real wastewater sample.

The application of UV-based processes for the removal of persistent pollutants was also explored. Vacuum-UV systems (combined VUV and UVC irradiation) proved to quickly remove the antifungal clotrimazole via direct and indirect photolysis even at environmental concentrations without the addition of chemicals or catalysts. Analyzing the toxicity of aqueous clotrimazole before and after UV exposure a significant decrease in toxicity was observed explained by the formation of photoproducts less toxic than the parent compound. The continuous progress on green energy and the technological development on more energy efficient UV lamps can establish these processes as an attractive solution for water disinfection and micropollutants removal considering that does not require the addition of chemicals.

Finally, the aqueous degradation pathways of two CECs, maprotiline and aliskiren was elucidated for the first time. These substances were initially selected as compounds of particular interest due to the lack of information about their environmental fate and their potential harmful impacts on the environment. For this, river water samples were spiked at low concentration ($\mu\text{g/L}$) and exposed to laboratory degradation conditions. Maprotiline led to the formation of 12 photoproducts, structurally elucidated through LC-HRMS,

resulting from the hydroxylation in different positions and the corresponding dehydrogenated molecules, followed by further transformations. While aliskiren led to the formation of 6 photoproducts resulted from the drug of monohydroxylation, oxidation and loss of molecule moieties with subsequent transformations. The degradation pathways from both drugs were also proposed. Additionally, retrospective suspect screening of environmental matrices confirmed that the identified transformation products by laboratory-scale experiments are formed in real environmental waters. Therefore, future research should focus on evaluating the toxicity of the formed TPs.

In the light of an overall balance and future perspectives, it seems clear that the reduction of the emissions of CECs into the environment should be achieved through the introduction of proactive measures and the improvement of the WWTPs efficiency. The distinct nature of the CECs (functional groups, polarity, concentration, etc.) and the complexity of water matrices (varies from site to site) make their removal in the WWTPs a complex challenge. Treatment update requires the introduction of tertiary treatment with appropriate abatement technologies able to remove pollutants to the defined level of the effluent water quality. Advanced oxidation processes here explored, such as photo-Fenton, photocatalysis or UV based processes can be appropriate in specific circumstances as a single treatment or combined with adsorption and/or filtration. For examples, AOPs can be applied as post-treatment to the pollutants concentrate after the filtration processes. However, the pollutants nature and content, water properties and site-specific limitations require a previous analysis of the efficiency, economic feasibility and cost to determine the most suitable solutions for the advanced treatment of a particular wastewater. Moreover, a strong synergic between the policymakers and the scientific community, valuing the continuous progress in the analytical tools, toxicity assays and advanced treatments, is essential to minimize this global threat.

References

- [1] World Water Development Report | United Nations Educational, Scientific and Cultural Organization, (2020).
- [2] Naciones Unidas, United Nations Secretary-General's Plan: Water Action Decade 2018-2028, (2018) 25.
- [3] 21 551 chemicals on EU market now registered - All news - ECHA.
- [4] UNESCO World Water Assessment Programme, Paris, 2019.
- [5] NORMAN Databases.
- [6] T. Nawaz, S. Sengupta, Contaminants of Emerging Concern: Occurrence, Fate, and Remediation, Elsevier Inc., 2018.
- [7] J. Hollender, B. van Bavel, V. Dulio, E. Farmen, K. Furtmann, J. Koschorreck, U. Kunkel, M. Krauss, J. Munthe, M. Schlabach, J. Slobodnik, G. Stroomberg, T. Ternes, N.S. Thomaidis, A. Togola, V. Tornero, High resolution mass spectrometry-based non-target screening can support regulatory environmental monitoring and chemicals management, *Environ. Sci. Eur.* 31 (2019).
- [8] W. Brack, S. Ait-Aissa, R. Altenburger, I. Cousins, V. Dulio, B. Escher, A. Focks, A. Ginebreda, D. Hering, K. Hilscherová, J. Hollender, H. Hollert, A. Kortenkamp, M.L. de Alda, L. Posthuma, E. Schymanski, H. Segner, J. Slobodnik, Let us empower the WFD to prevent risks of chemical pollution in European rivers and lakes, *Environ. Sci. Eur.* 31 (2019) 10–12.
- [9] S. Sauvé, M. Desrosiers, A review of what is an emerging contaminant, *Chem. Cent. J.* 8 (2014) 1–7.
- [10] W.W.P. Lai, Y.C. Lin, H.H. Tung, S.L. Lo, A.Y.C. Lin, Occurrence of pharmaceuticals and perfluorinated compounds and evaluation of the availability of reclaimed water in Kinmen, *Emerg. Contam.* 2 (2016) 135–144.
- [11] M. Patel, R. Kumar, K. Kishor, T. Mlsna, C.U. Pittman, D. Mohan, Pharmaceuticals of emerging concern in aquatic systems: Chemistry, occurrence, effects, and removal methods, *Chem. Rev.* 119 (2019) 3510–3673.
- [12] N.A. Alygizakis, H. Besselink, G.K. Paulus, P. Oswald, L.M. Hornstra, M. Oswaldova, G. Medema, N.S. Thomaidis, P.A. Behnisch, J. Slobodnik, Characterization of wastewater effluents in the Danube River Basin with chemical screening, in vitro bioassays and antibiotic resistant genes analysis, *Environ. Int.* 127 (2019) 420–429.
- [13] K.M. Blum, S.H. Norström, O. Golovko, R. Grabic, J.D. Järhult, O. Koba, H. Söderström Lindström, Removal of 30 active pharmaceutical ingredients in surface water under long-term artificial UV irradiation, *Chemosphere.* 176 (2017) 175–182.

- [14] Q. Bu, X. Shi, G. Yu, J. Huang, B. Wang, Assessing the persistence of pharmaceuticals in the aquatic environment: Challenges and needs, *Emerg. Contam.* 2 (2016) 145–147.
- [15] T. von der Beek, F.A. Weber, A. Bergmann, S. Hickmann, I. Ebert, A. Hein, A. Küster, Pharmaceuticals in the environment-Global occurrences and perspectives, *Environ. Toxicol. Chem.* 35 (2016) 823–835.
- [16] A.J. Ebele, M. Abou-Elwafa Abdallah, S. Harrad, Pharmaceuticals and personal care products (PPCPs) in the freshwater aquatic environment, *Emerg. Contam.* 3 (2017) 1–16.
- [17] G. Vandermeersch, H.M. Lourenço, D. Alvarez-Muñoz, S. Cunha, J. Diogène, G. Cano-Sancho, J.J. Sloth, C. Kwadijk, D. Barcelo, W. Allegaert, K. Bekaert, J.O. Fernandes, A. Marques, J. Robbins, Environmental contaminants of emerging concern in seafood - European database on contaminant levels, *Environ. Res.* 143 (2015) 29–45.
- [18] A. Küster, N. Adler, Pharmaceuticals in the environment: Scientific evidence of risks and its regulation, *Philos. Trans. R. Soc. B Biol. Sci.* 369 (2014).
- [19] D.S. Maycock, C.D. Watts, Pharmaceuticals in Drinking Water, *Environ. Heal.* (2011) 472–484.
- [20] S. Zhou, C. Di Paolo, X. Wu, Y. Shao, T.B. Seiler, H. Hollert, Optimization of screening-level risk assessment and priority selection of emerging pollutants – The case of pharmaceuticals in European surface waters, *Environ. Int.* 128 (2019) 1–10.
- [21] S.M. Berg, Q.T. Whiting, J.A. Herli, R. Winkels, K.H. Wammer, C.K. Remucal, The Role of Dissolved Organic Matter Composition in Determining Photochemical Reactivity at the Molecular Level, *Environ. Sci. Technol.* 53 (2019) 11725–11734.
- [22] M. Bodrato, D. Vione, APEX (Aqueous Photochemistry of Environmentally occurring Xenobiotics): A free software tool to predict the kinetics of photochemical processes in surface waters, *Environ. Sci. Process. Impacts.* 16 (2014) 732–740.
- [23] N. Creusot, C. Casado-Martinez, A. Chiaia-Hernandez, K. Kiefer, B.J.D. Ferrari, Q. Fu, N. Munz, C. Stamm, A. Tlili, J. Hollender, Retrospective screening of high-resolution mass spectrometry archived digital samples can improve environmental risk assessment of emerging contaminants: A case study on antifungal azoles, *Environ. Int.* 139 (2020) 105708.
- [24] J. Bhagat, N. Singh, N. Nishimura, Y. Shimada, A comprehensive review on environmental toxicity of azole compounds to fish, *Chemosphere.* 262 (2021) 128335.
- [25] Y. Zhong, Z.F. Chen, S.S. Liu, X. Dai, X. Zhu, G. Zheng, S. Liu, G. Liu, Z. Cai, Analysis of azole fungicides in fish muscle tissues: Multi-factor optimization and application to environmental samples, *J. Hazard. Mater.* 324 (2017) 535–543.

- [26] V. Burkina, G. Zamaratskaia, R. Oliveira, G. Fedorova, K. Grabicova, H. Schmidt-Posthaus, C. Steinbach, I. Domingues, O. Golovko, S. Sakalli, R. Grabic, T. Randak, V. Zlabek, Sub-lethal effects and bioconcentration of the human pharmaceutical clotrimazole in rainbow trout (*Oncorhynchus mykiss*), *Chemosphere*. 159 (2016) 10–22.
- [27] J. Stadnicka-Michalak, K. Schirmer, R. Ashauer, Toxicology across scales: Cell population growth in vitro predicts reduced fish growth, *Sci. Adv.* 1 (2015) 1–9.
- [28] P. Matthiessen, L. Weltje, A review of the effects of azole compounds in fish and their possible involvement in masculinization of wild fish populations, *Crit. Rev. Toxicol.* 45 (2015) 453–467.
- [29] Z.F. Chen, G.G. Ying, Occurrence, fate and ecological risk of five typical azole fungicides as therapeutic and personal care products in the environment: A review, *Environ. Int.* 84 (2015) 142–153.
- [30] G.D. de Alkimin, J. Santos, A.M.V.M. Soares, B. Nunes, Ecotoxicological effects of the azole antifungal agent clotrimazole on the macrophyte species *Lemna minor* and *Lemna gibba*, *Comp. Biochem. Physiol. Part - C Toxicol. Pharmacol.* 237 (2020).
- [31] M.J. Bromley, G. Van Muijlwijk, M.G. Fraczek, G. Robson, P.E. Verweij, D.W. Denning, P. Bowyer, Occurrence of azole-resistant species of *Aspergillus* in the UK environment, *J. Glob. Antimicrob. Resist.* 2 (2014) 276–279.
- [32] M. Sanguinetti, B. Posteraro, B. Fiori, S. Ranno, R. Torelli, G. Fadda, Mechanisms of azole resistance in clinical isolates of *Candida glabrata* collected during a hospital survey of antifungal resistance, *Antimicrob. Agents Chemother.* 49 (2005) 668–679.
- [33] P. Sehonova, Z. Svobodova, P. Dolezelova, P. Vosmerova, C. Faggio, Effects of waterborne antidepressants on non-target animals living in the aquatic environment : A review, *Sci. Total Environ.* 631–632 (2018) 789–794.
- [34] J.M. Martin, M. Saaristo, H. Tan, M.G. Bertram, V. Nagarajan-Radha, D.K. Dowling, B.B.M. Wong, Field-realistic antidepressant exposure disrupts group foraging dynamics in mosquitofish, *Biol. Lett.* 15 (2019) 20190615.
- [35] UNESCO and HELCOM, Pharmaceuticals in the aquatic environment of the Baltic Sea region – A status report. UNESCO Emerging Pollutants in Water Series – No. 1, UNESCO Publishing, Paris, 2017.
- [36] A. Zenker, M.R. Cicero, F. Prestinaci, P. Bottoni, M. Carere, Bioaccumulation and biomagnification potential of pharmaceuticals with a focus to the aquatic environment, *J. Environ. Manage.* 133 (2014) 378–387.
- [37] N. Ellepola, T. Ogas, D.N. Turner, R. Gurung, S. Maldonado-Torres, R. Tello-Aburto, P.L. Patidar, S. Rogelj, M.E. Piyasena, G. Rubasinghege, A toxicological study on photo-degradation products of environmental

- ibuprofen: Ecological and human health implications, *Ecotoxicol. Environ. Saf.* 188 (2020) 109892.
- [38] A.B.A. Boxall, C.J. Sinclair, K. Fenner, D. Kolpin, S.J. Maund, When Synthetic Chemicals Degrade in the Environment, *Environ. Sci. Technol.* 70 (2004) 368–375.
- [39] R.I.L. Eggen, J. Hollender, A. Joss, M. Schärer, C. Stamm, Reducing the discharge of micropollutants in the aquatic environment: The benefits of upgrading wastewater treatment plants, *Environ. Sci. Technol.* 48 (2014) 7683–7689.
- [40] M. Bourgin, B. Beck, M. Boehler, E. Borowska, J. Fleiner, E. Salhi, R. Teichler, U. von Gunten, H. Siegrist, C.S. McArdell, Evaluation of a full-scale wastewater treatment plant upgraded with ozonation and biological post-treatments: Abatement of micropollutants, formation of transformation products and oxidation by-products, *Water Res.* 129 (2018) 486–498.
- [41] Introduction to the EU Water Framework Directive - Environment - European Commission.
- [42] EU, Directive 2000/60/EC, *Off. J. Eur. Communities. L* (2000) 1–73.
- [43] Directive 2008/105/EC.
- [44] Directive (EU) 2020/2184.
- [45] Y. Deng, R. Zhao, Advanced Oxidation Processes (AOPs) in Wastewater Treatment, *Curr. Pollut. Reports.* 1 (2015) 167–176.
- [46] M. Salimi, A. Esrafil, M. Gholami, A. Jonidi Jafari, R. Rezaei Kalantary, M. Farzadkia, M. Kermani, H.R. Sobhi, Contaminants of emerging concern: a review of new approach in AOP technologies, *Environ. Monit. Assess.* 189 (2017) 414–436.
- [47] H. Lu, J. Wang, F. Li, X. Huang, B. Tian, H. Hao, Highly efficient and reusable montmorillonite/Fe₃O₄/humic acid nanocomposites for simultaneous removal of Cr(VI) and aniline, *Nanomaterials.* 8 (2018) 537–552.
- [48] Z. Chen, H. Yi, M. Cheng, M. Zhang, G. Zeng, X. Liu, L. Chen, L. Li, L. Qin, B. Li, C. Lai, D. Huang, Fabrication of CuS/BiVO₄ (0 4 0) binary heterojunction photocatalysts with enhanced photocatalytic activity for Ciprofloxacin degradation and mechanism insight, *Chem. Eng. J.* 358 (2018) 891–902.
- [49] S. Wacławek, H. V. Lutze, K. Grübel, V.V.T. Padil, M. Černík, D.D. Dionysiou, Chemistry of persulfates in water and wastewater treatment: A review, *Chem. Eng. J.* 330 (2017) 44–62.
- [50] M.C. Pereira, L.C.A. Oliveira, Iron oxide catalysts: Fenton and Fenton-like reactions - a review, *Clay Miner.* 47 (2012) 285–302.
- [51] S. Enami, Y. Sakamoto, A.J. Colussi, Fenton chemistry at aqueous interfaces, *Proc. Natl. Acad. Sci.* 111 (2014) 623–628.
- [52] W. Huang, M. Luo, C. Wei, Y. Wang, K. Hanna, G. Mailhot, Enhanced heterogeneous photo-Fenton process modified by magnetite and EDDS: BPA degradation, *Environ. Sci. Pollut. Res.* 24 (2017) 10421–10429.

- [53] C. Minero, M. Lucchiari, V. Maurino, D. Vione, A quantitative assessment of the production of OH and additional oxidants in the dark Fenton reaction: Fenton degradation of aromatic amines, *RSC Adv.* 3 (2013) 26443–26450.
- [54] H. Bataineh, O. Pestovsky, A. Bakac, PH-Induced mechanistic changeover from hydroxyl radicals to iron(IV) in the Fenton reaction, *Chem. Sci.* 3 (2012) 1594–1599.
- [55] S.H. Bossmann, E. Oliveros, S. Göb, S. Siegwart, E.P. Dahlen, L. Payawan, M. Straub, M. Wörner, A.M. Braun, New evidence against hydroxyl radicals as reactive intermediates in the thermal and photochemically enhanced Fenton reactions, *J. Phys. Chem. A.* 102 (2002) 5542–5550.
- [56] W. Huang, M. Brigante, F. Wu, C. Mousty, K. Hanna, G. Mailhot, Assessment of the Fe(III)-EDDS complex in Fenton-like processes: From the radical formation to the degradation of bisphenol A, *Environ. Sci. Technol.* 47 (2013) 1952–1959.
- [57] Y. Wu, M. Passananti, M. Brigante, W. Dong, G. Mailhot, Fe(III)–EDDS complex in Fenton and photo-Fenton processes: from the radical formation to the degradation of a target compound, *Environ. Sci. Pollut. Res.* (2014) 12154–12162.
- [58] A.D. Bokare, W. Choi, Review of iron-free Fenton-like systems for activating H₂O₂ in advanced oxidation processes, *J. Hazard. Mater.* 275 (2014) 121–135.
- [59] F. Fu, D.D. Dionysiou, H. Liu, The use of zero-valent iron for groundwater remediation and wastewater treatment: A review, *J. Hazard. Mater.* 267 (2014) 194–205.
- [60] P. Avetta, A. Pensato, M. Minella, M. Malandrino, V. Maurino, C. Minero, K. Hanna, D. Vione, Activation of persulfate by irradiated magnetite: Implications for the degradation of phenol under heterogeneous photo-fenton-like conditions, *Environ. Sci. Technol.* 49 (2015) 1043–1050.
- [61] M. Minella, N. De Bellis, A. Gallo, M. Giagnorio, C. Minero, S. Bertinetti, R. Sethi, A. Tiraferri, D. Vione, Coupling of nanofiltration and thermal Fenton reaction for the abatement of carbamazepine in wastewater, *ACS Omega.* 3 (2018) 9407–9418.
- [62] C. Walling, Fenton's Reagent Revisited, *Acc. Chem. Res.* 8 (1975) 125–131.
- [63] G. Ruppert, R. Bauer, G. Heisler, The photo-Fenton reaction - an effective photochemical wastewater treatment process, *J. Photochem. Photobiol. A Chem.* 73 (1993) 75–78.
- [64] A. Mirzaei, Z. Chen, F. Haghghat, L. Yerushalmi, Removal of pharmaceuticals from water by homo/heterogeneous Fenton-type processes – A review, *Chemosphere.* 174 (2017) 665–688.
- [65] M. Minella, G. Marchetti, E. De Laurentiis, M. Malandrino, V. Maurino, C. Minero, D. Vione, K. Hanna, Photo-Fenton oxidation of phenol with magnetite as iron source, *Appl. Catal. B Environ.* 154–155 (2014) 102–

109.

- [66] L. Demarchis, M. Minella, R. Nisticò, V. Maurino, C. Minero, D. Vione, Photo-Fenton reaction in the presence of morphologically controlled hematite as iron source, *J. Photochem. Photobiol. A Chem.* 307–308 (2015) 99–107.
- [67] M. Munoz, Z.M. de Pedro, J.A. Casas, J.J. Rodriguez, Preparation of magnetite-based catalysts and their application in heterogeneous Fenton oxidation - A review, *Appl. Catal. B Environ.* 176–177 (2015) 249–265.
- [68] D. Palma, A.B. Prevot, M. Brigante, D. Fabbri, G. Magnacca, C. Richard, G. Mailhot, R. Nisticò, New insights on the photodegradation of caffeine in the presence of bio-based substances-magnetic iron oxide hybrid nanomaterials, *Materials (Basel)*. 11 (2018) 1–17.
- [69] R.C.C. Costa, M.F.F. Lelis, L.C.A. Oliveira, J.D. Fabris, J.D. Ardisson, R.R.V.A. Rios, C.N. Silva, R.M. Lago, Novel active heterogeneous Fenton system based on $\text{Fe}_{3-x}\text{M}_x\text{O}_4$ (Fe, Co, Mn, Ni): The role of M^{2+} species on the reactivity towards H_2O_2 reactions, *129* (2006) 171–178.
- [70] W. Wu, Q. He, C. Jiang, Magnetic iron oxide nanoparticles: Synthesis and surface functionalization strategies, *Nanoscale Res. Lett.* 3 (2008) 397–415.
- [71] F. Franzoso, R. Nisticò, F. Cesano, I. Corazzari, F. Turci, D. Scarano, A. Bianco Prevot, G. Magnacca, L. Carlos, D.O. Mártire, Biowaste-derived substances as a tool for obtaining magnet-sensitive materials for environmental applications in wastewater treatments, *Chem. Eng. J.* 310 (2017) 307–316.
- [72] P. Singhal, S.K. Jha, S.P. Pandey, S. Neogy, Rapid extraction of uranium from sea water using Fe_3O_4 and humic acid coated Fe_3O_4 nanoparticles, *J. Hazard. Mater.* 335 (2017) 152–161.
- [73] S. Koesnarpadi, S.J. Santosa, D. Siswanta, B. Rusdiarso, Humic acid coated Fe_3O_4 nanoparticle for phenol sorption, *Indones. J. Chem.* 17 (2017) 274–283.
- [74] J.D. Hu, Y. Zevi, X.M. Kou, J. Xiao, X.J. Wang, Y. Jin, Effect of dissolved organic matter on the stability of magnetite nanoparticles under different pH and ionic strength conditions, *Sci. Total Environ.* 408 (2010) 3477–3489.
- [75] J. Liu, Z. Zhao, G. Jiang, Coating Fe_3O_4 magnetic nanoparticles with humic acid for high efficient removal of heavy metals in water, *Environ. Sci. Technol.* 42 (2008) 6949–6954.
- [76] L. Peng, P. Qin, M. Lei, Q. Zeng, H. Song, J. Yang, J. Shao, B. Liao, J. Gu, Modifying Fe_3O_4 nanoparticles with humic acid for removal of Rhodamine B in water, *J. Hazard. Mater.* 209–210 (2012) 193–198.
- [77] L. Carlos, D.O. Mártire, M.C. Gonzalez, J. Gomis, A. Bernabeu, A.M. Amat, A. Arques, Photochemical fate of a mixture of emerging pollutants in the presence of humic substances, *Water Res.* 46 (2012) 4732–4740.

- [78] S. Koesnarpadi, S.J. Santosa, D. Siswanta, B. Rusdiarso, Synthesis and characterization of magnetite nanoparticle coated humic acid ($\text{Fe}_3\text{O}_4/\text{HA}$), *Procedia Environ. Sci.* 30 (2015) 103–108.
- [79] F. Aparicio, J.P. Escalada, E. De Gerónimo, V.C. Aparicio, F.S.G. Einschlag, G. Magnacca, L. Carlos, D.O. Mártire, Carbamazepine degradation mediated by light in the presence of humic substances-coated magnetite nanoparticles, *Nanomaterials*. 9 (2019) 1–12.
- [80] Y. Nosaka, A.Y. Nosaka, Generation and Detection of Reactive Oxygen Species in Photocatalysis, *Chem. Rev.* 117 (2017) 11302–11336.
- [81] Q. Wang, K. Domen, Particulate Photocatalysts for Light-Driven Water Splitting: Mechanisms, Challenges, and Design Strategies, *Chem. Rev.* 120 (2020) 919–985.
- [82] U. Ulmer, T. Dingle, P.N. Duchesne, R.H. Morris, A. Tavasoli, T. Wood, G.A. Ozin, Fundamentals and applications of photocatalytic CO_2 methanation, *Nat. Commun.* 10 (2019) 1–12.
- [83] M. Bodzek, M. Rajca, Photocatalysis in the treatment and disinfection of water. Part I. Theoretical backgrounds, *Ecol. Chem. Eng. S.* 19 (2012) 489–512.
- [84] M.N. Chong, B. Jin, C.W.K. Chow, C. Saint, Recent developments in photocatalytic water treatment technology: A review, *Water Res.* 44 (2010) 2997–3027.
- [85] P.S. Basavarajappa, S.B. Patil, N. Ganganagappa, K.R. Reddy, A. V. Raghu, C.V. Reddy, Recent progress in metal-doped TiO_2 , non-metal doped/codoped TiO_2 and TiO_2 nanostructured hybrids for enhanced photocatalysis, *Int. J. Hydrogen Energy.* 45 (2020) 7764–7778.
- [86] J.M. Herrmann, Heterogeneous photocatalysis: Fundamentals and applications to the removal of various types of aqueous pollutants, *Catal. Today.* 53 (1999) 115–129.
- [87] A. nan Wang, Y. Teng, X. feng Hu, L. hua Wu, Y. juan Huang, Y. ming Luo, P. Christie, Diphenylarsinic acid contaminated soil remediation by titanium dioxide (P25) photocatalysis: Degradation pathway, optimization of operating parameters and effects of soil properties, *Sci. Total Environ.* 541 (2016) 348–355.
- [88] A. Fujishima, T. Watanabe, K. Hashimoto, K. Ishibashi, Quantum yields of active oxidative species formed on TiO_2 photocatalyst, *J. Photochem. Photobiol. A Chem.* 134 (2000) 139–142.
- [89] M.G. Peleyeju, E.L. Viljoen, WO_3 -based catalysts for photocatalytic and photoelectrocatalytic removal of organic pollutants from water – A review, *J. Water Process Eng.* 40 (2021) 101930.
- [90] C. Byrne, G. Subramanian, S.C. Pillai, Recent advances in photocatalysis for environmental applications, *J. Environ. Chem. Eng.* 6 (2018) 3531–3555.
- [91] S.A. Bin Asif, S.B. Khan, A.M. Asiri, Visible light functioning photocatalyst

- based on Al₂O₃ doped Mn₃O₄ nanomaterial for the degradation of organic toxin, *Nanoscale Res. Lett.* 10 (2015) 355.
- [92] A. Hernández-Ramírez, I. Medina-Ramírez, *Photocatalytic Semiconductors*, Springer International Publishing, Cham, 2015.
- [93] S. Liang, K. Xiao, Y. Mo, X. Huang, A novel ZnO nanoparticle blended polyvinylidene fluoride membrane for anti-irreversible fouling, *J. Memb. Sci.* 394–395 (2012) 184–192.
- [94] Ü. Özgür, Y.I. Alivov, C. Liu, A. Teke, M.A. Reshchikov, S. Doğan, V. Avrutin, S.J. Cho, H. Morkoç, A comprehensive review of ZnO materials and devices, *J. Appl. Phys.* 98 (2005) 1–103.
- [95] A. Janotti, C.G. Van De Walle, Fundamentals of zinc oxide as a semiconductor, *Reports Prog. Phys.* 72 (2009) 126501.
- [96] J. Fenoll, E. Ruiz, P. Hellín, P. Flores, S. Navarro, Heterogeneous photocatalytic oxidation of cyprodinil and fludioxonil in leaching water under solar irradiation, *Chemosphere.* 85 (2011) 1262–1268.
- [97] K. Qi, B. Cheng, J. Yu, W. Ho, Review on the improvement of the photocatalytic and antibacterial activities of ZnO, *J. Alloys Compd.* 727 (2017) 792–820.
- [98] S.G. Kumar, K.S.R.K. Rao, Comparison of modification strategies towards enhanced charge carrier separation and photocatalytic degradation activity of metal oxide semiconductors (TiO₂, WO₃ and ZnO), *Appl. Surf. Sci.* 391 (2017) 124–148.
- [99] C. Di Valentin, G. Pacchioni, Trends in non-metal doping of anatase TiO₂: B, C, N and F, *Catal. Today.* 206 (2013) 12–18.
- [100] M. Pirhashemi, A. Habibi-Yangjeh, S. Rahim Pouran, Review on the criteria anticipated for the fabrication of highly efficient ZnO-based visible-light-driven photocatalysts, *J. Ind. Eng. Chem.* 62 (2018) 1–25.
- [101] M. Fakhrol Ridhwan Samsudin, L. Tau Siang, S. Sufian, R. Bashiri, N. Muti Mohamed, R. Mahirah Ramli, Exploring the role of electron-hole scavengers on optimizing the photocatalytic performance of BiVO₄, *Mater. Today Proc.* 5 (2018) 21703–21709.
- [102] B. Abebe, H.C.A. Murthy, E. Amare, Enhancing the photocatalytic efficiency of ZnO: Defects, heterojunction, and optimization, *Environ. Nanotechnology, Monit. Manag.* 14 (2020) 100336.
- [103] M. Ahmad, E. Ahmed, Y. Zhang, N.R. Khalid, J. Xu, M. Ullah, Z. Hong, Preparation of highly efficient Al-doped ZnO photocatalyst by combustion synthesis, *Curr. Appl. Phys.* 13 (2013) 697–704.
- [104] D. Zhu, T. Hu, Y. Zhao, W. Zang, L. Xing, X. Xue, High-performance self-powered/active humidity sensing of Fe-doped ZnO nanoarray nanogenerator, *Sensors Actuators, B Chem.* 213 (2015) 382–389.
- [105] W. Bousslama, H. Elhouichet, M. Férid, Enhanced photocatalytic activity of Fe doped ZnO nanocrystals under sunlight irradiation, *Optik (Stuttg).* 134 (2017) 88–98.

- [106] M.M. Ba-Abbad, M.S. Takriff, A. Benamor, A.W. Mohammad, Synthesis and characterisation of Co²⁺-incorporated ZnO nanoparticles prepared through a sol-gel method, *Adv. Powder Technol.* 27 (2016) 2439–2447.
- [107] A. Šutka, T. Käämbre, R. Pärna, I. Juhneviča, M. Maiorov, U. Joost, V. Kisand, Co doped ZnO nanowires as visible light photocatalysts, *Solid State Sci.* 56 (2016) 54–62.
- [108] A. Savoyant, H. Alnoor, O. Pilone, O. Nur, M. Willander, Core-defect reduction in ZnO nanorods by cobalt incorporation, *Nanotechnology.* 28 (2018) 1–7.
- [109] K. Jug, V.A. Tikhomirov, Comparative studies of cation doping of ZnO with Mn, Fe, and Co⁺, *J. Phys. Chem. A.* 113 (2009) 11651–11655.
- [110] Y. Il Kim, R. Seshadri, Optical properties of cation-substituted zinc oxide, *Inorg. Chem.* 47 (2008) 8437–8443.
- [111] Y. Kumar, A. Sahai, S.F. Olive-Méndez, N. Goswami, V. Agarwal, Morphological transformations in cobalt doped zinc oxide nanostructures: Effect of doping concentration, *Ceram. Int.* 42 (2016) 5184–5194.
- [112] K. Zoschke, N. Dietrich, H. Börnick, E. Worch, UV-based advanced oxidation processes for the treatment of odour compounds: Efficiency and by-product formation, *Water Res.* 46 (2012) 5365–5373.
- [113] M.B. Ahmed, J.L. Zhou, H.H. Ngo, W. Guo, N.S. Thomaidis, J. Xu, Progress in the biological and chemical treatment technologies for emerging contaminant removal from wastewater: A critical review, *J. Hazard. Mater.* 323 (2017) 274–298.
- [114] M. Bobu, A. Yediler, I. Siminiceanu, F. Zhang, S. Schulte-Hostede, Comparison of different advanced oxidation processes for the degradation of two fluoroquinolone antibiotics in aqueous solutions, *J. Environ. Sci. Heal. - Part A Toxic/Hazardous Subst. Environ. Eng.* 48 (2013) 251–262.
- [115] X. Zhao, J. Jiang, S. Pang, C. Guan, J. Li, Z. Wang, J. Ma, C. Luo, Degradation of iopamidol by three UV-based oxidation processes: Kinetics, pathways, and formation of iodinated disinfection byproducts, *Chemosphere.* 221 (2019) 270–277.
- [116] P. Xie, S. Yue, J. Ding, Y. Wan, X. Li, J. Ma, Z. Wang, Degradation of organic pollutants by Vacuum-Ultraviolet (VUV): Kinetic model and efficiency, *Water Res.* 133 (2018) 69–78.
- [117] K. Zoschke, H. Börnick, E. Worch, Vacuum-UV radiation at 185nm in water treatment - A review, *Water Res.* 52 (2014) 131–145.
- [118] Z. Wu, L. Yang, Y. Tang, Z. Qiang, M. Li, Dimethoate degradation by VUV/UV process: Kinetics, mechanism and economic feasibility, *Chemosphere.* 273 (2021) 129724.
- [119] R.K. Szabó, C.S. Megyeri, E. Illés, K. Gajda-Schranz, P. Mazellier, A. Dombi, Phototransformation of ibuprofen and ketoprofen in aqueous solutions,

- Chemosphere. 84 (2011) 1658–1663.
- [120] M. Bagheri, M. Mohseni, Pilot-scale treatment of 1,4-dioxane contaminated waters using 185 nm radiation: Experimental and CFD modeling, *J. Water Process Eng.* 19 (2017) 185–192.
- [121] T. Oppenlander, Mercury-free Vacuum-(VUV) and UV Excilamps: Lamps of the Future?, *IUVA News.* 7 (2005) 16–20.
- [122] International Union of Pure and Applied Chemistry. Commission on Equilibrium Data., E.P. Serjeant, B. Dempsey, International Union of Pure and Applied Chemistry. Commission on Electrochemical Data., Ionisation constants of organic acids in aqueous solution, Pergamon Press, 1979.
- [123] C.D. Herzfeldt, R. Kümmel, Dissociation constants, solubilities and dissolution rates of some selected nonsteroidal antiinflammatories, *Drug Dev. Ind. Pharm.* 9 (1983) 767–793.
- [124] G. Zeng, C. Zhang, G. Huang, J. Yu, Q. Wang, J. Li, B. Xi, H. Liu, Adsorption behavior of bisphenol A on sediments in Xiangjiang River, Central-south China, *Chemosphere.* 65 (2006) 1490–1499.
- [125] M.D. Alotaibi, B.M. Patterson, A.J. McKinley, A.Y. Reeder, A.J. Furness, Benzotriazole and 5-methylbenzotriazole in recycled water, surface water and dishwashing detergents from Perth, Western Australia: Analytical method development and application, *Environ. Sci. Process. Impacts.* 17 (2015) 448–457.
- [126] O.A.H. Jones, N. Voulvoulis, J.N. Lester, Aquatic environmental assessment of the top 25 English prescription pharmaceuticals, *Water Res.* 36 (2002) 5013–5022.
- [127] A.E. Harvey, J.A. Smart, E.S. Amis, Simultaneous spectrophotometric determination of iron(II) and total iron with 1,10-phenanthroline, *Anal. Chem.* 27 (1955) 26–29.
- [128] G. Magnacca, A. Allera, E. Montoneri, L. Celi, D.E. Benito, L.G. Gagliardi, M.C. Gonzalez, D.O. Mártire, L. Carlos, Novel magnetite nanoparticles coated with waste-sourced biobased substances as sustainable and renewable adsorbing materials, *ACS Sustain. Chem. Eng.* 2 (2014) 1518–1524.
- [129] L. Carlos, M. Cipollone, D.B. Soria, M. Sergio Moreno, P.R. Ogilby, F.S. García Einschlag, D.O. Mártire, The effect of humic acid binding to magnetite nanoparticles on the photogeneration of reactive oxygen species, *Sep. Purif. Technol.* 91 (2012) 23–29.
- [130] JCPDS Card No. 75-033, n.d.
- [131] U. Panne, V.-D. Hodoroba, A. Paul, G. Ababei, R.J. Schneider, M. Neamtu, C. Nadejde, Green Fenton-like magnetic nanocatalysts: Synthesis, characterization and catalytic application, *Appl. Catal. B Environ.* 176–177 (2015) 667–677.
- [132] Y. Fu, Hong-bo; Quan, Xie; Chen, Shuo; Zhao, Hui-min; Zhao, Interactions of HA and hematite FTIR study, *J. Environ. Sci.* 17 (2005) 43–47.

- [133] N.S. McIntyre, D.G. Zetaruk, X-ray photoelectron spectroscopic studies of iron oxides - *Analytical Chemistry*, *Anal. Chem.* 49 (1977) 1521–1529.
- [134] R. Di Corato, A. Aloisi, S. Rella, J.M. Greneche, G. Pugliese, T. Pellegrino, C. Malitesta, R. Rinaldi, Maghemite nanoparticles with enhanced magnetic properties: One-Pot preparation and ultrastable dextran shell, *ACS Appl. Mater. Interfaces*. 10 (2018) 20271–20280.
- [135] T.C. Lin, G. Seshadri, J.A. Kelber, A consistent method for quantitative XPS peak analysis of thin oxide films on clean polycrystalline iron surfaces, *Appl. Surf. Sci.* 119 (1997) 83–92.
- [136] A.P. Grosvenor, B.A. Kobe, M.C. Biesinger, N.S. McIntyre, Investigation of multiplet splitting of Fe 2p XPS spectra and bonding in iron compounds, *Surf. Interface Anal.* 36 (2004) 1564–1574.
- [137] H. Niu, D. Zhang, S. Zhang, X. Zhang, Z. Meng, Y. Cai, Humic acid coated Fe₃O₄ magnetic nanoparticles as highly efficient Fenton-like catalyst for complete mineralization of sulfathiazole, *J. Hazard. Mater.* 190 (2011) 559–565.
- [138] S. Bertinetti, M. Minella, K. Hanna, C. Minero, D. Vione, Degradation of ibuprofen with a Fenton-like process triggered by zero-valent iron (ZVI-Fenton), *Environ. Res.* Submitted (2019).
- [139] S. He, Y. Chen, H. Wang, W. Yang, Y. Gao, Y. Zhao, Degradation of 4-Chlorophenol by means of Fenton oxidation processes: mechanism and kinetics, *Water. Air. Soil Pollut.* 228 (2017) 284–293.
- [140] F. Duan, Y. Yang, Y. Li, H. Cao, Y. Wang, Y. Zhang, Heterogeneous Fenton-like degradation of 4-chlorophenol using iron/ordered mesoporous carbon catalyst, *J. Environ. Sci. (China)*. 26 (2014) 1171–1179.
- [141] N.P.. Gonçalves, M. Minella, G. Mailhot, M. Brigante, A. Bianco Prevot, Photo-activation of persulfate and hydrogen peroxide by humic acid coated magnetic particles for Bisphenol A degradation, *Catal. Today*. 361 (2021) 43–49.
- [142] D. Lgs 152/06,
https://www.gazzettaufficiale.it/atto/serie_generale/caricaDettaglioAtt/originario?atto.dataPubblicazione Gazzetta=2006-04-14&atto.codiceRedazionale=006G0171.
- [143] S. Mandal, Reaction rate constants of hydroxyl radicals with micropollutants and their significance in advanced oxidation processes, *J. Adv. Oxid. Technol.* 21 (2018) 178–195.
- [144] R.E. Huie, C.L. Clifton, P. Neta, Electron transfer reactions rates and equilibria of the carbonate and sulfate radical anions, *Radiat. Phys. Chem.* (1991) 477–481.
- [145] I.A. Ike, K.G. Linden, J.D. Orbell, M. Duke, Critical review of the science and sustainability of persulphate advanced oxidation processes, *Chem. Eng. J.* 338 (2018) 651–669.
- [146] L.W. Matzek, K.E. Carter, Activated persulfate for organic chemical

- degradation: A review, *Chemosphere*. 151 (2016) 178–188.
- [147] A. Jonidi Jafari, B. Kakavandi, N. Jaafarzadeh, R. Rezaei Kalantary, M. Ahmadi, A. Akbar Babaei, Fenton-like catalytic oxidation of tetracycline by AC@Fe₃O₄ as a heterogeneous persulfate activator: Adsorption and degradation studies, *J. Ind. Eng. Chem.* 45 (2017) 323–333.
- [148] Y. Wu, A. Bianco, M. Brigante, W. Dong, P. de Sainte-claire, K. Hanna, G. Mailhot, Sulfate radical photogeneration using Fe-EDDS: influence of critical parameters and naturally occurring scavengers, *Environ. Sci. Technol.* 49 (2015) 14343–14349.
- [149] X. Wang, W. Dong, M. Brigante, G. Mailhot, Hydroxyl and sulfate radicals activated by Fe(III)-EDDS/UV: Comparison of their degradation efficiencies and influence of critical parameters, *Appl. Catal. B, Environ.* 245 (2018) 271–278.
- [150] Y. Yuan, F. Geng, B. Shi, B. Lai, Simultaneous thermal activation of persulfate/Fenton system for high-concentration N,N-Dimethylacetamide degradation: Parameter optimization and degradation mechanism, *Environ. Eng. Sci.* 36 (2018) 12–22.
- [151] N.P.F. Gonçalves, M. Minella, D. Fabbri, P. Calza, C. Malitesta, E. Mazzotta, A. Bianco Prevot, Humic acid coated magnetic particles as highly efficient heterogeneous photo-Fenton materials for wastewater treatments, *Chem. Eng. J.* 390 (2020) 124619.
- [152] D.C. Harris, *Quantitative Chemical Analysis*, W. H. Freeman Ed. (USA), 2010.
- [153] M.I. Litter, M.A. Blesa, Photodissolution of iron oxides. IV. A comparative study on the photodissolution of hematite, magnetite, and maghemite in EDTA media, *Can. J. Chem.* 70 (1992) 2502–2510.
- [154] J. Gomis, M.G. Gonçalves, R.F. Vercher, C. Sabater, M.-A. Castillo, A. Bianco Prevot, A.M. Amat, A. Arques, Determination of photostability, biocompatibility and efficiency as photo-Fenton auxiliaries of three different types of soluble bio-based substances (SBO), *Catal. Today*. 252 (2015) 177–183.
- [155] W. Huang, A. Bianco, M. Brigante, G. Mailhot, UVA-UVB activation of hydrogen peroxide and persulfate for advanced oxidation processes: Efficiency, mechanism and effect of various water constituents. *Journal of Hazardous Materials*, 347, 279–28, *J. Hazard. Mater.* 347 (2018) 279–287.
- [156] G. V. Buxton, C.L. Greenstock, W.P. Helman, A.B. Ross, Critical review of rate constants for reactions of hydrated electrons, hydrogen atoms and hydroxyl radicals ($\cdot\text{OH}/\cdot\text{O}^-$) in aqueous solution, *J. Phys. Chem. Ref. Data*. 17 (1988) 513–886.
- [157] C.L. Clifton, R.E. Huie, Rate constants for hydrogen abstraction reactions of the sulfate radical, $\text{SO}_4^{\cdot-}$. *Alcohols*, *Int. J. Chem. Kinet.* 21 (1989) 677–687.

- [158] J. De Laat, H. Gallard, Catalytic decomposition of hydrogen peroxide by Fe(III) in homogeneous aqueous solution: Mechanism and kinetic modeling, *Environ. Sci. Technol.* 33 (1999) 2726–2732.
- [159] H. Gallard, J. De Laat, Kinetic modelling of Fe(III)/H₂O₂ oxidation reactions in dilute aqueous solution using atrazine as a model organic compound, *Water Res.* 34 (2000) 3107–3116.
- [160] H. Kusic, I. Peternel, S. Ukic, N. Koprivanac, T. Bolanca, S. Papic, A.L. Bozic, Modeling of iron activated persulfate oxidation treating reactive azo dye in water matrix, *Chem. Eng. J.* 172 (2011) 109–121.
- [161] M. Khandarkhaeva, A. Batoeva, M. Sizykh, D. Aseev, N. Garkusheva, Photo-Fenton-like degradation of bisphenol A by persulfate and solar irradiation, *J. Environ. Manage.* 249 (2019) 109348.
- [162] M. Zhang, H. Dong, L. Zhao, D. Wang, D. Meng, A review on Fenton process for organic wastewater treatment based on optimization perspective, *Sci. Total Environ.* 670 (2019) 110–121.
- [163] D. Zhao, X. Liao, X. Yan, S.G. Huling, T. Chai, H. Tao, Effect and mechanism of persulfate activated by different methods for PAHs removal in soil, *J. Hazard. Mater.* 254–255 (2013) 228–235.
- [164] J.J. Pignatello, E. Oliveros, A. MacKay, Advanced oxidation processes for organic contaminant destruction based on the fenton reaction and related chemistry, *Crit. Rev. Environ. Sci. Technol.* 36 (2006) 1–84.
- [165] D. Lgs 3 aprile 2006, n. 152, https://www.gazzettaufficiale.it/atto/stampa/serie_generale/originario, D. Lgs 3 April. 2006, n. 152, https://www.gazzettaufficiale.it/atto/stampa/serie_generale/originario.
- [166] E. Ortega-Gómez, M.M.B. Martín, B.E. García, J.A. Sánchez Pérez, P. Fernández Ibáñez, Solar photo-Fenton for water disinfection: An investigation of the competitive role of model organic matter for oxidative species, *Appl. Catal. B Environ.* 149 (2014) 484–489.
- [167] N. Rioja, S. Zorita, F.J. Peñas, Effect of water matrix on photocatalytic degradation and general kinetic modeling, *Appl. Catal. B Environ.* 180 (2016) 330–335.
- [168] M. Sánchez-Polo, M.M. Abdel daïem, R. Ocampo-Pérez, J. Rivera-Utrilla, A.J. Mota, Comparative study of the photodegradation of bisphenol A by HO, SO₄⁻ and CO₃⁻/HCO₃⁻ radicals in aqueous phase, *Sci. Total Environ.* 463–464 (2013) 423–431.
- [169] H. Liu, J. Yang, Y. Zhang, L. Yang, M. Wei, X. Ding, Structure and magnetic properties of Fe-doped ZnO prepared by the sol-gel method, *J. Phys. Condens. Matter.* 21 (2009) 145803.
- [170] K.C. Christoforidis, A. Iglesias-Juez, S.J.A. Figueroa, M. Di Michiel, M.A. Newton, M. Fernández-García, Structure and activity of iron-doped TiO₂-anatase nanomaterials for gas-phase toluene photo-oxidation, *Catal. Sci.*

- Technol. 3 (2013) 626–634.
- [171] T. Umebayashi, T. Yamaki, H. Itoh, K. Asai, Analysis of electronic structures of 3d transition metal-doped TiO₂ based on band calculations, *J. Phys. Chem. Solids*. 63 (2002) 1909–1920.
- [172] J. Zhang, X. Chen, Y. Shen, Y. Li, Z. Hu, J. Chu, Synthesis, surface morphology, and photoluminescence properties of anatase iron-doped titanium dioxide nano-crystalline films, *Phys. Chem. Chem. Phys.* 13 (2011) 13096–13105.
- [173] J. Zhu, W. Zheng, B. He, J. Zhang, M. Anpo, Characterization of Fe-TiO₂ photocatalysts synthesized by hydrothermal method and their photocatalytic reactivity for photodegradation of XRG dye diluted in water, *J. Mol. Catal. A Chem.* 216 (2004) 35–43.
- [174] C. Adán, A. Bahamonde, M. Fernández-García, A. Martínez-Arias, Structure and activity of nanosized iron-doped anatase TiO₂ catalysts for phenol photocatalytic degradation, *Appl. Catal. B Environ.* 72 (2007) 11–17.
- [175] Priyanka, V.C. Srivastava, Photocatalytic oxidation of dye bearing wastewater by iron doped zinc oxide, *Ind. Eng. Chem. Res.* 52 (2013) 17790–17799.
- [176] T.T.T. Dang, S.T.T. Le, D. Channei, W. Khanitchaidecha, A. Nakaruk, Photodegradation mechanisms of phenol in the photocatalytic process, *Res. Chem. Intermed.* 42 (2016) 5961–5974.
- [177] Z. Guo, R. Ma, G. Li, Degradation of phenol by nanomaterial TiO₂ in wastewater, *Chem. Eng. J.* 119 (2006) 55–59.
- [178] K. Okamoto, Y. Yamamoto, H. Tanaka, M. Tanaka, A. Itaya, Heterogeneous Photocatalytic Decomposition of Phenol over TiO₂ Powder, *Bull. Chem. Soc. Jpn.* 58 (1985) 2015–2022.
- [179] S. Carbonaro, M.N. Sugihara, T.J. Strathmann, Continuous-flow photocatalytic treatment of pharmaceutical micropollutants: Activity, inhibition, and deactivation of TiO₂ photocatalysts in wastewater effluent, *Appl. Catal. B Environ.* 129 (2013) 1–12.
- [180] C. Martínez, S. Vilariño, M.I. Fernández, J. Faria, M.L. Canle, J.A. Santaballa, Mechanism of degradation of ketoprofen by heterogeneous photocatalysis in aqueous solution, *Appl. Catal. B Environ.* 142–143 (2013) 633–646.
- [181] A. Jakimska, M. Śliwka-Kaszyńska, J. Reszczyńska, J. Namieśnik, A. Kot-Wasik, Elucidation of transformation pathway of ketoprofen, ibuprofen, and furosemide in surface water and their occurrence in the aqueous environment using UHPLC-QTOF-MS Euroanalysis XVII, *Anal. Bioanal. Chem.* 406 (2014) 3667–3680.
- [182] P. A.L., The Scherrer Formula for X-Ray Particle Size Determination, *Phys. Rev.* 56 (1939) 978–982.
- [183] Yashpal, V. Sharma, B. V. Manoj Kumar, Issues in determining size of

- nano-crystalline Ceramic Particles by X-ray diffraction, *Mater. Today Proc.* 2 (2015) 3534–3538.
- [184] C.C. Ding, S.Y. Wu, L.N. Wu, Y.Q. Xu, L.J. Zhang, The investigation of the defect structures for Co^{2+} in ZnO microwires, thin films and bulks, *J. Phys. Chem. Solids.* 106 (2017) 94–98.
- [185] O. Raita, A. Popa, D. Toloman, M. Stan, A. Darabont, L. Giurgiu, Co^{2+} Ions in ZnO powders as seen by Magnetic Resonance, *Appl. Magn. Reson.* 40 (2011) 245–250.
- [186] P. Jakes, E. Erdem, Finite size effects in ZnO nanoparticles: An electron paramagnetic resonance (EPR) analysis, *Phys. Status Solidi - Rapid Res. Lett.* 5 (2011) 56–58.
- [187] S.K.S. Parashar, B.S. Murty, S. Repp, S. Weber, E. Erdem, Investigation of intrinsic defects in core-shell structured ZnO nanocrystals, *J. Appl. Phys.* 111 (2012) 1–7.
- [188] E. Cerrato, C. Gionco, M.C. Paganini, E. Giamello, E. Albanese, G. Pacchioni, Origin of Visible Light Photoactivity of the CeO_2/ZnO Heterojunction, *ACS Appl. Energy Mater.* 1 (2018) 4247–4260.
- [189] A. Savoyant, H. Alnoor, O. Pilone, O. Nur, M. Willander, Core-defect reduction in ZnO nanorods by cobalt incorporation, *Nanotechnology.* 28 (2017) 285705.
- [190] H. Liu, B. Shen, M. Xing, J. Zhang, B. Tian, Vacuum-activated Co^{2+} and Ti^{3+} co-modified TiO_2 with stable and enhanced photocatalytic activity, *Res. Chem. Intermed.* 42 (2016) 3459–3471.
- [191] E. Cerrato, C. Gionco, M.C. Paganini, E. Giamello, E. Albanese, G. Pacchioni, Origin of Visible Light Photoactivity of the CeO_2/ZnO Heterojunction, *ACS Appl. Energy Mater.* 1 (2018) 4247–4260.
- [192] A. Savoyant, H. Alnoor, O. Pilone, O. Nur, M. Willander, Core-defect reduction in ZnO nanorods by cobalt incorporation, *Nanotechnology.* 28 (2017) 1–7.
- [193] A. Fujishima, X. Zhang, D.A. Tryk, TiO_2 photocatalysis and related surface phenomena, *Surf. Sci. Rep.* 63 (2008) 515–582.
- [194] M.A. Henderson, A surface science perspective on TiO_2 photocatalysis, *Surf. Sci. Rep.* 66 (2011) 185–297.
- [195] Y. Lu, Y. Lin, D. Wang, L. Wang, T. Xie, T. Jiang, A high performance cobalt-doped ZnO visible light photocatalyst and its photogenerated charge transfer properties, *Nano Res.* 4 (2011) 1144–1152.
- [196] O. Altintas Yildirim, H. Arslan, S. Sönmezoğlu, Facile synthesis of cobalt-doped zinc oxide thin films for highly efficient visible light photocatalysts, *Appl. Surf. Sci.* 390 (2016) 111–121.
- [197] A. Jelic, M. Gros, A. Ginebreda, R. Cespedes-Sánchez, F. Ventura, M. Petrovic, D. Barcelo, Occurrence, partition and removal of pharmaceuticals in sewage water and sludge during wastewater treatment, *Water Res.* 45 (2011) 1165–1176.

- [198] J. Wilkinson, P.S. Hooda, J. Barker, S. Barton, J. Swinden, Occurrence, fate and transformation of emerging contaminants in water: An overarching review of the field, *Environ. Pollut.* 231 (2017) 954–970.
- [199] Z.F. Chen, G.G. Ying, Occurrence, fate and ecological risk of five typical azole fungicides as therapeutic and personal care products in the environment: A review, *Environ. Int.* 84 (2015) 142–153.
- [200] M. Kahle, I.J. Buerge, A. Hauser, M.D. Müller, T. Poiger, Azole fungicides: Occurrence and fate in wastewater and surface waters, *Environ. Sci. Technol.* 42 (2008) 7193–7200.
- [201] P.H. Roberts, K. V. Thomas, The occurrence of selected pharmaceuticals in wastewater effluent and surface waters of the lower Tyne catchment, *Sci. Total Environ.* 356 (2006) 143–153.
- [202] OSPAR, Background Document on Clotrimazole (2013 update) - Hazardous Substances Series, (2013) 49.
- [203] T. Porsbring, H. Blanck, H. Tjellström, T. Backhaus, Toxicity of the pharmaceutical clotrimazole to marine microalgal communities, *Aquat. Toxicol.* 91 (2009) 203–211.
- [204] R.F.P. Nogueira, M.C. Oliveira, W.C. Paterlini, Simple and fast spectrophotometric determination of H₂O₂ in photo-Fenton reactions using metavanadate, *Talanta.* 66 (2005) 86–91.
- [205] ISO 11348-1, Geneva, Switzerland, 2007.
- [206] M. Eldridge, J. Sanseverino, G. de Aragao Umbuzeiro, G. S., Analysis of Environmental Samples with Yeast-Based Bioluminescent Bioreporters, in: *Environ. Monit., InTech*, 2011.
- [207] J. Sanseverino, M.L. Eldridge, A.C. Layton, J.P. Easter, J. Yarbrough, T.W. Schultz, G.S. Sayler, Screening of potentially hormonally active chemicals using bioluminescent yeast bioreporters, *Toxicol. Sci.* 107 (2009) 122–134.
- [208] ISO 8692, Geneva, Switzerland, 2012.
- [209] ISO 6341, Geneva, Switzerland, 2012.
- [210] D. Vione, P. Calza, F. Galli, D. Fabbri, V. Santoro, C. Medana, The role of direct photolysis and indirect photochemistry in the environmental fate of ethylhexyl methoxy cinnamate (EHMC) in surface waters, *Sci. Total Environ.* 537 (2015) 58–68.
- [211] B. Hensen, O. Olsson, K. Kümmerer, The role of irradiation source setups and indirect phototransformation: Kinetic aspects and the formation of transformation products of weakly sunlight-absorbing pesticides, *Sci. Total Environ.* 695 (2019) 133808.
- [212] A. Kryczyk, P. Żmudzki, P. Koczurkiewicz, J. Piotrowska, E. Pękała, U. Hubicka, The impact of ZnO and TiO₂ on the stability of clotrimazole under UVA irradiation: Identification of photocatalytic degradation products and in vitro cytotoxicity assessment, *J. Pharm. Biomed. Anal.* 145 (2017) 283–292.

- [213] S.M. Tawakkol, Y.M. Fayez, N.M. Fahmy, H.M. Lotfy, M.A.A. Shehata, Monitoring of clotrimazole degradation pathway in presence of its co-formulated drug, *J. Chromatogr. Sci.* 57 (2019) 518–527.
- [214] D. Papagiannaki, C. Medana, R. Binetti, P. Calza, P. Roslev, Effect of UV-A, UV-B and UV-C irradiation of glyphosate on photolysis and mitigation of aquatic toxicity, *Sci. Rep.* 10 (2020) 1–12.
- [215] X. Peng, Q. Huang, K. Zhang, Y. Yu, Z. Wang, C. Wang, Distribution, behavior and fate of azole antifungals during mechanical, biological, and chemical treatments in sewage treatment plants in China, *Sci. Total Environ.* 426 (2012) 311–317.
- [216] B. Duhm, H. Medenwald, W. Maul, The pharmacokinetics of clotrimazole 14C, *Postgrad. Med. J.* 50 (1974) 13–16.
- [217] OSPAR, Clotrimazole OSPAR Commission 2005 Update, 2005.
- [218] K.H. Büchel, The History of Azole Chemistry, in: 1986: pp. 1–23.
- [219] P.C. von der Ohe, V. Dulio, NORMAN Prioritisation framework for emerging substances, 2013.
- [220] F. Freeling, N.A. Alygizakis, P.C. von der Ohe, J. Slobodnik, P. Oswald, R. Aalizadeh, L. Cirka, N.S. Thomaidis, M. Scheurer, Occurrence and potential environmental risk of surfactants and their transformation products discharged by wastewater treatment plants, *Sci. Total Environ.* 681 (2019) 475–487.
- [221] R. Aalizadeh, P.C. von der Ohe, N.S. Thomaidis, Prediction of acute toxicity of emerging contaminants on the water flea *Daphnia magna* by Ant Colony Optimization-Support Vector Machine QSTR models, *Environ. Sci. Process. Impacts.* 19 (2017) 438–448.
- [222] N.A. Alygizakis, P. Oswald, N.S. Thomaidis, E.L. Schymanski, R. Aalizadeh, T. Schulze, M. Oswaldova, J. Slobodnik, NORMAN digital sample freezing platform: A European virtual platform to exchange liquid chromatography high resolution-mass spectrometry data and screen suspects in “digitally frozen” environmental samples, *TrAC - Trends Anal. Chem.* 115 (2019) 129–137.
- [223] K.S. Diamanti, N.A. Alygizakis, M.C. Nika, M. Oswaldova, P. Oswald, N.S. Thomaidis, J. Slobodnik, Assessment of the chemical pollution status of the Dniester River Basin by wide-scope target and suspect screening using mass spectrometric techniques, *Anal. Bioanal. Chem.* 412 (2020) 4893–4907.
- [224] I. Liška, F. Wagner, M. Sengl, K. Deutsch, J. Slobodník, M. Paunovic, Joint Danube Survey 4 Scientific Report: A Shared Analysis of the Danube River, Vienna, 2021.
- [225] J. Slobodnik, B. Alexandrov, V. Komorin, A. Mikaelyan, A. Guchmanidze, M. Arabidze, A. Korshenko, National Pilot Monitoring Studies and Joint Open Sea Surveys in Georgia, 2017.
- [226] J.K. Aronson, *Meyler’s Side Effects of Drugs: The International*

- Encyclopedia of Adverse Drug Reactions and Interactions, 16th Edition, Elsevier Science, 2016.
- [227] U. Breyer-Pfaff, M. Kroeker, T. Winkler, P. Kriemler, Isolation and identification of hydroxylated maprotiline metabolites, *Xenobiotica*. 15 (1985) 57–66.
- [228] R. Loos, R. Carvalho, D.C. António, S. Comero, G. Locoro, S. Tavazzi, B. Paracchini, M. Ghiani, T. Lettieri, L. Blaha, B. Jarosova, S. Voorspoels, K. Servaes, P. Haglund, J. Fick, R.H. Lindberg, D. Schwesig, B.M. Gawlik, EU-wide monitoring survey on emerging polar organic contaminants in wastewater treatment plant effluents, *Water Res.* 47 (2013) 6475–6487.
- [229] S. Das, N.M. Ray, J. Wan, A. Khan, T. Chakraborty, M.B. Ray, Micropollutants in Wastewater: Fate and Removal Processes, in: *Physico-Chemical Wastewater Treat. Resour. Recover.*, InTech, 2017: pp. 75–107.
- [230] S.K. Suh, J.B. Smith, Maprotiline Hydrochloride, *Anal. Profiles Drug Subst. Excipients*. 15 (1986) 393–426.
- [231] R. Frank, W. Klöpffer, Spectral solar photon irradiance in Central Europe and the adjacent North Sea, *Chemosphere*. 17 (1988) 985–994.
- [232] G.K.C. Low, S.R. McEvoy, R.W. Matthews, Formation of Nitrate and Ammonium Ions in Titanium Dioxide Mediated Photocatalytic Degradation of Organic Compounds Containing Nitrogen Atoms, *Environ. Sci. Technol.* 25 (1991) 460–467.
- [233] T.O. Nicolescu, Interpretation of Mass Spectra, in: *Mass Spectrom.*, InTech, 2017.
- [234] W.M. Horspool, F. Lenci, F. Lenci, *CRC Handbook of Organic Photochemistry and Photobiology*, Volumes 1 & 2, Second Edition, CRC Press, 2003.
- [235] C. Sirtori, A. Agüera, W. Gernjak, S. Malato, Effect of water-matrix composition on Trimethoprim solar photodegradation kinetics and pathways, *Water Res.* 44 (2010) 2735–2744.
- [236] T. Katagi, Direct photolysis mechanism of pesticides in water, *J. Pestic. Sci.* 43 (2018) 57–72.
- [237] Y. Wang, F.A. Roddick, L. Fan, Direct and indirect photolysis of seven micropollutants in secondary effluent from a wastewater lagoon, *Chemosphere*. 185 (2017) 297–308.
- [238] M.M. Dong, R. Trenholm, F.L. Rosario-Ortiz, Photochemical degradation of atenolol, carbamazepine, meprobamate, phenytoin and primidone in wastewater effluents, *J. Hazard. Mater.* 282 (2015) 216–223.
- [239] C. Rering, K. Williams, M. Hengel, R. Tjeerdema, Comparison of Direct and Indirect Photolysis in Imazosulfuron Photodegradation, *J. Agric. Food Chem.* 65 (2017) 3103–3108.
- [240] C. Minero, S. Chiron, G. Falletti, V. Maurino, E. Pelizzetti, R. Ajassa, M.E. Carlotti, D. Vione, Photochemical processes involving nitrite in surface water samples, *Aquat. Sci.* 69 (2007) 71–85.

- [241] L.C. Bodhipaksha, C.M. Sharpless, Y.P. Chin, A.A. MacKay, Role of effluent organic matter in the photochemical degradation of compounds of wastewater origin, *Water Res.* 110 (2017) 170–179.
- [242] A. Stankiewicz, J. Giebułtowski, U. Stankiewicz, P. Wroczyński, G. Nałecz-Jawecki, Determination of selected cardiovascular active compounds in environmental aquatic samples - Methods and results, a review of global publications from the last 10 years, *Chemosphere.* 138 (2015) 642–656.
- [243] A.A. Godoy, F. Kummrow, P.A.Z. Pamplin, Occurrence, ecotoxicological effects and risk assessment of antihypertensive pharmaceutical residues in the aquatic environment - A review, *Chemosphere.* 138 (2015) 281–291.
- [244] L.H.M.L.M. Santos, A.N. Araújo, A. Fachini, A. Pena, C. Delerue-Matos, M.C.B.S.M. Montenegro, Ecotoxicological aspects related to the presence of pharmaceuticals in the aquatic environment, *J. Hazard. Mater.* 175 (2010) 45–95.
- [245] S.T. Duggan, C.M. Chwieduk, M.P. Curran, Aliskiren: a review of its use as monotherapy and as combination therapy in the management of hypertension, *Drugs.* 70 (2010) 2011–2049.
- [246] Aliskiren | DrugBank Online, (n.d.).
- [247] F. Waldmeier, U. Glaenzel, B. Wirz, L. Oberer, D. Schmid, M. Seiberling, J. Valencia, G.J. Riviere, P. End, S. Vaidyanathan, Absorption, distribution, metabolism, and elimination of the direct renin inhibitor aliskiren in healthy volunteers, *Drug Metab. Dispos.* 35 (2007) 1418–1428.
- [248] NORMAN Database System, (n.d.).
- [249] N. Yadav, A. Goyal, Simultaneous Estimation of Aliskiren and Amlodipine in Combined Tablet Formulation by Simultaneous Equation and First Derivative Spectroscopic Methods *Organic and Medicinal Chemistry, Org. Med. Chem. J.* 6 (2018) 555676.
- [250] M.K. Kim, K.D. Zoh, Effects of natural water constituents on the photodecomposition of methylmercury and the role of hydroxyl radical, *Sci. Total Environ.* 449 (2013) 95–101.
- [251] J. Mack, J.R. Bolton, Photochemistry of nitrite and nitrate in aqueous solution: A review, *J. Photochem. Photobiol. A Chem.* 128 (1999) 1–13.
- [252] C. Marchina, G. Bianchini, C. Natali, M. Pennisi, N. Colombani, R. Tassinari, K. Knoeller, The Po river water from the Alps to the Adriatic Sea (Italy): new insights from geochemical and isotopic ($\delta^{18}\text{O}$ - δD) data, *Environ. Sci. Pollut. Res.* 22 (2015) 5184–5203.
- [253] J. Ma, N.J.D. Graham, Degradation of atrazine by manganese-catalysed ozonation: Influence of humic substances, *Water Res.* 33 (1999) 785–793.
- [254] R. Andreozzi, R. Marotta, N. Paxéus, Pharmaceuticals in STP effluents and their solar photodegradation in aquatic environment, *Chemosphere.* 50 (2003) 1319–1330.
- [255] M. Martínez-Zapata, C. Aristizábal, G. Peñuela, Photodegradation of the

- endocrine-disrupting chemicals 4n-nonylphenol and triclosan by simulated solar UV irradiation in aqueous solutions with Fe(III) and in the absence/presence of humic acids, *J. Photochem. Photobiol. A Chem.* 251 (2013) 41–49.
- [256] S. Chiron, C. Minero, D. Vione, Photodegradation processes of the antiepileptic drug carbamazepine, relevant to estuarine waters, *Environ. Sci. Technol.* 40 (2006) 5977–5983.
- [257] L. Kotthoff, S.L. O’Callaghan, J. Lisec, T. Schwerdtle, M. Koch, Structural annotation of electro- and photochemically generated transformation products of moxidectin using high-resolution mass spectrometry, *Anal. Bioanal. Chem.* 412 (2020) 3141–3152.
- [258] E.L. Schymanski, J. Jeon, R. Gulde, K. Fenner, M. Ruff, H.P. Singer, J. Hollender, Identifying small molecules via high resolution mass spectrometry: Communicating confidence, *Environ. Sci. Technol.* 48 (2014) 2097–2098.
- [259] B.S. Kushwah, J. Gupta, D.K. Singh, M. Kurmi, A. Sahu, S. Singh, Characterization of solution stress degradation products of aliskiren and prediction of their physicochemical and ADMET properties, *Eur. J. Pharm. Sci.* 121 (2018) 139–154.

Appendix A

Table A1. TGA weight loss percentages for all materials calculated from 200-800 °C range

Sample	% weight loss (200-800°C)
Fe ₃ O ₄	2.4
Fe ₃ O ₄ /0.5HA	7.4
Fe ₃ O ₄ /1HA	7.8
Fe ₃ O ₄ /2HA	10.0
Fe ₃ O ₄ /4HA	13.2
ox-Fe ₃ O ₄ /0.5HA	6.2

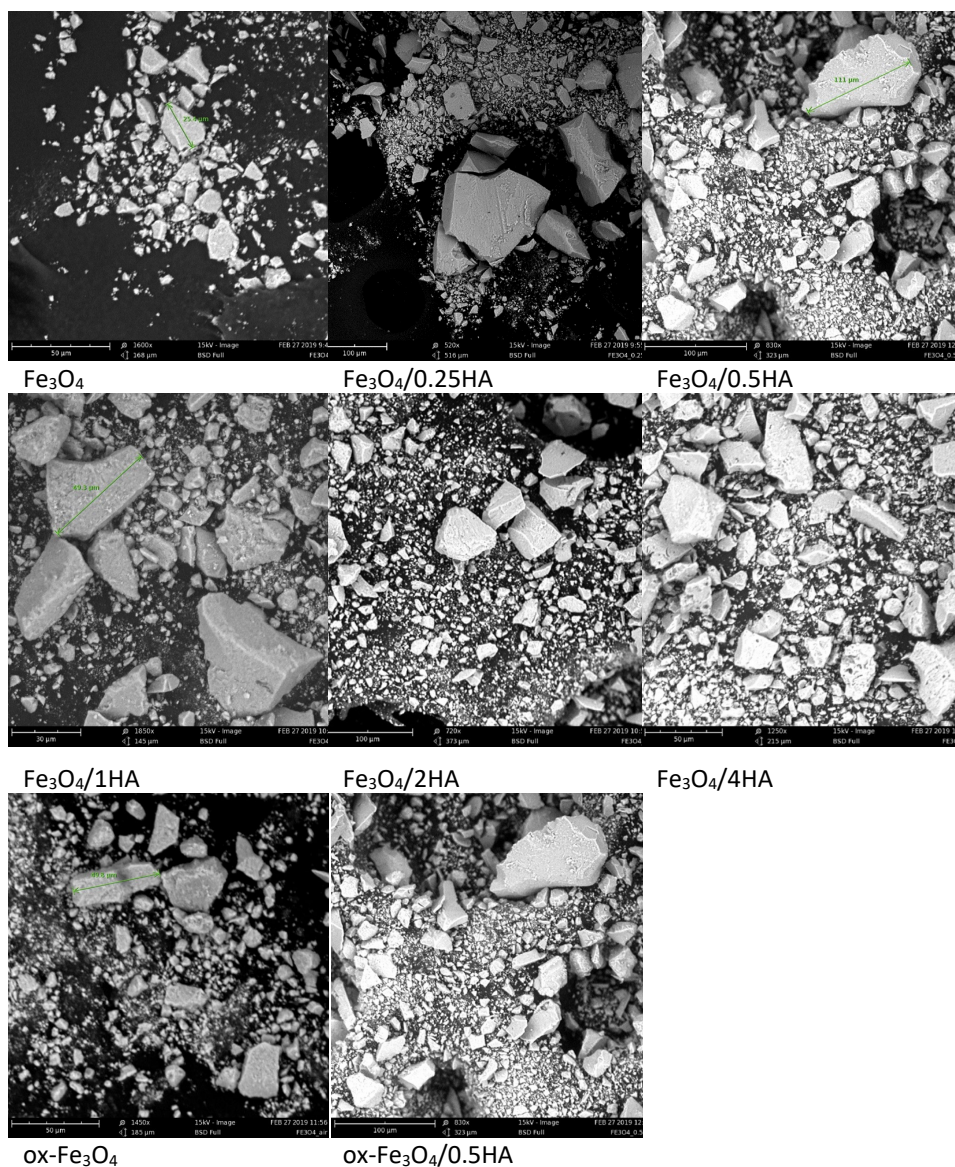


Figure A1. SEM micrograph of MNPs/HA and bare Fe₃O₄ samples.

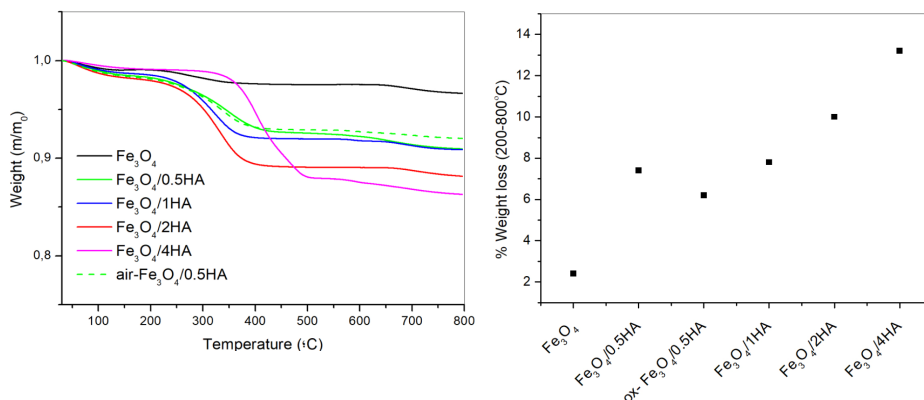


Figure A2. TGA curves obtained (top) and weight losses calculated in the 200–800°C range (bottom) for the HA, Fe₃O₄ and Fe₃O₄/HA MNPs.

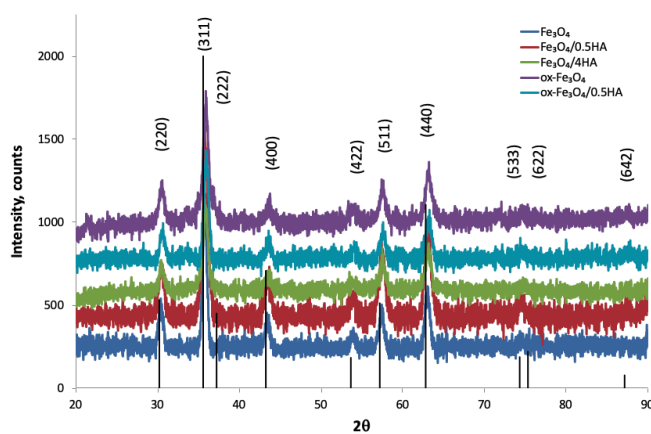


Figure A3. X-ray diffraction patterns of bare Fe₃O₄, and MNP/HA prepared in anoxic and air atmosphere.

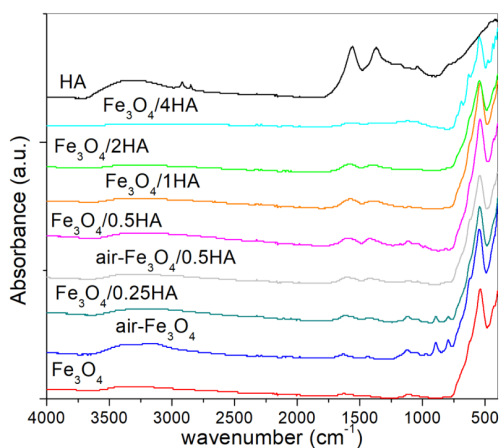


Figure A4. Absorbance FTIR spectra obtained for the HA, Fe₃O₄ and Fe₃O₄/HA MNPs.

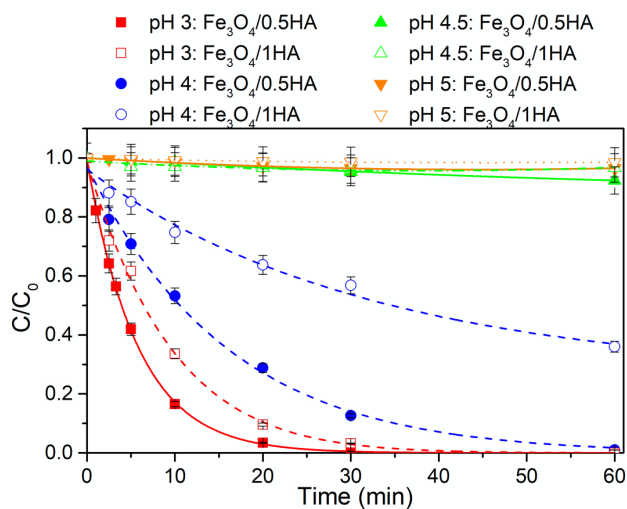


Figure A5. Fenton-like degradation of 4-chlorophenol (0.2 mmol L^{-1}) in the presence of H_2O_2 (1.0 mmol L^{-1}) and 100 mg L^{-1} MNPs at adjusted pH.

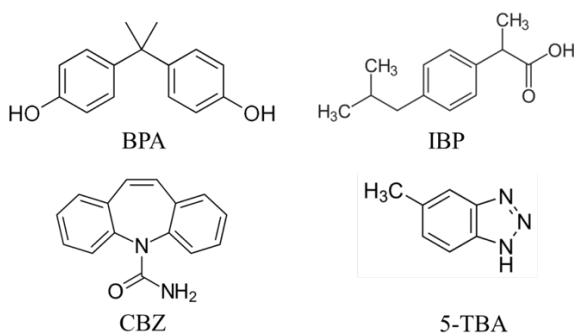


Figure A6. Molecular structure of the investigated CECs. BPA = Bisphenol A, IBU = ibuprofen, CBZ = carbamazepine and 5-TBA = 5-tolylbenzotriazole.

Appendix B

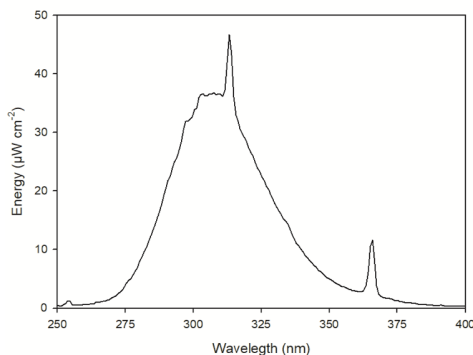


Figure B1. Emission spectrum of four Sankio denki G15T8E lamps reaching the solution surface.

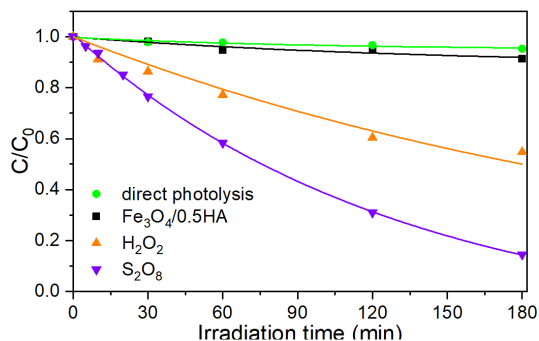


Figure B2. BPA degradation ($C_0 = 20 \mu\text{M}$) under different conditions: direct photolysis; effect of light activation of $\text{Fe}_3\text{O}_4/0.5\text{HA}$ (100 mg L^{-1}); effect of light activation of H_2O_2 (1 mM) and $\text{S}_2\text{O}_8^{2-}$ (1 mM).

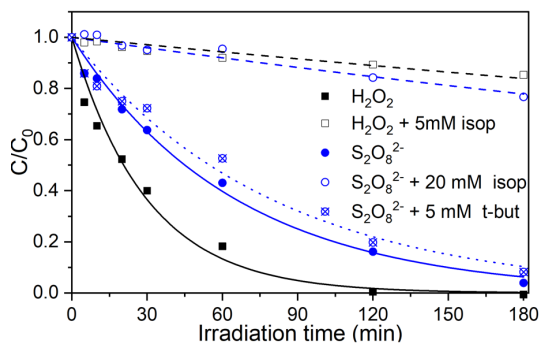


Figure B3. Effect of addition of isopropanol and *t*-butanol on BPA degradation in the presence of 100 mg L^{-1} of $\text{Fe}_3\text{O}_4/0.5\text{HA}$ and 1 mM of H_2O_2 at pH 3 or 1 mM of $\text{S}_2\text{O}_8^{2-}$ at pH 6.

Table B1. Kinetic constants (min^{-1}) calculated in the presence of H_2O_2 (1 mM) and $\text{S}_2\text{O}_8^{2-}$ (1 mM) activated by bare Fe_3O_4 and $\text{Fe}_3\text{O}_4/0.5\text{HA}$ (100 mg L^{-1}) at different pH under irradiation.

	H_2O_2		$\text{S}_2\text{O}_8^{2-}$	
	Fe_3O_4	$\text{Fe}_3\text{O}_4/0.5\text{HA}$	Fe_3O_4	$\text{Fe}_3\text{O}_4/0.5\text{HA}$
pH 3	0.0146	0.0318	0.0214	0.0323
pH 4	0.0039	0.0055	0.0151	0.0177
pH 6	0.0011	0.00152	0.0088	0.0154
pH 6.5	-	-	0.0062	0.0076

Appendix C

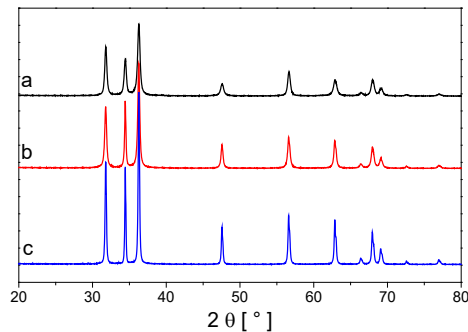


Figure C1. X-ray diffraction patterns of ZnO synthesized with the sol-gel (a, black), precipitation (b, red) and hydrothermal (c, blue) method.

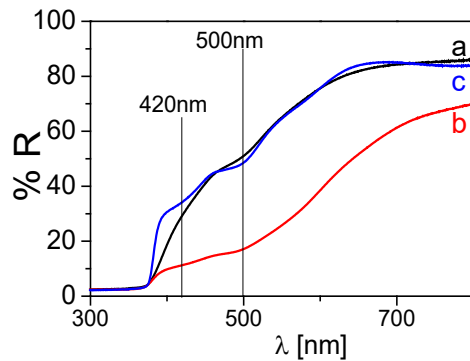


Figure C2. DR spectra of 3%Fe doped ZnO synthesized via the sol-gel (a), precipitation (b) and hydrothermal (c) method.

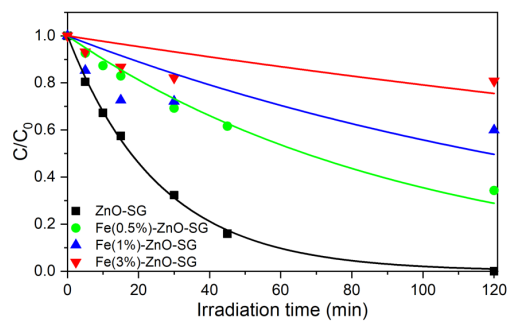


Figure C3. Phenol degradation (20 mg L^{-1}) in the presence of 1000 mg L^{-1} of Fe-ZnO-SG.

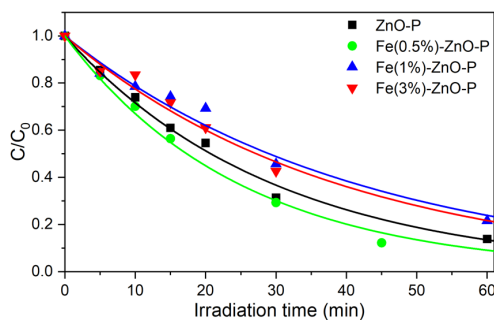


Figure C4. Phenol degradation (20 mg L^{-1}) in the presence of 1000 mg L^{-1} Fe-ZnO-P.

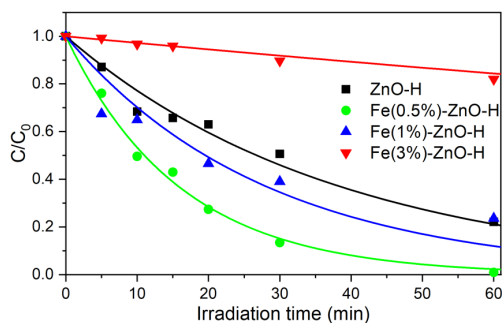


Figure C5. Phenol degradation (20 mg L^{-1}) in the presence of 400 mg L^{-1} Fe-ZnO-H.

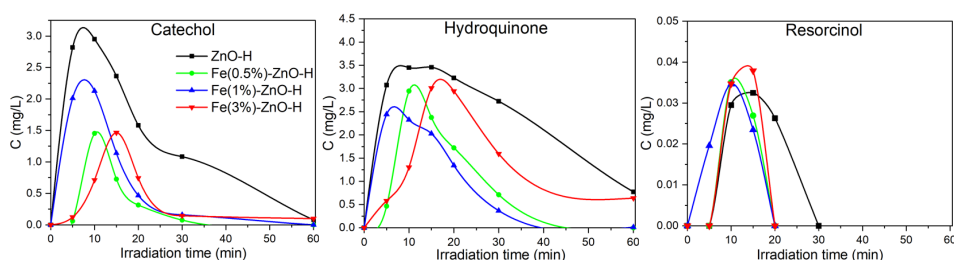


Figure C6. Catechol, hydroquinone and resorcinol evolution profiles over time in the presence of 1000 mg L^{-1} Fe-ZnO-H.

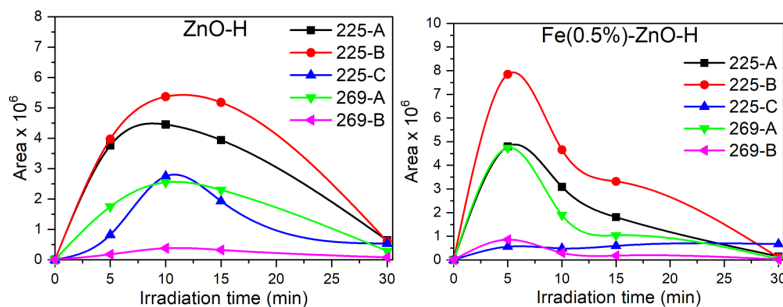


Figure C7. Formation profiles of the intermediates products detected for ketoprofen in the presence of 1000 mg L^{-1} of ZnO-H (left) and Fe(0.5%)-ZnO-H (right).

Table C1. Summary of *m/z* detected for ketoprofen degradation in Milli-Q water and wastewater.

<i>m/z</i>	r.t. (min)	Milli-Q water		Wastewater
		ZnO-H	Fe(0.5%)-ZnO-H	
209 ^a	3.3	√	√	√
225-A	2.9	√	√	√
225-B	3.5	√	√	√
225-C	4.4	√	√	√
269-A	3.0	√	√	√
269-B	3.6	√	√	√

^a Ketoprofen fragment ion *m/z*

Appendix D

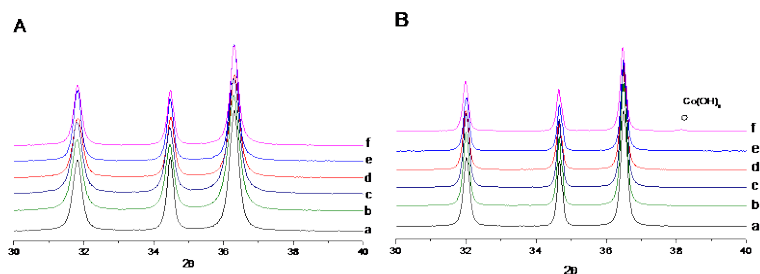


Figure D1. Enlarged region at $30^\circ < 2\theta < 40^\circ$, Diffratograms of bare and Co-ZnO prepared via (A) solution and (B) hydrothermal methods; a) pristine ZnO, b) 0.25% Co doped ZnO, c) 0.5% Co doped ZnO, d) 1% Co doped ZnO, e) 3% Co doped ZnO, f) 5% Co doped ZnO.

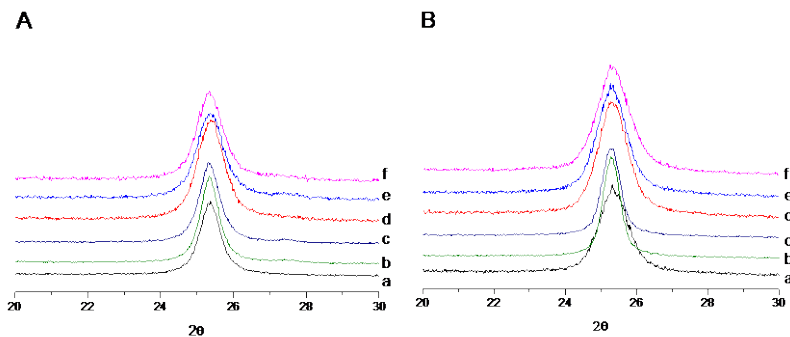
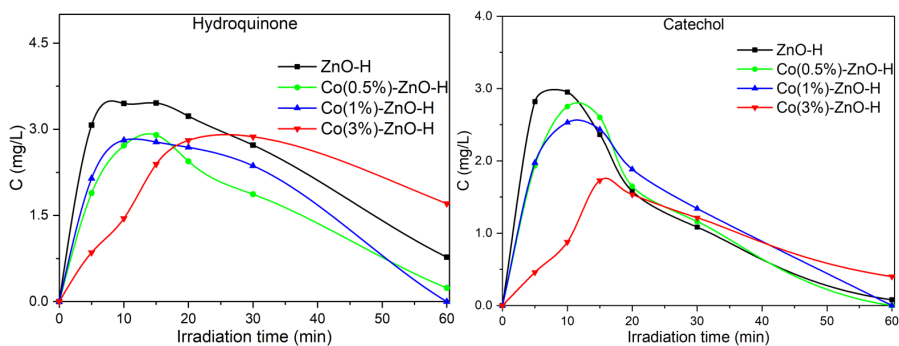


Figure D2. Enlarged region at $20^\circ < 2\theta < 30^\circ$ Diffratograms of bare and Co-TiO₂ prepared via (A) solution and (B) hydrothermal methods; a) pristine TiO₂, b) 0.25% Co doped TiO₂, c) 0.5% Co doped TiO₂, d) 1% Co doped TiO₂, e) 3% Co doped TiO₂, f) 5% Co doped TiO₂.



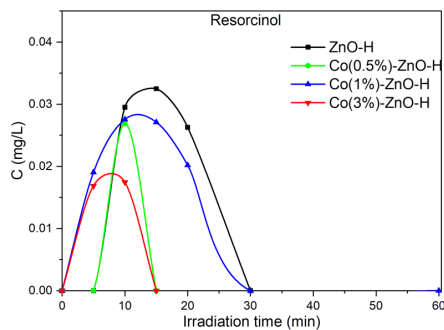


Figure D3. Formation profiles of phenol transformation products detected in the presence of 1000 mg L^{-1} of ZnO-H and Co doped ZnO-H.

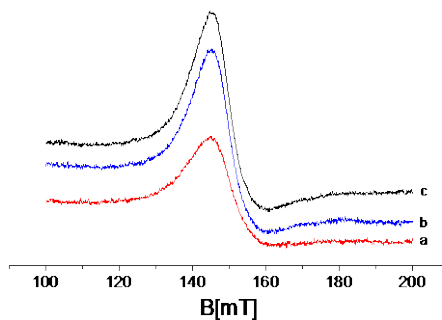


Figure D4. EPR spectra of Co-ZnO via solution synthesis a) 1% of Co, b) 3% of Co, c) 5% of Co.

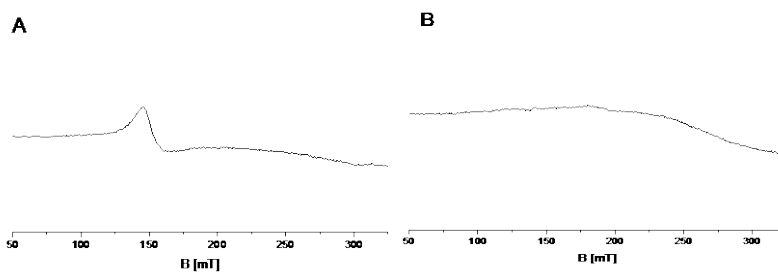
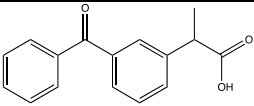
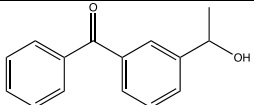
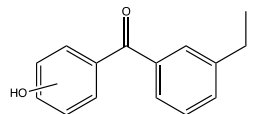
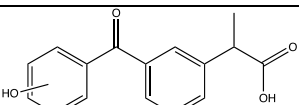


Figure D5. EPR spectra of A) Co(1%)-ZnO-H, and B) Co(1%)-TiO₂-H both obtained via hydrothermal synthesis.

Table D1. Transformation products identified for ketoprofen by LC/MS.

TPs	r.t. (min)	m/z	Structure
Ketoprofen	3.3	209	
225-A	2.9	225	
225-B	3.5		
225-C	4.4		
269-A	3.0	269	
269-B	3.6		

Appendix E

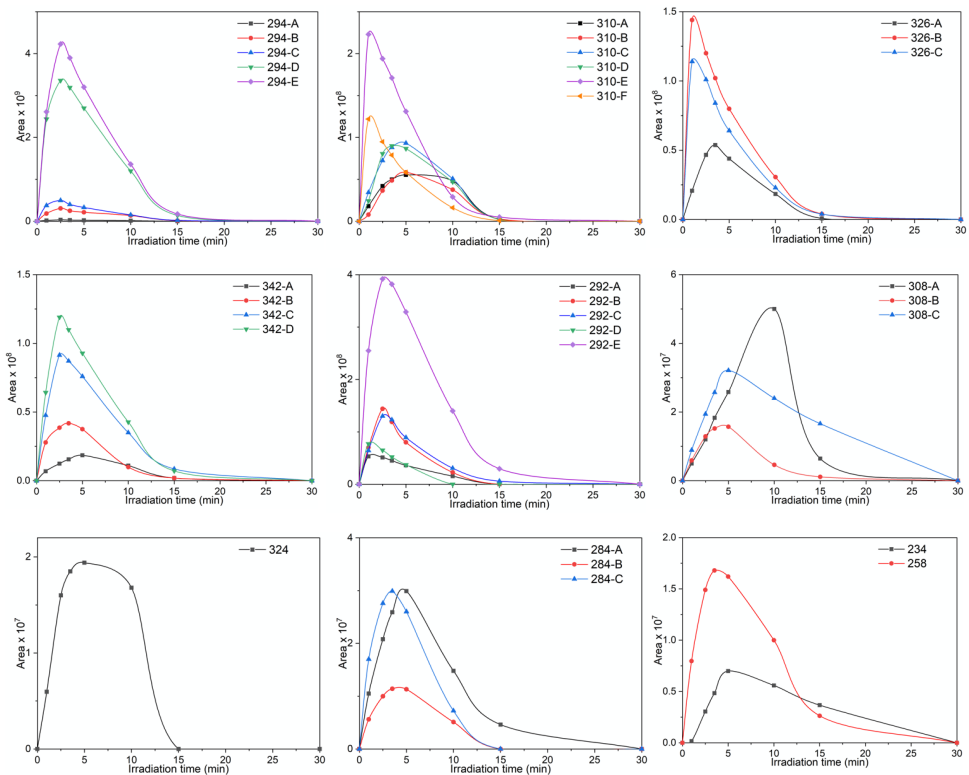


Figure E1. Profile over time of maprotiline TPs observed in Milli-Q water in the presence of TiO_2 .

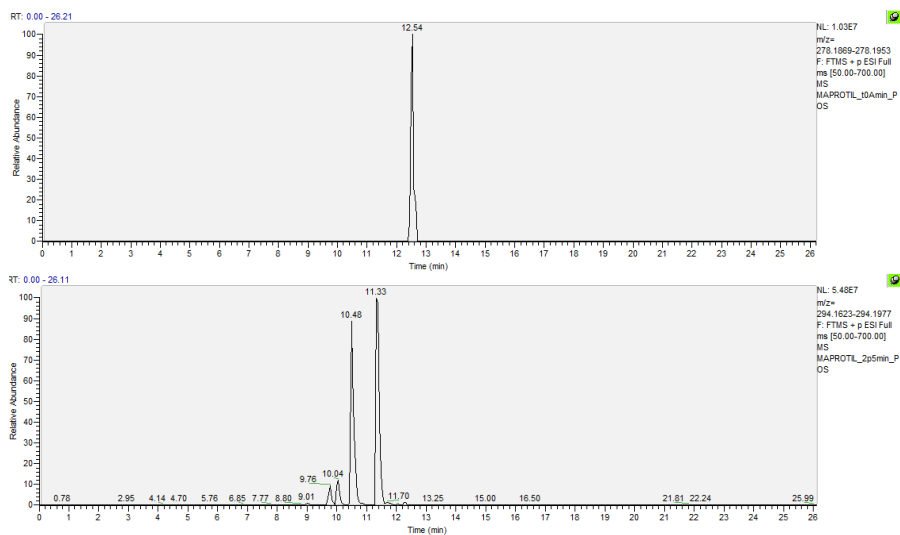


Figure E2. HPLC-HRMS chromatogram of maprotiline (top) and m/z 294 (bottom).

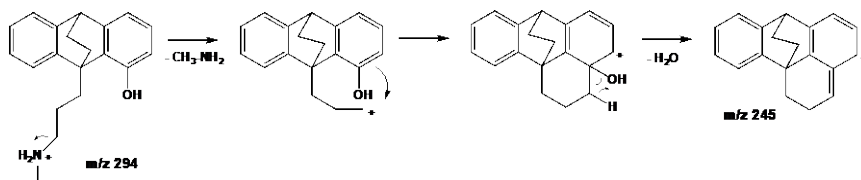


Figure E3. Specific CID mechanisms for the compound 294-D.

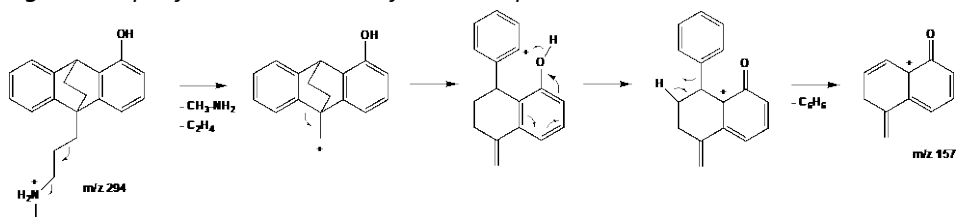


Figure E4. Specific CID mechanisms for the compound 294-E.

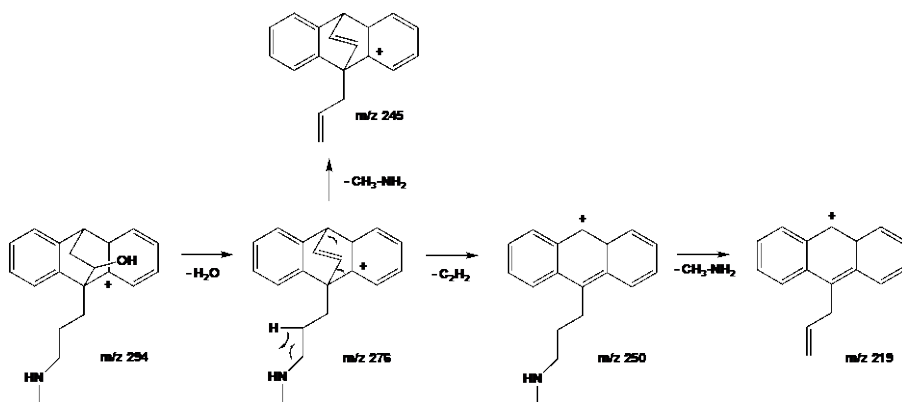


Figure E5. Specific CID mechanisms for the compound 294-B.

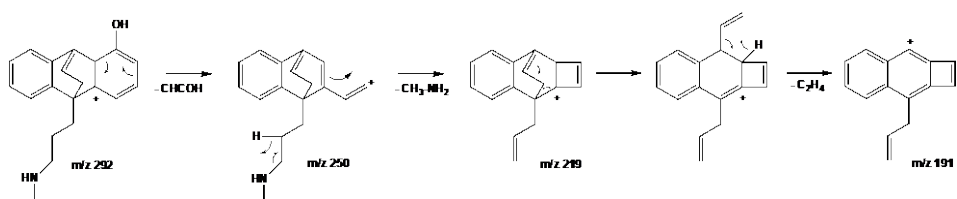


Figure E6. CID mechanisms for the compound 292-B issued from dehydrogenation of 294-E.

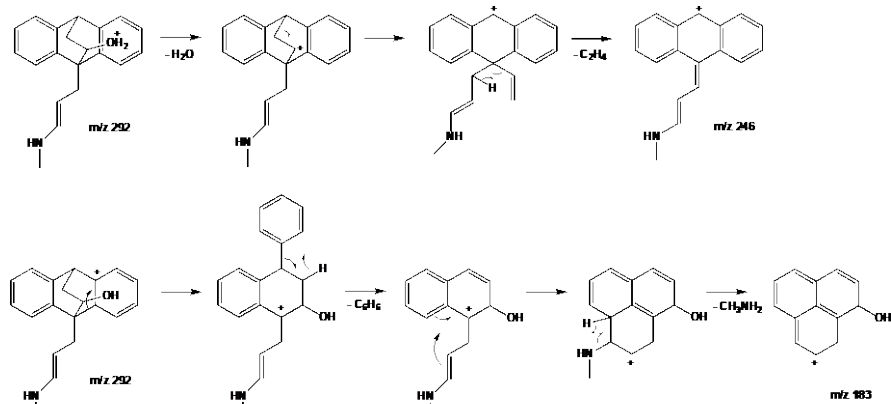


Figure E7. CID mechanism for the compound 292-E.

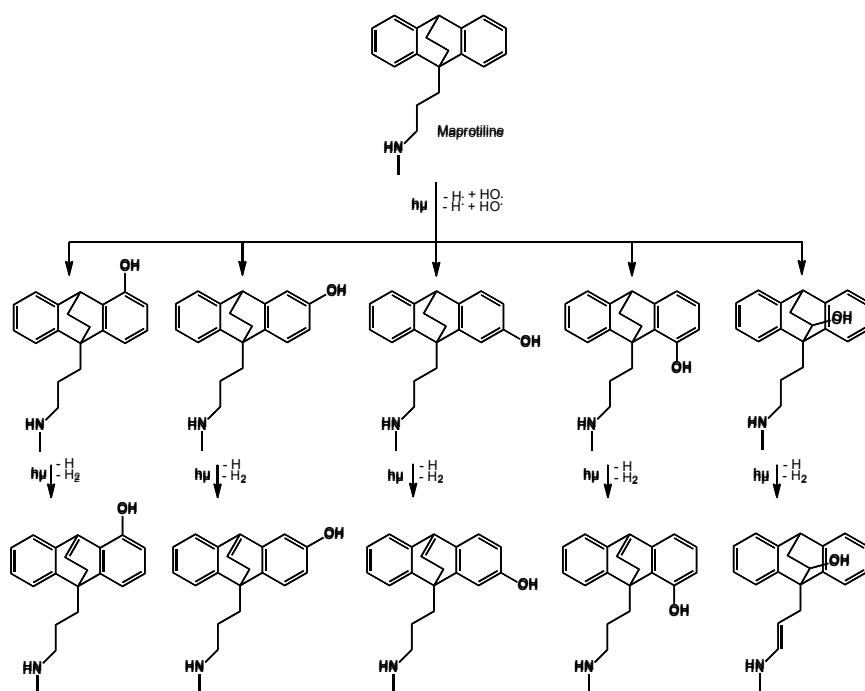


Figure E8. Dehydrogenation of species with MH^+ at m/z 294.

Table E1. Ions in common detected in CID experiments for m/z 310 transformation products.

m/z	Ion formula	310					
		A	B	C	D	E	F
310.1820	$C_{20}H_{24}NO_2^+$	+	+	+	+	+	+
292.1714	$C_{20}H_{22}NO^+$	+	+			+	
282.1506	$C_{18}H_{20}NO_2^+$			+	+		
279.1397	$C_{19}H_{19}O_2^+$	+		+			
261.1290	$C_{19}H_{17}O^+$	+	+				
251.1082	$C_{17}H_{15}O_2^+$			+	+		
233.0976	$C_{17}H_{13}O_2^+$		+		+	+	
217.1026	$C_{17}H_{13}^+$	+					+
191.0867	$C_{15}H_{11}^+$	+					+
185.0973	$C_{13}H_{13}O^+$	+		+			
169.1023	$C_{13}H_{13}^+$		+		+		
159.0815	$C_{11}H_{11}O^+$	+		+			
133.0657	$C_9H_9^+$	+		+			

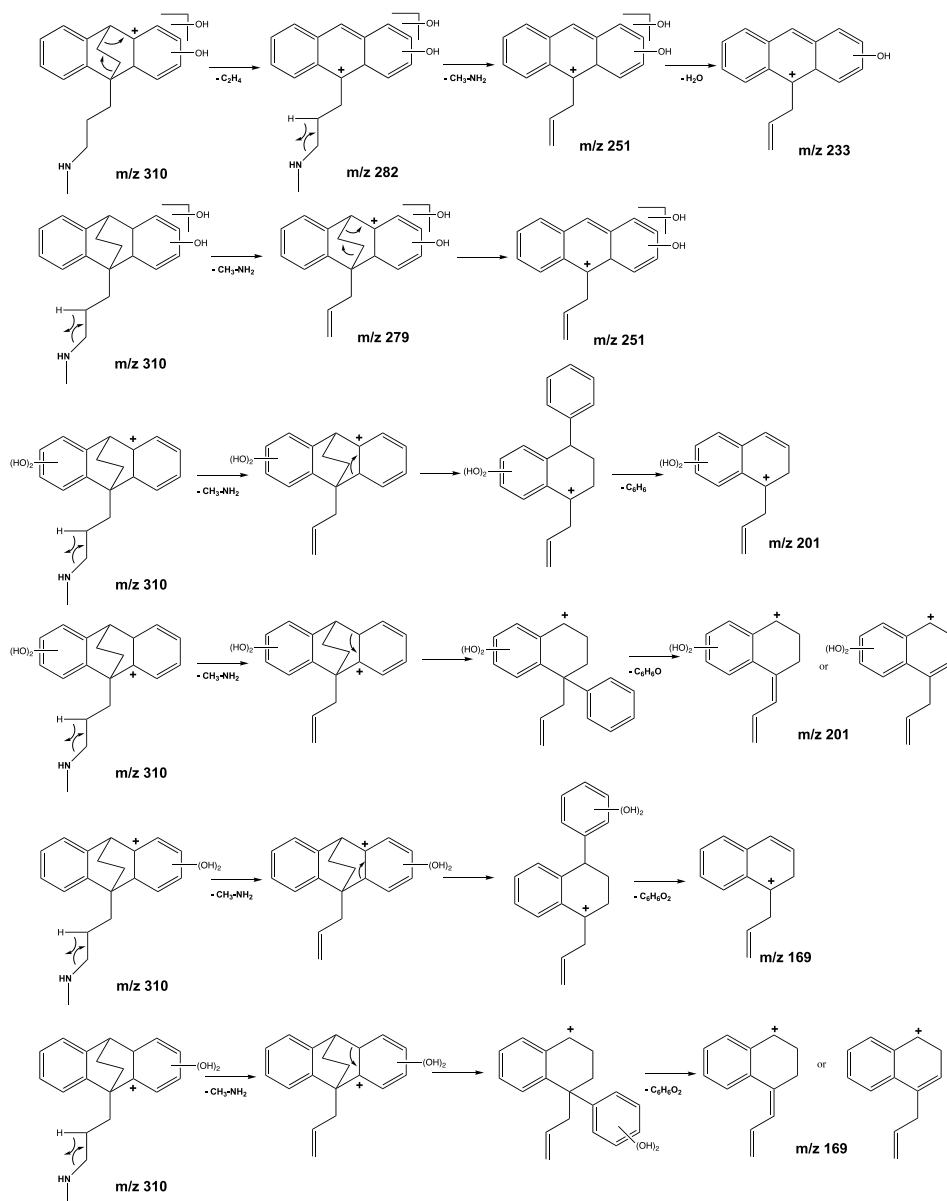


Figure E9. Suggested dissociation pathways for m/z 310 photoproducts.

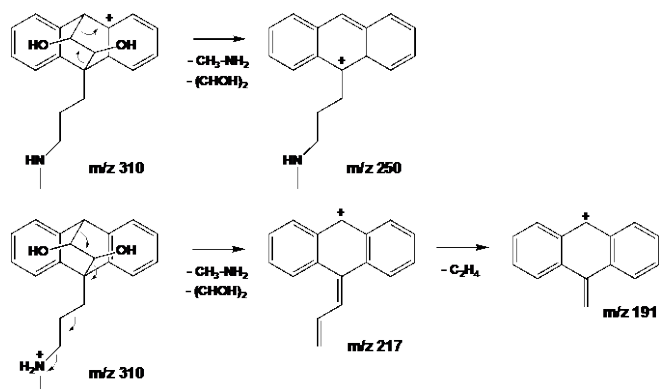


Figure E10. CID mechanisms for the compound 310-F.

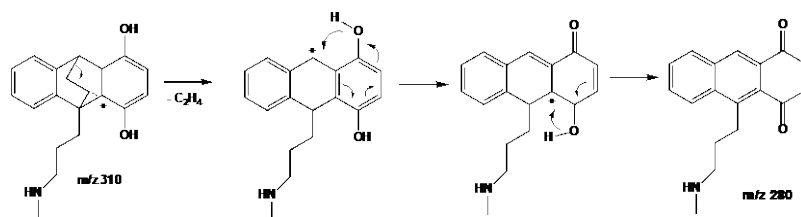


Figure E11. CID mechanisms for the compound 310-E.

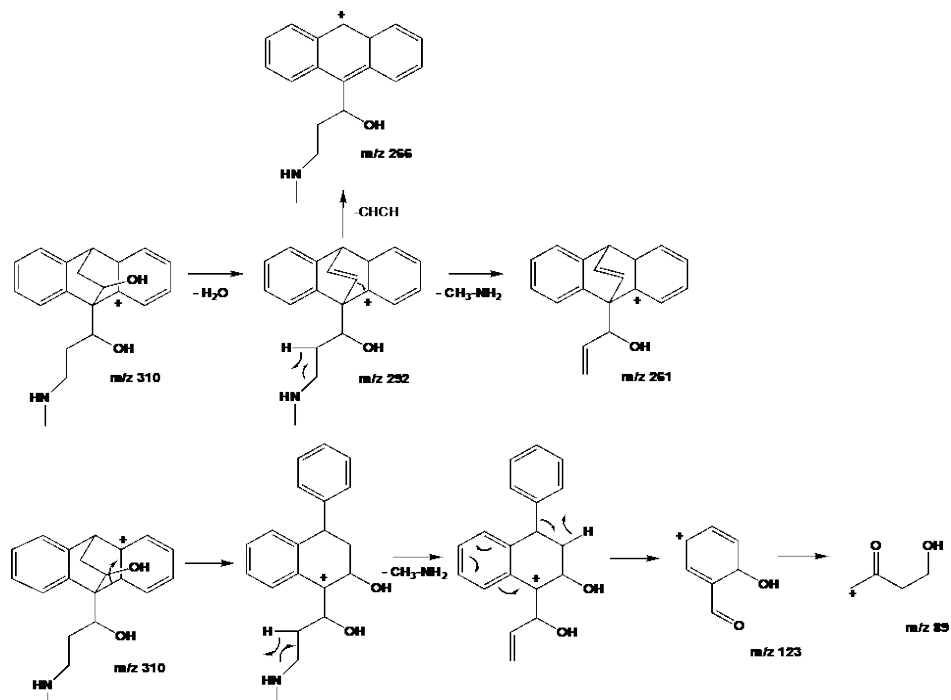


Figure E12. CID mechanisms for the compound 310-B.

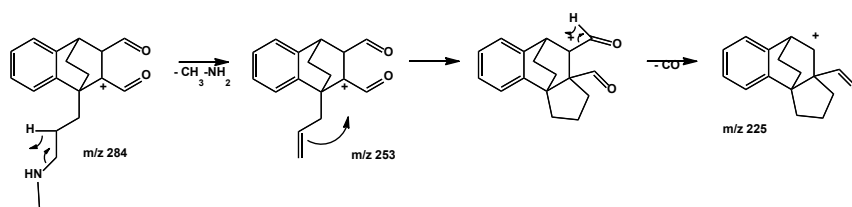


Figure E13. Suggested CID mechanism for the compound 284-A.

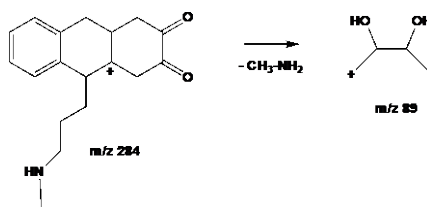


Figure E14. Suggested CID mechanism for the compound 284-B.

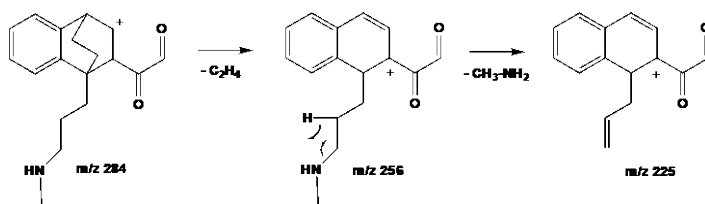


Figure E15. Suggested CID mechanism for the compound 284-C.

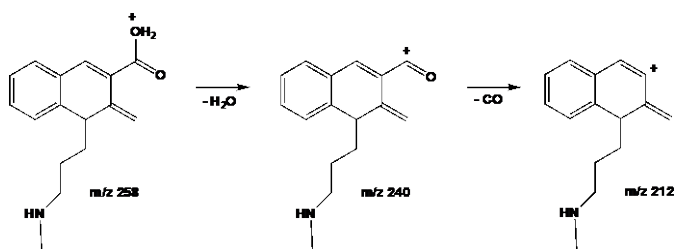


Figure E16. Suggested CID mechanism for the compound 258.

Appendix F

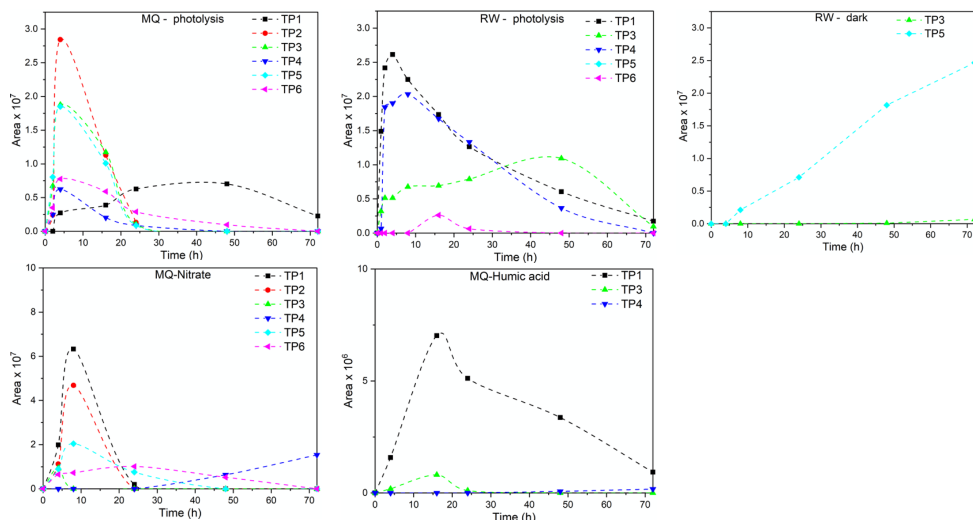


Figure F1. Profile over time of aliskiren TPs observed in Milli-Q water (MQ) and river water (RW) in the dark and under irradiation and in the presence of nitrate and humic acid.

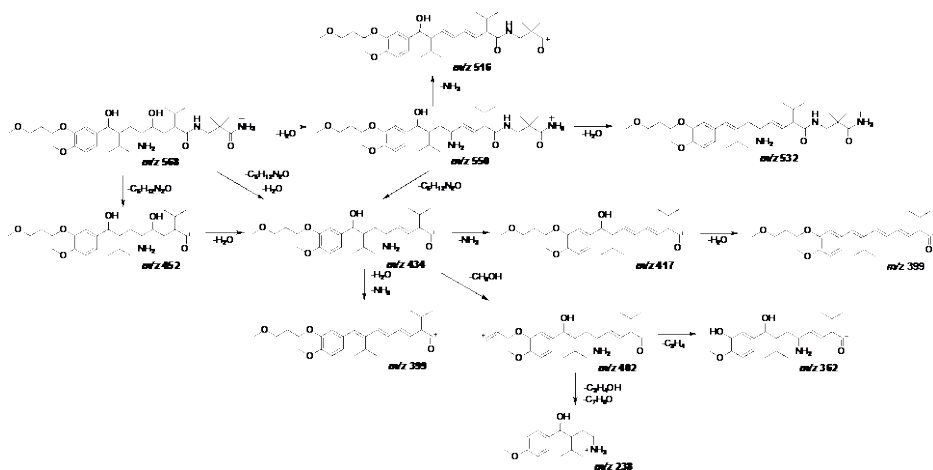


Figure F2. CID mechanism for the compound TP6.

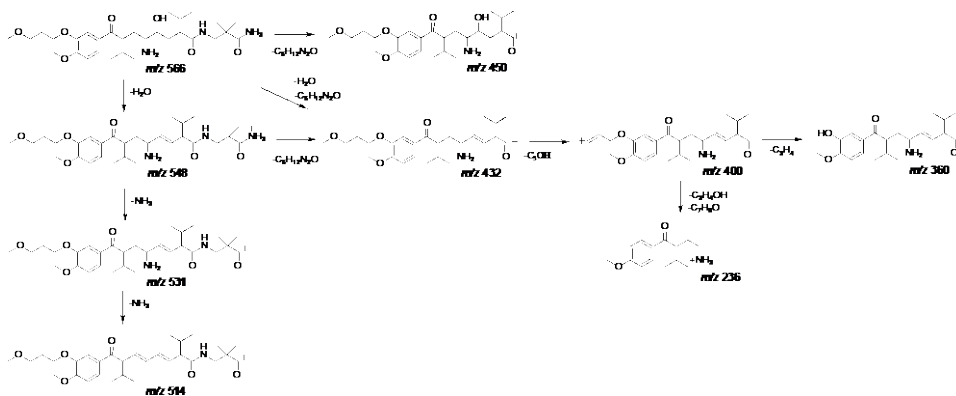


Figure F3. CID mechanism for the compound TP5.

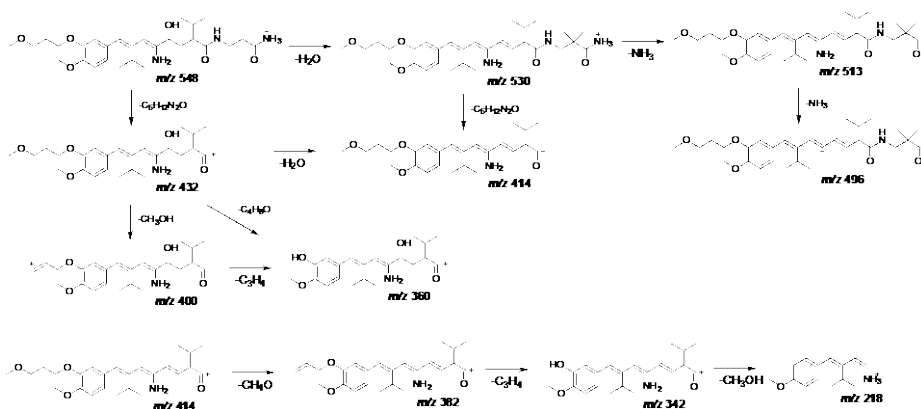


Figure F4. CID mechanism for the compound TP4.

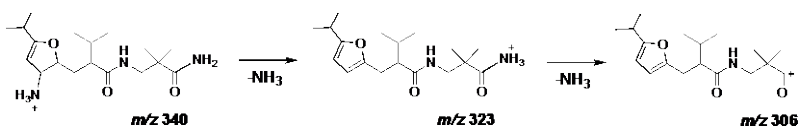


Figure F5. CID mechanism for the compound TP1.

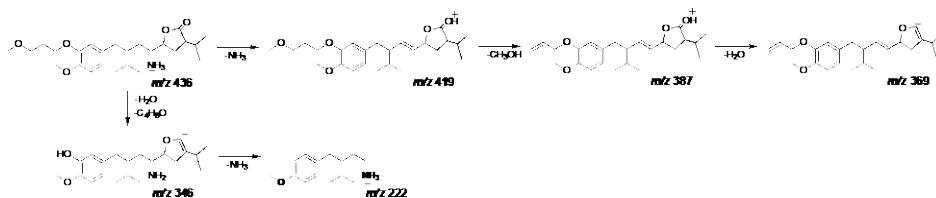


Figure F6. CID mechanism for the compound TP2.

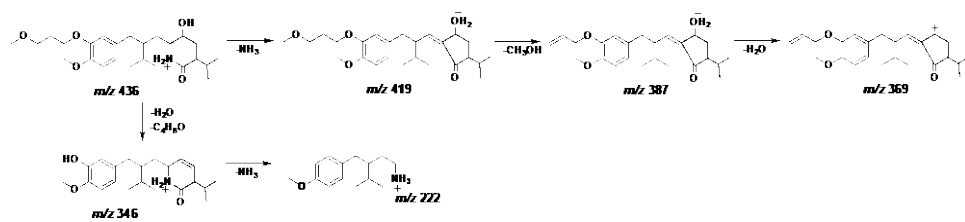


Figure F7. CID mechanism for the compound TP3.

Summary of PhD activities

Other Research Activities

Besides the work described in this thesis, during these 3 years I also have been involved in different projects that were not possible to include in this restricted dissertation:

Environmental Assessment of Humic Acid Coated Magnetic Materials used as Catalyst in photo-Fenton processes.

Mattia Costamagna, Nuno P.F. Gonçalves, Alessandra Bianco Prevot
Catalysts, 2020. 10, 771.

In a collaboration with Mattia Costamagna (UNITO), the overall environmental sustainability of using $\text{Fe}_3\text{O}_4/\text{HA}$ as heterogeneous photo-Fenton catalyst for the activation of hydrogen peroxide and persulfate was investigated in a comparative Life Cycle Assessment (LCA) study. The overall process sustainability was considered related to catalyst preparation, chemicals, pH adjustment and electricity consumption by a comparative LCA study between H_2O_2 and persulfate activation at laboratory scale. The analysis highlighted that the addition of humic substances to the particles allows the effectiveness of the catalyst to improve without increasing the environmental impacts. Additionally, it exposed that these processes are strongly correlated with energy consumption due to the irradiation and therefore with the efficiency of the process. For this reason, working at acidic pH allows us to contain the impacts since acidic conditions allow the pollutants within short irradiation times. However, the use of natural sunlight can indeed contribute to reduce the energy impact. Additionally, even if persulfate proved to promote a faster BPA removal at higher pH relatively to hydrogen peroxide, the last proved to be more environmentally friendly due to the lower impacts associated with its production.

ZnO/CeO₂ and ZnO/Yb₂O₃ mixed systems as photocatalysts for the abatement of organic pollutants.

Erik Cerrato, Nuno P.F. Gonçalves, Paola Calza, Maria Cristina Paganini
Catalysts, 2020, 10, 1222.

The incorporation of lanthanide elements in the ZnO structure was also explored to improve de charge separation by preparing heterosystems with CeO₂ and Yb₂O₃. The impact on the structural and optical properties was investigated by comparing with the pristine ZnO with two semiconductors based on ZnO: ZnO/CeO₂ and ZnO/Yb₂O₃ with the intention to highlight the different photocatalytic activities. The two samples were prepared via hydrothermal synthesis and fully characterized by X-ray diffraction technique, diffuse reflectance Ultraviolet-Visible spectroscopy (UV-Vis), high resolution transmission electron microscopy and finally with electron paramagnetic resonance spectroscopy. To study the impact of the mixed systems on the charge separation, their photocatalytic performance was evaluated by performing photocatalytic degradation experiments in the presence of selective quenching agents. The role of e⁻ was explored performing the degradation in the presence and absence of oxygen to prevent the formation of superoxide radical anion while the role of h⁺ was assessed by the addition of KBrO₃ - an electron scavenger thought the reducing of the charge recombination and in this way increasing its availability to form reactive species. Finally, the role of both •OH_{ads} and •OH_{free} was investigated by the addition of NaI and *tert*-butanol, respectively.

Doped Zinc Oxide Photocatalysts applied to water: decontamination and disinfection.

Ilaria Berruti, Nuno P.F. Gonçalves, Inmaculada Polo-Lopez, Isabel Oller, Cristina Paganini, Paola Calza

Submitted to Applied Catalysis B: Environmental.

In collaboration with Plataforma Solar de Almería, the potential use of natural solar radiation for the semiconductors photo-activation for simultaneous disinfection and decontamination of water was explored using the previously ZnO based photocatalysis doped with Fe, Ce and Yb. Laboratory scale trials were performed towards the simultaneous inactivation of three test pathogenic bacteria (*Escherichia coli*, *Enterococcus faecalis* and *Pseudomonas aeruginosa*) and three CECs (Diclofenac, Sulfamethoxazole and Trimethoprim). Different water matrices were explored under natural sunlight. It was demonstrated the feasibility of photocatalytic treatment, involving doped zinc oxide (with Ce, Yb and Fe), for the simultaneous inactivation of pathogens and removal of chemicals in complex matrix, exciting the semiconductors with an economically and ecologically source of light, such as natural solar radiation. Best results were found with Ce doped ZnO at 500 mg L⁻¹, concentration that allow to remove 80% of the mixture after 45 minutes, while inactivation of wild bacteria present in UWW was achieved after 120 minutes. The promising results raised future research to be focused on overcoming the limitations of the suspended material by the catalyst immobilization on a supported.

Comparison of advanced oxidation processes for the degradation of Maprotiline in water – kinetics, degradation products and potential ecotoxicity.

Nuno P.F. Gonçalves, Zsuzsanna Varga, Edith Nicol, Paola Calza, Stéphane Bouchonnet

Catalysts 2021, 11(2), 240.

During my secondment at École Polytechnique, the impact of different oxidation processes (photo-Fenton and photocatalysis) on the maprotiline degradation pathways was investigated by liquid chromatography-high resolution mass spectrometry (LC-HRMS). During this period, besides gaining experience on HRMS, I had the possibility to explore the in-house SPIX software to process HRMS data allowing to ensure the potential singular species formed reducing the end-used faults in complex matrices. Semiconductors photocatalysts, namely Fe-ZnO, Ce-ZnO and TiO₂, proved to be more efficient than heterogeneous photo-Fenton processes in the presence of hydrogen peroxide and persulfate. No significant differences were observed in the degradation pathways in the presence of photocatalysis, while the SO₄⁻ mediated process promote the formation of different TPs. Species resulting from ring-openings were observed with higher persistence in the presence of SO₄⁻. During this period, I had the opportunity to learn and apply Quantitative Structure-Activity Relationship models (QSAR) to predict the toxicity of chemical substances. QSAR in-silico tests on mutagenicity, developmental/reproductive toxicity, Fathead minnow LC50, D. magna LC50, fish acute LC50 allowed to estimate the toxicity of the identified transformation products. Low toxicant properties were estimated for TPs resulting from hydroxylation onto the bridge rather than onto aromatic rings, as well as those resulting from the ring-opening.

Biochar waste-based ZnO materials highly efficient photocatalyst for water treatment.

Nuno P.F. Gonçalves, Mirtha A.O. Lourenço, Simone R. Baleuri, Stefano Bianco, Pravin Jagdale, Paola Calza

In preparation.

In a collaboration with Istituto Italiano di Tecnologia, the photocatalytic activity of different ZnO based photocatalysts, supported in biochar from waste residues of chitosan and coffee, was evaluated for water remediation. The effect of carbon-based support in the material was evaluated by testing ZnO materials with different amounts of biochar from both (1% up to 52%) using phenol as a pollutant model molecule, under irradiation. The effect of functional groups in the carbon support was explored by using biochar from different waste sources as well as their subsequent oxidation and the use of commercial reduced graphene oxide (rGO). The effect of catalyst loading and reactive species was investigated as well. The best performing material was then tested for the photocatalytic degradation of mixture of four CECs from different categories with different chemical properties. Namely, Ibuprofen (anti-inflammatory drug), carbamazepine (psychiatric drug), 5-Methyl-1H-benzotriazole (anticorrosion inhibitor) and bisphenol A (compound used in plastic industry).

Additionally, I have been involved on additional goals of the ETN project focused on the identification of potential new CECs in environmental waters by untargeted analysis. Several water samples from different aquatic environments were collected over a period of time and treated for the GC and LC-HRMS.

Publications

Papers

1. *New insight into zinc oxide doped with iron and its exploitation to pollutants abatement.* Maria Cristina Paganini, Alice Giorgini, **Nuno P.F. Gonçalves**, Chiara Gionco, Alessandra Bianco Prevot, Paola Calza, *Catalysis Today*, 2019, 328, 230-234. doi.org/10.1016/j.cattod.2018.10.054
2. *The effect of cobalt doping on the efficiency of semiconductor oxides in the photocatalytic water remediation.* **Nuno P.F. Gonçalves**, MC Paganini, P. Armillotta, E. Cerrato, P. Calza, *Journal of Environmental Chemical Engineering* 2019, 7 (6) 103475. doi.org/10.1016/j.jece.2019.103475
3. *Photo-Activation of Persulfate and Hydrogen Peroxide by Humic Acid Coated Magnetic Particles for Bisphenol A Degradation.* **Nuno P.F. Gonçalves**, M. Minella, G. Mailhot, M. Brigante, A. Bianco Prevot, *Catalysis Today*, 2019, 361, 43-49. doi.org/10.1016/j.cattod.2019.12.028
4. *Humic Acid Coated Magnetic Particles as Highly Efficient Heterogeneous Photo-Fenton Materials for Wastewater Treatments.* **Nuno P.F. Gonçalves**, M. Minella, D. Fabbri, P. Calza, C. Malitesta, E. Mazzotta, A. Bianco Prevot, *Chemical Engineer Journal*, 2020, 390, 124619. doi.org/10.1016/j.cej.2020.124619
5. *Environmental Assessment of Humic Acid Coated Magnetic Materials used as Catalyst in photo-Fenton processes.* Mattia Costamagna, **Nuno P.F. Gonçalves**, Alessandra Bianco Prevot, *Catalysts*, 2020, 10, 771. doi.org/10.3390/catal10070771.
6. *ZnO/CeO₂ and ZnO/Yb₂O₃ mixed systems as photocatalysts for the abatement of organic pollutants.* Erik Cerrato, **Nuno P.F. Gonçalves**, Paola Calza, Maria Cristina Paganini, *Catalysts*, 2020, 10, 1222. [doi:10.3390/catal10101222](https://doi.org/10.3390/catal10101222)
7. *Study of the photoinduced transformations of maprotiline in river water using liquid chromatography high-resolution mass spectrometry.* **Nuno P.F. Gonçalves**, Zsuzsanna Varga, Stéphane Bouchonnet, V. Dulio, F. Dal Bello, C. Medana, Paola Calza, *Science of the Total Environment*, 2020, 755, 143556. doi.org/10.1016/j.scitotenv.2020.143556
8. *Comparison of advanced oxidation processes for the degradation of Maprotiline in water – kinetics, degradation products and potential ecotoxicity.* **Nuno P.F. Gonçalves**, Zsuzsanna Varga, Edith Nicol, Paola Calza, Stéphane Bouchonnet, *Catalysts* 2021, 11(2), 240. doi.org/10.3390/catal11020240

9. *Doped Zinc Oxide Photocatalysts applied to water: decontamination and disinfection.* Ilaria Berruti, **Nuno P.F. Gonçalves**, Inmaculada Polo-Lopez, Isabel Oller, Cristina Paganini, Paola Calza, *submitted to Applied Catalysis B: Environmental.*
10. *Degradation of the antifungal pharmaceutical clotrimazole by UVC and Vacuum UV irradiation: kinetics, transformation products and attenuation of toxicity.* **Nuno P.F. Gonçalves**, Oihane del Puerto, Claudio Medana, Paola Calza, Alessandra Bianco Prevot and Peter Roslev, *submitted to Journal of Hazardous Materials.*
11. *Elucidation of photoinduced transformations of Aliskiren in river water using liquid chromatography high-resolution mass spectrometry.* **Nuno P.F. Gonçalves**, Lucia Iezzi, Masho H. Belay, Valeria Dulio, Nikiforos Alygizakis, Federica Dal Bello, Claudio Medana, Paola Calza, *submitted to Science of the Total environment.*
12. *Biochar waste-based ZnO materials highly efficient photocatalyst for water treatment.* **Nuno P.F. Gonçalves**, Mirtha A.O. Lourenço, Simone R. Baleuri, Stefano Bianco, Pravin Jagdale, Paola Calza, *in preparation.*

Oral communications

1. *Humic Acid Coated Magnetic Nanoparticles as Highly Efficient Heterogeneous Photo-Fenton Materials for Wastewater Treatments.* **Nuno P.F. Gonçalves**, M. Minella, D. Fabbri, P. Calza, A. Bianco Prevot, 19th European Meeting on Environmental Chemistry, 3-6th December 2018, Royat, France.
2. *Deep insights into synthesis and performance of hybrid iron-based/humic acid nanoparticles for the degradation of organic pollutant.* Bianco Prevot, **N.P.F. Gonçalves**, P. Calza, M. Minella, D. Fabbri, G. Magnacca, M. Brigante, G. Mailhot, 2019 Workshop on Applications of Multi-scale Approaches in Environmental chemistry, 22-28th April 2019, Rennes, France.
3. *Advanced oxidation processes: new materials and applications.* **Nuno P.F. Gonçalves**, M. Minella, NIS Colloquium, 16-17th May 2019, UNITO, Italy.
4. *Photo-activation of persulfate and hydrogen peroxide by humic acid coated magnetic nanoparticles for bisphenol A degradation.* **Nuno P.F. Goncalves**, Marco Minella, Debora Fabbri, Paola Calza, Gilles Mailhot, Marcello Brigante, Alessandra Bianco Prevot, 6th European Conference on Environmental Applications of Advanced Oxidation Processes, 26-30th June 2019, Portoroz, Slovenia.

5. *Humic coated magnetic particles as highly efficient heterogeneous photo-Fenton materials for waste water treatments.* M. Minella, **Nuno P.F. Gonçalves**, D. Fabbri, P. Calza, C. Malitesta, E. Mazzotta, C. Minero, A. Bianco Prevot, XXVIII Congress of the Analytical Chemistry Division (BARI ANALITICA 2019), 22-26th September 2019, Bari, Italy.
6. *Comparative Study of Persulfate and Hydrogen Peroxide Activation by Humic Acid Coated Magnetic Materials for BPA degradation: A Life Cycle Assessment Evaluation.* **N.P.F. Gonçalves**, M. Costamagna, M. Minella, M. Brigante, A. Bianco Prevot, 20th European Meeting on Environmental Chemistry (EMEC20), 2-5th December 2019, Lodz, Poland.
7. *Water treatment and sustainability: focus on removal of contaminates of emerging concern.* **Nuno P.F. Gonçalves**, Zsuzsanna Varga, LCM seminar at Ecole Polytechnique, 13th December 2019, Palaiseau, France.
8. *Water Treatment Technologies”, Seminar at Chemistry Department.* **Nuno P.F. Gonçalves**, Aalborg University, 12th November 2020, Aalborg, Denmark.

Panel communications

1. *Development of oxides doped with transition metals and its exploitation to pollutants abatements.* P. Calza, A. Giorgini, **N. P.F. Gonçalves**, C. Gionco, A. Bianco Prevot, M.C. Paganini, 10th European meeting on Solar Chemistry and Photocatalysis: Environmental Applications (SPEA10), 4-8th June 2018, Almeria, Spain.
2. *The effect of cobalt doping on the efficiency of semiconductor oxides in the photocatalytic water remediation.* **N. P.F. Gonçalves**, M. C. Paganini, P. Armillotta, E. Cerrato, P. Calza, International Conference on Chemical Energy and Semiconductor Photochemistry, 4-6th September 2019, Trabzon, Turkey.
3. *Persulfate activation by hybrid magnetite/humic acid nanoparticles for the photodegradation of bisphenol A.* Bianco Prevot, **Nuno P.F. Gonçalves**, Paola Calza, M. Minella, D. Fabbri, M. Brigante, G. Mailhot, XXVIII Congress of the Analytical Chemistry Division, Bari, 22-26th September 2019, Italy.
4. *Elucidation of environmental fate of Maprotiline and Aliskiren drugs in natural waters: Identification of degradation products via HPLC-HRMS.* **Nuno P.F. Gonçalves**, Masho H. Belay, Elisa Robotti, Claudio Medana, Alessandra Bianco Prevot, Paola Calza, American Society of Mass Spectrometry 2020 Reboot - online, 1-12th June 2020.

5. *Ecotoxicity of azole fungicides after UVC and Vacuum-UV irradiation.* Oihane Del Puerto, **Nuno P.F. Gonçalves**, Paola Calza, Alessandra B. Prevot and Peter Roslev, Society of Environmental Toxicology and Chemistry, 3-6th May 2021, online.
6. Mitigation of glyphosate ecotoxicity by vacuum/UV-C treatment. Sigrid B. Fogh, Oihane Del Puerto, **Nuno P.F. Gonçalves** and Peter Roslev, Society of Environmental Toxicology and Chemistry, 3-6th May 2021, online.

PhD Schools Attended

- Summer School in statistics: “Introduction to Basic Statistical Tools and Data Analysis in Research, (Ioannina University/UPO University, 23-24th September 2020).
- Winter School on Mass Spectrometry, École Polytechnique de Paris, France, 4-8th March 2019.
- Summer School on Micropollutant Analysis and Abatement, AAU, Denmark, 27-29th August 2018.
- Winter School on Photochemistry and Depollution, CNRS, France, 25-27th April 2018.

Outreach Activities

- Researcher’s Night at Università Piemonte Orientale, Alessandria, Italy, 29th September 2018.
- AQUALity Lab, laboratorial experiments for 61 Students and 6 teachers from secondary school Lagrange in Cambiano, University of Turin, Italy, 20th February 2019.
- PrimaVera Festa, Experiments for students at school Mirafiori Primo Levi Liceo, Torino, Italy, 17th May 2019.
- Researcher’s Night at University of Turin, Italy, 27th September 2019.
- AQUALity Lab, laboratorial experiments for Junior High School students, University of Turin, Italy, 12th February 2020.

Co-supervisor Activities

- Master’s student: Simone R. Baleuri: “Synthesis of hybrid materials for wastewater treatment”, University of Turin, 2020-2021.

Didactic Activities

- Laboratory classes of Advanced Oxidation Processes - Prof. Alessandra Bianco Prevot, 14-21st May 2019.
- Laboratorial supervision of Germán Fernández Moreno - master's project- Erasmus Mundus/University of Valencia, University of Turin - 2019/2020.
- Laboratorial supervision of Lucia Iezi - master's project, University of Turin - 2019/2020.

Periods Abroad

- October 9th - December 7th 2018, January 2019 (3M)
CNRS – Clermont Ferrand, France. Tutor: Prof. Marcello Brigante
Identification of reactive species and mechanistic studies.
- October 20th - December 19th 2019 (2M)
École Polytechnique Palaiseau, France. Tutor: Prof. Stéphane Bouchonnet
Test modelisation approaches comparing with direct analysis of photo treated samples to identify CECs degradation products and degradation mechanisms.
- March 2nd- March 31st 2020 (1M)
LiqTech, Copenhagen, Denmark. Tutor: Dr. Victor Candelario
To study membrane processes and to help in developing a CECs analysis protocol with in-house instruments.
- October 18th- December 17th 2020 (2M)
Aalborg University, Denmark. Tutor: Prof. Peter Roslev
Methods for evaluating the toxicity of CECs and of their by-products.